Transactions of the ASME

Journal of Engineering for Gas Turbines and Power

Published Quarterly by The American Society of Mechanical Engineers

VOLUME 109 • NUMBER 1 • JANUARY 1987

TECHNICAL PAPERS

TECHNICAL BRIEFS

ANNOUNCEMENTS

Technical Editor
ARTHUR J. WENNERSTROM
Senior Associate Editor
G. K. SEROVY
Associate Editors
Advanced Energy Systems
S. I. FREEDMAN
Environmental Control
H. E. HESKETH
Fuels and Combustion Technologies
R. E. BARRETT
Gas Turbine
S. KUO
Internal Combustion Engine
K. J. SPRINGER
Nuclear Engineering
S. M. CHO
Power
R. W. PORTER

BOARD ON COMMUNICATIONS
Chairman and Vice-President
K. N. REID, JR.

Members-at-Large
W. BEGELL
J. T. COKONIS
M. FRANKE
W. G. GOTTENBERG
M. KUTZ
F. LANDIS
J. R. LLOYD
T. C. MIN
R. E. NICKELL
R. E. REDER
F. W. SCHMIDT

President, **N. D. FITZROY**
Executive Director,
PAUL ALLMENDINGER
Treasurer, **ROBERT A. BENNETT**

PUBLISHING STAFF
Mng. Dir., Publ., **J. J. FREY**
Dep. Mng. Dir., Pub.,
JOS. SANSONE
Managing Editor,
CORNELIA MONAHAN
Sr. Production Editor,
VALERIE WINTERS
Editorial Prod. Asst.
MARISOL ANDINO

Transactions of the ASME, Journal of Engineering for Gas Turbines and Power (ISSN 0022-0825) is published quarterly (Jan., Apr., July, Oct.) for $85 per year by The American Society of Mechanical Engineers, 345 East 47th Street, New York, NY 10017. Second class postage paid at New York, NY and additional mailing offices. POSTMASTER: Send address change to The Journal of Engineering for Gas Turbines and Power, c/o The AMERICAN SOCIETY OF MECHANICAL ENGINEERS, 22 Law Drive, Box 2300, Fairfield, NJ 07007-2300."

CHANGES OF ADDRESS must be received at Society headquarters seven weeks before they are to be effective. Please send old label and new address.

PRICES: To members, $24.00, annually; to nonmembers, $85.00.

Add $6.00 for postage to countries outside the United States and Canada.

STATEMENT from By-Laws. The Society shall not be responsible for statements or opinions advanced in papers or ... printed in its publications (B 7.1, para. 3).

COPYRIGHT © 1987 by the American Society of Mechanical Engineers. Reprints from this publication may be made on condition that full credit be given the TRANSACTIONS OF THE ASME – JOURNAL OF ENGINEERING FOR GAS TURBINES AND POWER, and the author, and date of publication be stated.

INDEXED by Engineering Information

Downloaded 03 Jun 2010 to 171.66.16.159. Redistribution subject to ASME license or copyright; see http://www.asme.org/terms/Terms_Use.cfm

Thermodynamic Evaluation of Gas Turbine Cogeneration Cycles: Part I—Heat Balance Method Analysis

I. G. Rice, P.E.
Consultant,
Spring, TX 77383
Fellow ASME

This paper presents a heat balance method of evaluating various open-cycle gas turbines and heat recovery systems based on the first law of thermodynamics. A useful graphic solution is presented that can be readily applied to various gas turbine cogeneration configurations. An analysis of seven commercially available gas turbines is made showing the effect of pressure ratio, exhaust temperature, intercooling, regeneration, and turbine rotor inlet temperature in regard to power output, heat recovery, and overall cycle efficiency. The method presented can be readily programmed in a computer, for any given gaseous or liquid fuel, to yield accurate evaluations. An X–Y *plotter can be utilized to present the results.*

Introduction

Open-cycle gas turbines are being applied in increasing numbers and sizes for cogeneration around the world whereby both power and heat are produced for process use with the heat, generally in the form of steam. There are a number of gas turbines on the market today – ranging from 1 MW to 100 MW – providing a variety of cycle efficiencies, cycle pressure ratios, firing temperatures, exhaust temperatures, and exhaust flow rates. Heat recovery of one form or another plays an important part in equipment selection; and the variations and interrelationship of gas turbine efficiency, excess air, exit temperature, and exhaust gas mass flow rates are sometimes not fully understood or appreciated, particularly regarding the power-to-steam ratio.

The first law of thermodynamics is applied in this paper whereby a graphic solution has been developed to provide insight into the overall thermodynamic process of producing both (*a*) power, and (*b*) heat in terms of (*c*) fuel consumed per unit mass of air flow of a system, (*d*) excess air present, and (*e*) the final stack temperature exiting the system. This paper sets forth a graphic solution to the problem and provides a means to visually understand the interaction of the abovementioned five variables for purposes of optimization. Insight into future and more advanced gas turbines optimized for cogeneration is given.

Early work was done on the heat balance approach some 25 years ago [1] when applying industrial gas turbines to chemical plants, refineries, and paper mills. Later, in 1968, a more detailed heat balance explanation was published [2] giving an abbreviated graphic solution. A broader and more inclusive method is now presented in this paper which can be adapted to computers for quite exact results and then graphed by an X–Y plotter directly from the computer.

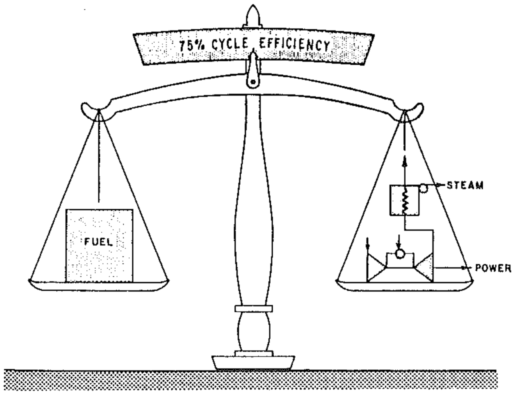

Fig. 1 Heat balance scales

It should be stated that thermodynamics is not the total cogeneration consideration. There are six general areas of concern for overall gas turbine cogeneration evaluation: (1) cycle efficiency, (2) ratio of power to steam, (3) capital costs, (4) operating costs, (5) maintenance costs, and (6) government requirements. The high ratio of gas turbine power to steam is the primary reason for selecting a gas turbine. Therefore incremental power can dictate for a given steam demand. Other factors such as shipment time, unit size, and user experience can also affect selection, but this paper focuses on thermodynamics and cycle efficiency evaluation and points to the division of power to steam when evaluating one gas turbine compared to another.

Heat Balance

A pictorial representation of the heat balance method is shown in Fig. 1. The fuel input (heat release) is on the left of the scales which must equal the total output on the right of the

---

Contributed by the Gas Turbine Division of The American Society of Mechanical Engineers and presented at the 31st International Gas Turbine Conference and Exhibit, Düsseldorf, Federal Republic of Germany, June 8–12, 1986. Manuscript received at ASME Headquarters December 26, 1985. Paper No. 86-GT-6.

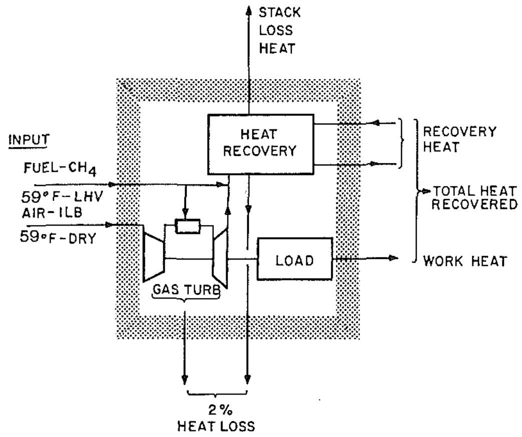

Fig. 2 Generalized heat balance diagram

scales where the output is the sum of all the outputs. The scales of justice, so to speak, of the heat balance are set forth by the first law and must be obeyed. As an indication of the justice rendered, an overall cycle efficiency is shown as 75 percent for the power and steam output and the particular power-to-steam ratio required.

A schematic diagram of the heat balance is shown in Fig. 2. Air and fuel enter at an ambient ISO of 59°F (15°C) on the left side. Work and heat exit to the right whereas the equipment system loss, shown as 2 percent, flows downward. The stack loss exits upward. All outputs are thus included. The ISO inlet temperature of 59°F is assumed as the datum. However, any ambient temperature can be selected for any particular heat balance desired.

Current simple-cycle gas turbine efficiencies run from about 25 percent to 37 percent based on the lower heating value (LHV) of the fuel. Thus, 63–75 percent of the heat is rejected as sensible heat in the exhaust and as equipment loss. Gas turbines are unique in one respect, in that only 1½–3 percent of the heat released by the fuel is rejected as equipment heat system loss associated with (1) casing radiation and convection, (2) bearings, (3) air leakage, (4) incomplete combustion, and (5) turbine-driven auxiliaries such as shaft-driven pumps.

The parasitic system heat losses of heat recovery boilers, fired and unfired, range from about ½ percent to 1½ percent of the heat being recovered. Therefore, it is for the above two considerations of the gas turbine and heat recovery equipment that an overall 2 percent equipment loss can be assumed for simple-cycle turbines for most cases and good results obtained. However, this total loss can be varied to meet any particular case. The full spectrum from the gas turbine operating alone, to nonfired heat recovery, to supplementary fired systems, and finally to fully fired boilers with 10 percent excess air can be analyzed graphically by selecting the proper variables and coordinates as will be explained.

Fuel Burned

There are a variety of fuels that can be burned in gas turbines, and the type of fuel burned has a slight effect on gas turbine efficiency and exhaust temperature. A review of this effect is given in [3]. It is assumed that the fuel burned is at the required pressure which is generally the case for gas turbine cogeneration plants where natural gas is available from high-pressure pipelines. The generalized equation of reaction is given as

$$c(\text{fuel}) + O_2 \rightarrow c_1(CO_2) + c_2(H_2O) \qquad (1)$$

where c, c_1, and c_2 are the coefficients of the chemical reaction. The effect of any particular hydrocarbon fuel is slight for most gas turbine fuels, excluding pure hydrogen on one end of the spectrum and methyl alcohol on the other.

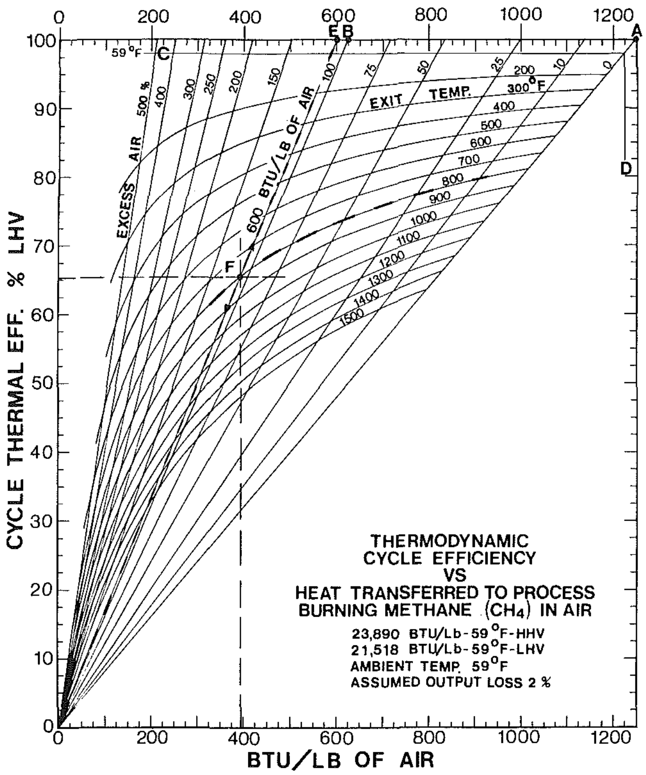

Fig. 3 Thermodynamic heat balance map

Most cogeneration gas turbines burn natural gas which is basically methane (CH_4). Therefore, the graphs and examples used in this paper are based on this type fuel. The procedure given can be followed for any other specific fuel now that computers and appropriate software programs are available for very accurate enthalpies of the products of combustion for any particular fuel/air ratio. Boiler people generally speak in terms of excess air, and therefore excess air is used in the graphic solution. However, the air/fuel ratio, or the reciprocal, fuel/air ratio or theoretical air can be applied as will be shown. The Keenan and Kaye *Gas Tables* is given as reference for fuels, calculating procedures, and enthalpies used in this paper [4].

Calculations

The following convenient formulas are given and used in the development of the solution

Specific fuel input

$$= \frac{\text{Specific heat release LHV of fuel}}{\text{Theoretical air} \times (1+X)} \qquad (2)$$

where specific fuel input is in Btu/lb of air or kJ/kg of air and X is the fractional value of excess air.

$$F/A = \frac{1}{\text{Theoretical air } \times \ (1+X)} \qquad (3)$$

where F/A is the fuel/air ratio by weight and A/F is the air/fuel ratio by weight.

Considering a 2 percent total parasitic system loss as explained earlier, the formula for cycle efficiency is given as follows

$$\text{Cycle efficiency} = 0.98 \times \left[\frac{(\text{Specific fuel input}) - (h_2 - h_1)(1 + F/A)}{\text{Specific fuel input}}\right] \qquad (4)$$

where specific fuel input is the total fuel input per unit mass of air flow; h_2 is the stack enthalpy of the gas flow; h_1 is the stack enthalpy cooled to 59°F (15°C) of gas flow with no condensation taking place (sensible heat only); F/A is the fuel/air ratio by weight.

Formula (4) can be simplified to a more usable form as given below

$$\text{Cycle efficiency} = 0.98 \times \left[1 - \frac{(h_2 - h_1) \times (1 + F/A)}{\text{Specific heat release LHV} \times F/A}\right] \quad (5)$$

Sample calculations are given in the appendix.

Heat Balance Graph

It is desirable for evaluation purposes to place five pertinent variables on one graph in a form in which each variable can be separated, ascertained, and read. These variables are: (1) fuel input, (2) work output, (3) gas turbine exhaust temperature, (4) heat to the process, and (5) final system stack temperature.

An X-Y plot of cycle efficiency (LHV) versus heat to the overall process in terms of work and/or process heat expressed specifically per unit mass of airflow can be cross-plotted with both fuel lines and exit temperature lines to provide the desired result. This type graph for methane fuel is presented as Fig. 3 where work and thermal heat are interchangeable according to the first law of thermodynamics. This interchange is important to remember.

On the very top line of the graph starting at 100 percent efficiency and zero heat output and moving to the right to Point A, points are plotted for the heat being released for various values of excess air ranging from 500 percent to 0 percent (stoichiometric). Point A value is 1247.42 Btu/lb of air (2901.5 kJ/kg) for methane fuel using formula (2) with zero fraction of excess air. At 500 percent excess air the value is calculated to be 207.90 Btu/lb (483.6 kJ/kg). This top line represents 100 percent heat recovery of the products of combustion when cooled to the ISO inlet of 59°F, the assumed datum.

Straight lines are drawn from the top points to the origin of the graph for zero efficiency and zero output. Obviously, along these straight lines cycle efficiency is directly proportional to heat transferred to the process (work or thermal heat). At 50 percent cycle efficiency the output for zero excess air is half of the stoichiometric value, or 623.71 Btu/lb of air (1450.7 kJ/kg). Likewise, for 100 percent excess air and 100 percent cycle efficiency the value at point B is again 623.71. The straight lines thus plotted represent the particular fuel burned per pound of air for the particular amount of excess air.

It should be noted that Fuel/Air ratio notation F/A and Air/Fuel ratio notation A/F as well as percent theoretical air can be used interchangeably. Excess air is selected only as a guide or "feel" to boiler engineers and those familiar in working with this term. Excess air also gives a better visualization of what takes place and shows how much extra air is present up and beyond what is required for stoichiometric combustion.

The next step in the development of the graph is to block out 2 percent cycle efficiency from the top of the graph for the assumed amount of parasitic system loss not recoverable as represented by horizontal line C to vertical line D. This heat is lost and is not available to the process as earlier concluded. The map of the area below and to the left of lines C to D represents the total availability of the heat. Lines C to D also represent the datum for a 59°F ambient as noted on the graph in Fig. 3. Finally, by applying formula (5) for each excess air line, points are obtained for selected exit temperatures from 200 to 1500°F (93.3 to 816°C). Sample calculations are given in the appendix. Curved temperature lines are now drawn crosswise through the straight fuel lines to provide a complete map for the five variables listed previously.

As an example of how the graph works, assume that fuel is burned giving a fuel input value of 600 Btu/lb of air, point E, which corresponds to 107.9 percent excess air calculated from formula (2) for the gas being cooled to 59°F. It is desirable to consider the gas at 800°F (426.7°C), point F. The cycle efficiency can be read off the graph as 65.6 percent and the heat transferred to the process as 394 Btu/lb of air (916.4 kJ/kg). Note again that this transferred energy can be in the form of work or heat or a combination of the two where work and heat are interchangeable.

Current Gas Turbine Evaluations

Pertinent data on five industrial gas turbines presently on the market today representing the state of the art are given in Table 1. These data are plotted on an expanded and sectionalized portion of Fig. 3 which is presented as Fig. 4. Cycle

Table 1 Base-load gas turbine data, ISO conditions*

	A GE LM2500PE	B R-R R-B211C	C GE LM5000A	D W 501-D	E GE PG7111E
1 Shaft output**					
HP	29,500	34,000	43,525	138,699	103,682
kW	22,007	25,364	32,469	103,469	77,347
2 Cycle efficiency					
Percent LHV	37.0	36.4	37.4	33.4	32.3
3 Cycle pressure ratio	18.7	20.0	30.0	14.0	11.7
4 Air flow					
lb/s	147.5	196.2	265.0	801.0	605.0
kg/s	66.9	89.0	120.2	323.3	274.4
5 Specific work output					
Btu/lb air	141.4	122.6	116.2	122.4	121.2
kJ/kg air	328.9	285.2	270.3	284.7	281.9
6 Turbine rotor inlet temperature					
°F	2214	2133	2113	2025	2019
°C	1212	1162	1156	1107	1104
7 Exhaust temperature					
°F	955	887	797	970	1000
°C	513	475	425	521	538
8 Exhaust excess air					
percent	226	270	302	241	232

---

*Data published by *Gas Turbine International Catalog*, 1984–1985 [6]

**Assumed generator loss of 2 percent added as required

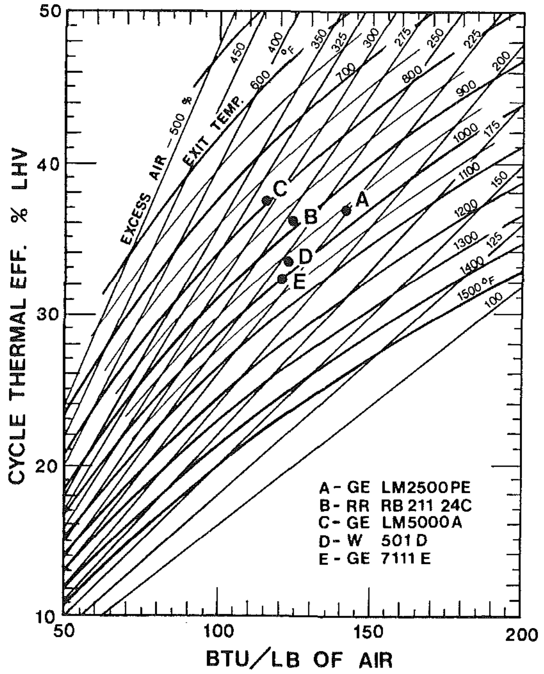

Fig. 4 Heat balance examples for five current gas turbines

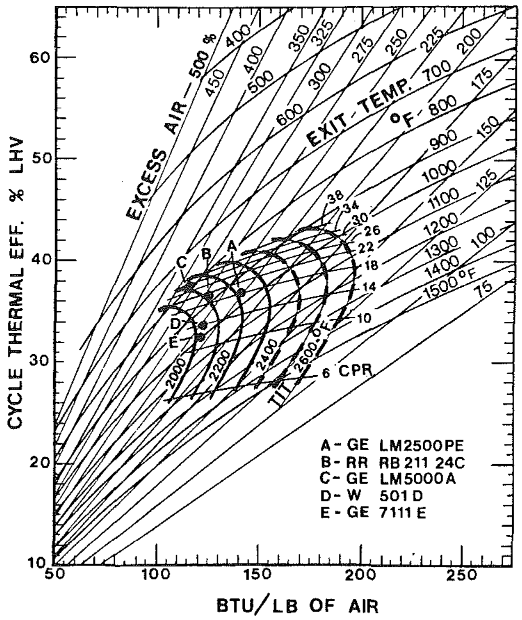

Fig. 5 Effect of cycle pressure ratio and turbine inlet temperature on heat balance

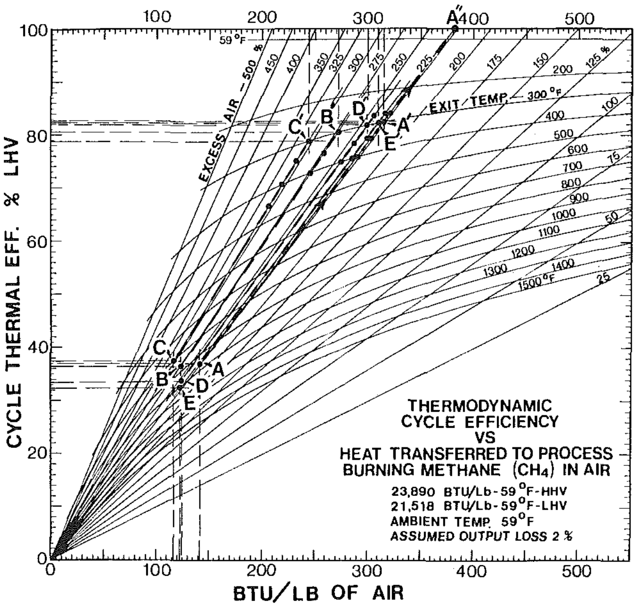

Fig. 6 Heat recovery for five gas turbines

efficiency, work output, fuel input (excess air), and exhaust temperature are all shown on the graph for each of the five turbines.

It can be noted that turbine A, the LM2500, with the highest turbine rotor inlet temperature (TRIT) of 2214°F (1212°C) and a cycle pressure ratio (CPR) of 18.7, produces the highest specific work output of 141.4 Btu/lb of air (328.9 kJ/kg) at a respectable cycle efficiency of 37 percent LHV. When these data are plotted on the heat balance graph of Fig. 4, particular attention is given to the exhaust temperature shown on the graph to correspond very closely with the 955°F (513°C) given in Table 1. This very close correlation shows that the 2 percent system loss selection is quite appropriate.

Data points for turbines B, C, D, and E are all plotted on Fig. 4, and in each case the correlation of all the data is excellent, again showing that the 2 percent system loss is most appropriate; and it can be concluded that the heat balance approach of Figs. 3 and 4 can be used for most, if not all, simple-cycle gas turbines to yield very accurate results. This method of heat balance analysis has actually been used on a large number of gas turbines over a period of years by the author with very good results. Erroneous gas turbine data will show up immediately on the graph.

Effect of CPR and TRIT. Lines of cycle pressure ratio (CPR) and turbine rotor inlet temperature (TRIT) superimposed on Fig. 4 for the data points of the five gas turbines of Table 1 are shown in Fig. 5. The full story is now represented graphically on one chart to correlate the additional variables of CPR and TRIT. There is almost a perfect match for the TRITs and CPRs for all five gas turbines. The CPR and TRIT lines for values of TRIT from 2000 to 2300°F (1093 to 1260°C) are shown as solid lines and are representative of state-of-the-art machines. TRIT lines for 2400 to 2600°F (1316 to 1427°C) are shown as dashed lines and are extrapolations and projections of future and more advanced industrial gas turbines not yet available.

Heat Recovery Without Supplementary Firing

As stated in the introduction of this paper, the gas turbine itself cannot be evaluated by cycle efficiency alone. Heat recovery must also be included. The gas turbine and heat recovery systems must be treated as a whole wherein the heat going into work and the heat going into steam must both be weighted separately and jointly. Reference is now made to Fig. 6 which provides a means of evaluating the gas turbine heat recovery system for each of the five gas turbines listed in Table 1.

Turbine A data for the LM2500 are plotted as point A on Fig. 6. Considering a final stack temperature of 300°F (149°C) the heat is recovered at a constant percent excess air from point A to point A′ wherein no fuel is added in the process. The total fuel consumed is the projection to point A″ giving 382.2 Btu/lb of air (141.4/0.37) (889 kJ/kg). The heat converted to gas turbine work plus the heat recovery heat from A to A′ is shown to be 314.5 Btu/lb of air (731.5 kJ/kg) of which 141.4 Btu/lb (328.9 kJ/kg) is in the form of work. The overall cycle efficiency is shown on the graph to be 82.3 percent LHV. Observe the division of work and heat.

Gas turbines D and E yield the same overall cycle efficiency

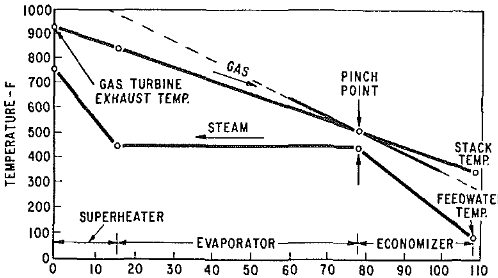

Fig. 7 Temperature-enthalpy diagram for heat recovery boiler

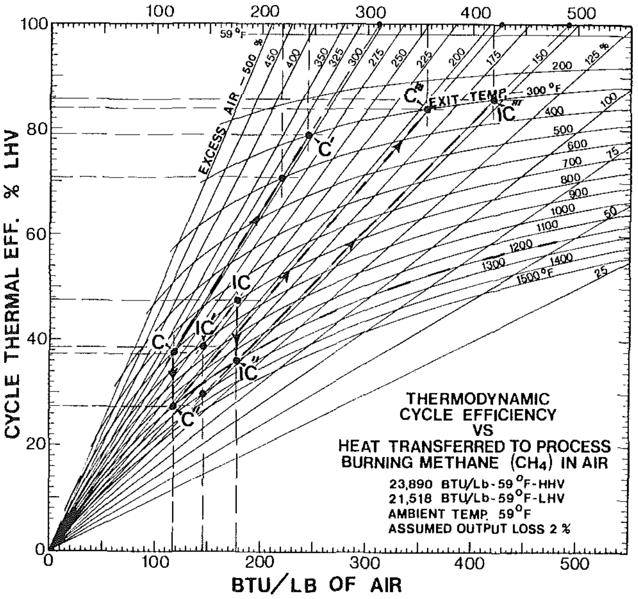

Fig. 8 Supplementary firing for heat recovery

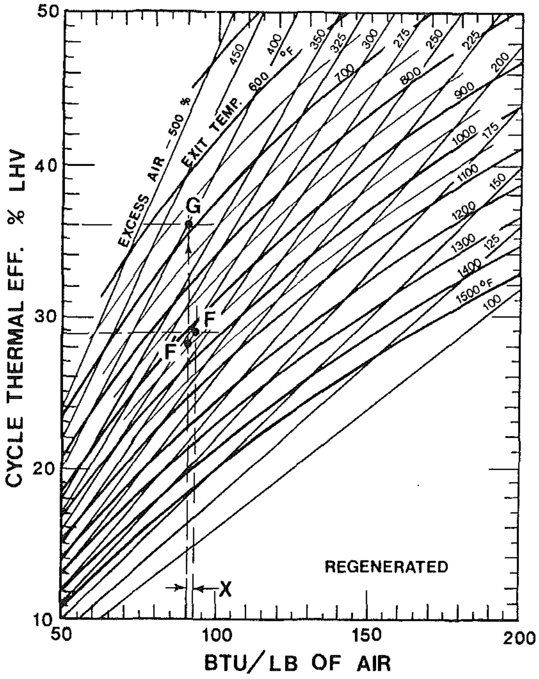

Fig. 9 Regenerated gas turbine cycle heat balance

of about 82 percent LHV because they operate at about the same excess air. Note that these two units each produce about the same work output per unit mass air flow and they have relatively close CPRs, TRITs, and exhaust temperatures. However, turbine A produces appreciably more specific work and about the same heat to steam resulting in a higher ratio of power to steam at a higher overall cycle efficiency. Turbine B, having a higher CPR and a slightly lower exhaust temperature, but with greater excess air, yields an overall cycle system efficiency of about 80.2 percent LHV for a 300°F (149°C) stack temperature as shown in Fig. 6. The relationship of ratio of power to steam and overall cycle efficiency shows up on the bottom line of this graph.

Turbine C, which has the highest gas turbine cycle efficiency, the highest CPR, the highest percent excess air, the lowest exhaust temperature, and the lowest specific work output per unit of mass air flow also yields the lowest system overall cycle efficiency of about 78.8 percent for a 300°F (149°C) stack temperature. When utilizing heat recovery boilers, there is another factor that must be considered due to turbine C's lower exhaust temperature of 797°F (425°C). Reference is made to Fig. 7 showing the effect of the boiler pinch point on final stack temperature obtainable as a function of gas turbine exhaust temperature. Therefore, considering even moderate boiler pressures, a stack temperature notably higher than 300°F (149°C) is all that can be realized as represented by the three dots below point C′. A dual pressure boiler can be applied to help lower the stack temperature.

Turbines A, D, and E can generate higher pressure and temperature steam than turbine C for any given stack temperature. This higher pressure steam at a higher temperature can be expanded through a topping steam turbine to generate incremental power at about 80 percent efficiency to further increase the overall ratio of power to steam.

In conclusion, Turbine A yields the highest specific work output and the highest overall system combined cycle efficiency. The work output increase over the other four units is significant when considering that work (power in the form of kW) is worth about three times that of the heat recovered. This decided advantage is due to the CPR yielding about the optimum (maximum) specific work (Fig. 5) and the highest TRIT giving incremental work over the other units wherein a high exhaust temperature is realized for heat recovery boilers. However, the shaft output of the five units varies from 22,007 kW for turbine A to 103,469 kW for turbine D, and selection can be influenced by other factors mentioned in the introduction.

Turbine C does not perform too well for either specific work output or overall system cycle efficiency even with its TRIT of 2113°F (1156°C). However, as can be seen from Fig. 5, if this unit is fired at a TRIT of 2400°F (1316°C) the reverse would be the case and turbine C would yield the highest specific work and a maximum overall system cycle efficiency. An effort is being made to achieve this end by applying steam cooling [5]. Here again, other factors such as size, capital cost, and wide steam demand fluctuations can favor turbine C in its present form. Turbine C has the highest simple-cycle efficiency of the five turbines as can be noted.

Supplementary Firing and Heat Recovery

Supplementary firing of the exhaust gases to any particular temperature provides a means to increase heat recovery, and this method is often used in cogeneration. Figure 8 is presented to illustrate what takes place and the effect supplementary firing has on overall system efficiency. Considering turbine C, if no supplementary firing takes place, heat is recovered from point C to point C′ as shown, to yield an overall cycle efficiency commensurate with the final stack temperature. Note that the overall cycle efficiency will range from about 60 to 79 percent depending upon the stack temperature achieved. When its exhaust is supplementary fired to 1200°F (649°C), as an example, there is no increase in work output, and the amount of fuel added is shown by point

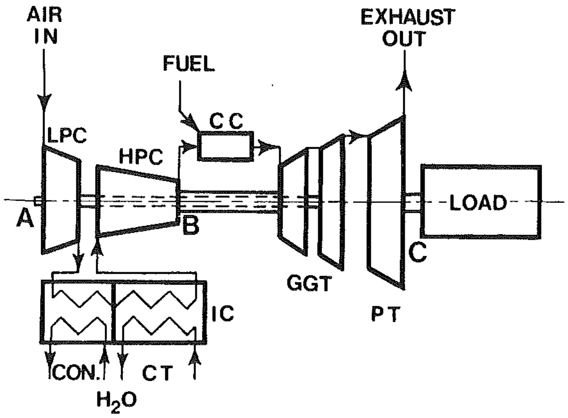

Fig. 10 Intercooled gas turbine schematic diagram

C moving vertically downward to point C″ as the exhaust temperature is raised from 797°F (425°C) to 1200°F (649°C), and the excess air is reduced from 302 percent to about 190 percent. Heat is then extracted to a stack temperature of perhaps 300°F (149°C), point C‴. Note that now the overall cycle efficiency has risen to about 82 percent and there is a slippage of the work-to-heat ratio.

Supplementary firing, as explained in the previous example, has increased the amount of heat to be recovered and at the same time has increased the overall cycle efficiency. A lower stack temperature is also realized. A higher pressure and temperature steam can be generated to yield topping steam turbine power. As can be observed, if the exhaust gases are supplementary fired to an even higher temperature than 1200°F (649°C) more process heat is recoverable, and the overall cycle efficiency continues to increase, but at a diminishing rate. Considering a fully fired boiler with 10 percent excess air, the overall cycle efficiency will rise to about 92 percent LHV which equates to the efficiency of a standard boiler with its efficiency generally given as 83 percent HHV for a 300°F (149°C) stack temperature for an ambient of 59°F (15°C). See Fig. 3 for this efficiency point.

Gas Turbine Regeneration

Figure 9 presents a heat balance graph on a regenerated cycle gas turbine and shows what takes place when a simple-cycle gas turbine is configured and fit with a regenerator. Published data for both a simple cycle and a regenerated cycle General Electric frame size 5 two-shaft turbine [M5352(B) and M5322R(B)] have been used [6].

Point F in Fig. 9 spots the performance data for the simple-cycle gas turbine. The published data correlate with the graph very well in all respects. A pressure loss is introduced by the introduction of the regenerator and a loss in work output takes place as denoted by point F′ and incremental work loss *X*.

The regenerated data are pinpointed at G. The graph also shows the stack temperature to be about 685°F (363°C) whereas the published data give 667°F (353°C). There appears to be about an 18°F (10°C) difference. It would seem that the 2 percent system loss assumed is a little too low and should be more correctly about 2.8 percent for a regenerative cycle where there is additional heat loss associated with convection and radiation loss of the piping and regenerator and possibly some small air leakage. Also the increased fixed losses are greater percentagewise in relation to the reduced fuel burned.

Gas Turbine Intercooling

Intercooling a high-cycle pressure-ratio gas turbine such as the LM5000 holds distinct possibilities. A schematic diagram of the cycle is shown in Fig. 10. Figure 11 is presented to show what takes place by intercooling a 30 CPR machine. Intercooling will increase work output and increase cycle efficiency slightly, but at the expense of some heat loss to the intercooler, as will be explained. The increase in work output raises the power-to-steam ratio which is important for cogeneration applications.

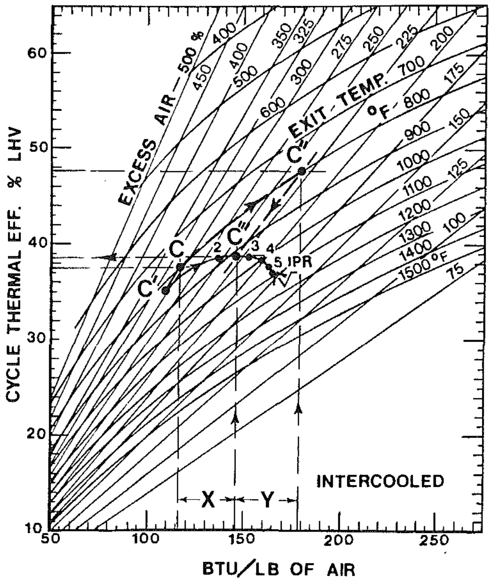

Fig. 11 Intercooled 30 CPR gas turbine heat balance showing effect of intercooler pressure ratio

It must be remembered that the bottom scale represents heat transferred to the thermodynamic process. This heat can be in the form of mechanical work or heat to a boiler or some other outside receiver, and the end point will always reflect the excess air, the stack temperature, and the cycle efficiency of the overall heat to the process. When considering intercooling, some of the heat is rejected to the cooling water, and the sum total of work and intercooler heat transfer makes up the total heat to the process for the end point (exhaust temperature). Returning to Fig. 11, and with reference to the preceding explanation, Point C represents the 30 CPR LM5000. The intercooler introduces about 3 percent pressure loss and point C moves to C′ considering no heat extraction by the intercooler. Work output efficiency points are plotted on the graph for different intercooling ratios of 2 to 5.48 (square root of 30). However, these end points do not reflect final exhaust temperature but only efficiency and percent excess air. These points are projections removing the intercooler loss as will be explained below.

Considering an intercooler ratio of 2.5 as an example, point C′ moves to point C″ at constant exhaust temperature of 797°F (425°C). Fuel is added to compensate for the lower compressor discharge temperature, and the excess air is reduced from 302 percent to about 230 percent. Work is increased by the amount shown as *X* while the intercooler heat rejection is represented by the amount *Y*. Point C″ is projected downward to point C‴ at constant excess air to remove the heat transferred to the intercooler to obtain gas turbine cycle efficiency. Data on the intercooler and gas turbine were taken from [6].

It can be noted that the gas turbine cycle efficiency rises slightly from the 37.4 percent of Table 1 to about 38.3 percent while the work output increases from the 116.2 value to 146 Btu/lb (339.6 kJ/kg) of air representing a sizable 25.6 percent increase in work output. However, the gas turbine exhaust temperature remains at about 800°F (427°C) as shown on the graph, point C″.

Heat recovery can be incorporated starting at point C″ and moving to the right at constant excess air to the desired final stack temperature. The amount of heat recovered, of course, starts at point C″ on the bottom scale so as not to include the intercooler loss. The final answer will have three output components: (*a*) work, (*b*) intercooler loss, and (*c*) heat to the heat recovery process. Note that while there is, in most instances, a nonrecoverable intercooler loss, the excess air is reduced and more heat can be extracted per unit mass of air by the heat recovery equipment because of the reduced slope of the lower excess air line which compensates somewhat for the intercooler loss.

Supplementary firing of the exhaust of an intercooled gas turbine is shown in Fig. 8, points IC, IC′, IC″, and IC‴, with the intercooling loss represented as (IC − IC′).

Summary

The graphic solution to the gas turbine heat balance problem, as presented in this paper, offers a rapid and accurate way of evaluating various open-cycle gas turbines and associated heat recovery and it shows the relationship of power-to-steam ratio to overall cycle efficiency and the potential cogeneration gains to be realized by increasing the turbine firing temperature. The effect of cycle pressure ratio has also been shown as well as the introduction of intercooling. The graphic solution presented can also be used for regenerative cycles compounded with intercooling as long as the first law of thermodynamics is not violated; that is, heat input must equal heat output wherein work and pure heat are interchangeable.

Specific formulas and sample calculations are given in the paper to allow the heat balance method presented to be programmed on a computer and plotted on an X-Y plotter for any number of different gas turbine and heat recovery cycles for various fuels and ambient conditions. This graphic solution provides considerable insight for cogeneration applications and takes the mystery out of variables such as cycle pressure ratio, firing temperature, excess air, exhaust temperature, and mass air flow.

Part II of this paper extends the graphic heat balance method to more complex cycles involving reheat and steam injection/cooling as well as intercooling and regeneration of the more advanced gas turbine cycles of the future.

Acknowledgments

Sincere appreciation is expressed to my wife, Carolyn Keyes Rice, for her continuing assistance, patience, and understanding. She has spent countless hours of her professional time on behalf of my research and study, and I am most grateful to her for this.

References

1 Rice, I. G., "Don't Waste That Gas Turbine Heat," *The Oil and Gas Journal*, Vol. 57, No. 27, June 29, 1959, pp. 66–70.

2 Rice, I. G., and Plumley, D. R., "Balance Your Gas Turbine Heat," *Hydrocarbon Processing*, Vol. 47, No. 4, Apr. 1968, pp. 154–160.

3 Leung, E. Y. W., "A Universal Correlation for the Thermal Efficiency of Open Gas Turbine Cycle With Different Fuels," ASME JOURNAL OF ENGINEERING FOR GAS TURBINES AND POWER, Vol. 107, July 1985, pp. 560–565.

4 Keenan, J. J., Kaye, J., and Chao, J., *Gas Tables*, Wiley, New York, 1980.

5 Casper, R. L., and Rucigay, J. C., "Design and Development of the General Electric LM5000 Industrial Package Power Plant," ASME Paper No. 85-GT-26.

6 *Turbomachinery International Handbook*, Vol. 25, No. 3, 1984–1985, pp. 1-110 and 1-111.

7 Rice, I. G., "Evaluation of the Compression-Intercooled Reheat Gas Turbine Combined Cycle," ASME Paper No. 84-GT-128.

APPENDIX

Sample Calculations

1 Input and output @ 100 percent efficiency for CH_4 fuel with 250 percent excess air

$$\frac{\text{Fuel input or output}}{\text{100 percent efficiency}} = \frac{\text{Heat release LHV}}{\text{TA}(1+X)} \tag{2}$$

$$= \frac{21{,}518}{17.25(1+2.50)} = 356.41 \text{ Btu/lb air}$$

2 Cycle efficiency @ 1000°F stack temperature, 250 percent excess air and 2 percent system loss for methane fuel

$$\text{Cycle efficiency} = 0.98\left[1 - \frac{(h_2 - h_1)\times(1+F/A)}{21{,}518 \times F/A}\right] \tag{5}$$

Step	Calculation	Results
1	Stack temperature, °F	1000
2	Excess air, percent	250
3	F/A – Formula (3) lb fuel/lb air	0.0165631
4	h_2 – Enthalpy of gas out Btu/lb gas	371.5*
5	h_1 – Enthalpy of gas cooled to 59°F, Btu/lb Gas	128.0*
6	Δh – Step 4 – Step 5 – Btu/lb gas	243.5
7	Cycle efficiency LHV formula (5)	0.29936

---

*Calculated from Keenan and Kaye *Gas Tables* for methane and component products of combustion

Fuel, CH_4 heating values and theoretical air values used in the calculations are as follows:

23,890 Btu/lb @ 59°F HHV
21,518 Btu/lb @ 59°F LHV
0.0579710 – Theoretical fuel – lb fuel/lb air
17.25 – Theoretical air – lb air/lb fuel

Thermodynamic Evaluation of Gas Turbine Cogeneration Cycles: Part II—Complex Cycle Analysis

I. G. Rice, P.E.
Consultant,
Spring, TX 77383
Fellow ASME

Complex open gas turbine cycles are analyzed by applying the heat balance method presented in Part I of this paper. Reheating, intercooling, regeneration, steam injection, and steam cooling are evaluated graphically to give a visual perspective of what takes place in terms of the overall heat balance when such complexities are introduced to the cycle. An example of a viable, new, intercooled regenerative cycle is given. A second example of a prototype reheat gas turbine is also included. The overall approach using the heat balance method can be applied to various cogeneration configurations when considering the more complex cycles of the future.

Introduction

Open-cycle gas turbines (simple and regenerative) have been widely applied throughout the world to various pipeline, refinery, petrochemical, paper mills, and utility plants over the past 35 years; more recently they have been applied to cogeneration, which is an outgrowth of this earlier, successful industrial experience. The simplicity of the first-generation simple-cycle machines coupled with their conservative firing temperatures and moderate cycle pressure ratios (CPRs) has been responsible, to a great extent, for their overall acceptance by industry.

The industrial gas turbine has come of age, and more complex cycles conceived and tried 30 years ago are now again appearing on the horizon with improved intercooling, regeneration, and even reheating. Developments of new blade cooling/steam injection techniques using air, steam, or a mixture thereof are underway. Greater use of ceramics is taking place. The second-generation industrial gas turbine introduced much higher CPRs upward of 30 in the 1970s. Turbine rotor inlet temperatures (TRITs) have risen to 2200°F (1204°C) as an extension of aircraft gas turbine developments.

The third-generation industrial gas turbine, fostered again by the aircraft industry and funded by NASA, is about ready to be launched. Even higher firing temperatures and CPRs are being planned which will incorporate more advanced computer-aided three-dimensional aerodynamics and improved materials of construction. This new family of advanced aircraft gas turbines being developed for ducted prop jets and unducted fan jets with CPRs of 38 to 42 and baseload turbine rotor inlet temperatures (TRITs) of 2250°F (1232°C) and above will provide prime candidates for the future industrial, utility, and cogeneration markets. History has a habit of repeating itself with regard to industrial use of proven aircraft gas turbine technology.

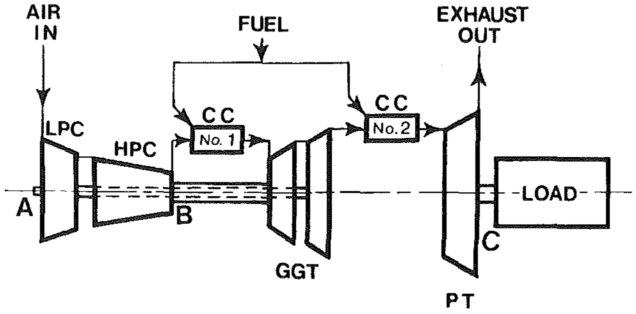

Fig. 1 *Reheat gas turbine schematic diagram*

The Japanese Government is funding an ambitious Research and Development program to develop a high CPR and TRIT reheat intercooled gas turbine targeted to achieve a 55 percent LHV combined-cycle efficiency. Advanced third-generation aircraft blade design and cooling techniques are being applied. This specific turbine will be discussed in this paper.

A close look at third-generation gas turbines will also be taken in the paper. The graphic heat balance solution presented in Part I will be applied to analyze some of these more advanced and complex cycles.

Reheat

Reheating is not new, and low-temperature application for peaking air storage is in successful operation today. Jet engine afterburning is also well known and established, but reheating for industrial gas turbines, when considering rather high TRITs, has not yet been developed. Technology is just now reaching a stage where such reheat is becoming practical and viable.

A schematic diagram of a reheat gas turbine is shown in Fig. 1 where a twin-spool high-cycle pressure ratio (CPR) gas generator exhausts to a reheat combustor, after which the reheated gas expands through a power turbine to drive a load. Performance calculations have been previously published on this particular arrangement [1, 2] giving performance parameters. An example of a 38 CPR gas generator firing at

---

Contributed by the Gas Turbine Division of The American Society of Mechanical Engineers and presented at the 31st International Gas Turbine Conference and Exhibit, Düsseldorf, Federal Republic of Germany. June 8-12, 1986. Manuscript received at ASME Headquarters December 26, 1985. Paper No. 86-GT-7.

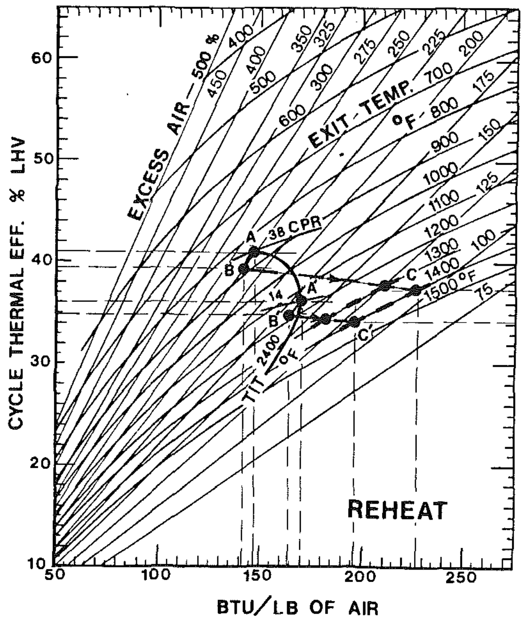

Fig. 2 Reheat gas turbine heat balance

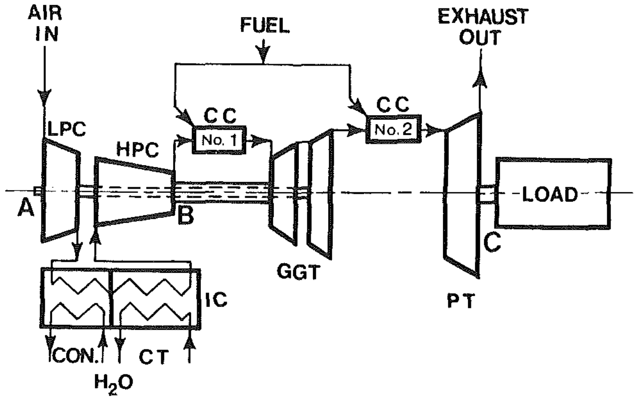

Fig. 3 Intercooled reheat gas turbine schematic diagram

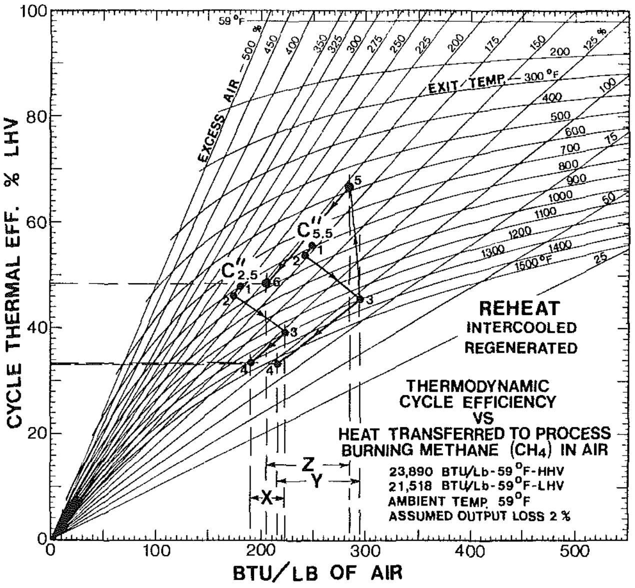

Fig. 4 Intercooled reheat and regenerated gas turbine heat balance graph

2400°F TRIT (1316°C) will illustrate how the heat balance graph of Fig. 5 of Part I of this paper can be used to analyze the introduction of reheat. It is assumed that adequate cooling and materials are incorporated in the design to operate at this CPR and TRIT (see Fig. 2).

The gas turbine will operate at about 41 percent cycle efficiency LHV and will have an output of about 147 Btu/lb of air (342 kJ/kg) as can be noted per point A. When a reheat combustor is added, a 3–4 percent pressure drop takes place and point A moves to point B where no reheat fuel is yet burned. The cycle efficiency drops and the exhaust temperature rises. Then fuel is burned in the reheat combustor and point B moves to point C. The exhaust temperature will rise in accordance with the amount of reheat fuel added, but generally the reheat TRIT will be about 250 to 300°F (139 to 167°C) lower than the gas generator TRIT. The last stage rotating blade, even when cooled, is generally the limiting factor, but the exhaust temperature can vary with the size of the unit (mass air flow). This limitation is similar to the last stage bucket situation of a steam turbine. Therefore, a point at 1300°F (704°C) exhaust temperature and another at 1400°F (760°C) are shown.

Note that the work output has increased considerably to about 226 Btu/lb of air (525 kJ/kg) for a 1400°F (760°C) exhaust which represents an increase in output from point A to point C of about 54 percent. Also note that the gas turbine cycle efficiency drops to about 37.3 percent in the process.

It is now assumed that a 14 CPR gas turbine is reheated from point A′ to point C′. It is apparent that both the cycle efficiency and work output will be lower for the 14 CPR machine compared to the 38 CPR machine. Actually, the power turbine (PT) expansion ratio will be about the same for either machine to yield very close to the same exhaust temperature, but the greater mass flow (lower specific work) of the 38 CPR turbine produces far more work. The 38 CPR turbine will burn more fuel per unit of mass gas flow in the reheat combustor because the hot gas going to the reheat combustor will be at a lower temperature. It is interesting to note in Fig. 2 that the excess air has been reduced to 105 percent for the 38 CPR machine compared to 120 percent for the 14 CPR turbine. The 38 CPR turbine will yield a higher overall cycle efficiency when heat recovery is incorporated and will be the optimum (maximum) work output for the given conditions.

This heat balance graph (Fig. 2) clearly shows, in fact, that the optimum reheat gas turbine for any given gas generator TRIT and reheat TRIT will be the gas turbine having the CPR corresponding to the peak simple cycle efficiency without reheat.

The 38 CPR turbine is about optimum and a much better selection than the 14 CPR turbine. The lower gas temperature to the reheat combustor is also a decided plus regarding reheat combustor liner cooling. This optimization has also been shown by detailed calculations [1].

Obviously, a 1300 to 1400°F (704 to 760°C) exhaust temperature is much better than an 850°F (454°C) exhaust temperature (point A) or an 1140°F (616°C) temperature, point A′, with respect to high-pressure and high-temperature superheat steam generation for combined cycles, and even for cogeneration where more modest steam conditions are encountered. The big advantage of the reheat gas turbine, aside from the higher exhaust temperature, comes in the appreciable increase in work output which can be noted in Fig. 2.

The reheat gas turbine heat recovery in terms of specific output can be determined by extending point C at constant excess air upward to the right to the desired final stack temperature. The amount of heat is obtained by multiplying the specific output by the airflow. The overall cycle efficiency for 105 percent excess air is determined to be about 84.5 percent LHV for a 300°F (149°C) stack as can be determined from Fig. 3 in Part I of this paper.

Intercooled-Reheat Cycles

Intercooling can be accomplished much easier than reheat,

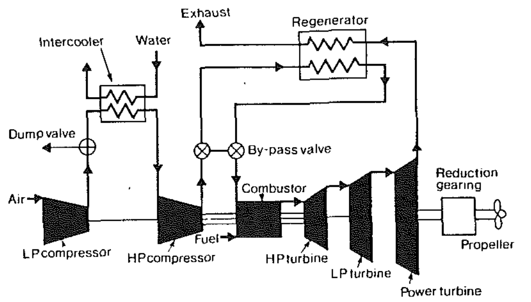

Fig. 5 Intercooled regenerated marine Spey schematic diagram taken from [4]

and intercooling has been applied for years to reduce work of compression of air and other gases. Intercooling for gas turbines dates back to the 1950s, but greater interest is now being shown by the US Navy in gas turbine intercooling, and various gas turbine manufacturers are also expressing interest, particularly when the intercooling is coupled with gas turbine regeneration. A schematic diagram of an intercooled reheat gas turbine to be analyzed by the heat balance method is presented in Fig. 3. Figure 4 illustrates what takes place when a 30 CPR gas turbine is intercooled and then regenerated.

Point $C''_{2.5}$ represents the gas turbine intercooled at a 2.5 compression ratio using data from [1-3] for a CPR of 30, a gas generator TRIT of 2100°F (1149°C), and a reheat temperature of 1825°F (996°C). Also refer to Figs. 5 and 11 of Part I for turbine C. It is important to note that point 1 represents the total cycle output of work and heat rejected to the intercooler. Starting at point 1 a reheat combustor pressure loss takes place and point 1 moves to point 2. The gas is reheated and then expanded in the power turbine to point 3. At point 3 the heat rejection X of the intercooler is graphically subtracted at constant excess air to arrive at point 4 which then gives the final gas turbine cycle efficiency of about 33.3 percent. The compressor discharge temperature is too high to consider regeneration, but heat can be recovered very effectively from point 3 at the 1300°F (704°C) exhaust temperature.

An optimum regeneration point near the square root of the total CPR is selected and labeled as point $C''_{5.5}$ where the square root of 30 is 5.5. The gas is reheated to point 3 as previously explained and the much greater amount of intercooler heat rejection is subtracted at constant excess air to point 4. More work is realized, but the gas turbine cycle efficiency stays about the same as before: 33.2 percent.

The high-pressure compressor discharge temperature is much lower for the $C''_{5.5}$ case and is about 480°F (249°C) thus making it possible to reduce the 1300°F (704°C) reheat exhaust to about 580°F (304°C) when incorporating a regenerator. Compressed air and exhaust back pressure loss is introduced because of the regenerator as shown on the graph in Fig. 4, moving from point 3 to 5. The large amount of heat Z rejected to the intercooler [about 80 Btu/lb of air (186 kJ/kg)] is subtracted to arrive at point 6 where it is noted that now the gas turbine cycle efficiency has risen to about 48.5 percent. Intercooler heat Y equals Z.

The intercooled cycle with intercooling taking place at a 2.5 ratio would be the better choice for heat recovery and cogeneration because of the relatively small amount of heat rejected to the intercooler [about 32 Btu/lb of air (74.4 kJ/kg)]. Likewise, this turbine could be far better for combined cycles.

Intercooled Regenerative Rolls-Royce Spey

The proposed US Navy intercooled regenerative (ICR) Rolls-Royce Spey SMIC gas turbine can be analyzed using the heat balance chart to show what takes place when the simple cycle Spey is modified to function in the following modes:

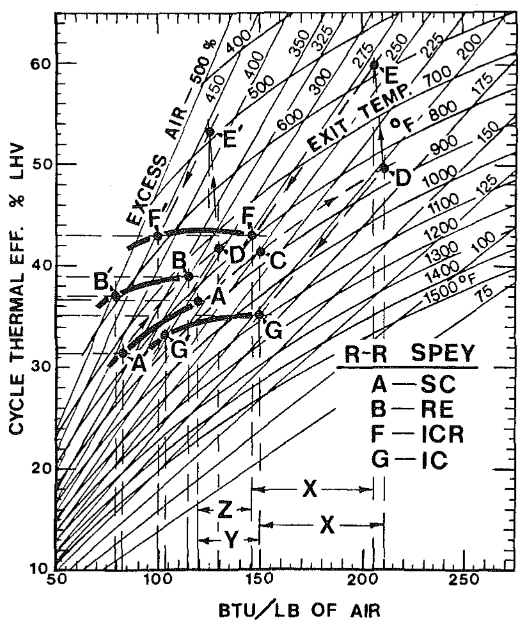

Fig. 6 R-R Spey simple cycle (SC), regenerated (RE), intercooled regenerative (ICR), and intercooled (IC) cycles at 100 and 50 percent output

1 As a simple cycle with no modifications;
2 as a regenerative cycle with regenerator added;
3 as an intercooled cycle with intercooler added;
4 as an intercooled regenerative cycle with both intercooler and regenerator added.

Figure 5 presents a schematic diagram of the intercooled regenerative cycle as taken from [4]. Figure 6 is a heat balance graph showing the four above modes of operation of the 18 CPR Spey for a full load combustor outlet temperature of 2240°F (1227°C). The simple-cycle Spey is projected to develop ISO 18 MW shaft power at 36.8 percent cycle efficiency at full load with an air flow of 143.3 lb/s (65.0 kg/s) and an exhaust temperature of 855°F (451°C). The ICR version is predicted to produce 22 MW shaft power at 43 percent efficiency at both full load and 50 percent load.

Data taken from [4] are used in the graphic heat balance analysis. Point A shows the simple-cycle full-load specific work output efficiency and exhaust temperature, and point A′ is the 50 percent load point. Dots B and B′ spot the regenerative cycle performance for full and half-load, respectively. Observe the output work loss going from simple to regenerative cycle (A to B). It can also be seen that, at full load, the simple-cycle exhaust temperature relative to the compressor discharge temperature does not allow for much heat to be regenerated; thus the final exhaust temperature of the regenerative cycle is rather high—about 750°F (399°C) whereas at half-load the exhaust temperature drops to about 600°F (316°C).

Points E and E′ plot the output and pseudo-efficiency for the intercooled regenerative cycle for full and half-load, respectively, where both output and efficiency reflect the work and the heat rejected to the cooling water. This heat rejection is readily calculated from the temperature drop of the low pressure compressor air. Observe how simple cycle points A and A′ move to points C and D—all at constant temperature—then to E and finally to F. Points E and E′ spot the final regenerator exit temperatures wherein the intercooler lowers the compressor discharge temperature and makes it possible to absorb more regenerated heat. The associated work loss that is introduced is shown. The intercooler heat is now subtracted at constant excess air (fuel) to arrive at points F and F′ for full load and half-load thus giving the two cycle efficiencies. The amount of heat rejected to the intercooler at full load is given by the output scale as being from point C to D and noted as *X*. The increase in work brought about by the savings in compressor work is likewise shown from points A to C for intercooling only (noted as *Y*) and A to F (*Z*) for both intercooling and regeneration. Points G and G′ spot the full-load and half-load cycle efficiency for intercooling and are the projection of point D at contant excess air.

It can be observed that the 50 percent output cycle efficiency for the ICR turbine is about the same as it is at 100 percent. This result is brought about by the relationship between intercooling, compressor discharge temperature, cycle pressure ratio, simple-cycle exhaust temperature regeneration, and final exit temperature, all of which aspects show up on the heat balance graph of Fig. 6.

The intercooled regenerative cycle offers a decided advancement in both part-load and full-load efficiency for ships and perhaps for other industrial applications. The introduction of reheat to the intercooled regenerative cycle would be another step forward. A cycle efficiency of 48 to 52 can be achieved by adding reheat to the intercooled regenerative cycle by applying a 30 to 38 CPR turbine such as the R-R RB211 535 E4, the P & W 2037, the International V2500 engine or any of the future high CPR turboprop jet engines under intensive study. The excellent part-load efficiency can also be retained, and no water would be required for a steam bottoming cycle. The Spey intercooled regenerated machine is a logical modular aeroderivative configuration, and such a machine will pave the way for the addition of reheat.

Stream Separation

Before discussing steam injection and steam blade cooling, it is necessary to first explain a useful technique of hypothetically separating the steam from the main gas stream. The steam is not actually physically separated, but it is only theoretically treated as an independent stream as an expediency for cycle analysis and cycle calculations. Total enthalpy of the flow is, of course, the sum of the partial enthalpy of each stream.

The procedure of using multiple streams of steam when calculating various single and double automatic extraction steam turbines serves as a very useful calculating tool; yet in actuality, multiple streams do not exist. The work from each hypothetical stream can be added together to obtain the total work [6]. A similar procedure can be used for gas turbines whereby the steam flow is separated from the main gas stream. This procedure has been effectively used for calculating steam-cooled reheat gas turbine cycles [7, 8].

In the case of the intercooled cycle previously reviewed, the cooling water extracts heat by means of a closed loop, and the heat extracted can be readily calculated by the enthalpy rise of the water and then related to one unit mass of the gas turbine air flow. Likewise, this amount of heat equals the enthalpy drop of the air being cooled.

When injecting water for direct contact evaporative cooling in an intercooler, as done by the Japanese on their reheat gas turbine [9], the net heat added to the water is easily determined by subtracting the enthalpy of the water (for the given amount evaporated) at its entering temperature from the enthalpy of this same amount of steam at the final exhaust temperature. It is true that more heat is actually transferred to this stream of H_2O by the burning of incremental fuel, but this extra amount of heat is extracted as useful work and shows up as work according to the first law. The H_2O enthalpy increase appears on the bottom scale of the heat balance chart as an output. This differential enthalpy, when multiplied by the H_2O flow in terms of the fraction of gas turbine air flow, gives the heat transferred to the H_2O per unit mass of air flow, where no work in the H_2O is included.

The heat balance chart (Fig. 4) gives the cycle efficiency for the final end point in terms of excess air and exit temperature.

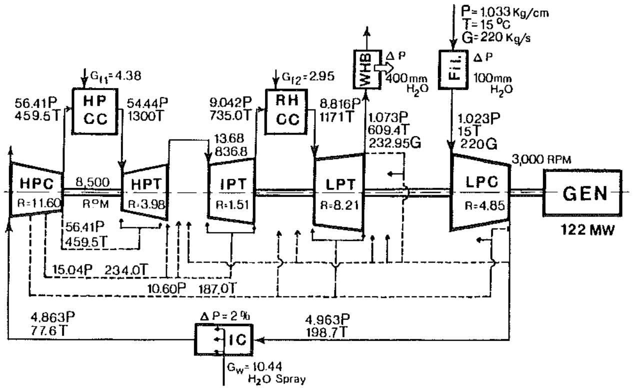

Fig. 7 Japanese AGTJ-100A intercooled reheat gas turbine schematic diagram

All the energy, both work and heat to the H_2O, must be accounted for in using the graph. The H_2O can be intercooler spray or steam injection or both. Given the following: (*a*) fuel burned, (*b*) work produced, (*c*) airflow, (*d*) gas turbine exhaust, (*e*) H_2O flow injected, and (*f*) the entering water and/or steam conditions, the final exit point can be spotted. Then the amount of work produced and heat going to the steam can be determined from the graph. Finally, the amount of sensible heat recoverable from the exhaust can be determined from the graph for any desired stack temperature. The steam tables can be applied for the enthalpy drop of the separated side stream of steam using a low partial pressure to assure no condensation.

The heat balance graph will not help the designer calculate any specific cycle, but it will provide an accurate check on the heat balance and provide a quick way of determining the recoverable heat. Also, the heat balance chart presents insight into how the reheat cycle with heat recovery can be optimized by the designer. Figure 4 clearly shows the effect excess air has on heat recovery and indicates that the best cycle has the lowest amount of excess air. When considering heat recovery for cogeneration and combined cycles, it is far better to exit the gas at an excess air value on the order of 100 percent for a reheat gas turbine than to exit the gas at a high value of some 250 percent as is the case for a simple-cycle gas turbine.

Japanese Reheat Intercooled Gas Turbine

A portion of the pertinent cycle data on the R & D Japanese reheat intercooled gas turbine is presented in Fig. 7 [9]. Figure 7 does not indicate what type of fuel is specified, and the specific fuel must be known to perform a close heat balance check. If a liquid fuel of 18,700 Btu/lb (LHV) is assumed, a gas turbine cycle efficiency of about 39 percent is calculated using the fuel weight flow figure given in Fig. 7. Also, for this type of fuel an excess air value of about 100 percent is calculated. Assuming the intercooler spray water to be at 59°F (15°C) the system heat addition from inlet H_2O enthalpy to exhaust H_2O enthalpy at 609.4°C (1128°F) would be about 75 Btu/lb of air (1745 kJ/kg) for the intercooler spray water added. These assumptions indicate that the gas turbine exhaust would be about 1150°F (621°C) versus 1128°F (609.4°C) given in Fig. 7. No closer check can be made without knowing the specific fuel being used.

Figure 8 presents cycle efficiency parameters as a function of cycle pressure ratio presented by the Japanese. Figure 9 is a plot of projected combined cycle efficiency versus plant output. The Japanese R & D reheat gas turbine was recently tested to 55 MW output. The combined-cycle efficiency (online performance) according to computer simulation of the bottoming cycle and actual test operation data for the gas turbine for a gas generator firing temperature of 1157°C (2115°F), a reheat

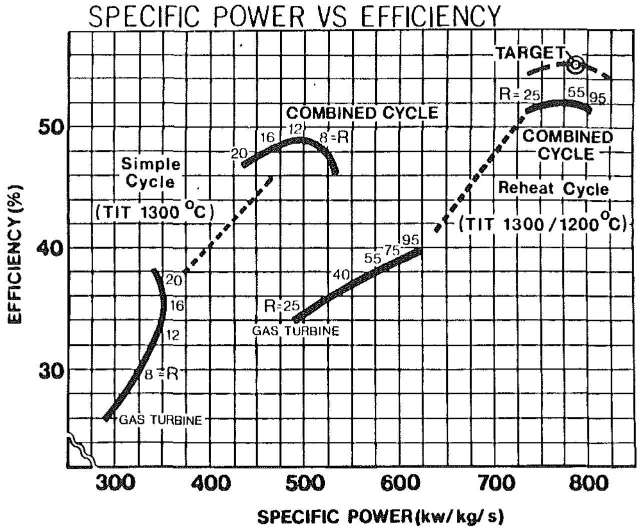

Fig. 8 Compression ratio, cycle efficiency, and specific power for Japanese combined cycle

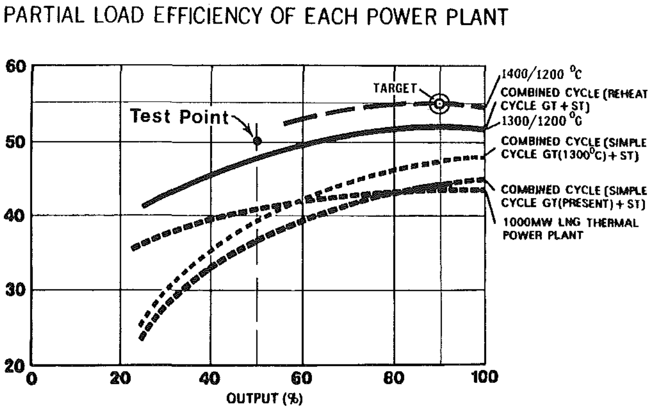

Fig. 9 Graph of combined-cycle efficiency versus output for various cycles

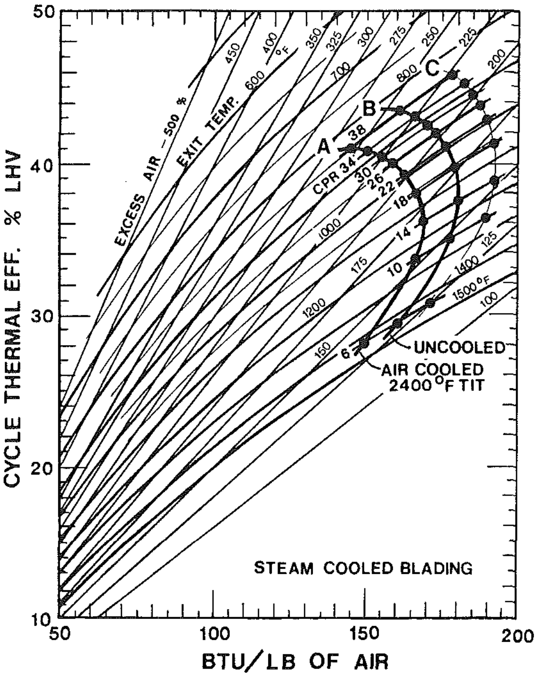

Fig. 10 Steam-cooled blading heat balance graph

temperature of 1038°C (1900°F) at a CPR of 28.1, and an exhaust temperature of 603.8°C (1119°F) was shown to be 50.2 percent (LHV) [10]. Note that at half-load the gas turbine exhaust temperature is very close to full-load temperature (603.8 versus 609.4°C). The Japanese research unit is presently being rebuilt due to a high-pressure compressor 13th stage blade failure and tests are to resume in June 1986 [10].

These test values of gas generator firing temperature and reheat firing temperatures as well as CPR are very close to the calculated values obtained for the LM5000 gas generator when applied in the reheat mode as published in the author's 1979 paper [2]. The tests substantiate the early projections of a 50 percent reheat combined-cycle efficiency for similar basic cycle parameters.

The Japanese tests on the AGT J-100A pilot plant reheat gas turbine have confirmed that the combined cycle will have an *extremely* high part-load efficiency [10]. The test point is spotted on Fig. 9, which shows the expected performance. The test point is some 4 percent better than predicted. A feasibility study is presently being made by the Japanese to investigate the possibility of the future application of the reheat gas turbine for a coal gasification system [10]. No other industrial gas turbine has ever achieved a combined-cycle efficiency as high as 50 percent at full load, let alone at half-load.

Steam-Cooled Blading

Steam cooling the nozzle vanes and rotating blades of a high TRIT gas turbine, particularly the first stage, offers distinct possibilities due to the fact that steam has different characteristics from air. Steam has over twice the specific heat, a lower viscosity, and a notably higher velocity for any given Mach number. Steam is also a nonluminous radiant absorber. Secondly, the compressor discharge temperature of a high CPR gas turbine can exceed 1000°F (538°C) making impingement and film cooling far more difficult. Thermal barrier ceramic coatings are being used on the vane platforms and even on the pressure side of the first-stage rotating blades of the R-R RB211 535 E4 turbine to reduce cooling requirements.

Steam has a very high specific heat near the saturation point, approaching one. Such steam can be used directly for convection cooling. The steam can alternately be mixed with compressor discharge air to lower the coolant temperature and to take advantage of steam's better cooling qualities. If 75 percent by weight of the compressor discharge air is mixed with 25 percent steam, the previously mentioned 1000°F (538°C) temperature can be reduced to about 780°F (416°C) and at the same time the volume of the steam (partial pressure) will be about 38 percent of the mixture. A 50 percent by weight mixture of steam would lower the coolant temperature to about 650°F (343°C), and the volume of steam would be about 63 percent. The lower temperature coolant could then be used in present blading configuration with very little, if any, design changes. The TRIT, at the same time, could be raised to perhaps 2400°F (1316°C) baseload. A further increase in TRIT could be accomplished using pure steam as the blade coolant wherein blading design changes could be made to take better advantage of the pure steam as a coolant.

Two basic cycle changes take place when applying steam as a blading coolant. First, the steam displaces the cooling air, and this increment of air can be heated to the full TRIT. Incremental work is thus produced. Secondly, the greater mass of the steam also expands and produces incremental work. Reference is made to Fig. 10, which is a plot of specific work for various CPRs for 2400°F TRIT (1316°C).

An air-cooled blading system is shown as curve A. Assume now that no cooling air is used. Curve A moves up to curve B. Actually curve B can be calculated far more accurately than curve A because the cooling and mixing not present to distort and complicate the expansion calculations. Such a noncooled turbine is not yet possible. Ceramics are not yet here for gas

Table 1 Integrated gas/steam cycle, ISO conditions; data for Fig. 11

Designated heat output	Calculated Btu/lb air	End point	Explanation
O-A	146	A	Air-cooled GT work output
A-B	15.9	B	Incremental work for noncooled GT
B-C	−4.0	C	Reheat combustor pressure loss
C-D	70.1	D	Work from reheat
O-D	228	D	Total work of noncooled GT
U	12	E	Work from cooling steam
E-F	16	F	Heat to steam in exhaust (open cycle)
W	28.01	F	Input heat to steam (open cycle
X	12.5	G	Heat to steam—GG casing (closed cycle)
Y	11.7	H	Heat to steam—PT casing (closed cycle)
Z	39.85	I	Heat to superheat steam (closed cycle)
V	80.05	–	Total heat added to steam
T	2.23	J	Incremental work for added fuel mass flow
O-J	325.28	J	Total output through GT (work and heat)
J-K	287	K	Heat to steam recovered from exhaust gas only by boiler
O-K	612.0	K	Total cycle output (work and heat)

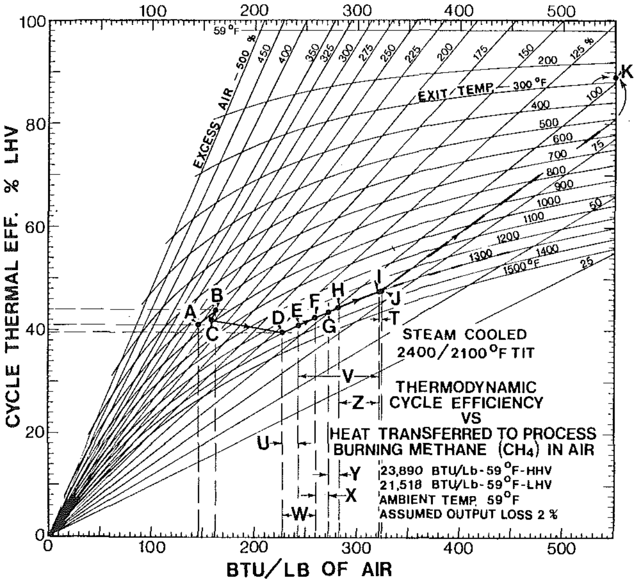

Fig. 11 Steam-cooled reheat gas turbine heat balance graph

turbines, but curve B allows us to project to curve C where steam is injected as the coolant and additional work is produced by the steam mass flow. The extent of the increase in incremental steam power will, to a great extent, depend upon the amount of steam injected and perhaps to a lesser extent upon the design of the blading and method of injecting the steam.

Figure 10 shows that there is more to be gained by steam cooling high CPR (30 to 40) *turbines than low CPR turbines.* Two reasons are cited: First, more cooling air is used for the high CPR turbines, and second, the steam produces more work when expanding through a higher expansion ratio. Therefore, there is more incentive to steam cool/inject a high CPR turbine.

There is another, and more subtle, third reason for steam injection/cooling. More fuel is burned to heat the incremental cooling air not used for cooling, and in the process the excess air is reduced. It has been shown graphically in Part I of this paper that reducing excess air increases heat recovery and overall cycle efficiency. When considering the reheat gas turbine, all the steam used to cool the gas generator blading is reheated to the full reheat TRIT to produce additional work and to again reduce excess air. In summary, steam cooling a high CPR reheat gas turbine, particularly the gas generator blading, offers the greatest potential [7, 8, 11, 12].

Analysis of Reheat Steam-Cooled Cycle

The graphic gas turbine heat balance procedure explained so far has led to the general conclusion that as much fuel should be burned in the gas turbine as possible to: (*a*) produce the maximum gas turbine work output, (*b*) provide the minimum exit excess air, and (*c*) to realize the maximum exhaust temperature for heat recovery.

Considering a hypothetical case, this general three-point conclusion can be applied to an integrated gas/steam cycle by applying a steam-cooled nonintercooled reheat gas turbine wherein steam is used to (1) cool the blading, (2) cool both the gas generator and power turbine casings and rotors, and (3) superheat the steam for the bottoming cycle by means of the reheat combustor. Backup data on the cycle are given in [2, 11, 13, 14]. A maximum amount of fuel is burned in the gas turbine. No intercooling is incorporated thus reducing an unrecoverable heat rejection. Steam superheating by superheat coils in the reheat combustor makes it possible to obtain a 300°F (149°C) stack temperature and utilize a standard 2400 psig-1000°F/1000°F reheat steam turbine (16.5 MPa-538°C/538°C). A complicated and expensive dual drum boiler and a more costly admission steam turbine are avoided.

Reference is made to Fig. 11, which shows the step-by-step accounting of the fuel (excess air), work, and recoverable heat. Table 1 provides a summary of the projected end points for each step and the heat accounting to satisfy the heat balance graph. The gas turbine exhaust temperature is assumed to remain constant at 1300°F (704.4°C) because the power turbine expansion ratio does not change to any appreciable extent and this temperature is about the material limit for the last stage. The reheat gas turbine has a 38 CPR, a gas generator TRIT of 2400°F (1316°C), and a reheat TRIT of 2100°F (1149°C) for ISO conditions.

Note that heat *Z* can vary. All of the initial superheating can be done in the boiler and only the steam reheating can be accomplished by the gas turbine reheat combustor. It must be remembered that the bottoming cycle efficiency is about 40 percent and adding too much heat by the reheat combustor could be counterproductive. Optimization would be required. Also, the amount of closed-cycle casing heat (G and H) is not precisely known and only estimates are given. The prospect of the steam turbine second reheat at the crossover to the low-pressure turbine is intriguing, however [13, 14].

When considering stream separation, which was explained previously in this paper, the heat recovered in the boiler as well as the open and closed-cycle steam consists of three parts: (1) the heat of the open cycle steam injected for blade cooling (point E to F) from 1300°F (704.4°C) down to water at 59°F (15°C), (2) the sensible heat in the exhaust gases at 80 percent excess air (point J to K) recovered to the 300°F (149°C) stack temperature, and (3) the total heat going to the closed steam cycle (point F to I). Steam flow and the bottoming cycle output is readily calculated using these values. The gas turbine work output consists of three parts: (1) graph origin to point

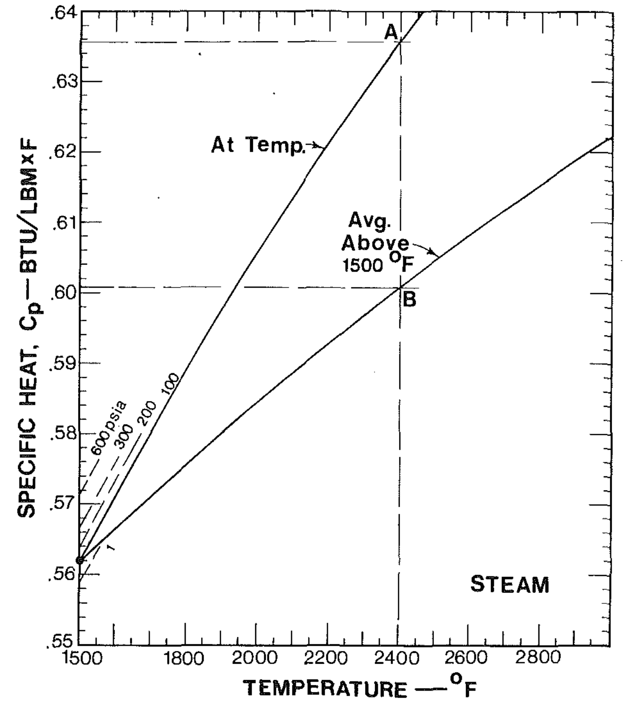

Fig. 12 Steam specific heat versus temperature graph

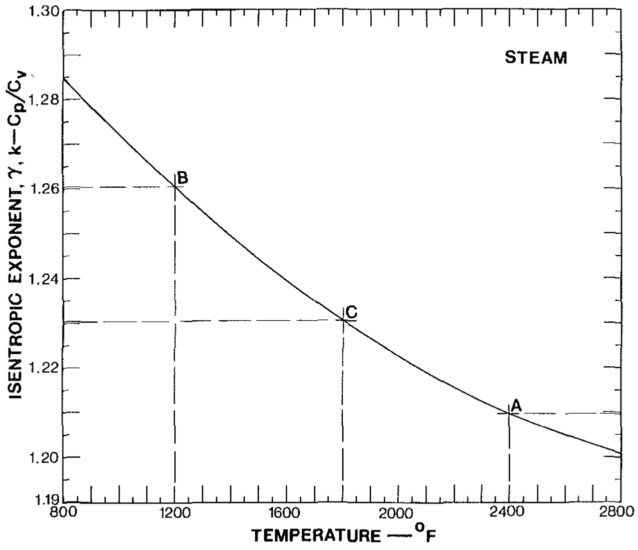

Fig. 13 Isentropic exponent versus temperature graph

D, (2) U, and (3) T. All that has to be remembered is to obey the first law regarding heat input and output. An accurate accounting of all the heat must be kept.

Figure 11 shows graphically what takes place and explains why such a high cycle efficiency, upward of 60 percent LHV, is possible with the integrated gas/steam cycle. The principle of maximum gas turbine output and minimum exhaust excess air is exploited in the example. More steam injection would be beneficial for both work output and cycle efficiency, but demineralized makeup water is expensive and a minimum flow is suggested in the open cycle.

High-Temperature Steam Properties

The ASME steam tables stop at 1500°F (816°C), and when calculating steam expansion work by the stream separation method it is necessary to remember that the Keenan and Kaye gas tables are developed for low pressures and high superheat. The gas tables are quite accurate for steam temperature above about 1200°F (649°C) and for low pressures, but the steam tables should be used when considering the enthalpy of the steam below about 1200°F (649°C). There is a need to extend the steam tables to about 3000°F (1649°C) for accurate calculation of high-temperature gas turbines where stream separation provides an easy and acceptable method of calculating performance. Of course, the more complicated method of using mole component enthalpies of the entire gas mixture is perhaps preferred for precise calculations and when an extensive computer program is available.

Steam Specific Heat. Figure 12 is a plot of steam specific heat versus temperature starting at 1500°F (816°C). Data for Fig. 12 have been taken from Keenan and Kaye's gas tables. The specific heat at the particular temperature is given by the left-hand curve and the average specific heat above 1500°F (816°C) is given to the right. It can be noted that the specific heat rises from about 0.562 at 1500°F (816°C) to some 0.635 at 2400°F (1316°C). This increase in specific heat makes it impractical to calculate expansion work by applying the standard thermodynamic formulas. However, the graph provides numbers for quick estimates.

Steam Isentropic Exponent. Steam isentropic exponent values are plotted against temperature in Fig. 13. At 1200°F (649°C) the exponent is shown as 1.261, point B. At point A, 2400°F (1316°C) the exponent drops to 1.209. An arithmetic average between these two temperatures at point C gives 1.231. Figure 13 can be used for quick answers using the thermodynamic equations, but again the gas tables are easy to use and provide quite accurate results. A computer program integrating the gas tables for H_2O for values above 1200°F (649°C) and the steam tables for values below 1200°F would be preferred.

Summary

The graphic heat balance method presented in Part I of this paper can be applied to rather complex cycles to yield accurate answers for any given fuel commonly burned in a gas turbine. The graphic solution gives insight into what takes place in terms of excess air, exit temperature, and heat transferred to the process whether it is work, heat rejected to cooling water, or heat transferred to steam.

A simple procedure of stream separation makes it possible to make an easy, simple accounting for the heat absorbed by evaporative intercoolers, combustor steam injection, or blade steam for cooling—the heat being the difference between entering enthalpy and exiting enthalpy of the separated side stream. This useful, sidestream tool makes it possible to check rather complex cycles and to analyze various modes of operation. Part-load performance can also be readily checked and analyzed by means of the graphic method.

Gas turbines with rather complex cycles can be expected to be applied by industry as the full impact of the third-generation gas turbine makes itself felt and such gas turbines can be advantageously used for cogeneration where a decided work output shift take place to increase the power to steam ratio. The graphic heat balance solution provides a better understanding of gas turbine cycles and heat recovery for cogeneration and combined cycles without getting into the mechanical details and component efficiencies of the gas turbine itself.

Acknowledgments

Appreciation is expressed for the continuing professional assistance of my wife, Carolyn Keyes Rice, in the Acknowledgments section of Part I.

References

1 Rice, I. G., "The Combined Reheat Gas Turbine/Steam Turbine Cycle, Part I, A Critical Analysis of the Combined Reheat Gas Turbine/Steam Turbine Cycle," ASME Journal of Engineering for Power, Vol. 102, Jan. 1980.

2 Rice, I. G., "The Combined Reheat Gas Turbine/Steam Turbine Cycle, Part II, The LM5000 Gas Generator Applied to the Combined Reheat Gas Turbine/Steam Turbine Cycle," ASME Journal of Engineering for Power, Vol. 102, Jan. 1980.

3 Rice, I. G., "Evaluation of the Compression Intercooled Reheat Gas Turbine Combined Cycle," ASME Paper No. 84-GT-128.

4 Thomas, W. J. R., and Higson, A. J., "An Intercooled Regenerative Rolls-Royce Spey Gas Turbine," ASME Paper No. 85-IGT-59.

5 Thomas, W. J. R., "The 18MW Rolls-Royce Spey Marine Gas Turbine," ASME Paper No. 85-GT-162.

6 Wilson, W. G., and Jacobs, D. L. E., "Short-Cut Methods of Evaluating Alternate Steam and Power Supplies for Paper Mills," *TAPPI Magazine*, Vol. 41, No. 10, Oct. 1958.

7 Rice, I. G., "Steam-Cooled Blading in a Combined Reheat Gas Turbine Reheat Steam Turbine Cycle, Part I, Performance Evaluation," ASME Paper No. 79-JPGC-GT-2.

8 Rice, I. G., "Steam-Cooled Blading in a Combined Reheat Gas Turbine/Reheat Steam Turbine Cycle, Part II, Design Considerations," ASME Paper No. 79-JPGC-GT-3.

9 Hori, A, and Takeya, K., "Outline of Plan for Advanced Research Gas Turbine," ASME Journal of Engineering for Power, Vol. 104, 1982.

10 Takeya, K., "Japanese High Efficiency Reheat Gas Turbine Development," Electric Power Research Institute Conference, San Francisco, Apr. 1985.

11 Rice, I. G., "The Reheat Gas Turbine With Steam Blade Cooling—a Means of Increasing Reheat Pressure, Output and Combined Cycle Efficiency," ASME Journal of Engineering for Power, Vol. 104, Jan. 1982.

12 Rice, I. G., "The Reheat Power Turbine With Steam Cooling—a Means of Increasing Reheat Temperature, Exhaust Temperature and Combined-Cycle Efficiency," ASME Paper No. 82-GT-134.

13 Rice, I. G., "Steam Cooled Gas Turbine Casings, Struts, and Disks in a Reheat Gas Turbine Combined Cycle, Part I, Compressor and Combustor," ASME Journal of Engineering for Gas Turbines and Power, Vol. 105, Oct. 1983.

14 Rice, I. G., "Steam Cooled Gas Turbine Casings, Struts and Disks in a Reheat Gas Turbine Combined Cycle, Part II, Gas Generator Turbine and Power Turbine," ASME Paper No. 83-GT-86, ASME Journal of Engineering for Gas Turbines and Power, Vol. 105, Oct. 1983.

F. F. Huang
Professor.

Ling Wang[1]
Visiting Research Scholar.

Department of Mechanical Engineering,
San Jose State University,
San Jose, CA 95192

Thermodynamic Study of an Indirect Fired Air Turbine Cogeneration System With Reheat

A previous study of an indirect fired air turbine cogeneration system has been extended to include the concept of reheat. The effects of the number of reheat stages and cycle pressure drops on system performance parameters (such as power and process heat production, fuel utilization efficiency, and second-law efficiency) are examined.

Introduction

The indirect fired gas turbine cogeneration system has been recognized as a promising concept for energy conservation [1-6]. Since this concept will permit the use of coal or other low-cost fuel, significant savings of gas and oil could be realized once this technology is fully developed. This technology is therefore particularly attractive for countries without an abundant supply of premium fuels.

In [7], a simple indirect fired air turbine cogeneration system was studied. This system has the virtue of simplicity. However, achieving turbine exit temperatures adequate for process steam production would require either a high turbine inlet temperature or a low pressure ratio. Since turbine inlet temperature for an indirect fired gas turbine is currently limited to about 1500°F (816°C), and a low pressure ratio would result in an unattractively low power-to-heat ratio, a more complex system is needed to achieve better thermodynamic performance. If reheat is employed, more power production and higher turbine exit temperature will result as in the case of a combined gas turbine–steam turbine system using reheat [8, 9]. The objective of this paper is to extend the previous study given in [7] to include reheat.

This paper deals with the thermodynamic aspects of a more complex cogeneration system. Expressions involving the relevant variables for fuel utilization efficiency (first-law efficiency), electrical to thermal energy ratio (power-to-heat ratio), and second-law efficiency (exergetic efficiency) are presented. The effects of the number of reheat stages and cycle pressure drops on system performance are examined. The results of this study, together with appropriate cost data, should be useful to decision makers in the selection of optimal parameters at the system design stage.

System Description

A gas turbine system in general could have any number of reheat stages. The schematic diagram of an indirect fired air turbine cogeneration system with one stage of reheat is shown in Fig. 1. The corresponding enthalpy-entropy diagram of the air turbine cycle is shown in Fig. 2.

The energy input to the air turbine cycle is heat added to the working fluid in the main air heater and the reheater. The fuel input to the system is the fuel supplied to the main air heater and the reheater. This quantity will depend primarily on the maximum cycle temperature at the main heater outlet and the reheat temperature at the reheater outlet. For our study, we shall consider that the reheat temperature is the same as the maximum cycle temperature. That is, we shall always have full reheat. We shall also assume that the heater efficiency is the same for all heaters.

The power output of the system will depend on the expansion ratio for each turbine. For our study, we shall use the same expansion ratio for each of the turbines. We further consider the adiabatic turbine efficiency to be the same for each turbine.

The hot turbine exhaust entering the heat recovery steam generator is the waste heat source for process heat production. The quantity and quality of process steam produced will depend on the temperature of air entering and the temperature of steam produced in the heat recovery steam generator as shown in Fig. 3. It may be seen from this figure that with the same pinch point and process steam temperature more process heat will be produced if hot air enters the steam generator at a higher temperature.

Expressions for System Performance Parameters

1 Power Output. The net power output of a cycle with one reheat is given as

$$\dot{W}_{\text{net}} = \dot{m}_a \left[(h_3 - h_4) + (h_5 - h_E) - (h_2 - h_1) \right] \qquad (1)$$

Assuming air to be an ideal gas with constant specific heats, we have, on the basis of the same expansion ratio and efficiency for each turbine and full reheat

$$\dot{W}_{\text{net}} = \dot{m}_a c_p \left[2\, \eta_T T_{\max} (1 - 1/\pi_T^{\alpha}) - T_1 (\pi_C^{\alpha} - 1)/\eta_C \right] \qquad (2)$$

---

[1] Associate Professor, Dalian Institute of Technology, Dalian, Liaoning, People's Republic of China.

Contributed by the Gas Turbine Division of The American Society of Mechanical Engineers and presented at the 31st International Gas Turbine Conference and Exhibit, Düsseldorf, Federal Republic of Germany, June 8-12, 1986. Manuscript received at ASME Headquarters January 9, 1986. Paper No. 86-GT-48.

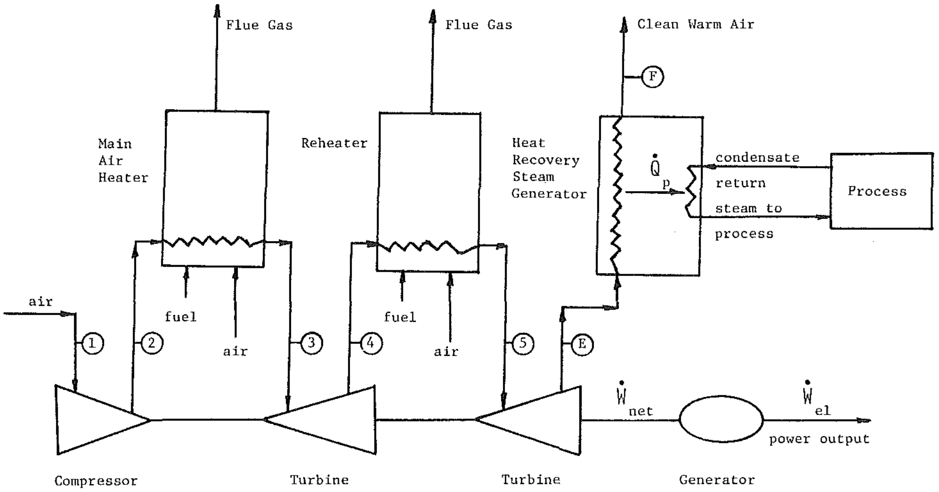

Fig. 1 Schematic diagram of an indirect fired air turbine cogeneration system with reheat

where

π_C is the compressor compression ratio
π_T is the turbine expansion ratio (3)
$\alpha = (k-1)/k$

For a system with N stages of reheat, we would have

$$\dot{W}_{\rm net} = \dot{m}_a c_p \left[(N+1)\eta_T T_{\rm max}(1 - 1/\pi_T^\alpha) - T_1(\pi_C^\alpha - 1)/\eta_C \right] \quad (4)$$

Dividing across by $(\dot{m}_a c_p T_1)$ to get the specific cycle power output, we have

$$\dot{w}_{\rm net} = \dot{W}_{\rm net}/(\dot{m}_a c_p T_1)$$
$$= (N+1)\eta_T \cdot \theta \cdot \psi_T - (\psi_C/\eta_C) \quad (5)$$

where

$$\theta = T_3/T_1 = T_{\rm max}/T_{\rm min} \quad (6)$$
$$\psi_C = \pi_C^\alpha - 1 \quad (7)$$
$$\psi_T = 1 - (1/\pi_T^\alpha) \quad (8)$$

The electrical power output of the system may be obtained from

Nomenclature

$\dot{B}_f$ = exergy of fuel input
$\dot{B}_p$ = exergy of process heat
c_p = specific heat at constant pressure
$\dot{E}_f$ = energy of fuel input
h = enthalpy
h_c = enthalpy of condensate return
h_f = enthalpy of saturated water at process steam pressure
h_g = enthalpy of saturated vapor at process steam pressure
k = ratio of specific heats
$\dot{m}_a$ = mass flow rate of air in air turbine cycle
$\dot{m}_s$ = mass flow rate of steam
N = number of stages of reheat
p = pressure (absolute)
pp = pinch point
$\Delta p/p$ = relative pressure drop in cycle
$\dot{Q}_{in}$ = heat input to air turbine cycle
$\dot{q}_{in}$ = specific heat input to air turbine cycle
$\dot{Q}_p$ = amount of process heat production
$\dot{q}_p$ = specific process heat production
R_{pH} = power to heat ratio
s = entropy
s_c = entropy of condensate return
s_g = entropy of saturated vapor at process steam pressure
T = temperature (absolute)
T_c = temperature of condensate return
T_E = temperature of air entering heat recovery steam generator
T_F = temperature of air leaving heat recovery steam generator
$T_{\rm max}$ = maximum cycle temperature
T_0 = temperature of the environment
T_p = saturation temperature at pressure of process steam
T_{pp} = temperature of air at pinch point
$\dot{W}_{\rm net}$ = net power output of air turbine cycle
$\dot{w}_{\rm net}$ = specific power output of air turbine cycle
$\dot{W}_{el}$ = electrical power output of system
$\dot{w}_{el}$ = specific electrical power output of system
α = defined by equation (3)
β = pressure drop factor, defined by equation (32)
ϵ_f = exergy factor of fuel input, defined by equation (29)
ϵ_p = exergy factor of process heat, defined by equation (28)
η_C = adiabatic compressor efficiency
η_f = fuel utilization efficiency, defined by equation (21)
η_g = electrical conversion efficiency, defined by equation (9)
η_H = air heater efficiency, defined by equation (15)
η_T = adiabatic turbine efficiency
η_{th} = air turbine cycle thermal efficiency, defined by equation (23)
$\eta_{\rm II}$ = second-law efficiency, defined by equation (26)
θ = ratio of maximum to minimum cycle temperature, defined by equation (6)
π_C = compressor compression ratio
π_T = turbine expansion ratio
τ = ratio of outlet to inlet temperature of air turbine cycle, defined by equation (19)
ψ_C = defined by equation (7)
ψ_T = defined by equation (8)

Subscripts

1,2, . . . ,5 = state points in air turbine cycle

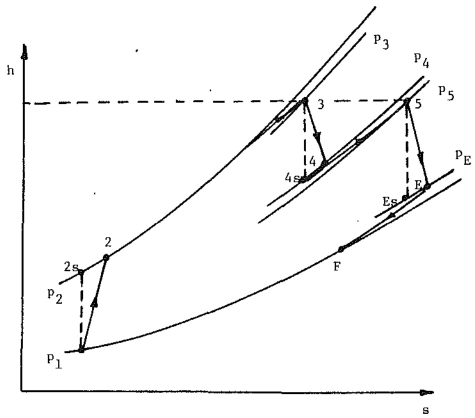

Fig. 2 Enthalpy-entropy diagram of air turbine cycle with reheat

$$\dot{W}_{el} = \eta_g \dot{W}_{net} \tag{9}$$

$$\dot{w}_{el} = \eta_g \dot{w}_{net} \tag{10}$$

where η_g, the electrical conversion efficiency, is defined by equation (9).

2 Energy Input. Heat input to the cycle with one stage of reheat is given as

$$\dot{Q}_{in} = \dot{m}_a \left[(h_3 - h_2) + (h_5 - h_4) \right] \tag{11}$$

Assuming ideal gas with constant specific heats, we have, on the basis of full reheat

$$\dot{Q}_{in} = \dot{m}_a c_p \left[T_{\max} - T_1 - T_1(\psi_C/\eta_C) + \eta_T \bullet T_{\max} \bullet \psi_T \right] \tag{12}$$

For a system with N stages of reheat, we would have

$$\dot{Q}_{in} = \dot{m}_a c_p \left[T_{\max} - T_1 - T_1(\psi_C/\eta_C) + N \bullet \eta_T T_{\max} \bullet \psi_T \right] \tag{13}$$

Dividing across by $(\dot{m}_a c_p T_1)$ to get specific heat input to cycle

$$\begin{aligned} \dot{q}_{in} &= \dot{Q}_{in}/(\dot{m}_a c_p T_1) \\ &= \theta - 1 - (\psi_C/\eta_C) + N \bullet \eta_T \bullet \theta \bullet \psi_T \end{aligned} \tag{14}$$

Energy of fuel input $\dot{E}_f$ may be obtained from

$$\dot{E}_f = \dot{Q}_{in}/\eta_H \tag{15}$$

where η_H, the air heater efficiency, is defined by equation (15).

3 Process Heat Production. The amount of process heat produced is given by

$$\dot{Q}_p = \dot{m}_a (h_E - h_F) \tag{16}$$

Assuming ideal gas with constant specific heats, we have

$$\dot{Q}_p = \dot{m}_a c_p \left[T_{\max} - \eta_T \bullet T_{\max} \bullet \psi_T - T_F \right] \tag{17}$$

Dividing across by $(\dot{m}_a c_p T_1)$ to get specific process heat production

$$\dot{q}_p = \dot{Q}_p/(\dot{m}_a c_p T_1) = \theta - \theta \bullet \eta_T \bullet \psi_T - \tau \tag{18}$$

where

$$\tau = T_F/T_1 \tag{19}$$

$$T_F = (T_p + pp) - \left[T_E - (T_p + pp) \right] (h_f - h_c)/(h_g - h_f) \tag{20}$$

Equations (18) and (20) are the same as those for the case of no reheat given in [7].

4 Fuel Utilization Efficiency (First-Law Efficiency). The ratio of all the useful energy extracted from the system (electricity and process heat) to the energy of fuel input is known as the fuel utilization efficiency (η_f) which is also known as the first-law efficiency since only energy accounting is involved. According to this definition, η_f is then given by the following expression

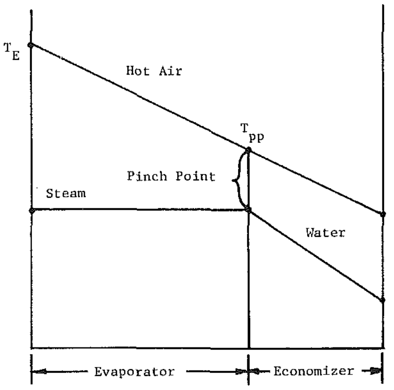

Fig. 3 Temperature profile in heat recovery steam generator

$$\eta_f = (\dot{W}_{el} + \dot{Q}_p)/\dot{E}_f \tag{21}$$

As shown in [7], equation (21) may be written as

$$\eta_f = \eta_H (\eta_g \bullet \eta_{th} + \dot{Q}_p/\dot{Q}_{in}) \tag{22}$$

where η_H is the heater efficiency, η_g is the electrical conversion efficiency, and

$$\eta_{th} = \dot{W}_{net}/\dot{Q}_{in} \tag{23}$$

is the air turbine cycle thermal efficiency.

Making use of equations (5), (14), and (18), η_f for a system with N stages of reheat may be written as

$$\begin{aligned} \eta_f = \eta_H \Bigg\{ & \eta_g \left[\frac{(N+1) \bullet \eta_T \bullet \theta \bullet \psi_T - (\psi_C/\eta_C)}{\theta - 1 - (\psi_C/\eta_C) + N \bullet \eta_T \bullet \theta \bullet \psi_T} \right] \\ & + \left[\frac{\theta - \eta_T \bullet \theta \bullet \psi_T - \tau}{\theta - 1 - (\psi_C/\eta_C) + N \bullet \eta_T \bullet \theta \bullet \psi_T} \right] \Bigg\} \end{aligned} \tag{24}$$

5 Electrical-to-Thermal Energy Ratio (Power-to-Heat Ratio). The cost effectiveness of any cogeneration system is directly related to the amount of power it can produce for a given amount of process heat needed. Thus the power-to-heat ratio R_{pH} is an important parameter used to assess the performance of such a system. Making use of equations (5), (10), and (18), R_{pH} for a system of N stages of reheat may be given as

$$\begin{aligned} R_{pH} &= \dot{W}_{el}/\dot{Q}_p \\ &= \eta_g \left[\frac{(N+1) \bullet \eta_T \bullet \theta \bullet \psi_T - (\psi_C/\eta_C)}{\theta - \theta \bullet \eta_T \bullet \psi_T - \tau} \right] \end{aligned} \tag{25}$$

6 Second-Law Efficiency (Exergetic Efficiency). An efficiency is a ratio of output to input. If we consider both output and input in terms of energy, we have the so-called first-law efficiency. Since exergy is more valuable than energy according to the second law of thermodynamics [10, 11], it is useful to consider both output and input in terms of exergy as shown in [7]. By definition, the second-law efficiency η_{II} is then given by the following expression

$$\eta_{II} = (\dot{W}_{el} + \dot{B}_p)/\dot{B}_f \tag{26}$$

where $\dot{W}_{el}$ is all exergy, $\dot{B}_p$ is the exergy content of process heat, and $\dot{B}_f$ is the exergy content of fuel input.

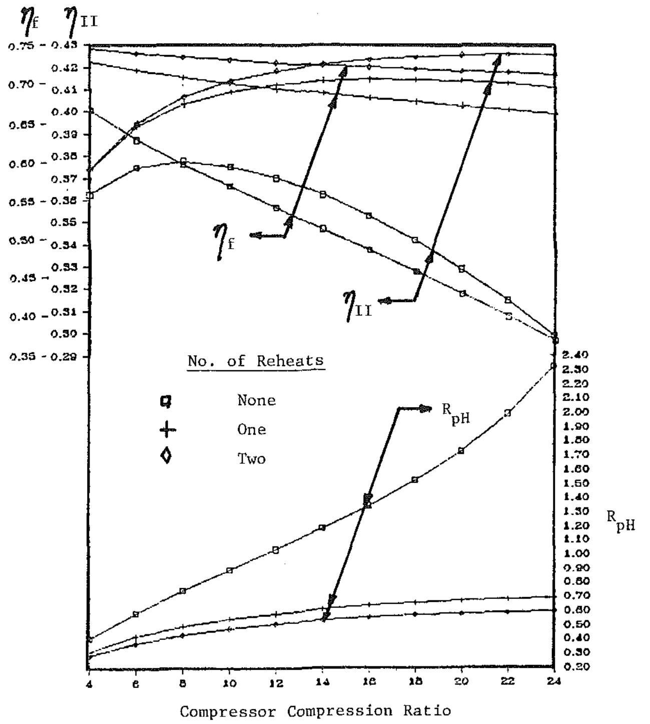

Fig. 4 Effect of number of stages of reheat on fuel utilization efficiency η_f, second-law efficiency η_{II}, and power-to-heat ratio R_{pH} with relative pressure drop of 3 percent in each heat transfer device

As shown in [7], equation (26) may be written as

$$\eta_{II} = (\eta_f/\epsilon_f)\left[\frac{(\dot{W}_{el}/\dot{Q}_p + \epsilon_p}{(\dot{W}_{el}/\dot{Q}_p)+1}\right] \tag{27}$$

where

$$\epsilon_p = \dot{B}_p/\dot{Q}_p \tag{28}$$

$$\epsilon_f = \dot{B}_f/\dot{E}_f \tag{29}$$

For most fuels, the exergy factor ϵ_f is close to unity. For process steam, the exergy factor ϵ_p is always less than unity, but it increases with the pressure of process steam produced. From [7], ϵ_p for our system is given as

$$\epsilon_p = 1 - T_0(s_g - s_c)/(h_g - h_c) \tag{30}$$

7 Turbine Expansion Ratio. The turbine expansion ratio may be expressed in terms of the compressor compression ratio and pressure drop to be used in each of the heat transfer devices involved. If p_{in} and p_{out} are the inlet pressure and outlet pressure of air for each heat transfer device, then

$$p_{out} = \beta p_{in} \tag{31}$$

and

$$\beta = 1 - (p_{in} - p_{out})/p_{in} = 1 - (\Delta p)/p \tag{32}$$

The quantity $(\Delta p)/p$ is known as the relative pressure drop. β may be called the pressure drop factor.

From Fig. 1, we thus have

$$p_3 = \beta_{23} p_2 \tag{33}$$

$$p_5 = \beta_{45} p_4 \tag{34}$$

$$p_F = \beta_{EF} p_E \tag{35}$$

where β_{23} is the pressure drop factor for the main air heater, β_{45} is the pressure drop factor for the reheater, and β_{EF} is the pressure drop factor for the steam generator.

Combining equations (33), (34), and (35), we have

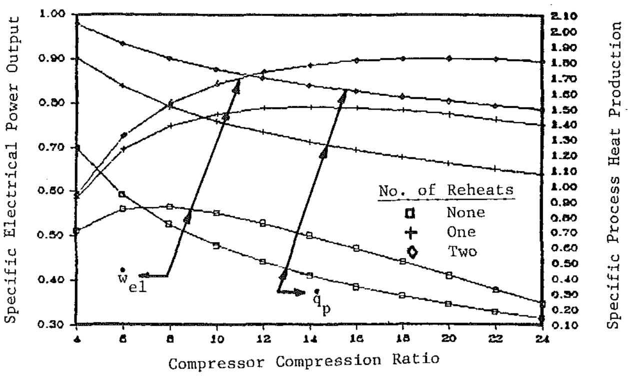

Fig. 5 Effect of number of stages of reheat on specific electrical power output $\dot{w}_{el}$ and specific process heat production $\dot{q}_p$ with relative pressure drop of 3 percent in each heat transfer device

$$\begin{aligned}(p_3/p_4)\bullet(p_5/p_E) &= \beta_{23}\bullet\beta_{45}\bullet\beta_{EF}\bullet(p_2/p_F)\\ &= \beta_{23}\bullet\beta_{45}\bullet\beta_{EF}\bullet\pi_C\end{aligned} \tag{36}$$

Now $(p_3/p_4) = (p_5/p_E) = \pi_T$.

For a system with one stage of reheat, the turbine expansion ratio would then be given by

$$\pi_T = (\beta_{23}\bullet\beta_{45}\bullet\beta_{EF}\bullet\pi_C)^{1/2} \tag{37}$$

For a system with two stages of reheat, the turbine expansion ratio would then be given by

$$\pi_T = (\beta_{23}\bullet\beta_{45}\bullet\beta_{67}\bullet\beta_{EF}\bullet\pi_C)^{1/3} \tag{38}$$

where β_{67} would be the pressure drop factor for the second reheater involved.

8 Compressor Compression Ratio for Maximum Cycle Power Output. The compressor compression ratio for maximum cycle power output was found to be close to the optimum compressor compression ratio for maximum second-law efficiency in the case of a simple air turbine cogeneration system with no reheat [7]. A similar situation exists for an air turbine cogeneration system with regenerative heating [6]. It appears that an expression giving the compressor compression ratio for maximum cycle power output could be useful.

To get maximum cycle power output, we must satisfy the following condition

$$\frac{\partial \dot{w}_{\text{net}}}{\partial \pi_C} = 0 \tag{39}$$

Making use of equations (5), (37), and (39), compressor compression ratio for maximum cycle power output for a system with one reheat is given by

$$(\pi_C)_{\text{opt}} = \left[\frac{\eta_T\bullet\eta_C\bullet\theta}{(\beta_{23}\bullet\beta_{45}\bullet\beta_{EF})^{\alpha/2}}\right]^{2/(3\alpha)} \tag{40}$$

Making use of equations (5), (38), and (39), compressor compression ratio for maximum cycle power output for a system with two reheats would be given by

$$(\pi_C)_{\text{opt}} = \left[\frac{\eta_T\bullet\eta_C\bullet\theta}{(\beta_{23}\bullet\beta_{45}\bullet\beta_{67}\bullet\beta_{EF})^{\alpha/3}}\right]^{3/(4\alpha)} \tag{41}$$

The quantity $(\beta_{23}\bullet\beta_{45}\bullet\beta_{EF})^{\alpha/2}$ in equation (40) and the quantity $(\beta_{23}\bullet\beta_{45}\bullet\beta_{67}\bullet\beta_{EF})^{\alpha/3}$ in equation (41) may be shown to be close to unity. This implies that $(\pi_C)_{\text{opt}}$ in general is essentially independent of pressure drops in cycle but increases with the number of reheats.

System Performance

To gain insight into the behavior of our system, we have limited our study to the production of power and saturated steam at 150 psia (approximately 1.0 MPa). To examine the effect of compressor compression ratio on the performance of our system operating under different conditions, the following common characteristics were chosen:

η_H, heater efficiency	85 percent
η_g, electrical conversion efficiency	96 percent
ϵ_f, exergy factor of fuel input	1.0
pp, pinch point	20°C
$T_{\max}$, maximum cycle temperature	1500°F (816°C)
T_c, temperature of condensate return	100°C
T_1, temperature of air at compressor inlet	15°C
T_0, temperature of the environment	15°C

With these common characteristics, the performance of our system will still depend on turbine efficiency, compressor efficiency, compressor compression ratio, cycle pressure losses, and the number of stages of reheat.

1 Effect of Number of Stages of Reheat. For this condition, the following additional characteristics were used:

η_T, adiabatic turbine efficiency	90 percent
η_C, adiabatic compressor efficiency	90 percent
$\Delta p/p$, relative pressure drop for each heat transfer device	3 percent

The performance of our system due to no reheat, one reheat, and two reheats is graphically shown in Figs. 4 and 5. From these figures, we may make the following observations:

(*a*) There is significant improvement in electrical power output, process heat production, fuel utilization efficiency, and second-law efficiency due to reheat. But the power-to-heat ratio decreases with reheat because improvement in process heat production is greater than the improvement in electrical power output.

(*b*) Optimum compressor compression ratio is determined by second-law efficiency results in all cases.

(*c*) Optimum compressor compression ratio increases with reheat.

(*d*) There is a fairly wide range for compressor compression ratio that may be used to give good second-law efficiency in the cases of one reheat and two reheats.

(*e*) The variation of electrical power output with compressor compression ratio essentially parallels that of the second-law efficiency in all cases.

2 Effect of Cycle Pressure Losses. For this condition, the following additional characteristics were used:

η_T, adiabatic turbine efficiency	90 percent
η_C, adiabatic compressor efficiency	90 percent
N, number of stages of reheat	One

The performance of our system operating with relative pressure drops of 3 and 5 percent in each heat transfer device in the cycle are graphically shown in Figs. 6 and 7. We note that the fuel utilization efficiency is essentially independent of pressure drops. On the other hand, the second-law efficiency and the power-to-heat ratio clearly reflect the fact that higher pressure drop will degrade the thermodynamic performance more than lower pressure drop. We also note that the optimum compressor compression ratio is essentially independent of pressure losses in the cycle.

Summary

Many useful expressions have been developed for the study of an indirect fired air turbine cogeneration system with reheats. Performance data generated from these expressions should be useful to decision makers in the selection of optimal parameters at the system design stage.

Some of the important conclusions are:

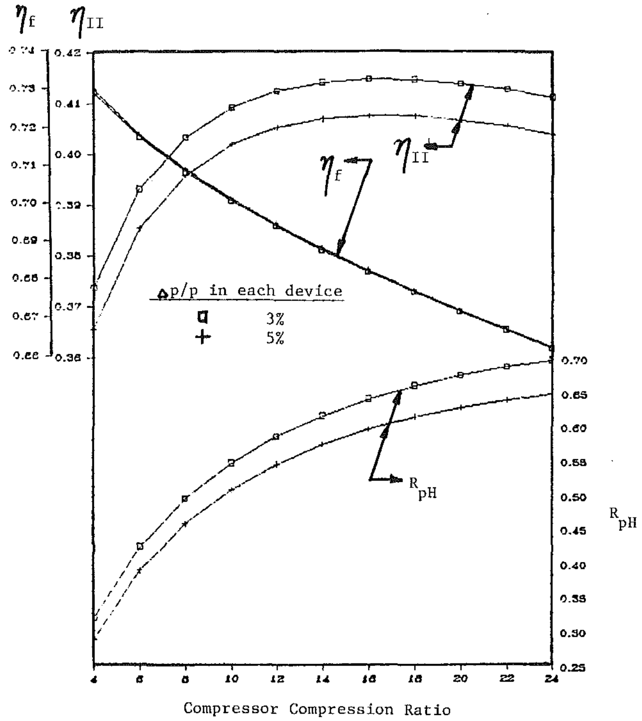

Fig. 6 Effect of pressure drop in heat transfer devices on fuel utilization efficiency η_f, second-law efficiency η_{II}, and power-to-heat ratio R_{pH} for system with one stage of reheat

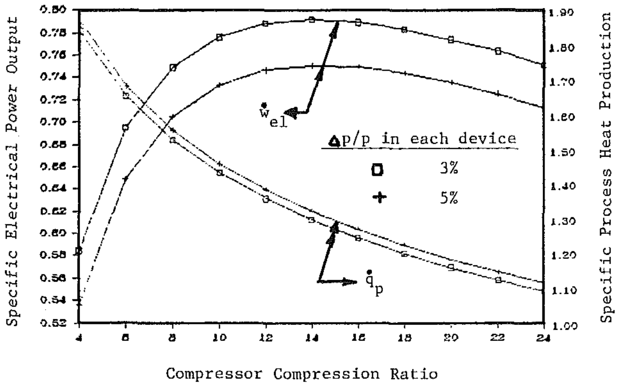

Fig. 7 Effect of pressure drop in heat transfer devices on specific electrical power output $\dot{w}_{el}$ and specific process heat production $\dot{q}_p$ for system with one stage of reheat

1 Specific power output, specific process heat production, fuel utilization efficiency, and second-law efficiency are improved due to one and two stages of reheat, but the power-to-heat ratio decreases with reheat.

2 Optimum compressor compression ratio for maximum second-law efficiency increases with reheat. For a system with no reheat, this optimum compressor compression ratio is about 8. For a system with one stage of reheat, it is about 16. For a system with two stages of reheat, it is about 22.

3 Maximum second-law efficiency does not vary too much over a fairly wide range of compressor compression ratio for one stage of reheat as well as for two stages of reheat.

4 As a first approximation, optimum compressor compression ratio for maximum second-law efficiency may be taken as the optimum compressor compression ratio for maximum cycle power output.

5 Optimum compressor compression ratio for maximum second-law efficiency is essentially independent of pressure losses in the cycle.

6 Second-law efficiency and power-to-heat ratio are better indicators of thermodynamic performance than fuel utilization efficiency.

Acknowledgments

This research is partly supported by a General Electric Company Faculty Fellowship awarded to one of us (F.F.H.).

References

1 Holcomb, R. S., "Development Progress on the Atmospheric Fluidized Bed Coal Combustor for Cogeneration Gas Turbine System for Industrial Cogeneration Plants," ASME JOURNAL OF ENGINEERING FOR POWER, Vol. 102, Apr. 1980.

2 Makansi, J., "External Combustor Enhances Prospects for Coal-Fired Gas Turbine," *Power*, Jan. 1985, pp. 63-64.

3 Wilkinson, W. H., "A Future for Indirect Coal-Fired Gas Turbine Cogeneration Systems," 16th IECEC Conference, Atlanta, GA, Aug. 9-14, 1981.

4 Foster-Pegg, R. W., "Coal Fired Air Turbine Cogeneration," 16th IECEC Conference, Atlanta, GA, Aug. 9-14, 1981.

5 Campbell, J., Jr., and Lee, J. C., "Indirect Fired Gas Turbine for Cogeneration—Open or Closed Cycle?," 17th IECEC Conference, Los Angeles, CA, Aug. 8-13, 1982.

6 Lee, J. C., "Performance Characteristics of Indirect Fired Gas Turbine/Cogeneration Cycles," ASME Paper No. 82-GT-196.

7 Huang, F. F., and Egolfopoulos, F., "Performance Analysis of an Indirect Fired Air Turbine Cogeneration System," ASME Paper No. 85-IGT-3.

8 Rice, I. G., "The Combined Reheat Gas Turbine/Steam Turbine Cycle: Part I—A Critical Analysis of the Combined Reheat Gas Turbine/Steam Turbine Cycle," ASME Paper No. 79-GT-7.

9 El-Masri, M. A., "On Thermodynamics of Gas Turbine Cycles: Part 3—Thermodynamic Potential and Limitations of Cooled Reheat Gas-Turbine Combined Cycles," ASME JOURNAL OF ENGINEERING FOR GAS TURBINES AND POWER, Vol. 108, No. 1, Jan. 1986, pp. 160-170.

10 Gaggioli, R. A., ed., *Thermodynamics: Second Law Analysis*, ACS Symposium Series 122, 1980.

11 Gaggioli, R. A., ed., *Efficiency and Costing: Second Law Analysis of Processes*, ACS Symposium Series 235, 1983.

Operating Experiences and Measurements on Turbo Sets of CCGT-Cogeneration Plants in Germany

K. Bammert
Professor Dr.-Ing.,
Institute for Turbomachinery,
University of Hannover,
Hannover, West Germany

Five closed-cycle gas turbine cogeneration plants have been built and commissioned in the Federal Republic of Germany. In all cases the working fluid was air. The facilities were designed as cogeneration plants to supply electricity as well as heat to electrical and heating networks. Each of the plants accumulated more than 100,000 operating hours. One of them, which has exceeded 160,000 hours of operation, is still working. An account has already been given of the experience with the air heaters of these plants, which were fired with coal, oil, gas, or combinations of these. This paper records the experience obtained with the turbo sets.

Introduction

A total of five closed-cycle air turbine cogeneration plants have been built in West Germany [1]. Of these, four plants were completed by GHH under their full responsibility, to be operated in the cities of Coburg ("Coheiz") and Oberhausen ("Obheiz 1") as municipal power stations, and as industrial power plants in the Haus Aden mine ("Adheiz") and the Gelsenkirchen steel plant ("Geheiz"). The fifth cogeneration plant was planned and built by GHH and EW in a joint venture, to be operated at EW's Ravensburg factory ("Raheiz") as an industrial power station. The main technical data of the five plants have been compiled in Table 1. All plants were used for combined electricity and heat generation. They were of a uniform external design. The turbo set consisted of a turbine as well as HP and LP compressors, and the heat-exchanging equipment of air heater, recuperator, precooler, and intercooler. Internally, the main difference between the turbo sets was that Raheiz was equipped with radial compressors [2], Coheiz with axial compressors and a radial end stage [3], whereas Adheiz, Obheiz 1, and Geheiz were fitted with axial compressors [4, 5]. The turbines were all of axial design. The heat-exchanging recuperators of Raheiz, Coheiz, and Adheiz had corrugated strip fin tubes [2, 3], while plain tubes were installed in the Obheiz 1 and Geheiz plants [5, 6]. The construction principle of radiation and convection parts with a roof-fired combustion chamber originally used in the Raheiz plant [2] was maintained in all other air heaters as well [7, 8]. The burners had to be adjusted to different fuels: Raheiz, Coheiz, and Obheiz 1 were operated on coal, Adheiz on mine gas and coal, and Geheiz on blast furnace gas and fuel oil. Depending on the amount of gas available in the pits or blast furnaces, the energy ratio of gas to coal or fuel oil in the Adheiz and Geheiz plants was fluctuating between 0 and 100 percent.

Of the five plants, four have meanwhile been decommissioned, each having achieved an operating time of about 120,000 hours [1]. The only plant still operating is Coheiz, which in the meantime has scored more than 160,000 working hours and where operation will be continued for several more years to come. As can be seen from Table 1, the electric power output was conclusively raised from plant to plant, i.e., starting with 2.3 MWe in Raheiz, up to 17.25 MWe in Geheiz. Additionally, there was a heating power of 1 to 1.5 MW per MWe of electric power in each of the plants. Even though the power plants achieved excellent operating results in every respect (efficiency and service life), they were not successful in the long term. The reason could have been that they were built at a time when great attention was devoted to the utilization of indigenous fuels. This situation gradually changed when cheap fuel oil and, at a later date, natural gas became available in the market. After years of development, when the oil crisis had made this aspect irrelevant, major changes were introduced to conventional steam power technology. Steam-operated power stations were built with ever-increasing capacities, which led to an improved utilization of the primary heat and to a major decrease in cost.

Even though the high cycle pressure of closed turbine systems permitted a reduction in the structural dimensions of the turbo set, recuperator, and coolers, the considerable expenditure required for the austenitic materials to be used for the radiation heating surfaces of the air heaters operating with atmospheric combustion made it very difficult to reduce the initial capital outlay. Production costs for electricity and heating power are lower when using low-cost combustible waste materials, such as heavy crudes with a high sulfur content which are burned in atmospheric fluidized bed combustors (AFBC) of closed-cycle gas turbines [9]. In addition to conventional applications in cogeneration plants [10], the closed-cycle gas turbine together with an HTR as a nuclear

---

Contributed by the Gas Turbine Division of THE AMERICAN SOCIETY OF MECHANICAL ENGINEERS and presented at the 31st International Gas Turbine Conference and Exhibit, Düsseldorf, Federal Republic of Germany, June 8-12, 1986. Manuscript received at ASME Headquarters January 20, 1986. Paper No. 86-GT-101.

Table 1 Main data and measured efficiencies of CCGT-cogeneration plants (built by GHH, erected and operating in Germany)

PLANT			Raheiz (Ravensburg)	Coheiz (Coburg)	Adheiz (Haus Aden)	Obheiz 1 (Oberhausen)	Geheiz (Gelsenkirchen)
Electric power (peak load) P_{max}		MWe	2.3	6.6	6.37	13.75	17.25
Efficiency at terminals		%	25.8	28.0	29.0	29.5	31.0
Electric power (base load) P		MWe	2.0	6.0	6.0	12.5	16.5
Peak load / base load P_{max}/P		%	15.0	10.0	6.2	10.0	4.5
Turbine	inlet	bar	30.5	29.7	30.4	34.3	37.8
		°C	660	680	681	710	711
Mass flow rate of turbine		kg/s	26.2	74.1	71.9	129.3	153.0
Specific mass flow rate		$\frac{kg/s}{MWe}$	11.5	11.2	11.3	9.4	8.9
Efficiencies	Turbine	%	87.5	89.5	90.0	90.0	89.7
	HP compressor	%	81.5	82.0	82.5	83.5	86.2
	LP compressor	%	82.0	82.0	83.0	85.0	86.0

power station [11] or as a converter in space power systems [12], which exclusively used closed systems, is a most attractive type of power plant.

Owing to their typical features, such as high operating pressure, indirect feed of the fossil, nuclear, or solar primary energy to the working fluid, capacity control via the cycle inventory, etc., closed gas turbine cycles greatly differ from other types of power station in both configuration and operating mode. Therefore, the experience of long years' standing accumulated in the five closed-cycle air turbine plants built and operated in Germany is to be attributed special significance. Detailed reports have already been submitted about the air heaters [5, 7, 8] as well as the heat-exchanging recuperators [2, 3, 6]. The present paper aims at closing a gap by discussing the experience achieved with the turbo sets.

System Description

Externally, all five air turbine plants have the same cycle diagram, i.e., an identical arrangement and number of components. On the other hand, there are differences in the internal conditions of state of the working air depending upon the differences in electric power rating. According to Fig. 1 the working air is precompressed in the LP compressor (*a*), to be cooled again in an intercooler (*b*), before being raised to the maximum process pressure in the HP compressor (*c*). Preheating in the recuperator (*d*) is followed by final heating in a fossil-fired air heater (*e*). Then, the working fluid is expanded in the turbine (*f*), before being restored to its former state in the recuperator (*d*) and, finally, in the precooler (*g*).

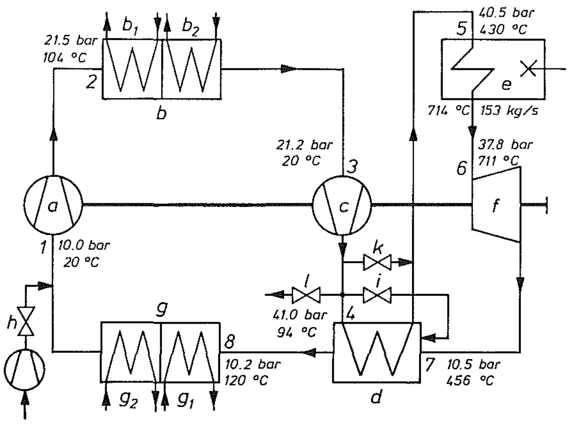

Fig. 1 Diagram of the CCGT-plant Geheiz: (*a*) LP compressor; (*b*) intercooler: (b_1) heating part, (b_2) cooling part; (*c*) HP compressor; (*d*) recuperator; (*e*) air heater; (*f*) turbine; (*g*) precooler: (g_1) heating part, (g_2) cooling part; (*h*) inlet valve; (*i*) bypass control valve; (*k*) heating-power bypass valve; (*l*) outlet valve

The conditions of state according to Fig. 1 correspond to the enthalpy/entropy diagram of Fig. 2. The data entered in

Nomenclature

AFBC = atmospheric fluidized-bed combustor
AH = air heater
BFG = blast furnace gas
C = compressor
CCGT = closed-cycle gas turbine
FCC = fluid catalytic cracking
HP = high pressure
HTR = high-temperature reactor
IC = intercooler
LP = low pressure
LNG = liquefied natural gas
PC = precooler
R = recuperator
T = turbine
d = design point
$\dot{m}$ = mass flow rate
P = power
p = pressure
Δp = pressure loss
s = suction line
t, T = temperature
$\dot{V}$ = volume flow rate
Φ = mass flow number
η = efficiency

German Utilities

Raheiz = CCGT-cogeneration plant at Ravensburg
Coheiz = CCGT-cogeneration plant at Coburg
Adheiz = CCGT-cogeneration plant at Haus Aden
Obheiz 1 = CCGT-cogeneration plant at Oberhausen
Geheiz = CCGT-cogeneration plant at Gelsenkirchen

Manufacturers

GHH = M.A.N. Maschinenfabrik Augsburg-Nürnberg AG, Machinery, Plant and Systems Division, Oberhausen-Sterkrade/Germany
EW = Escher Wyss AG, Ravensburg/Germany

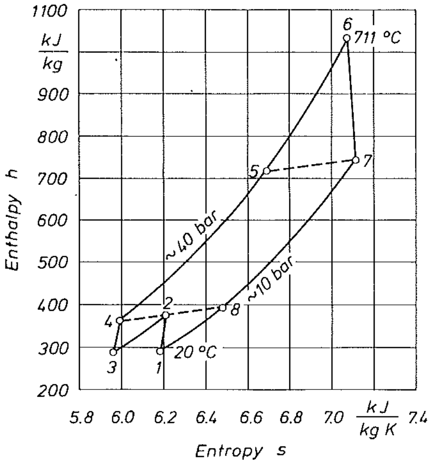

Fig. 2 Enthalpy/entropy diagram of the cycle shown in Fig. 1 (numerals at marked locations correspond to Fig. 1)

Fig. 1 relate to the electric peak load of the Geheiz plant. The cycle diagram is also representative of the other four plants. According to this illustration—and as per Table 1—the pressure upstream of the turbine is 37.8 bar, the temperature upstream of the turbine 711°C, the temperature upstream of the compressors 20°C, while the pressure upstream of the LP compressor is 10.0 bar. The turbine expansion ratio is 3.6. Assuming a differential temperature of 36°C on the hot side of the recuperator, this produces a heater inlet temperature of 430°C. The working air flows into the coiled tubes of the convection part in cross countercurrent to the burned gases. With a temperature of 580°C it flows then through the tubes of the radiation part from top to bottom in parallel with the flue gases, reaching a final temperature of 714°C.

With an electric power at terminals of 17.25 MWe, the mass flow rate at the turbine inlet is 153 kg/s. In the design point, the cycle air enters the precooler at a temperature of 120°C, while at the intercooler inlet it has a temperature of 104°C. These high temperature levels permit more than 60 percent of the waste heat to be utilized for heating purposes without affecting the plant efficiency at terminals of 31.0 percent. Coolers (*b*) and (*g*) in Fig. 1 are divided into a heating part (b_1), (g_1) and a cooling part (b_2), (g_2) on the water side. The water from the heating network is heated in the precooler and in the intercooler from 40 to 90°C (mixed temperature). Fresh water enters the cooling parts at 16°C and is heated to 30°C. On this basis, the total heating power works out as approximately 20 MW, and the remaining cooling power as approximately 10 MW.

Capacity control in normal operation is effected via the pressure level. On this approach, the temperatures and enthalpy drops remain constant as an initial approximation, while the power is varied about in proportion to the cycle pressure and thus to the circulating amount of working air (inventory control). The power controller is designed as a fixed-command unit. The adjusted cycle pressure setpoint is kept at a constant level through the admission of air from storage cylinders into the piping upstream of the LP compressor (inlet valve (*h*) in Fig. 1), or through the blowing-off of air from the piping downstream of the HP compressor (outlet valve (*l*) in Fig. 1).

Speed control of the plant in isolated operation as well as power control in the case of fast changes in load are effected by way of a bypass control valve (*i*) connecting the HP compressor outlet with the turbine outlet, thus bypassing the HP sides of the recuperator, air heater, and turbine. Since in normal operation the compressor power is about 2/3 of the turbine power, and considering that even with opened bypass control valve this power is still required by the compressors, only about 1/3 of the cycle air inventory must be discharged for reducing the effective power of the turbo set to zero. After the valve is closed, the full power is available instantaneously.

Increasing the heating power supply of the plant is achieved by throttling or completely stopping the supply of cooling water. This causes the compressor inlet temperature to rise, permitting the heating water to absorb a correspondingly higher amount of heat. If this approach is insufficient, the HP side of the recuperator can be bypassed by a heating-power bypass (*k*) (Fig. 1). The amount of heat then not transferred in the recuperator is transmitted to the heating water on the LP side in the precooler, and must be additionally provided on the HP side in the air heater.

The amount of heat to be transferred to the working air in the air heater is about proportional to the cycle air mass flow rate and thus the cycle pressure, since the inlet and outlet temperatures are kept at a constant level through the inventory control system. A ratio controller with imposed correcting variable adjusts the fuel energy input in proportion to the cycle pressure. The correcting variable intervening in the fuel-energy to cycle-pressure ratio is the air heater outlet temperature.

The cycle data used as a basis for the cycle diagram during the planning job were confirmed by full-load and part-load tests, like those carried out on the Geheiz plant [5]. This result was certainly promoted by the experience previously obtained in the Raheiz, Geheiz, Adheiz, and Obheiz 1 plants. Shutdown procedures with the Coheiz and Obheiz 1 stations—with the latter largely corresponding in design to the Geheiz plant—have shown that electric release of the full power is possible without causing the plant to trip. During these tests instant synchronization was possible again immediately after load release, and full power supply to the network was reachieved within less than one minute. Fuel readjustment was effected automatically within such a short period that no deviations were found on the temperature recorder [13]. The small overspeed during load release can be traced back to the fact that the compressor power input increases with the cubic power of speed; accordingly, an appreciable portion of the excess power is absorbed by rotor acceleration. The tests about the control and dynamic behavior of Obheiz 1 described in [14] were carried out to permit the results obtained to be transferred to helium turbines connected in an HTR cycle. A helium turbine in a HTR system is always started and stopped in the same way as a closed cycle air turbine, the only difference being that in addition to the outlet temperature the HTR inlet temperature must also be controlled. This is achieved through the use of an additional LP-side recuperator bypass.

Turbo Set Design

The two main components of a thermal power station, and thus also a CCGT-plant, are the heater for transmitting the fossil, nuclear, or solar energy to the working fluid, and the turbo set where the thermal energy of the fluid is converted into mechanical energy. In view of the great variety of fuels involved, if only in the field of fossil fuels and their combinations, the air heater of CCGT-plants is to be considered the most critical unit which, much in the same way as the combustion system, must withstand the highest material temperatures arising in the cycle. Detailed reports about this aspect with the solutions that have been found and on actual long-term experience have been presented in [7, 15]. The present paper will concentrate on turbo sets of CCGT-plants. As previously mentioned, the turbo set for the Geheiz plant illustrated in Fig. 3 is of the same design as the sets for Adheiz and Obheiz 1, and quite similar to the Raheiz and Coheiz systems. Therefore, the Geheiz turbo set will be described as a typical example in this report [15].

The effective power of the turbo set is transmitted to the generator at the turbine-side shaft journal via a toothed cou-

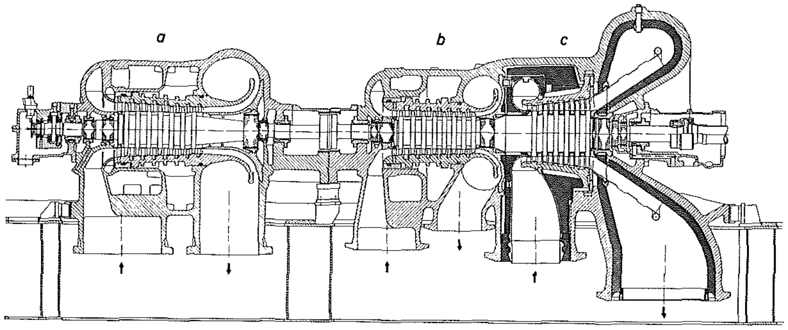

Fig. 3 Geheiz turbo set: (*a*) LP compressor; (*b*) HP compressor; (*c*) turbine

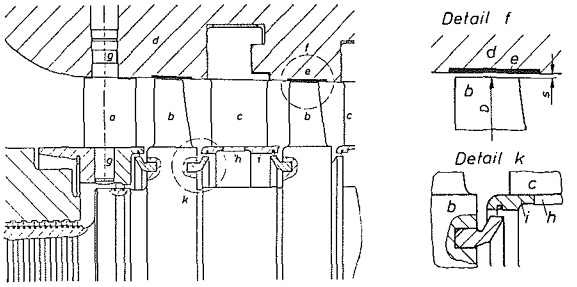

Fig. 4 Geheiz compressor (inlet section): (*a*) inlet stator blades; (*b*) rotor blades; (c) stator blades inside compressor; (*d*) stator blade carrier; (*e*) lining; (*f*) detail of rotor blade clearance; (*g*) adjusting journal; (*h*) grooved journal; (*i*) internal ring; (*k*) detail of labyrinth

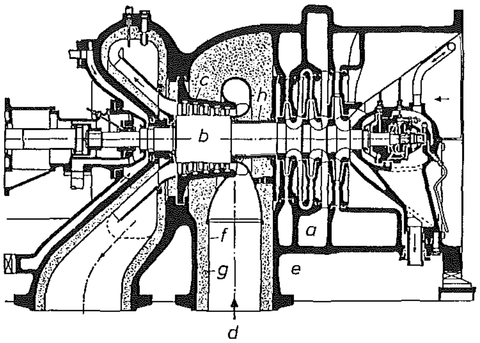

Fig. 5 Raheiz turbo set: (*a*) compressor (three radial stages); (*b*) turbine (five axial stages); (*c*) austenitic inner casing; (*d*) supply of hot air (double-jacket pipe); (*e*) nonalloyed outer casing; (*f*) thin-walled, perforated, and austenitic inner pipe; (*g*) insulation (mineral-wool); (*h*) annular gap

pling and planetary gear. The starting motor rated at about 5 percent of the generator capacity is coupled to the free shaft journal of the generator. The main oil pumps required for oil supply to the machinery are flanged to the gearing. The shaft turning device is arranged between gear and generator.

As shown in Fig. 3, the LP compressor (*a*) is contained in one casing, while the HP compressor (*b*) together with the turbine (*c*) is accommodated in the second casing. The LP rotor is rigidly connected to the HP rotor by a bolt-type coupling. The axial thrust produced by the compressors acts in a direction opposite to that of the turbine thrust. Any remaining thrust is absorbed by a small balancing drum and a double-action axial bearing located on the LP compressor suction side (Fig. 3, left). The rotor hubs of all three turbo machines are cylindrical in the bladed section, but of different diameters. The stator blade rings are fixed to special blade carriers mounted in the outer casing. In view of the large heat expansion the stator blade carrier of the turbine is guided by an annular flange on the outlet side with sealing against the outlet pressure. Centering on the outlet side is achieved by four radial sliding pads.

The compressor blading is designed for a reaction of 100 percent. The LP compressor has seven stages, and the HP compressor eight. The first stator blade ring is followed by normal stages which consist of rotor and stator blades. At the end of the compressor blading there is a ring of outlet stator blades. Figure 4 shows the inlet section of a compressor, where (*a*) designates the inlet stator blades, while (*b*) refers to the rotor blades, and (c) to the stator blades inside the compressor. With a reaction of 100 percent it is in the rotor blades where all the pressure build-up takes place. Therefore, the radial clearance at this location should be as small as possible. According to Fig. 4, the inner wall of the stator blade carrier (*d*) is machined down across the area of the axial rotor blade width, and is lined with low-abrasion material (*e*, Gupa FE 30 make). With this design there is an extremely small ratio of $s/D < 0.5$ per mile (cf. detail (*f*) in Fig. 4), where s is the radial clearance and D the rotor outer diameter. On initial startup of the compressor rotor the rotor blades may touch the inner wall of the stator blade carrier without any damage, thus theoretically producing "zero" clearance.

The blades (*a*) of the inlet stator blade ring are linked to adjustable journals (*g*). This permits the performance curves of the turbo machines to be optimally coordinated during the test run, on initial commissioning or after major inspection jobs. The result is an overall performance graph (Fig. 13) which will be discussed at a later stage of this report. To provide extra security, the stator blades inside the compressor (*c*) with their journals (*h*) are fixed to grooved internal rings (*i*) which toward the rotor have caulked-in sealing rings (cf. detail *k*). This avoids undesired flow conditions in the hub area if the degree of reaction differs from 100 percent on account of corrections in the blade position, fabrication or erection inaccuracies, etc.

The LP compressor casing is made of spheroidal cast iron, and the HP-group casing of cast steel. This choice of materials is possible in spite of the high working air temperature in the turbine because a double-jacket design was used on the turbine. According to this approach, the austenitic stator blade carrier and the austenitic inlet and outlet casings are isolated from the outer casing by insulating material. In addition, cooling air is admitted to the gap between the insulation and the inner wall of the outer casing; this gap is clearly shown in Fig. 3. To withstand the high temperatures in the turbine section, the HP rotor (HP compressor + turbine) was manufactured from a fully forged blank which—like the HP rotors of Raheiz, Coheiz, Adheiz, and Obheiz 1—consisted of highly heat-resistant austenitic material. The turbine blades, which were rated with a reaction of about 50 percent relative to the middle section of the last stage, were made of the same material and were supplied in precision-forged condition. There was no further remachining of the profiles; only the blade roots were treated by broaching. The LP compressor rotor is made of conventional ferritic material. Both machine casings are split horizontally, being suspended from four lateral brackets each and bolted to one another.

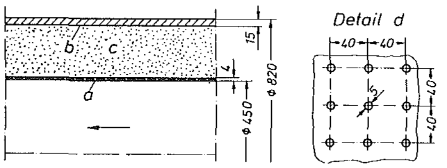

Fig. 6(*a*) Hot-air piping Coheiz: (*a*) perforated inner pipe; (*b*) pressure shroud; (*c*) insulation (mineral-wool); (*d*) detail of perforation of inner pipe; dimensions in mm

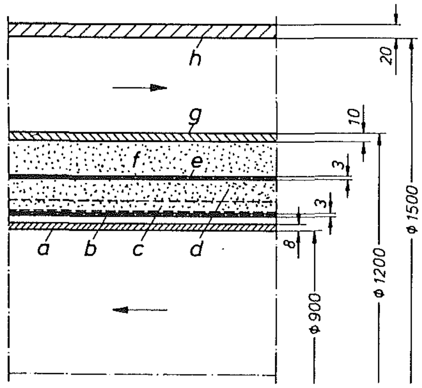

Fig. 6(*b*) Hot-gas piping Obheiz 2: (*a*) inner liner (core pipe); (*b*) perforated inner pipe); (*c*) insulation (KAO mats); (*d*) insulation (KAO wool); (*e*) perforated pipe; (*f*) insulation (KAO wool); (*g*) inner wall of annular duct; (*h*) outer wall of annular duct; ← from heater to turbine; → from HP compressor to recuperator, and from recuperator to heater; dimensions in mm

The double-jacket design was chosen for all turbines included in Table 1 (cf. Figs. 3 and 5). This also applies to the hot-air piping connecting the air-heater outlet header with the turbine. By way of an example, the hot-air piping of the Coheiz plant is illustrated in Fig. 6(*a*). Hot air at a temperature of 680°C (maximum 720°C) flows through the inner pipe (*a*) at a primary pressure of slightly more than 30 bar which is absorbed by the outer shroud (*b*). The thin-walled perforated pipe (*a*) made of austenitic material is thermally screened from the nonalloyed thick-gage pressure shroud (*b*) by an insulating layer consisting of rock wool. The perforation (*d*) of the thin-walled inner pipe, the mineral-wool density which is not allowed to contain even traces of sulfur, and the insulation layer thickness must be well coordinated in such a way that there is rapid propagation of pressure variations in the cycle air without any damage to the inner pipe or high local temperature peaks in the shroud. This basic principle was applied in all closed cycle air turbines, in order to avoid an austenitic outer casing.

Where the hot working gas coming from the heater or high-temperature reactor is not allowed to contact the insulating material, and where thick-gage austenitic pipe materials are to be avoided, a so-called coaxial piping is installed, such as the one of the Obheiz 2 helium turbine plant [16] shown in Fig. 6(*b*). The hot cycle gas flows through the central core pipe from the heater to the turbine (750°C, 27 bar). Hot gas stagnating between the perforated inner pipe (*b*) and the core pipe (*a*) is allowed to be in direct contact with the hot-gas flow through separately arranged bores in the core pipe (pressure equalization). The bored (perforated) inner pipe (*b*) has an insulation of KAO mats (*c*) and another insulation of KAO wool (*d*). There is a further perforated pipe (*e*) followed by an insulating layer (*f*) of KAO wool which extends to the inner wall (*g*) of the annular duct. Being confined toward the outside by a pressure shroud (*h*), this duct carries the working gas in counterflow to the hot gas either from the HP compressor outlet to the recuperator inlet, or from the recuperator outlet to the heater (high-temperature reactor) inlet. The inner liner/core pipe (*a*) and the perforated inner pipe (*b*) are made

Table 2 Working air conditions in the cycle of the plant Obheiz 1

Maximum continuous rating 13.75 MWe		Cycle data	
Component	Location	Pressure bar *)	Temperature °C
LP compressor	1 2	8.58 19.80	30 124.5
Intercooler heating part	3 4	19.75 19.65	124.5 48
Intercooler cooling part	4 5	19.65 19.55	48 30
HP compressor	6 7	19.52 36.69	30 99.5
Recuperator HP	8 9	36.59 36.16	99.5 419
Air heater	10 11	36.07 34.45	419 712
Turbine	12 13	34.34 8.98	710 447
Recuperator LP	14 15	8.95 8.75	447 129.5
Precooler heating part	16 17	8.73 8.64	129.5 50
Precooler cooling part	17 18	8.64 8.60	50 30

*) based on peak load 110 % (see table 3)

Table 3 Main data of the CCGT-cogeneration plant Obheiz 1

CYCLE		
Enthalpy drop of the turbine		289.11 kJ/kg
Enthalpy rise of the LP compressor		96.58 kJ/kg
Enthalpy rise of the HP compressor		72.15 kJ/kg
Effective enthalpy drop		120.38 kJ/kg
Enthalpy increase in the air heater		322.21 kJ/kg
Heat input (fuel)		374.67 kJ/kg
Cycle efficiency		37.36 %
Thermal efficiency		32.13 %
Mass flow rate (peak load)		129.30 kg/s
POWER	base load	peak load
Load	100	110 %
Gross electric power*)	12.98	14.28 MW
Net electric power	12.50	13.75 MW
Fuel power input	44.04	48.45 MW
Heating power (precooler)	9.68	10.64 MW
Heating power (intercooler)	9.32	10.24 MW
Heating power total	19.00	20.88 MW
Cooling power (precooler)	2.43	2.68 MW
Cooling power (intercooler)	2.19	2.41 MW
Cooling power total	4.62	5.09 MW
EFFICIENCY		
Efficiency at terminals		29.5 %
Heating utilization		43.1 %
Total utilization		72.6 %

*) including auxiliary-driven units

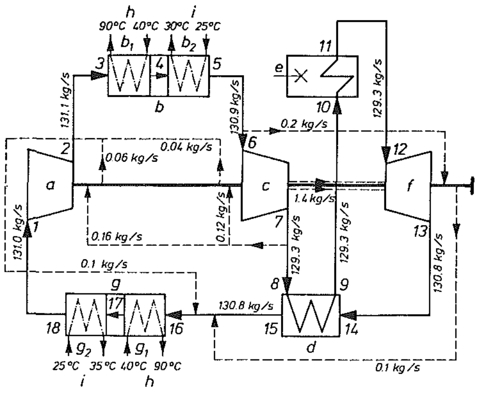

Fig. 7 Diagram of the CCGT-plant Obheiz 1: (*a*) LP compressor; (*b*) intercooler: (b_1) heating part, (b_2) cooling part; (*c*) HP compressor; (*d*) recuperator; (*e*) air heater; (*f*) turbine; (*g*) precooler: (g_1) heating part, (g_2) cooling part; (*h*) heat consumer system; (*i*) cooling tower; ——— cycle air; ------ cooling and sealing air; -·-·-·- heating and cooling water

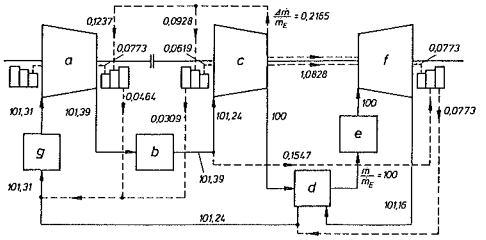

Fig. 8 Cooling and sealing air supply and return flows in implemented CCGT-plants (*cf. Table 1, Obheiz 1, etc.*): (*a*) LP compressor; (*b*) intercooler; (*c*) HP compressor; (*d*) recuperator; (*e*) air heater; (*f*) turbine; (*g*) precooler: $\dot{m}_E$ = mass flow rate of the heater; $\dot{m}$ = mass flow rate of the cycle; $\Delta\dot{m}$ = mass flow rate of the sealing air; ——— cycle air; ----- cooling and sealing air; all numerals are indicated in percent:

cycle air = $(\dot{m}/\dot{m}_E) \cdot 100$
sealing air = $(\Delta\dot{m}/\dot{m}_E) \cdot 100$

of highly heat-resistant austenitic steel, while the piping of the annular duct (*g* and *h*) consists of low-alloy steel. Depending upon the location of the internals inside the insulating areas (inner pipe (*e*), guide and sliding cams, supporting cones, spacer and retaining plates, compensators, etc.) materials within the above quality bracket can be used. The insulation (KAO material) is placed with a density of 300 kg/m^3. The hot-air piping dimensions shown in Fig. 6(*a*) are those of the 6.6-MWe Coheiz plant, while the hot-gas piping of Fig. 6(*b*) corresponds to the Obheiz 2 plant (50 MWe). The wall thicknesses entered in the illustrations give an impression of the savings in austenitic material realized in these plants.

Changes in Cycle Mass Flow Rate

According to Fig. 1, each turbo set of the five CCGT-plants listed in Table 1 consists of an LP compressor, HP compressor, and a turbine. Each component within the closed cycle of a plant does not handle the same amount of working air even in stationary load conditions, which is due to the supply and return of sealing air for the labyrinth seals, as can be clearly seen in Figs. 7 and 8. The schematic diagram of the Obheiz 1 turbine plant is illustrated in Fig. 7, where the reference points 1-18 correspond to those in Table 2. They describe the condition of the working fluid at the inlet and outlet of the respective unit. The pressures, which in the cycle are varied in proportion to the load, are related in Table 2 to the maximum continuous electric power of 13.75 MWe (110 percent load). The individual pressure losses of the air heater, recuperator, precooler and intercooler, and in the piping sections connecting the components, as well as the total pressure loss of the plant can be determined from Table 2. The associated temperatures hardly experience any change in the upper load range. The main technical data of the Obheiz 1 plant can be taken from Table 3, which in the upper section shows the turbine enthalpy drop and the enthalpy rise of the compressors. These provide the effective enthalpy drop and—with the enthalpy rise of the working fluid in the heater—the cycle efficiency. Allowance for the air heater efficiency of 86 percent then provides the thermal efficiency which signifies the ratio between the effective enthalpy drop and the external fuel heat input. Referring to 100 percent and 110 percent load, the middle section of Table 3 indicates the electric power at the generator terminals, and the cooler heating power. Using this as a basis, one can determine the values entered at the bottom of the table for the electric efficiency at terminals, heating utilization, and total utilization of the Obheiz 1 plant, which are all related to the fuel heat input.

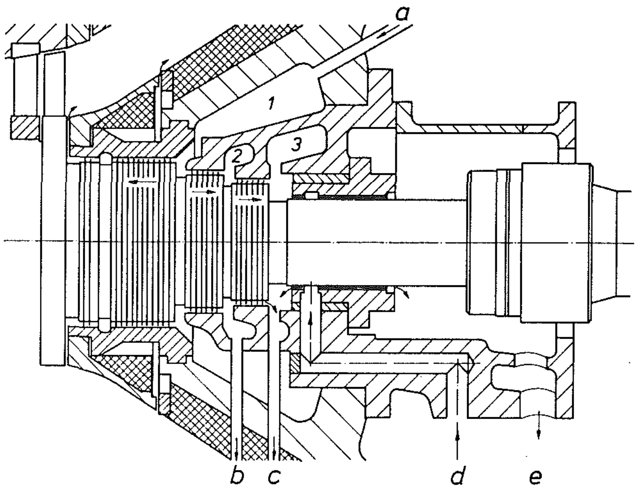

Fig. 9 Turbine outlet Geheiz: (*a*) sealing-air inlet to chamber 1; (*b*) sealing-air outlet from chamber 2; (*c*) sealing-air and oil outlet from chamber 3; (*d*) oil inlet to sealing/journal bearing; (*e*) oil outlet from sealing/journal bearing

The mass flow rates handled by the individual components, which are subject to variation according to the supply and return of both sealing and cooling air, have been quantitatively entered in the cycle diagram of Fig. 7. The cooling and sealing gas flow diagram illustrated in Fig. 8 was derived from Fig. 7; the nondimensional figures entered in this illustration are characteristic values and largely apply also to the other four turbo sets in Table 1. The thick lines in Fig. 8 show the three turbo machines and the heat-exchanging units, while the route and flow direction of the working air in the piping connecting the components is illustrated by thin lines, and the supply and return flows of sealing air by broken lines. Because of the representative character, all numerals in Fig. 8 are referred to the air heater design mass flow rate $\dot{m}_E$. The numerical values on the thin lines provide the percentage throughput $(\dot{m}/\dot{m}_E) \cdot 100$, where $\dot{m}$ is the respective mass flow rate between the individual components. The numerals on the broken lines indicate the sealing-air supply or return flow $(\Delta\dot{m}/\dot{m}_E) \cdot 100$ referred to $\dot{m}_E$, where $\Delta\dot{m}$ is the respective sealing-air flow.

Sealing Air in the LP and MP Sections

At the casing bushings of the LP compressor (inlet and outlet sides), HP compressor (inlet), and turbine (outlet), the rotors are sealed off by an air-sealing system which is of the same design at all four locations. To provide a typical example, the rotor bushing at the turbine outlet side has been illustrated in Fig. 9. The bushing consists of three serrated labyrinth seals, chambers 1, 2, and 3, and a combined sealing/journal bearing.

The sealing-air system is designed to isolate the cycle air

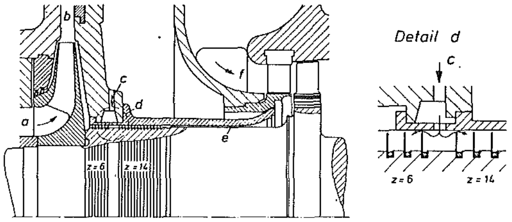

Fig. 10 Coheiz turbo set (HP section): (*a*) HP compressor (7 axial stages + 1 radial end stage); (*b*) disk-type diffusor; (*c*)sealing-air supply (tapped downstream of the disk-type diffusor); (*d*) detail of "see-through" labyrinth seal without defined chambers; (*e*) annular gap; (*f*) turbine (5 axial stages); (*z*) number of labyrinth tips

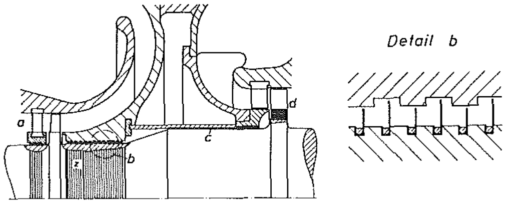

Fig. 11 Obheiz 1 turbo set (HP section): (*a*) HP compressor (11 axial stages); (*b*) detail of labyrinth seal with defined chambers; (*c*) annular gap; (*d*) turbine (6 axial stages); (*z*) number of labyrinth tips: 16 with Adheiz, 25 with Obheiz 1 and Geheiz

from the bearing lube oil. Since the cycle pressures are subject to variation depending on the imposed load, it must be ensured in all operating conditions that no oil enters the cycle, i.e., that the oil leaving the bearings is picked up by sealing air. In other words, the bearing lube-oil and sealing-air pressures are required to react to any changes in the cycle air pressure.

The sealing air drawn from the piping between intercooler and HP compressor inlet (cf. Fig. 8) is admitted to chamber 1 via a pressure control valve (location (*a*) in Fig. 9). From this point, part of the air flows into chamber 2 through the labyrinths while the remaining part is entrained by the working fluid leaving the turbine blading. Chamber 2 on the turbine outlet side is linked to chambers 2 of the other three sealing-air systems via location (*b*). The leakage flows from chamber 1 to chambers 2 are divided into three partial streams. Chamber 2 on the LP compressor inlet side is supplied with sealing air from the other No. 2 chambers. The air is absorbed by the working fluid of the LP compressor. Furthermore, via a solenoid valve, chambers 2 are connected to the recuperator/precooler cycle piping (cf. Fig. 8) which absorbs most of the air; the remaining air flow is used for feeding the seal-oil chambers 3 via labyrinths from chambers 1 through chambers 2.

The seal-oil chambers 3 and the seal-oil tank are interconnected by a pressure equalizing piping. The pressure is slightly below the pressure level in chambers 2 at all times. The circular-cylindrical six-lobe bearing with six oil grooves is designed as a sealing/journal bearing. The bearing oil enters the bearing body at location (*d*) shown in Fig. 9, and then flows into the bearing annulus at a controlled pressure level which is kept by about 2 bar above the pressure in the seal-oil tank. Part of the oil is short-circuited into chamber 3, where it is mixed with sealing air. The air/oil suspension leaves the casing at location (*c*) and is directed to the seal-oil tank, while the remaining oil flows on a longer route via location (*e*) to an oil tank subjected to atmospheric pressure.

Cooling and Sealing Air in the HP Section

Having to fulfill only sealing functions, the leakage and sealing air flows in the LP and MP sections are of a comparatively low magnitude when compared to the cooling and sealing air flow between the HP compressor outlet and the turbine inlet which at the same time fulfill the task of cooling the rotor hub in the 1st turbine stage area. The pressure differential existing between the HP compressor outlet and turbine inlet corresponds to the pressure losses in the HP-side recuperator, heater, and the piping connecting these from the HP compressor outlet to the turbine inlet. In the Raheiz plant it was still sufficient to provide a relatively short axial labyrinth between HP compressor and turbine; this labyrinth was designed as a cylindrical annular gap where the smooth rotor shaft rotates without any contact in a hollow-bored smooth sleeve. The longitudinal section of the turbo set Raheiz (Fig. 5) shows the constant annular gap which extends in axial direction in the HP section (location (*h*)); the gap is dimensioned for a cooling-air flow under normal load of about 1 percent of the HP compressor mass flow rate [2].

With a higher power output the absolute pressure in the cycle is increased (Table 1). This also means a higher pressure differential between the HP compressor outlet and the turbine inlet. Compared to the Raheiz plant, the differential pressure in the Coheiz, Adheiz, Obheiz 1, and Geheiz plants increases by a factor of between two and three. Therefore, a serrated labyrinth was installed upstream the annular gap on these turbo sets. In the Coheiz plant, so-called half-labyrinths were used, i.e., "see-through" labyrinth seals without defined chambers (cf. Fig. 10, detail (*d*)). In contrast, in the Adheiz, Obheiz 1, and Geheiz plants, where there is full axial admission to the compressors and turbine, labyrinths with defined chambers were installed (cf. Fig. 11, detail (*b*)). The bent sealing strips were expanded into the rotor shaft, and were mounted without any clearance relative to the stationary casing section. Should there be any touching, the friction heat produced does not bend the austenic rotor through local heating.

As a representative example of all three plants, Fig. 3 illustrates the Geheiz turbo set [5] which, like the other two sets, is characterized by a smaller hub diameter in the compressors than in the turbine; also, the leakage flow is about 1 percent of the HP compressor mass flow rate. In all cases this air flow is used for cooling the shaft and hub in the inlet section of the turbine rotor. It was possible in all plants to keep the cooling-air flow at a constant percentage of about 1 percent; this was due to the fact that the time-related increase in the turbine inlet temperature from 660°C (Raheiz) to 711°C (Geheiz) was accompanied by an improvement in the austenitic rotor materials. The short axial extension of the labyrinths between the HP compressor outlet and the turbine inlet permitted a small bearing spacing, and thus a high rotor stability in the HP turbo set, to be achieved.

As long as the specified leakage air flows are not known (preliminary design), calculations for the cycle are performed with a constant mass flow $\dot{m}_E$, and the total efficiency is determined by making allowance for a so-called volumetric efficiency η_V which is at a level of about 0.98. After completion of the detail design of all components, cycle calculations are made with precise data of mass flow rate for the various units (i.e., machinery, apparatus, piping, etc.), and the volumetric efficiency is then omitted. As can be seen from the numerical data entered in Figs. 7 and 8, the cooling air flow is added to the cycle air flow at a location downstream of the turbine because on account of its low temperature at the turbine inlet as well as through friction and turbulence effects in the film, formation of the cooling air along the hub wall, and between this flow and the main air stream, there is hardly any contribution by the cooling air to the turbine effective power.

Measuring Results and Efficiencies Achieved

The measured efficiencies and power data of the five implemented CCGT-plants have been compiled in Table 1. The individual efficiencies of both the compressors and the turbines were determined from the measured conditions at the

Table 4 Volume flow rates at inlet of the turbo sets Coheiz and Geheiz

PLANT·			Coheiz	Geheiz
Electric power (peak laod)		MWe	6.6	17.25
Mass flow rate of turbine		kg/s	74.1	153.0
Turbine inlet pressure		bar	29.7	37.8
Turbine inlet temperature		°C	680	711
Inlet pressure HP compressor LP compressor		bar	 12.9 7.9	 21.2 10.0
Inlet temperature HP compressor LP compressor		°C	 20 20	 20 20
Volume	Turbine	m³/s	6.83	13.10
flow rate	HP compressor		4.83	6.07
at inlet	LP compressor		7.89	12.87

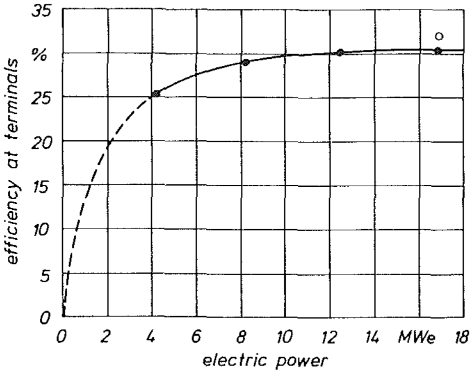

Fig. 12 Efficiency at terminals versus electric power in the Geheiz plant: ● combustion of 90 percent BFG and 10 percent fuel oil; ○ 100 percent fuel-oil firing

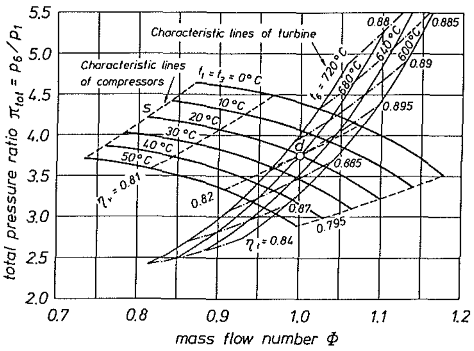

Fig. 13 Performance characteristics of the Coheiz plant: (*d*) design point; (*p*) pressure; (*t*) temperature; (*s*) surge limit; (1, 3, 6) state upstream compressors or turbine; (η_v,η_t) compressor or turbine efficiency

machine inlet and outlet. The efficiency of the total plant, the so-called electric efficiency at terminals, is the relation between the electric power output at the generator terminals and the fuel heat input to the heater as a function of time. The measuring results according to Table 1 were obtained during testing, mostly acceptance tests [3-5, 17]. During the tests, which were performed with a fixed design temperature upstream of the turbo machines while also ensuring security from overloading, the cycle inventory was increased until the electric power at terminals corresponding to the maximum peak load—or the required partial load—had been reached.

The power figures at terminals entered in Table 1 indicate the peak load $P_{\max}$ and the base load P. Values for $P_{\max}$ partly exceed P by a considerable margin. With increasing experience in both construction and operation—especially in air heaters affected by major uncertainties in the design of the radiation and convection chambers when handling solid, liquid, or gaseous fuels and their mixtures (such as coal/mine gas, or BFG/oil)—the relation of $P_{\max}/P$ was reduced from 15 via 10 to 6.2, and finally even to 4.5 percent. All variables in Table 1, i.e., variables of state and mass flow rates, refer to the respective peak load values. The individual efficiencies of the turbo machines were measured in the range of P and $P_{\max}$; there was hardly any variation in these load ranges because volume flow rates were constant and fluctuations in the Reynolds number were limited to the above indicated percentage range.

As can be seen from Table 1, the electric power at terminals was raised from one plant to another, i.e., from 2.3 to 17.25 MWe (and the corresponding heating power from 2.4 to 20 MW). This was accompanied by an increase in the state variables upstream of the turbine (pressure and temperature), mass flow rates, machine efficiencies of the turbine as well as the LP and HP compressors, and finally in the efficiency at terminals. The high specific mass flow rate is a result of the high density of the working fluid (air).

The rise in the turbine inlet temperature coincided with the development of highly heat-resistant austenitic pipe materials for the fossil-fired radiation heaters. Film cooling along the hub at the turbine inlet was installed in all five plants. The rise in temperature upstream of the turbine from 660 to 711°C thus corresponds to a temperature gradient of about 5°/year which is well known in stationary gas turbine construction.

Progress in blading aerodynamics permitted the machine efficiencies to be continually improved. On turbines with a mostly axial admission of the working fluid this development led to isentropic efficiencies up to 90 percent (Table 1). While in the Raheiz plant, the compressors were of fully radial design, the Coheiz machinery was of axial-flow type with a radial end stage on the HP compressor; finally, in the Adheiz, Obheiz 1, and Geheiz plants, the compressors were fully of the axial type. Combined with ever-increasing volume flow rates from one plant to the other (Table 4) and increasingly better blade aerodynamics, isentropic efficiencies of more than 86 percent were achieved [5]. The temperature difference of the recuperator was 30°C in the first four plants (Table 1), and 26°C with Geheiz. As a consequence of the higher turbine inlet temperatures and machine efficiencies, the efficiency at terminals in the various plants rose from 25.8 to 31.0 percent. Even though the electric power in the Coheiz and Adheiz plants was almost the same, the efficiency at terminals of Adheiz increased by 1 percent due to the higher machine and diffusor efficiencies. The overall effect of the measured data in terms of the turbomachinery and air-heater efficiency as well as the recuperator temperature difference can be well represented in an illustrative way for all five CCGT-plants.

Figure 12 shows the efficiency at terminals versus the electric power for the Geheiz plant. The curve drawn as a thick line indicates the efficiency when operating the air heater on 90 percent BFG and 10 percent fuel oil. It should be noted as a characteristic feature of CCGT-plants that the curve has a relatively flat pattern between full load and half-load. A marked drop in the plant efficiency does not become apparent until at quarter-load (broken line). This most favorable reaction can be traced back to the inventory control where temperature and flow rates are kept at an almost constant level even in part-load operation. Figure 12 further shows the plant efficiency under full-load conditions with 100 percent fuel-oil firing. The difference from the full-load point of the thick line is due to the higher efficiency of the air heater when fired with oil.

Figure 13 is the measured overall performance graph of the Coheiz plant, which is fired with coal [3]. The graph which illustrates the characteristic lines of the compressors and turbine is structured to indicate the total pressure ratio p_6/p_1 versus the mass flow numbers Φ [10]. p_6 signifies the turbine inlet pressure, and p_1 the inlet pressure into the LP compressor. The mass flow number is calculated according to the following relation

$$\Phi=\frac{\dot{m}}{\dot{m}_d}\cdot\frac{p_d}{p}=\frac{\dot{V}}{\dot{V}_d}\cdot\frac{T_d}{T}.$$

In this equation, $\dot{m}$ indicates the mass flow, p the pressure, $\dot{V}$ the volume flow rate, and T the absolute temperature. The data to be entered in the design point (d) are the design data at the inlet of the turbine or LP compressor. At Coheiz and Adheiz these performance characteristics were recorded for the first time in CCGT-plants. In view of their general validity, the dependent variables are presented in a dimensionless form.

Since the actual mass flow rates cannot be determined with full precision (inaccuracies in radial clearances, leakages, etc.), point (d) is not perfectly reached on initial commissioning or after major plant stoppages, as has been shown by the experience accumulated with the Coheiz, Adheiz, Obheiz 1, the Geheiz plants. By appropriately adjusting the first stator blade rows of the LP and HP compressors (Fig. 4), the absorption capacity of the three turbo machines can be matched in such a way that the design point is very closely approached. This measure was also introduced to the Coheiz plant during initial trial operation, to be reviewed and confirmed after an operating period of 10,000 h. Then, the operating data were recorded which produced the overall performance graph shown in Fig. 13. In the meantime the Coheiz plant has scored more than 160,000 operating hours without any major variation in the originally measured data. The condition of the plant is excellent enough to forecast a further operating period of some 20,000 hours.

Owing to the fact that in the case of inventory control the electric power at terminals can be varied in proportion to the cycle primary pressure through charging/decharging of the cycle (cf. Fig. 1 valves (h) and (l)), there is the previously mentioned possibility that a reserve in capacity of 4 to 15 percent can be considered in the planning in terms of the electric peak-load power. Accordingly, the turbo set casings, pipework, headers, etc. were rated and inspected according to the ASME *Boiler and Piping Code* as well as the German *Boiler and Vessel Specification*. The overload reserve reduces the operating risk if with design data setting the electric base-load power is not achieved (which with the CCGT-plants handled in this report proved to be not necessary), or transient power peaks are absorbed, or the working-medium temperature upstream of the compressors is increased if there is an excessive demand for heating power (severe winter days) [3]. This, of course, is to the debit of the electricity output. The Coheiz and Adheiz plants which are operated in an optimum way according to their characteristic lines of turbine and compressors are typical of this operating mode. A performance graph of this kind for the Coheiz plant is illustrated in Fig. 13.

Operation of the five CCGT-plants built in Germany has yielded appreciable long-term experience not only under stationary conditions, but also in dynamic behavior, i.e., the transient course of cycle pressure, temperature, mass flow rate, output, and rotor speed, affected by, connected with, and disconnected from the grid [18, 19]. The turbomachinery and the heat-exchanging apparatus achieved the expected efficiencies and proved themselves in operation. The results obtained with air as the working medium can be further improved, and the experience gathered can be transferred to closed-cycle gas turbines being operated, for instance, on helium [16] or nitrogen [20] as the cycle medium.

In closed-cycle processes using air as the working fluid there is room for improvement, on the one hand, in terms of plant efficiency without any effects on the hot side by adding a refrigeration loop downstream of the coolers (precooler, intercooler), thus lowering the working-air temperature in the main cycle upstream of the compressors to less than the ambient temperature level [21]. On the other hand, in combined heating/power applications, the utilization of primary energy can be improved by 10 to 15 percent by increasing the waste-heat temperature level also in the cooling parts of the precooler and intercooler (see (b_2) and (g_2) of Fig. 1 or Fig. 7) within the refrigeration process to such a value that—similar to the heating power of heating parts (b_1) and (g_1)—it can be utilized for actual heating purposes. In this way the refrigeration process incorporated in the main cycle is converted into a heat-pump process [21, 22]. Similarly, through intervention on the cold side of the closed cycle, plant efficiency can be noticeably improved by utilizing the exergy of LNG released in connection with re-evaporation [20]. In this approach the working fluid (nitrogen) in the LNG evaporator, which replaces the coolers of the main cycle, is reduced to a temperature level far below ambient temperature so that the power absorbed by the compressors in the cycle is much lower than in a plant where the lower process temperature is defined by ambient conditions. Further, major design details that had given excellent service on the hot side of implemented CCGT-plants were transferred to other installations as well. Typical examples of this are the blading, rotor cooling system, configuration of the casing and labyrinths, etc., which were largely incorporated in FCC plants [23]; in consequence, FCC expanders include many characteristic features of closed-cycle gas turbines.

Just like the turbo sets described in this report, the associated recuperators and air heaters were improved by ongoing development from one implemented CCGT-plant to the other. In addition to the heat transmission capacity (temperature difference), it is also the pressure drop in recuperators of CCGT sets which exerts a great effect on the efficiency of the total plant. However, as it is not possible to precisely precalculate these variables, measurements were made in implemented plants to obtain correction data for the selective and reliable rating and optimization of recuperators [6]. As previously mentioned, the air heater poses the greatest problems both in design and under a cost aspect in any CCGT-plant. The five air heaters, which each consisted of a radiation and a convection part, fully performed their job, but one should not forget the immense development work required for them, if only on account of the great variety of fuels used (coal, fuel oil, gas) [7]. With an outlet temperature of 714°C (air heater Geheiz), the highest tube wall temperatures in the radiation part range from 770 to 789°C [5, 15]. Unlike in a steam boiler, the working-air pressure is only about 40 bar, so that these temperatures can be controlled with commercially available austenitic materials.

Conclusion

The thermal power transmitted or converted in the various components of a closed-cycle gas turbine is usually much higher than the power supplied to the electric generator. The amount of working fluid circulating in the cycle is affected by the supply and return of sealing and cooling gas, gaps and clearances, leakages, casing and bearing seals, etc. All this has an effect on both the power and efficiency of the individual components and the plant as a whole. Whereas the aerodynamic rating of the blading in turbomachinery is part of the generally known state-of-the-art, the configuration and arrangement of labyrinths and clearances, matching of pressures in the labyrinth chambers, selection of the correct sealing-gas and cooling-gas flows, etc., described in this report are of a similarly great importance. The experience accumulated in this regard can well be transferred to working gases other than air.

When planning cogeneration plants with closed-cycle gas turbines one should take care not to generate more heating power than is to be supplied by the cycle as electrical energy at a maximum yield. The bypasses on the high-pressure and low-pressure sides [24] should only be used to cover transient peak loads. The supply of heat via a bypass in continuous operation of the plant requires an increased expenditure for high-grade materials in the air heater, which bears no relation to the generally available possibilities of generating heating power by more simple means and thus more economically.

References

1 Bammert, K., and Groschup, G., "Status Report on Closed-Cycle Power Plants in the Federal Republic of Germany," *Trans. ASME*, Vol. 99, 1977, pp. 37-46.

2 Bammert, K., Keller, C., and Kress, H., "Pulverized Coal-Fired Closed-Cycle Air Turbine Plant for the Cogeneration of Heat and Electricity" [in German], *BWK* (*Brennstoff-Wärme-Kraft*), Vol. 8, 1956, pp. 471-478.

3 Bammert, K., "Twenty-Five Years of Operating Experience With the Coal-Fired Closed-Cycle Gas Turbine Cogeneration Plant at COBURG," ASME JOURNAL OF ENGINEERING FOW POWER, Vol. 105, 1983, pp. 806-815.

4 Holzapfel, H., "Closed-Cycle Air Turbine Cogeneration Plant at Oberhausen" [in German], *MTZ* (*Motortechn. Zeitschrift*), Vol. 23, 1962, pp. 375-383.

5 Bammert, K., Bohnenkamp, W., and Rehwinkel, H., "Test Results for the Blast Furnace Gas and Oil-Fired Gelsenkirchen Closed-Cycle Air Turbine Plant" [in German], *Stahl und Eisen*, Vol. 91, 1971, pp. 309-314.

6 Bammert, K., Kläukens, H., and Mukherjee, S. K., "Design of Heat Exchangers for Closed-Cycle Gas Turbine Plants" [in German], *BWK* (*Brennstoff-Wärme-Kraft*), Vol. 22, 1970, pp. 275-279.

7 Bammert, K., "Long-Term Experience With Coal Fired Heaters in German Closed-Cycle Air Turbine Plants," *Atomkernenergie/Kerntechnik*, Vol. 38, 1981, pp. 241-256.

8 Deuster, G., "Long-Time Operating Experiences With Oberhausen Closed-Cycle Gas Turbine Plant," ASME Paper No. 70-GT-73.

9 Pietsch, A., Mason, J. L., Wilson, T. R., and Harper, A. D., "5 MW Closed-Cycle Gas Turbine," ASME Paper No. 84-GT-268.

10 Bammert, K., "Performance of a Closed-Cycle Air Turbine Plant as a Heating Power Plant Under Changing Operating Conditions" [in German], *Konstruktion*, Vol. 8, 1956, pp. 443-452.

11 McDonald, C. F., Cavallaro, L., Kapich, D., and Medwid, W. A., "Very High Small Nuclear Gas Turbine Power Plant Concept (HTGR-GT/BC) for Special Applications," ASME Paper No. 84-GT-269.

12 Parker, G. H., and Pierce, B. L., "Design Considerations for Nuclear Reactor Gas Turbine Space Power Systems," ASME Paper No. 83-GT-20.

13 Holzapel, H., "Closed-Cycle Gas Turbines as Heating Power Stations" [in German], *Technische Berichte*, GHH, Vol. 4, 1961, pp. 1-14.

14 Bammert, K., Krey, G., and Küper, K. D., "Performance of High-Temperature Reactor and Helium Turbine," *Kerntechnik*, Vol. 11, 1969, pp. 77-87.

15 Bammert, K., "The Thermal Load of Tubes in Radiation Heaters," *Forschung im Ingenieurwesen*, Vol. 48, 1982, pp. 160-165.

16 Bammert, K., and Deuster, G., "Layout and Present Status of the Closed-Cycle Helium Turbine Plant at Oberhausen," ASME Paper No. 74-GT-132.

17 Bammert, K., and Keller, C., "Measurement Results From the First Pulverized Coal-Fired Air Turbine Cogeneration Plant" [in German], *BWK* (*Brennstoff-Wärme-Kraft*), Vol. 12, 1960, pp. 62-64.

18 Bammert, K., and Posentrup, H., "The Behavior of a Closed-Cycle Gas Turbine With Time Dependent Operating Conditions" [in German], *VDI-Forschungsheft*, Vol. 588, 1978, pp. 1-36.

19 Bammert, K., and Krey, G., "Dynamic Behavior and Control of Single-Shaft Closed-Cycle Gas Turbines," *Trans. ASME*, Vol. 93, 1971, pp. 447-453.

20 Krey, G., "Utilization of the Cold by LNG Vaporization With the Closed-Cycle Gas Turbine" [in German], *Atomkernenergie*, Vol. 32, 1978, pp. 259-264.

21 Bammert, K., and Reiter, U., "The Closed-Cycle Gas Turbine With a Refrigeration Cycle and Heat Pump" [in German], *Wärme*, Vol. 88, 1982, pp. 91-94.

22 Bammert, K., and Reiter, U., "The Application of Heat Pump Cycles in Combination With Compression Processes," *VDI Reports*, No. 539, 1984, pp. 817-841.

23 Jeske, H. O., and Sandstede, H., "Turbine Blade Behavior in Gas Streams Containing High Dust Loads," *Forschung im Ingenieurwesen*, Vol. 51, 1985, pp. 52-62.

24 Grim, W. M., Fraize, W. E., Malone, G. A., and Kinney, C., "Closed-Cycle Cogeneration for the Future," ASME Paper No. 84-GT-272.

J. W. Baughn
Professor.

R. A. Kerwin
Research Assistant.

Department of Mechanical Engineering,
University of California,
Davis, CA 95616

A Comparison of the Predicted and Measured Thermodynamic Performance of a Gas Turbine Cogeneration System

The thermodynamic performance of a gas turbine cogeneration system is predicted using a computer model. The predicted performance is compared to the actual performance, determined by measurements, in terms of various thermodynamic performance parameters which are defined and discussed in this paper. These parameters include the electric power output, fuel flow rate, steam production, electrical efficiency, steam efficiency, and total plant efficiency. Other derived parameters are the net heat rate, the power-to-heat ratio, and the fuel savings rate. This paper describes the cogeneration plant, the computer model, and the measurement techniques used to determine each of the necessary measurands. The predicted and the measured electric power compare well. The predicted fuel flow and steam production are less than measured. The results demonstrate that this type of comparison is needed if computer models are to be used successfully in the design and selection of cogeneration systems.

Introduction

Cogeneration is considered here to be the simultaneous production of electrical (or shaft) energy and useful thermal energy from the same facility [1, 2]. It is a far more efficient use of fossil fuels than separate production [3–5]. Since the electric energy can generally be returned to a grid, it can be considered a byproduct if it is not needed at the cogeneration site [6]. The interest in cogeneration has been especially keen in California (USA) where policies and pricing (of the electric byproduct) have strongly encouraged cogeneration [7].

Conventional plants use boilers to produce required thermal energy and purchase required electricity from a utility. In this case the electrical generation efficiency ranges from 34 percent to about 40 percent. When useful thermal energy and electricity are produced simultaneously, by cogeneration, the overall efficiency can exceed 80 percent.

The most common cogeneration technologies available today are all topping cycles. These technologies include the noncondensing steam turbine, the gas turbine (GT), and the IC (or Diesel) engine [8]. The present study examines the performance of a gas turbine cogeneration system located at the University of California, Davis campus.

In order to describe the performance of a cogeneration system it is necessary to determine various thermodynamic parameters. These thermodynamic parameters can be useful in determining the merits and economics of cogeneration systems [9, 10]. These parameters can be determined by measurements or by computer modeling of a given cogeneration system. In an earlier study, the performance of this plant was analyzed using a computer program [1].

In this paper, results from an extensively modified computer program are compared to a set of plant measurements. The measurements are taken under actual operating conditions. This type of comparison is necessary if accurate calculations of performance and return on investment are to be made. Large inaccuracies in such predictions often occur [11].

It should be noted that the economics and performance of cogeneration systems are complex and involve far more than the thermodynamic parameters considered here.

Cogeneration Plant Description

The cogeneration plant at U.C. Davis began operation in 1980 and has an output of approximately 3 MW of electric power and 9070 kg/hr (20,000 lbm/hr) of 1.14 MPa (150 psig) steam. The electricity is returned to the local grid and the steam is used to supplement the two main boilers on campus which are rated at approximately 45,000 kg/hr (100,000 lbm/hr) each. The plant is operated continuously and is used for the base load. This plant is typical of this type of gas turbine cogeneration system [12, 13]. A diagram of the U.C. Davis cogeneration system is shown in Fig. 1. The main components of the system are a gas turbine (Allison 501) coupled to a generator and an unfired waste heat recovery boiler. It has an inlet air heat exchanger which uses water from a preexisting absorption chiller to cool the inlet air during the hot season. There are three main fluid paths: air/exhaust, feedwater/steam, and chilled water.

Contributed by the Gas Turbine Division of The American Society of Mechanical Engineers and presented at the 31st International Gas Turbine Conference and Exhibit, Düsseldorf, Federal Republic of Germany, June 8–12, 1986. Manuscript received at ASME Headquarters February 7, 1986. Paper No. 86-GT-162.

Air/Exhaust. Air enters through an inlet silencer and filter and passes through an inlet cooling heat exchanger. A small part of the flow is then diverted to cool the generator while the balance of the flow enters the gas turbine where it is compressed; combusted products then pass through the evaporator and economizer sections of a forced recirculation boiler and finally leave the plant through an exit silencer and exhaust stack at approximately 154°C.

Feedwater/Steam. Feedwater enters the cogeneration plant from the main boiler plant at approximately 116°C. It flows through an economizer in which its temperature is increased to approximately 181°C and then enters a recirculation tank. Water from this tank is continuously pumped through an evaporator where approximately 10 percent of the water is evaporated on each pass. The dry saturated steam at 1.14 MPa is separated and returned to the main boiler plant to join the steam from the main boilers.

Chilled Water. Chilled water for the inlet air cooling is provided at a nominal temperature of 7°C from steam-powered absorption chillers. These chillers are used to provide cooling to a number of buildings on campus and are much larger than required for this inlet air cooling. This represents a parasitic steam load on the cogeneration plant since a portion of the plant output steam must be used to replace the steam required to produce this chilled water.

Thermodynamic Parameters. The thermodynamic parameters considered here include the electric power output, the fuel input, the steam output, the steam efficiency, and the electric efficiency. Other derived parameters are the net heat rate, the power-to-heat ratio, and the fuel savings rate. Each is defined below.

The electric power output is the generator output less the parasitic loads of fans, pumps, etc. The fuel input is in terms of energy units and is based on the lower heating value of the fuel. As discussed later, the performance curves for the gas turbine used do not distinguish between distillate and gaseous fuel, although such distinction may be necessary.

The steam output can be in mass flow units or in energy output units. If it is in energy units, the feedwater and blowdown makeup water temperatures must be known.

The steam efficiency is defined as the ratio of the feedwater/steam thermal energy transfer rate Q_s less any parasitic steam loads Q_p to the fuel energy input rate, Q_{in} (based on the heating value and flow rate of the fuel).

$$\eta_s = (Q_s - Q_p)/Q_{in} = Q_{s,\mathrm{net}}/Q_{in} \qquad (\mathrm{MW_{th}/MW_{th}})$$

The electric efficiency is defined as the ratio of the generator electric power output W_g less any parasitic electric loads W_p (i.e., fans, pumps, etc.) to the fuel energy input rate

$$\eta_e = (W_g - W_p)/Q_{in} = W_{g,\mathrm{net}}/Q_{in} \qquad (\mathrm{MW_{el}/MW_{th}})$$

The plant efficiency is the sum of the steam efficiency and electric efficiency in the absence of any additional heat recovery systems (which is the current operating mode of this plant).

The net heat rate NHR is the ratio of the fuel energy input rate, less the amount that would be necessary to produce the useful thermal energy separately by conventional means, to the net electricity

$$\mathrm{NHR} - (Q_{in} - Q_{s,\mathrm{net}}/\eta_{\mathrm{aux}})/W_{g,\mathrm{net}} \qquad (\mathrm{MW_{th}/MW_{el}})$$

where $Q_{s,\mathrm{net}}/\eta_{\mathrm{aux}}$ is the energy that would be necessary to produce the thermal energy by a conventional boiler with an efficiency of η_{aux} (a value of 0.80 is used in this study). The lower the net heat rate the more efficiently the fuel is being used.

The power-to-heat ratio PHR is the ratio of the net electric power generated to the useful thermal energy produced

$$\mathrm{PHR} = W_{g,\mathrm{net}}/Q_{s,\mathrm{net}} \qquad (\mathrm{MW_{el}/MW_{th}})$$

The fuel savings rate FSR is the fuel saved over that required for separate production of the electricity and thermal energy per unit of useful thermal energy produced. It is proportional to the difference in the standard heat rate of a central utility power plant and the net heat rate of the cogeneration plant. The fuel savings rate is this difference times the power-to-heat ratio [9]. For example, if we assumed a heat rate of 2.5 $\mathrm{MW_{th}/MW_{el}}$ (an efficiency of 40 percent) for a conventional central utility power plant, the FSR is given by

$$\mathrm{FSR} = (2.5 - \mathrm{NHR})(\mathrm{PHR}) \qquad (\mathrm{MW_{th}/MW_{th}})$$

The fuel savings rate predicts the rate of energy conservation and is particularly interesting in considering the merits of cogeneration systems. It should be noted that the use of the fuel savings rate assumes that the electric energy produced can be used to displace fuel use at a central utility plant.

Measurement Methods and Data

Three sets of measurements taken on the cogeneration plant are listed in Table 1. These measurements fall into two categories: those needed to actually calculate the above thermodynamic performance parameters, and those necessary to compare this performance to predictions (e.g., the ambient air temperature may affect the performance but is not actually used to calculate any of the thermodynamic parameters given above). A data acquisition system was used for most of the temperature and flow measurements. The measurements were taken at intervals of 5 to 30 min over a 2 to 3 hr steady operating period and the values given in the data set of Table 1 are time averaged. A brief description of the measurement methods follows.

Air/Exhaust. Ambient conditions were measured using a mercury barometer, an electronic humidity meter, and a type J thermocouple for ambient pressure, humidity, and temperature, respectively. Pressure and humidity were measured hourly from direct readouts while the temperature

Nomenclature

C_{pe} = exhaust gas specific heat (temperature dependent)
h_{fw} = feedwater enthalpy
h_g = steam-saturated vapor enthalpy
m_a = air flow rate
m_{BD} = blowdown flow rate
m_{cs} = chiller steam flow requirement
m_f = fuel flow rate
m_{fw} = feedwater flow rate
m_g = generator air flow rate
m_s = steam flow rate
p_a = ambient pressure
P_b = gear box output power
P_f = generator fan power
P_g = generator output power
P_o = isentropic fan power
P_{oc} = oil cooler pump power
P_{rp} = recirculation pump power
p_s = steam pressure
$p_{\mathrm{sat},a}$ = ambient water vapor saturation pressure
P_t = turbine shaft power
T_a = ambient temperature
T_{ci} = chilled air temperature
T_{fw} = feedwater temperature
T_s = steam temperature
T_{te} = turbine exit temperature
T_{ti} = turbine inlet temperature
v_a = air specific volume
V_g = generator air volumetric flow rate
w = turbine rpm
x = steam quality
δ = inlet turbine inlet pressure ratio
Δp_r = recirculation pressure drop
η_f = generator fan efficiency
η_b = gearbox efficiency
η_{rp} = recirculation pump efficiency

Table 1 Data set

Measurand*	Units	Plant Measurements A	B	C
Ambient Temperature	°F	80.3	87.8	96.2
Ambient Pressure	in. hg.	29.9	30.0	29.9
Relative Humidity	%	47.0	24.4	24.9
Chilled Air Temperature	°F	54.5	54.8	61.6
Turbine Inlet Temperature	°F	1760	1760	1760
Turbine Rotational Speed	RPM	14,450	14,500	14,500
Natural Gas Flow Rate	SCFM	755	753	739
Generator Electric Output	MW	2.97	2.98	2.88
Parasitic Voltage	V	489	490	488
Parasitic Current	A	50	50	50
Feedwater Flow Rate	lbm/hr	21,009	22,542	21,573
Feedwater Temperature	°F	231	227	236
Chilled Water Temp-Inlet	°F	44.7	44.8	49.2
Chilled Water Temp-Outlet	°F	59.0	61.2	67.5
Chilled Water Flow Rate	lbm/hr	70,410	72,687	70,921
Steam Pressure	psig	150	151	150
Stack Exhaust	°F	362	362	362

*Units Recorded as Measured

NOTE: Gas Turbine Exhaust Temperature was measured at a later date for a single run as 969°F.

was recorded with an automatic data acquisition system (HP 3056DL) every 15 min. Chilled air temperature was also measured automatically every 15 min using a type J thermocouple inserted directly into the inlet air duct downstream of the chilling coil. Turbine inlet temperature and stack exhaust temperature were measured using installed type K thermocouples and a direct readout. The turbine inlet temperature readout is an average of 12 thermocouple outputs distributed evenly among the six combustion cans. In a separate experiment turbine exhaust temperature was measured with the data acquisition system using a type K thermocouple inserted into (and traversing) the exhaust flow.

Feedwater/Steam. The instantaneous feedwater flow rate was measured by the data acquisition system every 5 min using a calibrated turbine flow meter. The plant does not have a steam flow rate meter installed and the estimated cost of installing such a meter was prohibitive, so steam flow rate is inferred from the feedwater flow rate. No blowdown was made during the measurement periods. No independent measurement of the exit steam quality was made.

Chilled Water. The chilled water flow rate is also recorded by the data acquisition system using a turbine flow meter. Readings were taken at 15-min intervals. Chilled water temperatures into and out of the plant were measured using type K thermocouples which were mounted beneath insulation directly on the copper pipe surfaces.

Turbine/Electric. Fuel flow rate into the combustor is measured with timed readings of a totalizing turbine meter. Turbine rotational speed is measured using a magnetic pickup hooked to a gage readout, while generator power output, parasitic load voltage, and parasitic current are also displayed using standard dial gage outputs.

Computer Program

The computer program "UCDCGN" simulates the performance of the U.C. Davis cogeneration plant. It is based on an earlier program described in [1, 9]. Substantial revisions have been made to improve its flexibility and accuracy. The computational procedure used to simulate the thermodynamic performance of the plant is outlined in the Appendix. To perform its simulation, the program uses six data sets:

1 A set of initial conditions and input data including ambient air conditions, steam exit pressure and quality, component efficiencies, engine operating parameters, and the lower heating value of the fuel.

2–5 Four digitized sets of manufacturer's performance curves for the Allison 501KB gas turbine engine. These curves relate air intake, fuel energy input, shaft horsepower and turbine exit temperature to such operating parameters as turbine inlet temperature, rotary turbine speed, and dry air conditions at the compressor inlet.

6 A digitized set of temperature, pressure, and enthalpy relationships for water at saturated conditions.

For the purposes of calculating density and enthalpy changes, air is assumed to be a perfect gas. For the exhaust gas a temperature-dependent specific heat is used.

The chilled water used by the cooling coils is provided by a separate, steam-driven absorption chiller system. Based on chiller operating experience, a value of 1 kg of steam per 2.32 MJ of cooling was chosen as typical.

Following the procedure shown in the Appendix, the program begins by determining the required water liquid, vapor, and steam properties. It then uses the input data and digitized performance curves to obtain the gas turbine operating parameters (i.e., air and fuel flow rates, power output, and exhaust temperature). The parasitic power, steam, and air requirements are then calculated and are used to determine the plant thermodynamic parameters discussed above.

Results and Discussion

Measurements. Table 1 contains results for three sets of measurements for the plant. The data were taken during the summer and have relatively close ambient temperatures. The turbine was operated at a turbine inlet temperature of 1760°F, which is slightly below the rated value of 1800°F. Our local utility provided a lower heating value for the fuel during the time the tests were run of 906.5 Btu/scf.

These measurements were used to calculate the thermodynamic performance parameters for the plant shown in Table 2. Since only the feedwater flow rate is measured (not the exit qualities) the net steam energy rates require an assumed exit quality. Two qualities (98 and 90 percent) are included in Table 2. The assumption of 1 kg of steam per 2.32 MJ of air cooling was used to calculate the parasitic steam load. This is based on operating experience with the chillers.

Computer Predictions. The ambient and operating condi-

Table 2 Performance parameters derived from measurements

	Units	A	B	C
Net Electric Energy Rate	MW	2.95	2.95	2.86
Net Fuel Energy Rate	MW	12.03	12.00	11.78
Gross Steam Flow Rate	kg/sec	2.65	2.84	2.72
Gross Steam Energy Rate (1)	MW	6.00 (5.61)	6.45 (6.02)	6.16 (5.76)
Net Steam Flow Rate (2)	kg/sec	2.53	2.69	2.56
Net Steam Energy Rate (1)	MW	5.73 (5.36)	6.11 (5.70)	5.79 (5.42)
Electric Efficiency		0.245	0.246	0.243
Steam Efficiency		0.475	0.517	0.492
Total Efficiency		0.720	0.763	0.735
Net Heat Rate (3)	-	1.65 (1.81)	1.48 (1.65)	1.61 (1.74)
Power to Heat Ratio	-	0.51 (0.55)	0.48 (0.52)	0.50 (0.53)
Fuel Savings Rate Rate (4)	-	0.43 (0.38)	0.49 (0.44)	0.45 (0.40)

(1) Based on assumed exit quality of 98% (assumed quality of 90% in parentheses)

(2) Based on calculated requirement for steam cooling.

(3) The boiler used for comparison has an assumed efficiency of 80%.

(4) The central utility electric plant used for comparison has an assumed efficiency of 40%.

Table 3 Computer model performance results: measurement for input data

Performance Parameter	Unit	A (% dif.*)	B (% dif.*)	C (% dif.*)
Net Electric Energy Rate	MW	2.92 (1.0%)	2.91 (1.4%)	2.85 (0.4%)
Net Fuel Energy Rate	MW	11.04 (9.0%)	11.11 (8.0%)	10.84 (8.7%)
Gross Steam Flow Rate	kg/sec**	2.23 (19%) (2.39) (11%)	2.24 (27%) (2.40) (18%)	2.24 (21%) (2.40) (13%)
Gross Steam Energy Rate	MW	5.11	5.13	5.09
Net Steam Flow Rate	kg/sec	2.10	2.07	2.07
Net Steam Energy Rate	MW	4.80	4.74	4.70
Electric Efficiency		0.264	0.264	0.264
Steam Efficiency		0.431	0.425	0.432
Total Efficiency		0.695	0.689	0.696
Net Heat Rate (NHR)		1.74	1.77	1.74
Power to Heat Ratio (PHR)		0.61	0.62	0.61
Fuel Savings Rate (FSR)	-	0.47	0.45	0.46

* % difference between measurement and computed (i.e. +% indicates measurement is higher.

** Based on assumed exit quality of 98% (assumed quality of 90% in Parenthesis)

tions for the data sets of Table 1 were input into the computer program and the results are shown in Table 3. All the results in Table 3 assume an exit quality of 98 percent since this is the design value for the plant.

Examining the results we note first that the predicted net electric power from the plant is consistently in excellent agreement with the measurements, differing by less than 1.4 percent.

The predicted fuel input energy rates, however, are consistently less than measured by 8-9 percent. The predictions are based on the gas turbine performance curves and are for a new and clean nominal (average) engine. A dirty compressor may increase fuel consumption. A check with the manufacturer also suggested that the use of natural gas may cause a 3-4 percent increase in fuel energy rate, even though the current performance curves make no distinction between gaseous and distillate fuels [14]. This higher fuel flow rate should cause a higher turbine exhaust temperature. The turbine exhaust temperature was measured at a later date for operating conditions similar to those of the earlier measurements. The measurement of 969°F is higher than the computer predictions of 930°F, consistent with the higher fuel flow at a given output power.

To compare the predicted and measured steam rates it is necessary to assume that the measured feedwater flow rate is equal to the gross steam flow rate. This should be a good assumption since there was no blowdown during the measurements and there was no evidence of any significant leaks during these measurements. It is also necessary to assume an exit quality, since the computer program actually

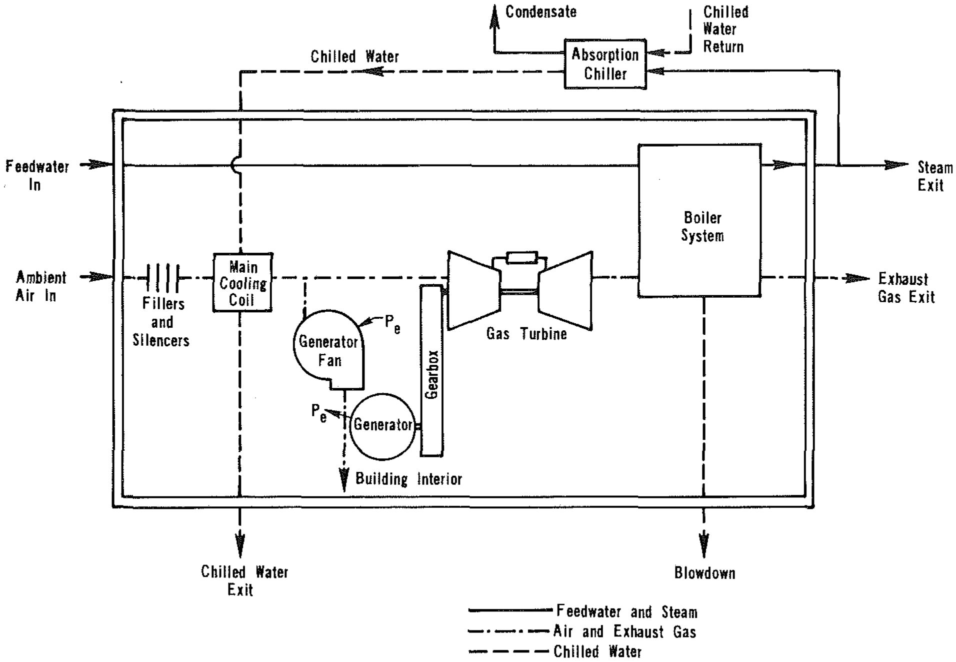

Fig. 1 Diagram of UCD gas turbine cogeneration system

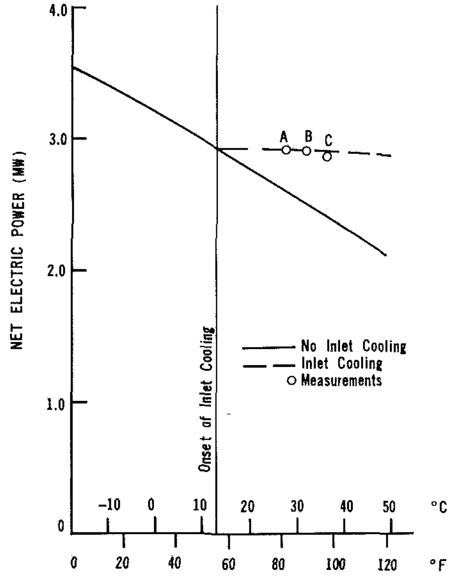

Fig. 2 A comparison of the computed and measured power output (measurements are with inlet cooling)

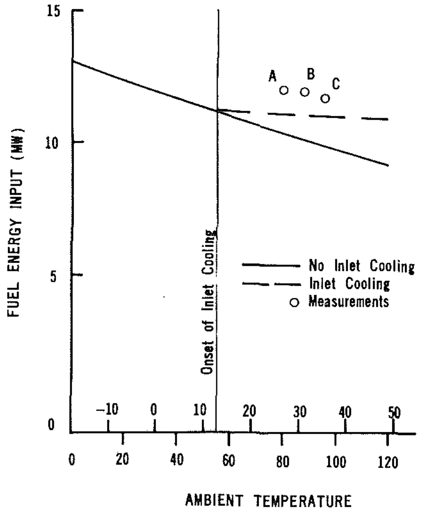

Fig. 3 A comparison of the computed and measured fuel flow rates (measurements are with inlet cooling)

predicts a steam energy rate from which the flow rate is calculated (based on the exit quality and steam properties). Unfortunately, the exit quality is not measured. As shown in Table 3, the computer program prediction is consistently less than the measured gross steam flow rate by 19–27 percent assuming an exit quality of 98 percent. If the exit quality were 90 percent this difference would be 11–18 percent. The plant operators have observed high liquid flow rates in the downstream drains and suspect a much lower quality than the design value of 98 percent possibly caused by damage to the steam separator at the exit of the recirculation tank.

Part of the difference (approximately 7 percent) in predicted and measured gross steam output is also due to the higher turbine exhaust gas temperature mentioned above. It thus appears that two effects (a higher exhaust gas temperature and a quality a bit lower than 90 percent) could cause the difference between measured and computed steam output.

The remaining thermodynamic parameters discussed above are also listed in Table 3 for the computer predictions. They are not compared in this table to the measurements, since the comparisons would be skewed by the discrepancy in the gross steam flow rates.

Ambient Temperature Effects. The computer program has been used to study the effect of ambient temperature on the plant performance. Typical input conditions (close to the measurement conditions) were used while varying the ambient temperature only. The effect of ambient temperature on the net electric power is shown in Fig. 2. The measurements are close to the predicted values with inlet cooling (inlet cooling was used during the measurements).

The effect of ambient temperature on fuel energy input is shown in Fig. 3. The gross steam flow rate is shown in Fig. 4. In this case, an additional computation with the computer program is made for an exit quality of 90 percent.

The computed net heat rate (NHR) is shown in Fig. 5 as a function of the ambient temperature. Recall that the NHR is like an inverse electric plant efficiency and is analogous to the

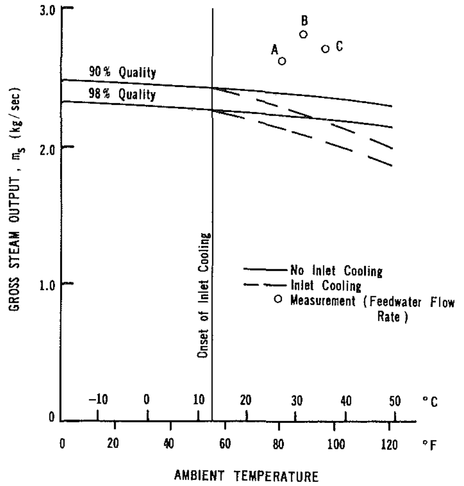

Fig. 4 A comparison of the computed and measured steam output (measurements are with inlet cooling and use feedwater flow rate)

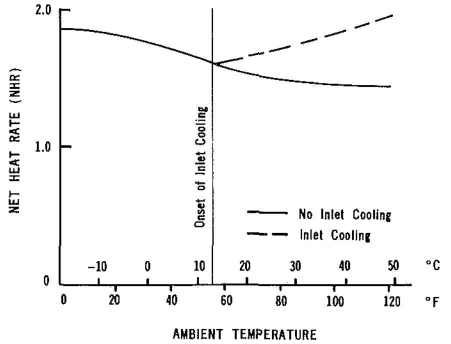

Fig. 5 Effect of ambient temperature on computed net heat rate (NHR)

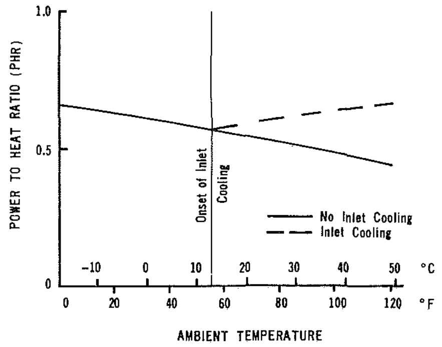

Fig. 6 Effect of ambient temperature on computed power-to-heat ratio (PHR)

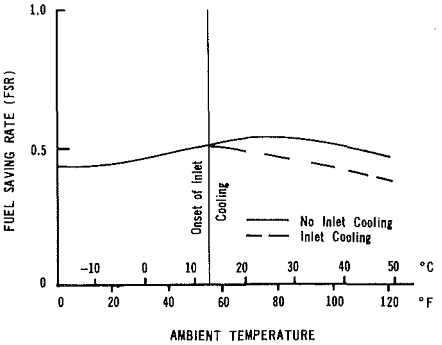

Fig. 7 Effect of ambient temperature on computed fuel saving rate (FSR)

heat rate of a central utility plant, corrected for the cogeneration plant steam output. Figure 5 shows an interesting variation. In the absence of inlet cooling, the NHR decreases as the ambient temperature is increased. This is partly due to the reduced electric output. The use of inlet cooling at the higher temperatures increases the electric power output (see Fig. 2) but also increases the NHR (i.e., decreases the electric efficiency).

The advantage of the inlet cooling is shown in Fig. 6 where the power-to-heat ratio (PHR) is shown as a function of the ambient temperature. The inlet cooling reverses the drop in PHR with increasing ambient temperature.

The fuel savings rate (FSR) shown in Fig. 7 as a function of ambient temperature has a curious behavior. In the absence of inlet cooling it actually has a maximum at approximately 25°C. The inlet cooling reduces the FSR showing that the additional electric power obtained by inlet cooling is not as efficient as that obtained in the absence of inlet cooling. The plant capacity is increased at the cost of efficiency when inlet cooling is used.

Conclusion

The predictions of a computer program have been compared to measurements on the UCD cogeneration plant. It was found that the computer model predicts the electric power output quite closely, but not the fuel consumption and the steam production.

As an example of how such a computer program may be used for design and economic analyses, a set of runs examining the effect of ambient temperature have been made. These have included the effect of inlet air cooling using an absorption cycle chiller, an approach which is used at the UCD plant.

These results demonstrate the value of a computer program to predict the performance of cogeneration plants, but also demonstrate that measurements are needed on plants under actual operating conditions. The actual performance may be quite different than the predictions. In future work in this area, we hope to obtain better performance data on the gas turbine and hope to refine the measurements including some means of obtaining the steam exit quality. We also hope to obtain measurements over a broader range of ambient temperatures.

Acknowledgments

The authors gratefully acknowledge the support of the University of California UERG, California Energy Studies Program.

References

1 Baughn, J. W., McKillop, A. A., and Treleven, K., "Analysis of the Performance of a Gas Turbine Cogeneration Plant," ASME Journal of Engineering for Power, Vol. 105, Oct. 1983, pp. 816-820.

2 Wilson, W. B., "Conserving Energy via Cogeneration," *Mechanical Engineering*, Vol. 101, No. 8, Aug. 1979, pp. 21-27.

3 Barnes, R. W., and Wilkinson, B. W., *Cogeneration of Electricity and Useful Heat*, CRC Press, Boca Raton, 1980.

4 Chjiogioji, M. H., *Industrial Energy Conservation*, Marcel Dekker, New York, 1979.

5 *Combined Production of Electric Power and Heat, A Seminar of the United Nations Economic Commission for Europe*, Pergamon Press, 1980.

6 "Cogeneration, Energy for the 80's and Beyond," Governors Office of Planning and Research, State of California, June 1981.

7 Resources Dynamics Corporation, "Cogeneration Handbook," prepared for California Energy Commission, Sept. 1982, pp. 1-2.

8 Baughn, J. W., and Bagheri, N., "The Effect of Thermal Matching on the Thermodynamic Performance of Gas Turbine and IC Engine Cogeneration Systems," ASME Paper No. 85-IGT-106.

9 Treleven, K., "Off-Design Operation of a Cogeneration Plant; A Thermodynamics and Economic Analysis," M. S. Thesis, University of California, Davis, 1982.

10 Treleven, K., Baughn, J. W., and McKillop, A. A., "A Model for the

Economic Analysis of Cogeneration Plants With Fixed and Variable Output," *Energy, The International Journal*, Vol. 8, No. 7, 1983, pp. 547–552.

11 Ahner, D. J., and Hall, E. W., "Avoid Using Average Values in Capacity-factor Calculations," *Power*, Aug. 1985, pp. 49–52.

12 Allen, R. P., and Kovacik, J. M., "Gas Turbine Cogeneration – Principles and Practice," ASME Paper No. 84-GT-145.

13 Leibowitz, H., and Tabb, E., "The Integrated Approach to a Gas Turbine Topping Cycle Cogeneration System," ASME Paper No. 84-GT-141.

14 Stefenaidis, S., Detroit Allison, personal communication.

APPENDIX

Outline of Computation Procedure Used in Computer Program

1 The program begins by determining various thermodynamic properties including the water vapor pressure in the air, the feedwater enthalpy, and the steam enthalpies.

$$P_{\mathrm{sat},a} = f(T_a),\ \mathrm{R.H.} = f(p_a, p_{\mathrm{sat},a})$$

$$h_{fw} = f(T_{fw}),\ h_g = f(p_s),$$

$$h_f = f(p_s),\ h = h_f + x\, h_{fg}$$

2 The gas turbine performance is then obtained from a stored data set:

$$m_f = f(T_a, T_{ti}, w, \delta)$$

$$p_t = f(T_a, T_{ti}, w, \delta)$$

$$T_{te} = f(T_{ti}, w), \quad m_a = f(T_a, T_{ti}, w, \delta)$$

$$AF = f(m_a, m_f)$$

3 The generator cooling air flow rate and power are determined:

$$m_g = V_g/v_a,\ p_o = f(p_a, \Delta p_f, m_g)$$

$$p_f = p_o/\eta_f$$

4 The steam requirements for the inlet air cooling system are calculated:

$$m_{cs} = f(m_a, T_a, T_{ci})$$

5 The gear box and generator effects are determined:

$$p_b = p_t\, \eta_b,\ p_g = p_b\, \eta_g$$

6 The boiler steam output and feedwater flow are calculated:

$$m_s = f(m_a, m_f, T_{te}, T_s, c_{pe})$$

$$m_{fw} = f(m_s, m_{BD}, x)$$

7 The parasitic electric loads are determined:

$$p_{oc} = f(V_o, A)_o$$

$$p_{rp} = f(R_{rp}, m_{fw}, \Delta p_r)$$

8 Computer results and output are calculated and include:

(*a*) Net dry steam flow rate
(*b*) Net wet steam flow rate
(*c*) Net dry steam energy rate
(*d*) Net wet steam energy rate
(*e*) Total parasitic electric load
(*f*) Net electric power output
(*g*) Steam efficiency η_s
(*h*) Electric efficiency η_e
(*i*) Plant efficiency η_{tot}
(*j*) Net heat rate, NHR
(*k*) Power-to-heat rate, PHR
(*l*) Fuel savings rate, FSR

The Effect of Thermal Matching on the Thermodynamic Performance of Gas Turbine and IC Engine Cogeneration Systems

J. W. Baughn
Professor.

N. Bagheri
Research Assistant.

Department of Mechanical Engineering,
University of California,
Davis, CA 95616

Computer models have been used to analyze the thermodynamic performance of a gas turbine (GT) cogeneration system and an internal combustion engine (IC) cogeneration system. The purpose of this study was to determine the effect of thermal matching of the load (i.e., required thermal energy) and the output steam fraction (fraction of the thermal output, steam and hot water, which is steam) on the thermodynamic performance of typical cogeneration systems at both full and partial output. The thermodynamic parameters considered were: the net heat rate (NHR), the power-to-heat ratio (PHR), and the fuel savings rate (FSR). With direct use (the steam fractions being different), the NHR of these two systems is similar at full output, the NHR of the IC systems is lower at partial output, and the PHR and the FSR of the GT systems are lower than those of the IC systems over the full range of operating conditions. With thermal matching (to produce a given steam fraction) the most favorable NHR, PHR, and FSR depend on the method of matching the load to the thermal output.

Introduction

Cogeneration is considered here to be the simultaneous production of electrical energy (or shaft power) and useful thermal energy from the same facility, although broader definitions are sometimes used [1-3]. It is a far more efficient use of fossil fuels than separate production and should be considered whenever there is a need for thermal energy such as hot water or steam. Since the electrical energy can generally be returned to a grid, it can be considered a byproduct if it is not needed at the cogeneration site [4]. The interest in cogeneration was rekindled throughout the world in the mid-1970s as a result of the rising cost of fuel (for example, see [5]). This interest has been, and continues to be, especially keen in California (USA) where policies and pricing (of the electrical byproduct) have strongly encouraged cogeneration [6].

Conventional (noncogeneration) plants use separate boilers to produce the required thermal energy and either purchase the required electricity from a utility or produce it separately in the plant. This separate production of electricity and heat can waste a great deal of energy in fossil fuel power plants. The range in electrical generation efficiency for these plants is from 34 percent, in older plants, to about 40 percent for the newest steam power plants. Therefore, about one third of the energy embodied in the fuel converts to electricity and the rest is wasted. When useful thermal energy and electricity are produced simultaneously, by cogeneration, the overall efficiency can exceed 80 percent.

The most common cogeneration technologies available today are all topping cycles. These technologies include the noncondensing steam turbine, the gas turbine, and the IC (or diesel) engine. Only the GT and IC engine systems are considered here. IC engine systems are usually selected for applications with electrical loads below 800 kW while either IC or GT engine systems are selected for electrical loads from approximately 800 kW to 10 MW. For applications above 10 MW, large gas turbines and steam cycles are used [6].

The output of the GT cogeneration system can be entirely pressurized steam, which has broad application. If a part of the thermal load (i.e., the required thermal energy for a particular application) is at lower temperatures and can use hot water, then a portion of the steam can be converted into hot water through a heat exchanger. On the other hand, the IC engine system produces both pressurized steam and hot water. These can be matched to a given application of steam and hot water in several ways as described below.

Since IC systems produce large amounts of hot water they have often been used when a major part of the thermal load was hot water. Since GT systems provide the major part of their thermal output at higher temperatures, they are often used where higher pressure steam is required. Other advantages and disadvantages of these types of systems are given in [6].

In this paper we attempt to compare the thermodynamic

Contributed by the Gas Turbine Division and presented at the 1985 Beijing International Gas Turbine Symposium and Exposition, Beijing, People's Republic of China, September 1-7, 1985. Manuscript received by the Gas Turbine Division January 2, 1986. Paper No. 85-IGT-106.

performance of these two common systems for a range of load steam fractions.

Some measures for comparing cogeneration technologies include the net heat rate, the power-to-heat ratio, and the fuel savings rate.

The net heat rate NHR is the ratio of the fuel chargeable to power to the net electricity generated. The fuel chargeable to power is the total amount of fuel consumed minus the amount that would have been consumed to produce the useful thermal energy separately. It is determined by

$$\mathrm{NHR} = (Q_{in} - Q_h/\eta_{\mathrm{aux}})/W_{g,\mathrm{net}} \qquad \mathrm{MW}_{th}/\mathrm{MW}_{el}$$

where Q_h is the energy that would be necessary to produce the thermal energy by a conventional boiler or water heater with a given efficiency of η_{aux} (a value of 0.85 is used in this study). The lower the net heat rate the more efficiently the fuel is being used.

The power-to-heat ratio PHR is the ratio of the net electricity generated to the thermal energy produced.

$$\mathrm{PHR} = W_{g,\mathrm{net}}/Q_h \qquad \mathrm{MW}_{el}/\mathrm{MW}_{th}$$

The IC engine systems generally have the highest PHR, about twice that of the gas turbine and ten times that of the steam turbines [6]. The PHR of the IC engine systems is usually higher than most industrial plants need, so IC engine systems are usually attractive in applications when either electrical needs are higher or the excess electrical power can be sold.

The fuel savings rate FSR is the fuel saved over that required for separate production of the electricity and thermal energy per unit of total thermal energy produced. It is proportional to the difference in the standard heat rate of a central utility power plant and the net heat rate of the cogeneration plant. The fuel savings rate is this difference times the power-to-heat ratio [7]. For example if we assumed a heat rate of 2.5 $\mathrm{MW}_{th}/\mathrm{MW}_{el}$ (an efficiency of 40 percent) for a conventional central utility power plant, the FSR is given by

$$\mathrm{FSR} = (2.5 - \mathrm{NHR}) * \mathrm{PHR}$$

The fuel savings rate predicts the amount of energy conservation and is of great importance in the comparison of different types of cogeneration systems. It should be noted that use of the fuel savings rate assumes that the electrical energy produced can be used to displace fuel use at a central utility plant.

Each of the above thermodynamic parameters can be useful in determining the merits and economics of cogeneration systems [8]. They can be determined by measurements or by modeling of a given cogeneration system. In an earlier study these parameters, and others, were determined for a specific GT system located at the University of California at Davis using a computer model of this plant [9]. In the present study this earlier model has been made more general and a similar model prepared for an IC engine cogeneration system. The objective of this study is to use these computer models to determine the above thermodynamic parameters for a range of operating conditions.

It should also be noted that the decision between different systems is a complex one and involves far more than just the thermodynamic parameters considered here.

Cogeneration Systems

The two different types of cogeneration systems considered here generally have different thermal outputs, the GT cogeneration systems providing entirely steam (which can be reduced to hot water if desired), and the IC engine systems providing both steam and hot water, with a major part of the thermal energy output being in the form of hot water (which cannot produce steam).

There are two different ways to match a cogeneration system to the thermal energy requirements for a particular application:

1 The system can be sized to meet the electrical demand of the application and an auxiliary boiler and or a water heater is used to provide additional thermal energy. This case is referred to as a power match.

2 The system can be sized to meet the thermal requirement of the application and electricity is then either purchased from the utility or sold to the utility depending on the electrical requirement of the application. This case is referred to as a thermal match.

Only case 2, the thermal match, is considered in this research since in California, utilities are required to purchase excess cogeneration power at a price equivalent to the costs they avoid (referred to as "avoided costs") by not producing that power [6].

The thermal load (to be matched to the system output), steam and/or hot water, can be characterized by three sets of parameters:

1 steam and hot water supply temperatures and pressures,
2 hot water and condensate return temperatures,

Nomenclature

Blow = steam blowdown
C_p = specific heat
EFF = effectiveness
FSR = fuel savings rate
GT = gas turbine engine
H = enthalpy
IC = internal combustion
IC1 = turbocharged dual fuel IC engine
IC2 = turbocharged spark ignition IC engine
IC3 = dual fuel IC engine
m = mass flow rate
NHR = net heat rate
P = pressure
PHR = power-to-heat ratio
Q = thermal energy rate
rpm = revolutions per minute
S = steam output rate
T = temperature
TIT = turbine inlet temperature
V = volume flow rate
W = power
WR = rated power
η = efficiency
ρ = density
ϕ = relative humidity

Subscripts

a = air
ac = air cooler
amb = ambient
aux = auxiliary
ax = air heat exchanger
bd = blowdown heat exchanger
con = condensate
cw = cooling jacket
e = exit
eng = engine
ex = exhaust gas
f = fuel
g = generator
gb = gear box
gf = generator fan
gm = generator fan motor
h = thermal energy available from the system
hw = hot water
hwr = hot water return
i = input
lf = filter pressure loss
lo = lube oil
loss = steam loss
mw = makeup water
ox = oil heat exchanger
rw = recirculation water
s = steam
sat = saturated
tur = turbine

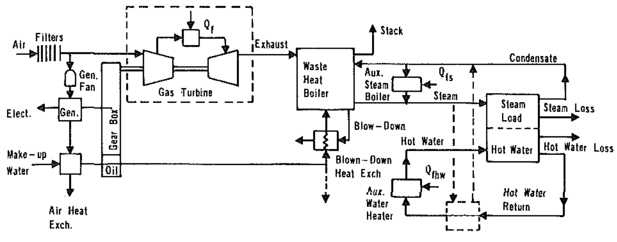

Fig. 1 Diagram of generalized gas turbine cogeneration system

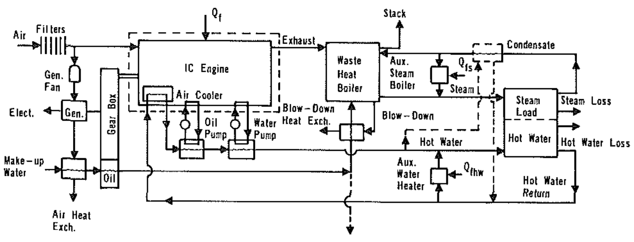

Fig. 2 Diagram of generalized IC engine cogeneration system

3 the ratio of the steam output rate to the total thermal energy output (steam plus hot water), $m_s/(m_s+m_{hw})$. This ratio is called the steam fraction here and is denoted by R_s.

The results of particular interest in this paper are the variation of the NHR, PHR, and FSR with fraction of rated engine power output for direct use of the thermal output, and the NHR, PHR, and FSR as a function of the steam fraction (for a range of zero to one) with thermal matching used to match the system to a particular thermal load. The steam pressure is assumed to be 100 psia in all cases, and the hot water temperature is assumed to be 180°F. Analyses using different steam pressures showed the results to be somewhat insensitive to this parameter. In the gas turbine case, different steam fractions are achieved by using some of the produced steam to produce hot water. Therefore, for the full range of the steam fraction from zero to one no auxiliary boiler is needed and, as would be expected, the values of the FSR are not functions of the steam fraction output.

In the case of the IC engine cogeneration systems, different values of the steam fractions are obtained in two different ways:

Case a. The steam output flow rate is considered to be the fixed parameter and for different steam fractions the appropriate values of the hot water flow rates are calculated. Since these calculated hot water flow rates are always less than the amount that is produced by the system (in these results) the extra hot water is discarded. It is assumed that the condensate temperature is higher than the hot water temperature and therefore the hot water cannot be used to preheat the condensate. Note that a steam fraction of 1.0 in this case implies that all the output hot water is discarded. At first appearance, this seems wasteful, but as seen in the results, it may have advantages in certain circumstances. In this case an auxiliary steam boiler is not needed.

Case b. The output hot water flow rate is considered to be the fixed parameter and for different steam fractions the required values of the steam flow rates are calculated. Since these calculated steam flow rates are much greater than the amount that the system produces, the difference is produced in an auxiliary steam boiler. This auxiliary boiler can be a separate component, or the waste heat boiler (or Heat Recovery Steam Generator, as it is often called) can be fired as described by Allen and Kovacik [10].

Gas Turbine Cogeneration System

The gas turbine studied in this research is a 3.0 MW size engine similar to that operated at the University of California Davis campus. This size gas turbine is representative of the gas turbines used in cogeneration systems of equal or larger sizes.

A diagram of the gas turbine cogeneration system considered here is shown in Fig. 1. It consists basically of a gas turbine coupled to a generator through a gear box, an unfired waste heat boiler, an auxiliary steam boiler, and an auxiliary water heater. It is quite similar to the integrated system described by Leibowitz and Tabb [11]. It should be noted that the system considered here does not include a regenerator or a steam turbine (hybrid system) since systems using these components are more complex and less common. The addition of a regenerator or a steam turbine would improve the GT system performance.

There are basically four fluid paths in Fig. 1:

1 The air and exhaust flow through the gas turbine and waste heat boiler;

2 the condensate-steam flow through the waste heat boiler and auxiliary steam boiler;

3 the makeup water through the heat recovery devices; and

4 hot water flow through the auxiliary water heater.

The performance characteristics of the gas turbine are taken from performance curves of the Allison 501 [12] which is the gas turbine unit in use at the U. C. Davis campus.

It should be noted that in the present study the auxiliary water heater of the GT system is not used since the hot water can be produced directly from the steam (see dotted line in Fig. 1). It was included for completeness and possible future studies.

IC Engine Cogeneration System

A diagram of the generalized IC engine cogeneration system considered here is shown in Fig. 2. The four fluid paths described for the gas turbine cogeneration system also exist in this system; the only difference is observed in the hot water path. There are three heat recovery sources in the hot water path in which thermal energy is recovered. These sources are: the air cooler, the lube oil, and the cooling jacket.

The data for the performance of the IC engines considered in this study are taken from data on IC engines manufactured by Fairbanks Morse company and are selected as representative of these types of engines. Three different types of IC engine configuration are considered: turbocharged dual fuel (TDF) referred to here as IC1, turbocharged spark ignition (TSI) referred to here as IC2, and dual fuel (PC 2.3) referred to here as IC3. In this study only 12-cylinder IC engines have been considered. The reason for selecting this size is that the ratings of the IC engines considered and the gas turbine considered are comparable (i.e., 2.5-5.0 MW). It should be mentioned, however, that the sizes of the IC engines will not have any effect on the overall conclusions drawn from this study since the output power and the available thermal energy of the IC engines are proportional to the number of cylinders.

For the IC system, the auxiliary boiler is used for case *b* thermal matching only. Note that this could also be accomplished by firing the waste heat boiler with no effect on the results given here if the efficiencies were equal.

Computer Programs

The computational procedure used in the computer programs is given in Appendix A, together with the pertinent equations used in each step. The initial conditions read into the programs include the ambient conditions, component effi-

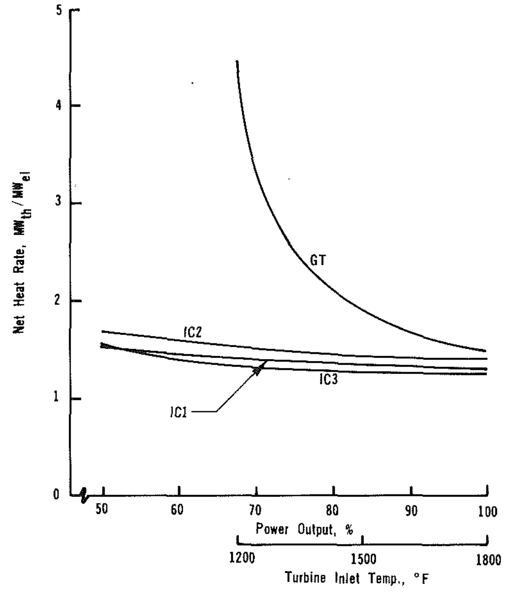

Fig. 3 Effect of power setting on the net heat rate

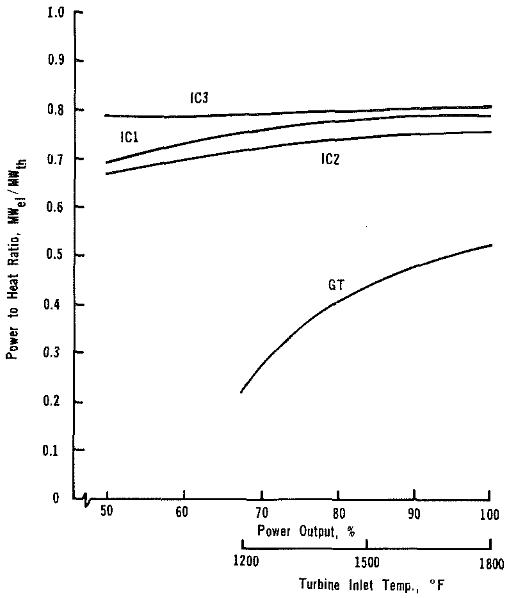

Fig. 4 Effect of power setting on the power-to-heat ratio

ciencies and effectivenesses, steam and hot water flow rates and enthalphies, and operating parameters such as the turbine shaft speed, turbine inlet temperature (for GT), percentage of power output (for IC), and pressure drop through the filters and silencers. Some comments about the models and equations are:

(*a*) Air was assumed to be a perfect gas for the purpose of calculating density and changes in enthalpy.

(*b*) Performance characteristics of the Allison 501 GT were placed in subroutine data sets from the manufacturer's performance curves [12].

(*c*) Performance characteristics of the IC engines were also prepared into subroutine data sets using the manufacturer's data [13].

(*d*) The volumetric flow rate of air used to cool the generator was assumed constant and used for both systems.

(*e*) The blowdown and steam loss rates were specified as a percentage of the steam output rate.

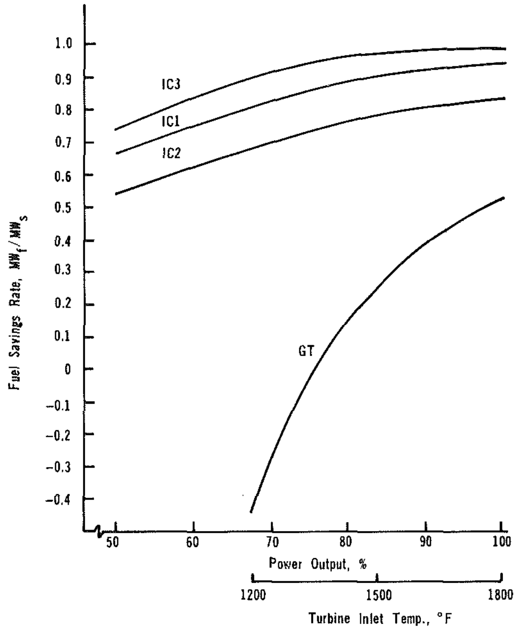

Fig. 5 Effect of power setting on the fuel savings rate

(*f*) The calculation of the enthalpy change in the exhaust of the GT was based on a variable specific heat as given in [9].

(*g*) The power used by the recirculation pump was fixed at 6.27 kW and that used by the condensate and hot water pumps was assumed to be proportional to the steam and hot water flow rates, respectively.

For more details of the models and for the listing of the actual computer programs, see [14].

Results and Discussion

The NHR is shown in Fig. 3 for the case of direct use of the thermal output as a function of the power output. Note that in this case the steam fractions of the systems are different and there is no thermal matching of the output and a thermal load. As seen in this figure, the NHR of the GT and IC systems are close at full power output. However, the NHR of the GT system increases dramatically for partial power output. At approximately 73 percent of full power output, the GT system reaches a NHR of 2.5, which is comparable to a central utility power plant. At lower power outputs, the GT cogeneration system will be less efficient than separate production of the thermal energy and electricity. Over the full range of the power output, the IC systems have a NHR which is more efficient than separate production.

The PHR is shown in Fig. 4 for the case of direct use of the thermal energy as a function of the power output. For the IC systems the PHR is a mild function of the power output, the power and thermal energy decreasing proportionately. For the GT system, the power output decreases more rapidly than thermal output so the PHR decreases as the power output is reduced.

The FSR rate is shown in Fig. 5 for the case of direct use as a function of power output. The combination of lower NHR and higher PHR causes the IC systems to have a much higher FSR over the full range of operating conditions. It should be noted that in this comparison, there is no thermal matching of the output and a thermal load, so the IC systems provide a major part of their output in the form of hot water. It is assumed, in this case, that the entire output, hot water and steam, can be used.

The net heat rate with thermal matching to a given steam fraction is shown in Fig. 6 for full power output. As noted

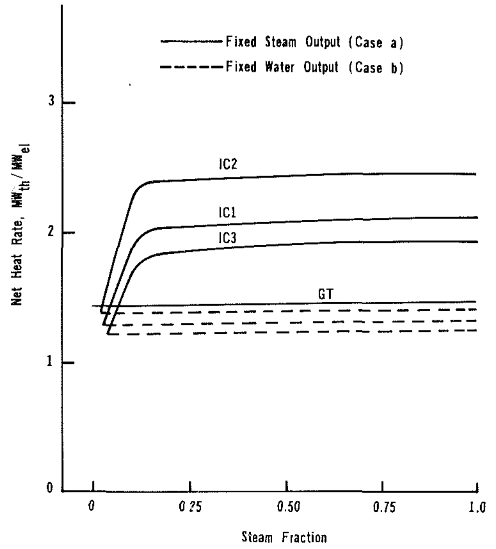

Fig. 6 Net heat rate variation with steam fraction (at 100 percent engine power output, 100 psia steam and 180°F hot water)

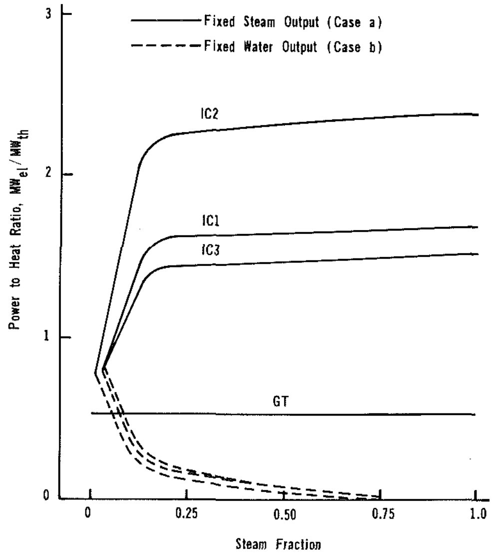

Fig. 8 Power-to-heat ratio variation with steam fraction (at 100 percent engine power output, 100 psia steam, and 180°F hot water)

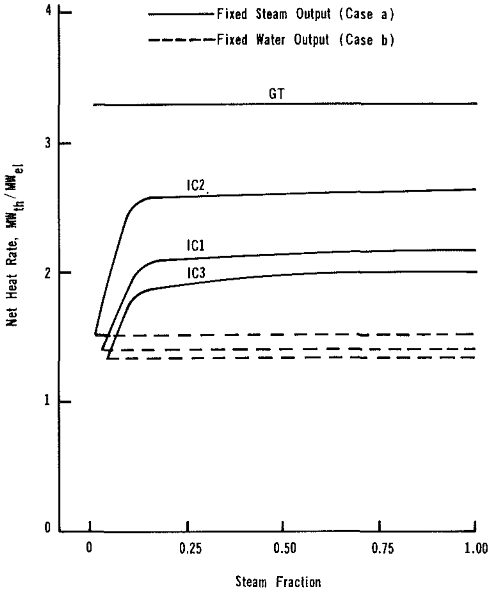

Fig. 7 Net heat rate variation with steam fraction (at 70 percent engine power output, 100 psia steam, and 180°F hot water)

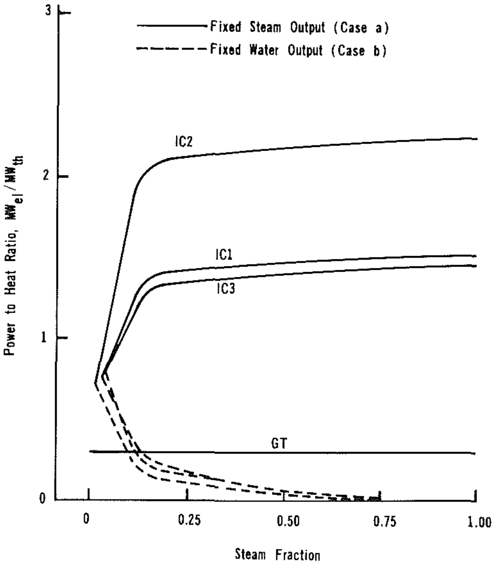

Fig. 9 Power-to-heat ratio variation with steam fraction (at 70 percent engine power output, 100 psia steam, and 180° hot water)

earlier, the NHR for the GT system and the IC system with case *b* matching is not a function of the steam fraction since for the GT system the steam can be used to produce hot water, and for the IC system the auxiliary heating efficiency is assumed to be the same for both cogeneration and separate production of the extra steam required. For case *a* matching, where a portion of the hot water is discarded, the NHR of the IC systems is greater than the GT system if any substantial amount of steam is required. At an output power of 70 percent, as shown in Fig. 7, the NHR of the GT system exceeds that of the IC systems over the full range of steam fractions.

The PHR with thermal matching is shown in Figs. 8 and 9 for full output and 70 percent output, respectively. For case *a* matching, the PHR of the IC systems exceed that of the GT systems over the full range of steam fractions. However, for case *b* matching, the PHR of the IC systems decreases with increasing steam fraction as more steam is produced by the auxiliary heating, eventually falling to a PHR of zero at a steam fraction of 1.0 (which requires an infinite amount of auxiliary steam production).

The FSR with thermal matching is shown in Figs. 10 and 11 for full output and 70 percent output, respectively. It is somewhat surprising to discover that the FSR for the IC1 and IC3 systems is greater than that of the GT systems over the full range of steam fractions considered. It is perhaps even more surprising to find that the FSR of case *a* matching is higher than case *b* matching. The reasons for this behavior can be found in the earlier figures for the NHR and the PHR. The high PHR's of the IC systems result in high FSR's. Furthermore, the drop in the PHR of the case *b* thermal matching with the steam fraction causes a corresponding drop in the FSR at higher values of the steam fraction.

It should be noted that the case *a* matching may result in systems which are simply too large to be economical. It should also be noted that it is implicitly assumed that the power generated can be used and that it is displacing fuel use at a central utility power plant.

Summary and Conclusions

Comparison of the two systems with direct use of the ther-

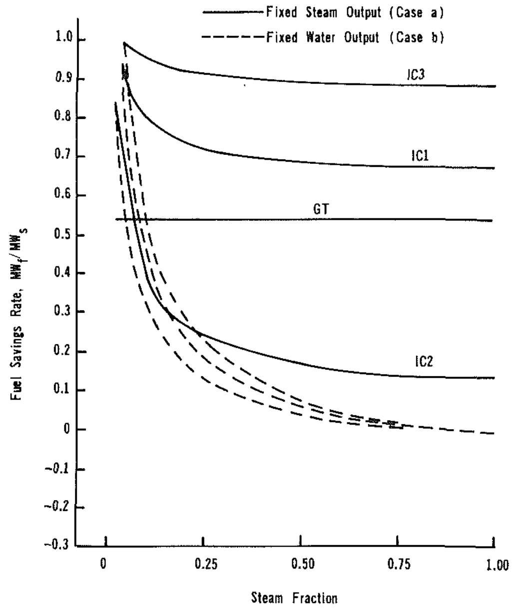

Fig. 10 Fuel savings rate variation with steam fraction (at 100 percent engine power output, 100 psia steam, and 180°F hot water)

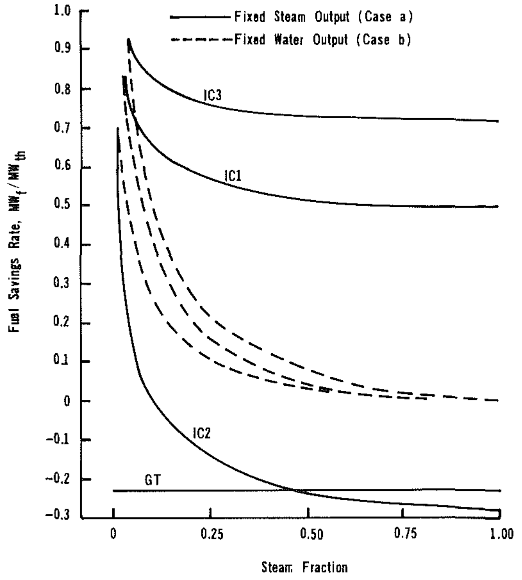

Fig. 11 Fuel savings rate variation with steam fraction (at 70 percent engine power output, 100 psia steam, and 180°F hot water)

mal output (no attempt to match the steam fraction) showed that the IC engine systems had a higher FSR than the GT systems for all engine power outputs. Negative FSR values were obtained by the GT at engine power outputs less than approximately 73 percent. At these outputs the NHR values become greater than the value of a standard central utility power plant and the thermodynamic advantage of cogeneration is lost. For all the engines considered the maximum FSR was obtained at full power output showing that it is more efficient (in terms of FSR) to operate these engines at this output and to sell the extra electricity (if there is any) to the local utility. The FSR's are again based on the assumption that all the thermal energy available from the system, in the form of steam and hot water, is utilized.

In order to consider the case of thermal matching we have introduced a new parameter, the steam fraction. For the GT, the FSR is not a function of the steam fraction since steam and hot water can be produced with equal ease.

For case *a* thermal matching it was found that even with no hot water heat recovery, the IC1 and IC3 engine systems had higher FSR's than the GT systems for the full range of engine power outputs. For lower steam fractions more hot water is utilized until full thermal energy recovery is obtained (i.e., the FSR increases with decreasing steam fraction and reaches a maximum; see Figs. 10 and 11).

Table 1 Base case condition

Ambient conditions
$T_{\mathrm{amb}} = 65°\mathrm{F}$
$P_{\mathrm{amb}} = 14.7$ psi
$\phi = 50$ percent
$P_{\mathrm{sat}} = 1.112$ psia
$T_{mw} = 72°\mathrm{F}$

Operating conditions
rpm
GT = 14,500
IC1 = 720
IC2 = 720
IC3 = 514
TIT = 1200°F to 1800°F
$T_{\mathrm{stack}} = 308°\mathrm{F}$ (GT and IC)
$m_{rw} = 56.4$ lbm/s
Blow = 3 percent
$S_{\mathrm{loss}} = 1$ percent

Component specifications
$\rho_{ef} = 7$ in. water = 0.25 psi
$V = 10{,}000$ cfm $= 0.0787$ m^3/s
WR_{gf} = power rating of generator fan = 21.1 Btu/s
$\eta_{gf} = 83$ percent
$\eta_{gm} = 89.9$ percent
$\eta_g = 98$ percent
$\eta_{gb} = 98$ percent
$\eta_{\mathrm{aux}} = 85$ percent
$\mathrm{EFF}_{bd} = 98$ percent
$\mathrm{EFF}_{ax} = 75$ percent
Rad. loss = 2 percent

The amount of the steam produced by an IC engine system depends on its size. The actual amount of steam produced by the IC engines in this study was 1.17 lb/s (IC1 at 2.5 MW) and 2.57 lb/s (IC3 at 5.0 MW) compared to 5.08 lb/s for the GT at 3.0 MW (for full power output and 100 psia steam). This shows the higher steam capability of the GT over the IC engines. If a given amount of steam were required the IC engines would have to be sized larger than a GT. Therefore, the high FSR of the IC engines will only be attractive if the resulting excess power can be used or sold (and such large IC engines exist and are economical). The IC2 engine is not as interesting because it produces mainly hot water.

In case *b*, with auxiliary heating used to increase the steam fraction for thermal matching, crossover points were observed for the FSR versus steam fraction curves of the GT and all the IC engine systems (see Figs. 10 and 11). It was assumed in this case that all the hot water produced by the IC engines is utilized; these high FSR values at low values of steam fraction will only be attainable if auxiliary steam heating is included in the steam and the produced hot water is utilized.

In conclusion, it is noted that the thermal matching of cogeneration systems should be examined carefully if the most efficient use of fossil fuel is to be accomplished. Finally, it should be restated that the selection of a cogeneration system is a complex technical and economic decision and many factors other than the thermodynamics considered in this study enter into such a decision.

References

1 Wilson, W. B., "Conserving Energy via Cogeneration," *Mechanical Engineering*, Vol. 101, No. 8, Aug. 1979, pp. 21-27.

2 Barnes, R. W., and Wilkinson, B. W., *Cogeneration of Electricity and Useful Heat*, CRC Press, Boca Raton, FL, 1980.

3 Chjiogioji, M. H., *Industrial Energy Conservation*, Dekker, New York, 1979.

4 "Combined Production of Electric Power and Heat," United Nations Economic Commission for Europe, Pergamon Press, New York, 1980.

5 "Cogeneration, Energy for the 80s and Beyond," Governors Office of Planning and Research, State of California, June 1981.

6 Resources Dynamics Corporation, "Cogeneration Handbook," prepared for California Energy Commission, Sept. 1982, p. 1-2 and pp. 3-4 to 3-9.

7 Trelevan, K., "Off-Design Operation of a Cogeneration Plant; A Thermodynamics and Economic Analysis," M. S. Thesis, University of California, Davis, CA, 1982.

8 Treleven, K., Baughn, J. W., and McKillop, A. A., "A Model for the Economic Analysis of Cogeneration Plants With Fixed and Variable Output," *Energy, The International Journal*, Vol. 8, No. 7, 1983, pp. 547-552.

9 Baughn, J. W., McKillop, A. A., and Treleven, K., "An Analysis of the Performance of a Gas Turbine Cogeneration Plant," ASME JOURNAL OF ENGINEERING FOR POWER, Vol. 105, Oct. 1983, pp. 816-820.

10 Allen, R. P., and Kovacik, J. M., "Gas Turbine Cogeneration – Principles and Practice," ASME JOURNAL OF ENGINEERING FOR GAS TURBINES AND POWER, Vol. 106, 1984, pp. 725-730.

11 Leibowitz, H., and Tabb, E., "The Integrated Approach to a Gas Turbine Topping Cycle Cogeneration System," ASME JOURNAL OF ENGINEERING FOR GAS TURBINES AND POWER, Vol. 106, 1984, pp. 731-736.

12 Engine Performance Presentation, Model 501-KB, Allison Gas Turbines, EDR 8064, Dec. 16, 1974.

13 Data sheets for IC engines from Fairbank Morse Company.

14 Bagheri, N., "Comparison of a Gas Turbine Cogeneration System and a Diesel Cogeneration System at Partial and Full load Operation," M. S. Thesis, University of California, Davis, 1984.

APPENDIX A

Computational Procedure Used in Computer Program

The equations and computational procedure used in both the GT and IC computer programs follows. (See the generalized diagrams, Figs. 1 and 2, for the system arrangements and the nomenclature for the symbols and subscripts.)

1 The dry inlet pressure to the GT and the IC engine is

$$P_{i,\text{eng}} = P_{\text{dry}} - P_{lf}$$

where $P_{\text{dry}} = P_{\text{amb}} - \phi P_{\text{sat}}$. The inlet temperature to the GT and the IC is assumed to be 65°F.

2 *GT.* The GT performance is obtained from a stored data set. Input are engine turbine inlet temperature, rpm, and engine dry inlet pressure. Output are fuel flow rate, turbine air flow rate, and turbine power outlet and exhaust temperature.

IC. The IC engine's performance is also obtained from a stored data set. The input is engine power output. The outputs are heat balance data for air cooler, lube oil, and cooling jacket, and exhaust flow rate, exhaust thermal energy, and exhaust temperature.

3 The generator fan air flow rate, power, and air outlet temperature are given by (GT and IC)

$$m_{gf} = V\rho_a$$

$$W_{gf} = WR_{gf}\,\eta_{gm}$$

$$T_{a,gf,e} = T_i - W_{gf}/(m_{gf} * C_{p,a})$$

4 The air flow rate through the filters and silencers is (GT and IC)

$$m_a = m_{gf} + m_{\text{eng},a}$$

and the exhaust flow rate is

$$m_{ex}(\text{GT}) = m_{\text{eng},a} + m_f$$

$m_{ex}(\text{IC})$ from data set.

5 Enthalpy change of the oil and work transmitted by the gear box are given by (GT and IC)

$$\Delta H_{\text{oil}} = (1 - \eta_{gb})\,W_{\text{out}}$$

$$W_{gb} = W_{\text{out}}\,\eta_{gb}$$

6 The electric power and the air temperature out of the generator are given by (GT and IC)

$$W_g = W_{gb}\eta_g$$

$$T_{a,g,e} = (W_{gb} - W_g)/(m_{gf} * C_{p,a}) + T_{a,gf,e}$$

7 The mass flow rate of the makeup water and the outlet makeup water temperature at the air, oil, and blowdown heat exchangers are

$$m_{mw} = (\text{blow} + S_{\text{loss}})m_s$$

$$T_{mw,ax,e} = T_{mw} + \Delta H_{ax}/m_{mw}$$

$$T_{mw,ox,e} = T_{mw,ax,e} + \Delta H_{\text{oil}}/m_{mw}$$

$$T_{mw,bd,e} = (\text{blow}/(\text{blow} + S_{\text{loss}})) * (T_s - T_{bd,e}) + T_{mw,ox,e}$$

An energy balance on the waste heat boiler gives

$$m_{\text{con}}(GT) = [0.98\,m_{ex}C_{p,\text{gas}}(T_{a,\text{tur},e} - T_{\text{stack}}) + m_{mw}H_{mw,bd,e} - m_{mw}(\text{blow}/(\text{blow} + S_{\text{loss}})H_{\text{blow}} - m_{mw}(S_{\text{loss}}/(\text{blow} + S_{\text{loss}}))H_s]/(H_s - H_{\text{con}})$$

and

$$m_{\text{con}}(\text{IC}) = [Q_{ex} + m_{mw}H_{mw,bd,e} - m_{mw}(\text{blow}/(\text{blow} + S_{\text{loss}})) \bullet H_{\text{blow}} + m_{mw}(S_{\text{loss}}/(S_{\text{loss}} + \text{blow})H_s]/(H_s - H_{\text{con}})$$

If m_s is greater than m_{con}, the difference is produced in the auxiliary steam boiler. This extra steam flow rate and the necessary thermal energy to produce it are given by (GT and IC)

$$m_{s,\text{aux}} = m_s - (S_{\text{loss}}/(\text{blow} + S_{\text{loss}}))m_{mw} - m_{\text{con}}$$

$$Q_{f,\text{aux}} = m_{s,\text{aux}}(H_s - H_{\text{con}})/\eta_{\text{aux}}$$

8 *GT.* Fuel energy required to produce a specified amount of hot water is given by

$$Q_{f,hw} = m_{hw}(H_{hw} - H_{hwr})/\eta_{\text{aux}}$$

IC. Hot water produced by the IC engine is given by

$$m_{hw} = (Q_{ac} + Q_{lo} + Q_{cw})/(H_{hw} - H_{hwr})$$

If the required hot water flow rate is greater than m_{hw}, the difference is produced in the auxiliary heater, and the required thermal energy is given by

$$Q_{hw,\text{aux}} = m_{hw,\text{aux}}(H_{hw} - H_{hwr})/\eta_{\text{aux}}$$

9 The net electricity power output is given by (GT and IC)

$$W_{g,\text{net}} = W_g - W_{gf} - W_{rw} - W_{\text{con}} - W_{hw}$$

10 The net heat rate, power-to-heat ratio, and fuel savings rate are given by

$$\text{NHR} = (Q_i - Q_h/\eta_{\text{aux}})/W_{g,\text{net}}$$

$$\text{PHR} = W_{g,\text{net}}/Q_h$$

$$\text{FSR} = (2.5 - \text{NHR})\text{PHR}$$

Parametric Analysis of Combined Gas-Steam Cycles

G. Cerri
Istituto di Macchine e Tecnologie
Meccaniche,
Università di Roma,
Rome, Italy

Combined gas-steam cycles have been analyzed from the thermodynamic point of view. Suitable thermodynamics indices – explained in Appendix A – have been utilized. The parameters that most influence efficiency have been singled out and their ranges of variability have been specified. Calculations have been carried out – see Appendix B – taking into account the state of the art for gas turbines and the usual values for the quantities of steam cycles. The results are given. The maximal gas turbine temperature has been varied between 800°C and 1400°C. The gas turbine pressure ratio has been analyzed in the range of 2-24. Afterburning has also been taken into consideration. Maximal efficiency curves and the corresponding specific work curves (referred to the compressed air) related to the parameters of the analysis are given and discussed.

Introduction

Man has a natural tendency to try to improve the efficiency of devices which convert thermal energy into mechanical work. Moreover the rise in fossil fuel costs is a stimulus for this kind of research.

Power plants where gas turbines, operating in open cycles, are combined with steam cycles are particularly interesting for their high conversion efficiency. The combination of the two kinds of cycles is possible due to the high exhaust heat temperature of gas turbines, which depends on the maximal gas temperature and pressure ratio. The present gas turbine power plants are recommended for covering peak loads or, in any case, in comparison with other engines, they are particularly suitable when a short operating time is required [1-3].

The development of gas turbines is mainly tied to the solution of technological problems connected with the increasing of the maximal gas temperature which is in the range of 800-1250°C in the biggest engines. The gas turbine manufacturers' efforts tend to raise the maximal gas temperature – at the inlet of the turbine – that in the future will reach 1400°C and higher.

On the other hand, the use of such high temperatures requires high pressure ratios to obtain good efficiency and prevents the utilization of cheap fuel. Thus the trend toward increasing the maximum temperature to raise the efficiency influences both construction costs and fuel costs.

For many years the attention of manufacturers and utility companies has been focused on combined gas-steam cycles. Many combinations are possible and gas turbines – besides generating mechanical power – can accomplish different tasks according to their position in the plants [4, 5].

The purpose of this study is to analyze combined plants where the exhaust gas, at the exit of the gas turbine, is utilized in a waste heat recovery boiler to produce steam which is expanded in a turbine and discharged in a condenser. Since the air-fuel ratio in the gas turbine combustion chamber is higher than the stoichiometric one, fuel can be added in the boiler (afterburning) to increase the steam production or to improve the quality of the steam. A schematic flow diagram of a combined plant is depicted in Fig. 1.

The present gas turbines which have maximal gas temperature and pressure ratio, typical for covering peak loads, are utilized in combined plants. The optimal design usually is reached by the right compromise, in selecting the best gas turbine, between the *pinch point* – which is connected with the dimension of the waste heat recovery boiler – and the performance of the plant.

Pfenninger [6] analyzed a plant in which the maximal gas temperature was $t_{3a} = 880°\text{C}$ and concluded that the gas turbine cycle must have the maximum exhaust gas enthalpy (i.e., the maximum product between the mass flow rate of the gas

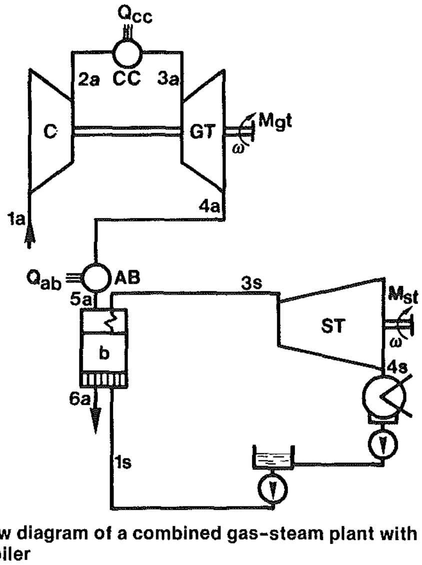

Fig. 1 Flow diagram of a combined gas-steam plant with a waste heat recovery boiler

---

Contributed by the Gas Turbine Division and presented at the 26th International Gas Turbine Conference and Exhibit, London, England, 1982. Manuscript received at ASME Headquarters April 9, 1986. Paper No. 82-GT-95.

and its temperature). The resulting pressure ratio was intermediate between those for which the specific work of the gas turbine and its efficiency are maximum. The afterburning was taken into consideration and conclusions were that for low afterburning rates the efficiency slightly decreased and then reached a maximum at a precise ratio between the gas turbine power and the total plant power. A certain stack excess of air corresponds to this ratio. Total output climbed up to the minimum excess of air in the exhaust gases.

Wunsch [5] claimed that the efficiency of combined gas-steam plants was more influenced by the gas turbine parameters (t_{3a}, β) than by those of the steam cycle, the parameters of which were fixed in an appropriate manner (he did not say precisely how). The conclusion was that the maximal combined gas-steam efficiency was reached when the exhaust gas turbine temperature was higher than the one corresponding to the maximum gas turbine efficiency. In the same study afterburning was taken into consideration and its influence was positive when the maximum gas turbine temperature was lower than about 950°C and negative for higher temperatures.

Fraise and Kinney [7] analyzed three gas turbine combined cycles, one of which was a one level pressure gas-steam cycle without extractions for regenerative preheating of the feedwater. The following parameters were assigned: the maximal gas turbine temperature, $t_{3a} = 1427°\text{C}$ (3060 R), the state of the steam $p_{2s} = 12.41$ MPa (1800 psia), $t_{3s} = 538°\text{C}$ (1460 R); moreover, other parameters of less importance for the analysis were assigned. As independent quantities the pressure ratio and the steam air mass flow ratio were taken. The minimum acceptable pinch point value was 28°C (50°F). Combustion losses and auxiliary power requirements were not accounted for. Compressor and gas turbine efficiencies were taken as independent of the pressure ratio. Afterburning was not taken into consideration. Three values of pressure ratio were analyzed: 12, 16, 20; efficiency and specific work output versus steam air mass flow ratio were given.

Tomlinson and George [8] analyzed a gas-steam combined cycle without afterburning because according to them it presented the maximal efficiency. The major assumptions underlying the analysis were that the efficiency of the steam cycle varies slightly with the characteristics of the gas turbine (t_{3a}, β) and the specific work of the steam cycle was empirically derived from the other already-working combined plants. The conclusion was that the gas-steam cycle overall efficiency was influenced only by the specific work of the gas turbine and consequently it reached the maximum value when the pressure ratio corresponded to the maximal specific gas turbine work.

In the present study a short thermodynamic analysis of one pressure level gas-steam combined cycle without regenerative extractions is carried out. The results of a parametric analysis of the cycle performance are given and discussed.

Thermodynamic Analysis

Referring to the combined gas-steam power plant sketched in Fig. 1 and to the corresponding cycle shown in Fig. 2 and taking into consideration plants with and without afterburning performance of the combined cycles can be expressed by means of total parameters of both gas and steam cycles. The specific work (referred to the unit of compressed air mass) is

$$W_0 = W_{0gt} + sW_{st} \tag{1}$$

$$\lambda = \frac{sW_{st}}{W_{0gt}} \tag{2}$$

and the efficiency is

$$\eta = \eta_{gt}\frac{1+\lambda}{1+q} \tag{3}$$

Nomenclature

C_p = specific heat at constant pressure, J/kg K
e = excess of air in combustion
H, h = enthalpy, J/kg
k_p = pressure loss coefficient
p_c = condenser pressure, Pa
Q = heat, J
q = ratio between the heat at the afterburner and the heat at the gas turbine combustion chamber
S = entropy, J/kg K
s = steam air mass ratio
T, t = temperature, K, °C
T_{6a}, t_{6a} = stack exhaust temperature, K, °C
T_c, t_c = condenser temperature, K, °C
X = wetness fraction of the steam
W = work, kJ
W_0 = specific work (referred to the compressed air), J/kg (air)
α = compressed air fuel ratio
α_{st} = stoichiometric air fuel ratio
β = gas turbine pressure ratio
Γ_i = net calorific power, J/kg
γ = fraction of compressed air for blade cooling and accessories
ϵ_b = boiler efficiency: ratio between the heat absorbed by the water (steam) and the heat given up by the exhaust gas stream
η = efficiency
λ = ratio between the steam turbine work and the gas turbine work
μ = merit number
ν = R/C_p = ratio between the constant of the gas and the mean specific heat at constant pressure in the transformation
ξ = thermal sources concentration index
σ = cycle reversibility factor
τ = Carnot number; ratio between the minimal and maximal cycle absolute temperatures
Δ = difference

Subscripts

a = air, exhaust gas
a = adiabatic
b = combustion; boiler
ab = afterburning
c = compressor
e = economizer
gt = gas turbine
m = mechanical
n = negative
p = positive
p = polytropic
s = steam
s = isentropic
st = steam turbine
1, 2, 3, . . . = initial and end points of transformations

Superscripts

h = thermodynamics
l = lower
t = technological
u = upper
$*$ = maximal
$\hat{}$ = mean

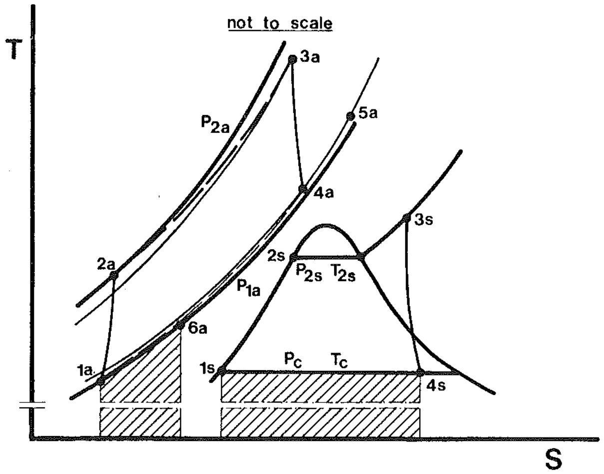

Fig. 2 Temperature entropy diagram of a combined gas-steam cycle

where $q = \alpha_{gt}/\alpha_{ab}$ is the ratio of the afterburning heat rate to the heat rate in the gas turbine combustion chamber.

Since the two cycles are not independent of each other the above relationships are not particularly suitable for finding the optimal thermodynamic operating conditions for combined cycles. It is necessary to find the dependence of combined cycle performance on other parameters; these can't be chosen in an obvious way and they do not depend on environmental or technological factors, such as T_1, p_{ia}, T_c, η_{pc}, η_{pt}, η_m, η_b, α_{st}, etc., which are not taken into consideration in the analysis. An exception is made for the maximum gas turbine temperature, the influence of which on the *Carnot number*[1] [9] is well known and justifies the efforts to increase it. The limitation on the maximum gas turbine temperature is of a technological nature.

Fundamentally it can be written

$$\eta = \eta(T_{3a}, \beta, s, p_{2s}, T_{3s}, q) \quad (4)$$

$$W_0 = W(T_{3a}, \beta, s, p_{2s}, T_{3s}, q) \quad (5)$$

Excluding the maximum gas temperature (T_{3a}), the influence of which has been already mentioned, performance of combined cycles depends on five parameters: β; s; p_{2s}; T_{3s}; q; on condition that the conservation of energy and thermal balance in the boiler are respected. The influence of the above five parameters on the efficiency of a gas-steam combined cycle can be qualitatively shown by means of suitable thermodynamic indices [9] (see appendix A):

- *thermal sources concentration index* $\xi = \xi_p/\xi_n$ where ξ_p is for the positive thermal sources and ξ_n for the negative ones;
- *cycle reversibility factor* $\sigma = \sigma_p/\sigma_n$ where σ_p and σ_n are the entropy variations corresponding to the positive and negative external heat exchange;
- *merit number* $\mu = \xi\sigma$.

Since the influence of the efficiency of the cycle of the above five parameters (β, s, p_{2s}, T_{3s}, q) is not obvious but rather complex, a thermodynamic analysis is performed by means of the abovementioned thermodynamic quantities.

(*a*) Thermal Positive Source Concentration Index. This index is influenced only by pressure ratio and afterburning rate. The pressure ratio makes it rise because of the heat exchanged in the combustion chamber. If afterburning occurs an increase of β makes T_{4a} decrease and so the pressure ratio influences ξ_p in a negative manner. The influence of the afterburning rate on ξ_p is positive when the final afterburning temperature is higher than T_{3a} and at the same time $T_{4a} > T_{2a}$. For the highest pressure ratio a low afterburning rate affects ξ_p negatively. The other parameters (s, T_{3s}, p_{2s}) do not directly affect the index ξ_p.

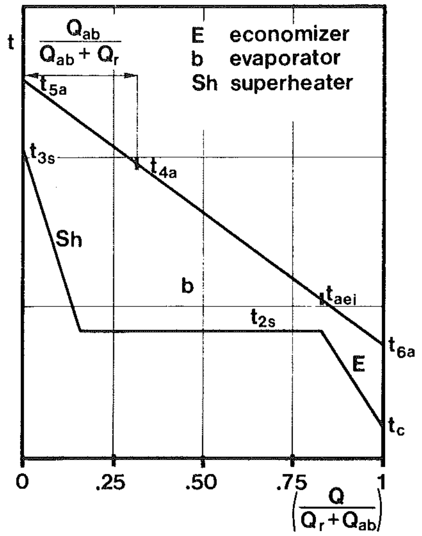

Fig. 3 Typical temperature variation in the boiler

(*b*) Thermal Negative Source Concentration Index. Combined gas-steam cycles present high efficiency, in comparison to other engines, due to the heat released at low temperature. The heat released by the exhaust gas is exchanged at temperatures in the range from the environmental temperature (t_{1a}) to that of the stack exhaust. The heat discharged by the steam is exchanged at the temperature of the condenser[2] (Fig. 2). Keeping the other parameters constant the increase in the pressure ratio makes the negative source temperatures distribution better until the minimum stack temperature or the minimum pinch point is reached.

When one of the two last values is achieved the influence of the pressure ratio becomes indirect related to the other parameters that have to be modified (changing the characteristic points of the steam cycle or varying the steam air ratio). If afterburning is not taken into consideration, the heat released at the condenser is reduced and that indirectly affects the index ξ_n negatively. The increase in steam air mass ratio affects the negative source temperature positively because it causes an increase of the heat delivered at the condenser. When the variation of this factor changes the other parameters its indirect influence depends on the quantity that is made to vary. The steam temperature at the exit of the heat recovery boiler influences the distribution of the temperatures of the negative sources – keeping the other parameters constant – because it makes the stack exhaust gas temperature decrease and the heat at the condenser increase (the end point of the expansion line moves toward the right, Fig. 2). When the variation of the temperature t_{3s} makes any other parameter vary the indirect influence of t_{3s} on the index ξ_n depends on the other modified quantity.

Keeping the other parameters constant an increase of the steam pressure affects the index ξ_n negatively because the stack exhaust temperature increases and the wetness fraction of the steam at the condenser increases (the end point of the expansion line moves toward the left, Fig. 2). The afterburning rate affects the index ξ_n only indirectly, since it is used for increasing the steam air mass ratio or for making the temperature of the steam increase.

---

[1] The Carnot number represents the minimum fraction of unused heat and is the ratio between the minimum and the maximum temperatures of the cycle: $\tau = T_1/T_3$.

[2] This is strictly true if the expansion ends in the saturated steam region. If the final point of expansion is in the superheated region the difference can be neglected. However, this case hardly ever occurs.

(*c*) **Cycle Reversibility Factor.** The gas–steam cycle irreversible production is mainly located in the compressor, in the gas turbine, in the steam turbine, and chiefly in the waste heat recovery boiler where heat exchange occurs between temperatures that can be considerably different (Fig. 3).

The increase of the pressure ratio affects the σ factor which decreases because of the less positive heat exchanged consequent to the rise of the final compression temperature. Increasing the steam air mass ratio makes the σ_n[3] factor increase or decrease depending on the value of T_{6a}, T_c, and η_s keeping the other parameters (β, T_{3s}, p_{2s}, q) constant. The steam temperature affects the value of the σ_n factor, making it decrease or increase depending on the stack exhaust gas temperature and on its value.[4]

The steam pressure affects only the σ_n factor (keeping the other parameters constant). Due to the rise of the steam pressure the stack exhaust gas temperature rises and makes the entropy increase, the wetness fraction of the steam decreases and makes the entropy diminish. The first absolute value of the entropy variation is usually higher than the second one.

As postcombustion occurs only to generate a higher steam air mass ratio or to increase the steam temperature, the afterburning rate affects σ_p directly and σ_n indirectly. The variation of σ_n is higher than the variation of σ_p.

(*d*) **Merit Number.** It can be stated therefore that the *merit number* is directly and indirectly influenced by all the five abovementioned parameters (β, s, T_{3s}, p_{2s}, q) because modifying one of them generally causes a variation of the others.

In Figs. 4 and 5 the above indices versus steam air mass ratio for constant steam pressure are given for combined gas–steam cycles having $t_{3a} = 1000°\text{C}$, $\beta = 8$, and without afterburning rate.

Considerations on Parametric Analysis of the Cycle Performance

The previous thermodynamic analysis has made it possible to demonstrate the importance of analyzing the performance of combined gas–steam cycles by means of the five parameters: β, s, p_{2s}, T_{3s}, q, for a given value of the maximum gas turbine temperature.

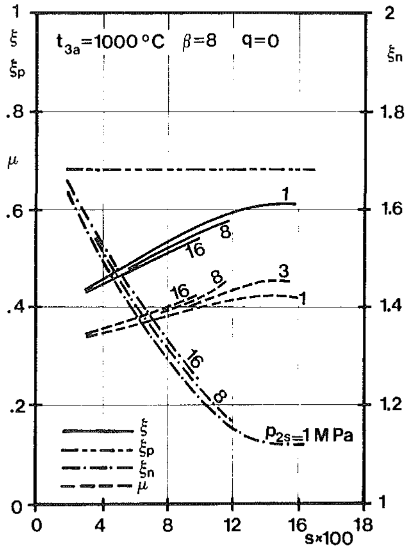

Fig. 4 ξ, ξ_p, ξ_n, and μ versus steam air mass ratio; $q = 0$

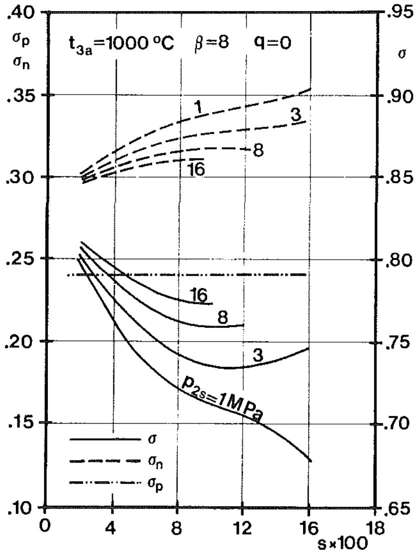

Fig. 5 σ, σ_p, σ_n versus steam air mass ratio; $q = 0$

The above quantities can vary only within certain ranges, according to energy balances, thermodynamic conditions, technological and physical factors:

(*a*) The pressure ratio can assume all the values between one and the value for which the specific work of the gas turbine is zero (i.e., $W_{0gt} > 0$);

(*b*) the steam temperature can assume all the values in the range from the saturation temperature t_{2s} (corresponding to p_{2s}), to the upper boundary t_{3s}^u. This last value can depend on technological factors ($t_{3s}^{u,t}$) or on thermodynamic conditions $t_{3s}^{uh} = t_{5a} - \Delta t_{as}$; ($\Delta t_{as}$ is positive and higher than a minimal value, which is generally related to economic considerations);

(*c*) the steam pressure is related to the wetness of the steam at the exit of the turbine which has to be higher than the minimum acceptable value: $X_{4s} \geq X_{4s}^l$. This condition can be transferred to the entropy of the steam $S_{3s} \geq S_{3s}^l$ and therefore the pair of values (t_{3s}, p_{2s}) has to satisfy this condition which usually limits the steam pressure. The minimal temperature difference at the pinch point can also limit the steam pressure;

(*d*) the ratio between the heat produced in the afterburner

---

[3] The heat exchanged (δQ) in connection with a variation of s (δs) causes the entropy changes

$$d\sigma_{na} = -\frac{\delta Q}{T_{6a}} \tag{6}$$

and

$$d\sigma_{ns} = \frac{(1-\eta_s)\delta Q}{T_c} \tag{7}$$

respectively for the stack exhaust gas and for the steam, η_s being the thermal efficiency of the steam cycle. By the two above relationships the variation of the negative reversibility factor, referred to the heat exchanged, is

$$\frac{d\sigma_n}{\delta Q} = \frac{(1-\eta_s)T_{6a} - T_c}{T_c T_{6a}} \tag{8}$$

[4] The heat exchanged (δQ) for a variation of $T_{3s}(\delta T_{3s})$ causes the following changes of entropy

$$d\sigma_{na} = -\frac{\delta Q}{T_{6a}} \tag{9}$$

and

$$d\sigma_{ns} = \frac{(1-\eta')\delta Q}{T_c} \tag{10}$$

for the stack exhaust gas and for the steam, respectively. Since

$$1 - \eta' = \frac{T_c}{T_{3s}} \tag{11}$$

the variation of σ_n with respect to δQ is

$$\frac{d\sigma_n}{\delta Q} = \frac{T_{6a} - T_{3s}}{T_{6a} T_{3s}} \tag{12}$$

and the result is usually negative.

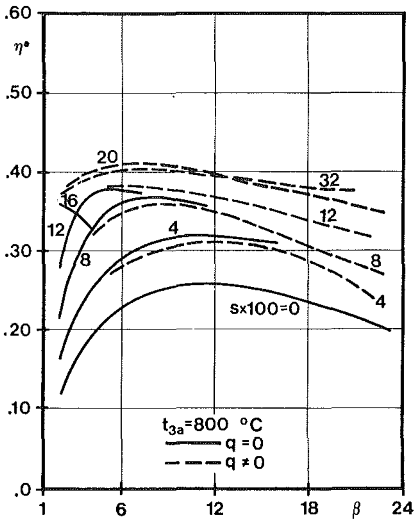

Fig. 6(*a*) Maximal efficiency versus gas turbine pressure ratio for constant steam air mass ratio

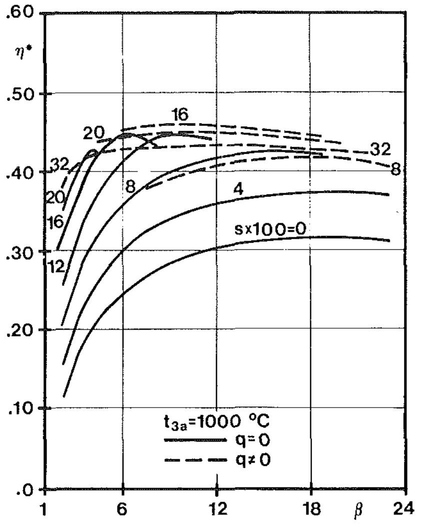

Fig. 7(*a*) Maximal efficiency versus gas turbine pressure ratio for constant steam air mass ratio

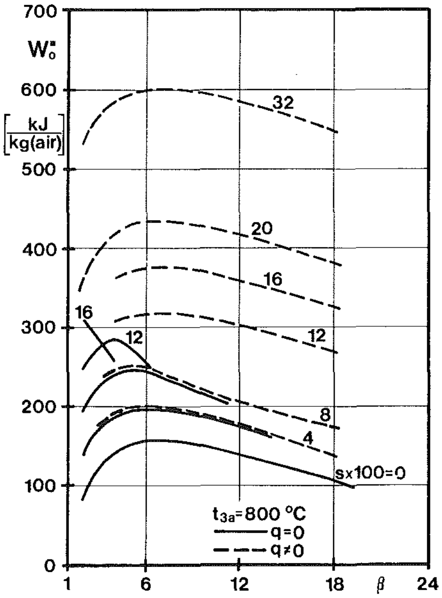

Fig. 6(*b*) Specific work corresponding to maximal efficiency cycles of Fig. 6(*a*)

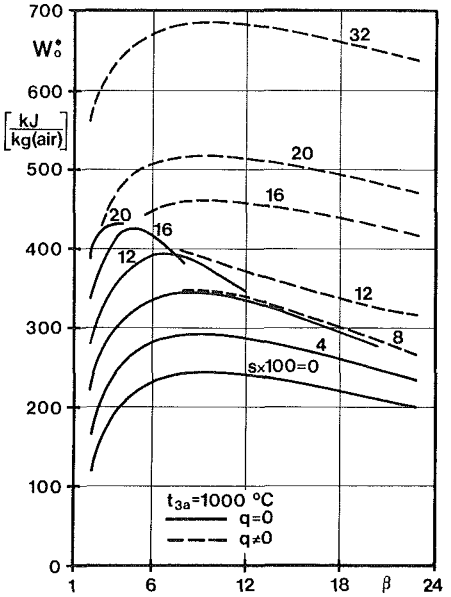

Fig. 7(*b*) Specific work corresponding to maximal efficiency cycles of Fig. 7(*a*)

and the one in the gas turbine combustion chamber can vary from zero (no afterburning occurs) to the value for which the excess of air at the stack is the minimum acceptable (e^l). Then q has an upper limit

$$q^u = \frac{\alpha_{gt}}{\alpha_{st}(1+e^l)} - 1$$

(*e*) the minimal difference of temperatures between the steam and the exhaust gas in the boiler (pinch point) has to be higher than a minimum positive value (Fig. 3) dependent on external factors: $\Delta T_{pp} \geq \Delta T_{pp}^l$;

(*f*) the stack exhaust temperature must not decrease below the values for which there is formation of corrosive condensates. Moreover the stack temperature can be limited by heat exchanger cost. Therefore for the stack temperature the condition is: $t_{6a} \geq t_{6a}^l$.

However, other conditions can be fixed by the designer of the cycle who can also decide which variables are independent and which ones are dependent. For example, β and s can be chosen as independent variables and the others can be calculated on condition that the overall efficiency be the maximum ($\eta^* = \eta(t_{3a}, \beta, s)$). The corresponding value of the specific work is W_0^*.

Results and Discussion

Numerical results of the calculations performed according to Appendix B are here presented. The assumptions underlying the analysis are:

$p_{1a} = 100$ kPa	$t_{1a} = 15°\text{C}$
$p_c = 5$ kPa	$t_c = 32.5°\text{C}$
$\eta_{pc} = 0.89$	$\eta_{pgt} = 0.88$
$\eta_{pst} = 0.86$	$\eta_{mc,gt,st} = 0.98$
$\eta_b = 0.98$	$\epsilon_b = 0.96$
$\Delta p_{2a}/p_{2a} = 0.03$	$\Delta p_{4a} = 5$ kPa
$\Gamma_i = 42700$ kJ/kg[5]	$\alpha_{st} = 14$

---

[5] It is supposed that the fuel used in the afterburner is the same utilized in the combustion chamber of the gas turbine.

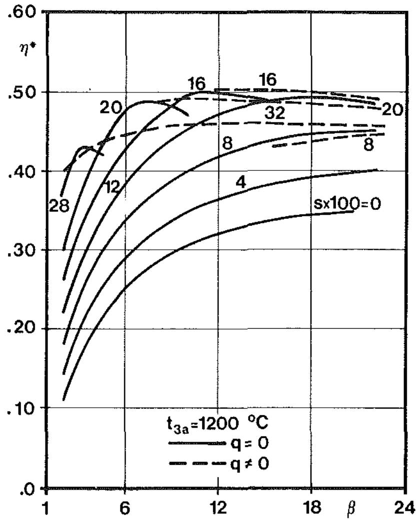

Fig. 8(*a*) **Maximal efficiency versus gas turbine pressure ratio for constant steam air mass ratio**

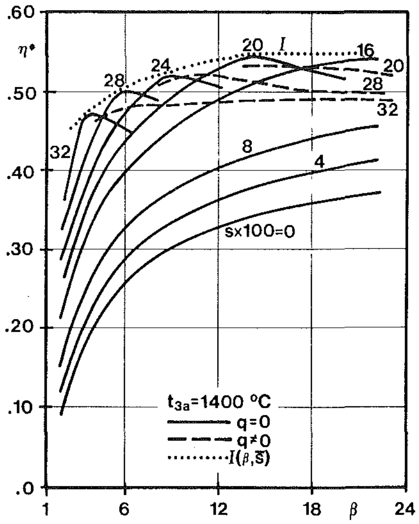

Fig. 9(*a*) **Maximal efficiency versus gas turbine pressure ratio for constant steam air mass ratio**

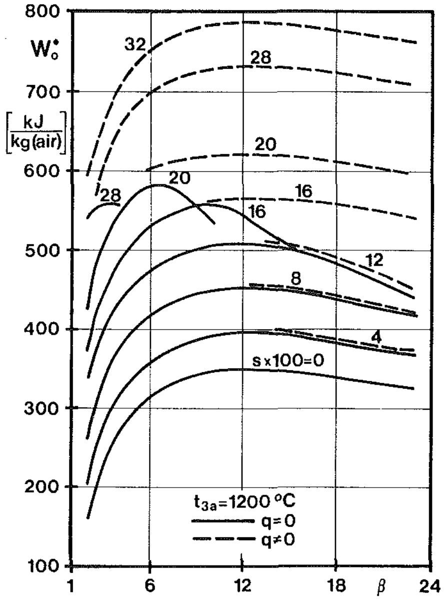

Fig. 8(*b*) **Specific work corresponding to maximal efficiency cycles of Fig. 8(*a*)**

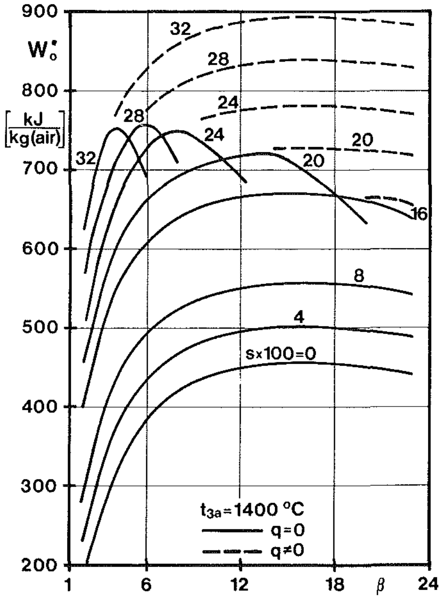

Fig. 9(*b*) **Specific work corresponding to maximal efficiency cycles of Fig. 9(*a*)**

$e^l = 0.06$ $\qquad$ $t^{ut}_{3s} = 538°\text{C}$

$\Delta t^l_{as} = 50°\text{C}$ $\qquad$ $S^l_{3s} = 6.24$ kJ/kg K $(X^l_{4s} \simeq 0.30)$

$\Delta t^l_{pp} = 30°\text{C}$ $\qquad$ $t^l_{6a} = 160°\text{C}$

Specific heats and the values of the other thermodynamic functions have been taken from [10, 11]. Steam pressure drop and the influence of the feedwater pump are negligible and so have not been taken into account. Calculations have been carried out in the maximum gas turbine 800°C–1400°C temperature range.

Maximum efficiency versus pressure ratio, keeping steam air mass ratio constant $(\eta^* = \eta(\beta, s)_{t_{3a}=\text{const}})$ is given in Figs. 6(*a*), 7(*a*), 8(*a*), 9(*a*), and the corresponding specific work in Figs. 6(*b*), 7(*b*), 8(*b*), 9(*b*); every pair of figures is for $t_{3a} = \text{const}$. Afterburning rate has been taken into account (dashed line in the figures), the temperature of the steam being the maximum acceptable value. From these results some important considerations can be stated:

1 For every pressure ratio, without afterburning the efficiency is maximum when a proper value of steam air ratio $\bar{s}$ is used. The corresponding efficiency is located on the envelope curve $I = I(\beta, \bar{s})$ of the maximum efficiency curves $(\eta^* = \eta(\beta)_{s=\text{const}})$, as in Fig. 9(*a*) (dotted line). For the same value of $\bar{s}$ the specific work is maximal too if $q = 0$, as can be deduced considering that α_{gt} is constant (it depends only on t_{3a} and β). It is worth pointing out that for a wide range of pressure ratio the efficiency is practically independent of it, as shown in Fig. 10(*a*) for $t_{3a} = 1000°\text{C}$ and for β from 4 to 16, η^* varies between $\simeq 43.0$ percent and $\simeq 44.8$ percent when $\bar{s}$ assumes values in the range of 0.08–0.20.

2 The maximal efficiency (η^*) and the corresponding specific work (W^*_0) versus the steam air ratio, keeping the pressure ratio constant, shows a nearly linear relationship except for the values of s close to zero and to $\bar{s}$ (Fig. 10).

3 Afterburning (dashed lines in Figs. 10*a* and 10*b*), for values of steam air ratio lower than $\bar{s}$, causes a decrease of efficiency. For values of s near and higher than $\bar{s}$ afterburning makes the efficiency increase until it reaches a maximum. The specific work varies in a nearly linear manner as shown in Fig.

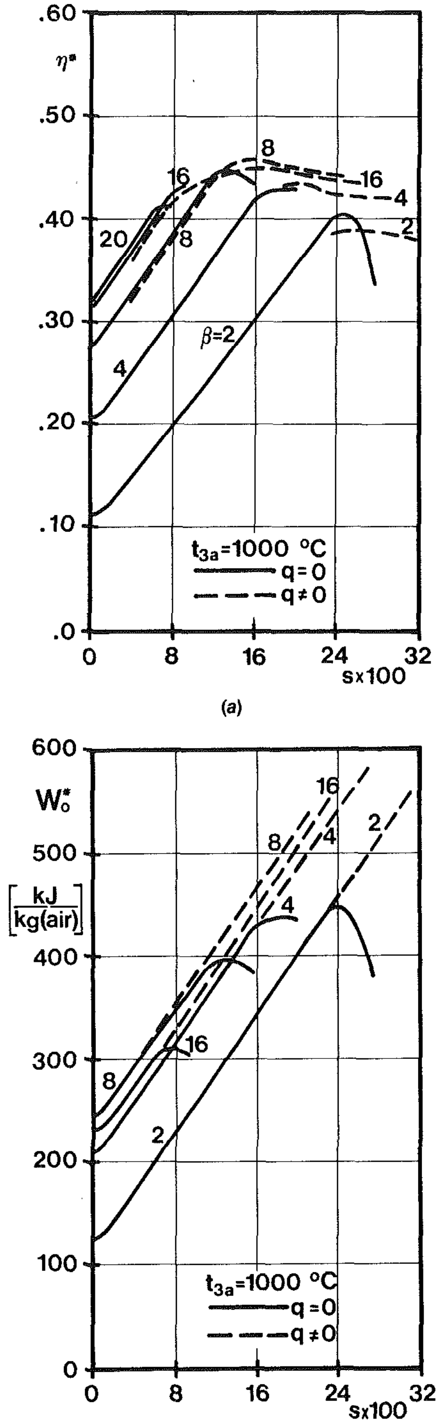

(a)

(b)

Fig. 10 Maximal efficiency (a) and the corresponding specific work (b) versus steam air mass ratio keeping pressure ratio constant

10(b). The influence of the afterburning rate for each value of t_{3a} depends on the pairs (β, s) as shown in Figs. 11(a) and 11(b). In fact for a certain value of the pressure ratio – according to the hypothesis here stated – and for the values of s in which a cycle without afterburning is possible, the afterburning rate causes a decrease of efficiency for the lower values of s. Increasing s the slope of curves $\eta=\eta(q)$ – keeping β and s constant – tends to increase and to become positive. So from a certain value of s the efficiency increases with q. For the value of s in which without afterburning the cycle is not possible, the afterburning rate causes just a little reduction of efficiency at first, compared to that corresponding to the minimal after-

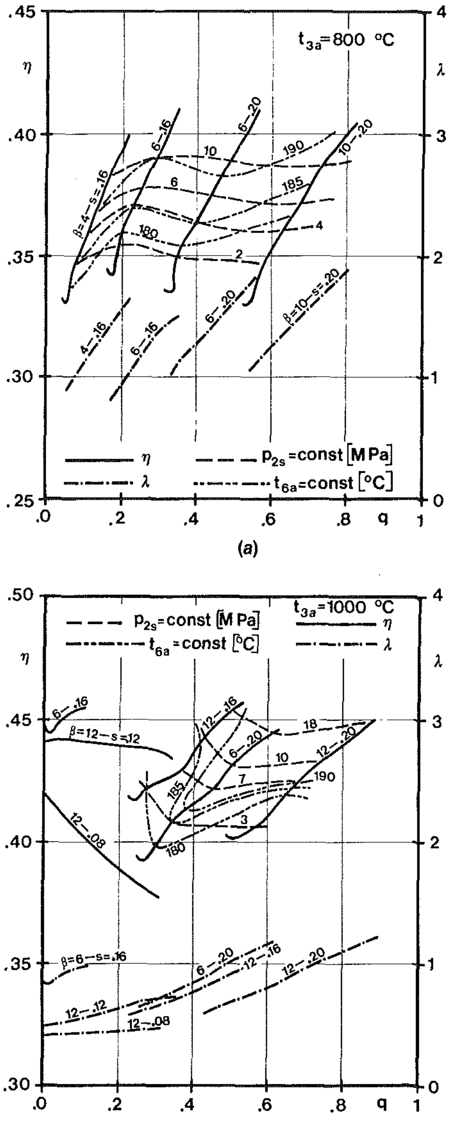

(a)

(b)

Fig. 11 Efficiency and steam air work ratio versus afterburning ratio $q=Q_{ab}/Q_{gt}$ [(a) $t_{3a}=800°C$; (b) $t_{3a}=1000°C$]

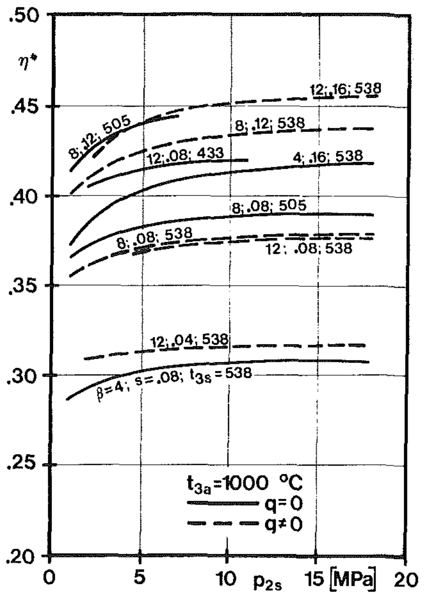

Fig. 12 Efficiency versus steam pressure

burning rate, and then the efficiency increases with q until it reaches a maximum value. Constant steam pressure and stack exhaust gas temperature are given in Fig. 11 and it can be pointed out that the efficiency increases with the steam pressure and the maximal value of the efficiency is reached at a stack exhaust gas temperature higher than the minimum acceptable value when afterburning occurs.

4 The greater the steam pressure is, the lower the effect of its variations is on efficiency, as shown in Fig. 12, where efficiency is given versus steam pressure keeping β, s, and t_{3s} constant.

5 The efficiency varies in a quasi-linear manner with the temperature of the superheated steam.

Concluding Remarks

Combined gas-steam cycles for power generation are of interest due to the high efficiency they are capable of reaching. The thermodynamic analysis carried out in the present study has shown the importance of the parameters examined.

Interesting perspectives in energy conversion from fossil fuels derive from the possibility of achieving an efficiency of 0.41 and 0.38 with and without afterburning, respectively, for a maximum gas turbine temperature of 800°C and for low pressure ratios (Fig. 6*a*), from the possibility of getting maximal efficiency values between 0.45 and 0.55 without afterburning for t_{3a} variable between 1000°C and 1400°C.

The results of this study clearly show that:

1 The pressure ratio of the gas turbine can be chosen in a wide range, because the efficiency is nearly independent of it within this range while depending on t_{3a}. Of course, a suitable choice of the other parameters is necessary;

2 the steam pressure influences the efficiency slightly when its value is sufficiently high;

3 the efficiency presents a quasi-linear increase with the rise of steam temperature t_{3s};

4 the afterburning rate increases the efficiency if the other parameters (t_{3a}, β, t_{3s}, p_{2s}, s) are properly chosen, and the maximum efficiency is reached when the stack exhaust temperature is higher than the minimal acceptable value. The influence of afterburning rate on efficiency is positive only if t_{3a} is sufficiently low.

The results presented here are for combined gas steam cycles with one steam pressure level and without regenerative extractions. The influence of two other parameters, *regeneration degree R* and *number of extractions Z*, will be analyzed in a future paper.

It must be remembered that combined gas-steam plants show good performance if suitably designed, but if the highest gas turbine temperatures are used expensive fuel must be utilized.

References

1 Aschener, F. S., "The Optimal Choice of Heat Engines for Power Plants of 10 MW to 250 MW Electric Output," *Israel Journal of Technology*, Vol. 10, No. 4, 1972, pp. 223-231.

2 Priddy, A. P., and Sullivan, J. J., "Engineering Considerations of Combined Cycles," *Combustion*, Mar. 1973, pp. 19-25.

3 Vivarelli, R., and Cerri, G., "Confronto termico economico tra motore diesel e turbomotore a gas nella produzione di energia elettrica," *La Termotecnica*, No. 3, Mar. 1976, pp. 114-122.

4 Jarach, F., and Sasso, R., "Potenziamento di centrali termoelettriche con installazione di una turbina a gas e riscaldamento recuperativo dell'acqua di alimento," *La Termotecnica*, No. 10, 1974, pp. 522-533.

5 Wunsch, A., "Centrales combinées à turbines à gaz et à vapeur. Situation actuelle et développements futurs," *Rev. Brown Boveri*, Vol. 65, No. 10, Oct. 1978, pp. 646-655.

6 Pfenninger, H., "Combined Steam and Gas Turbine Power Stations," *Brown Boveri*, pubbl. No. CH-T 040013E.

7 Fraize, W. E., and Kinney, C., "Effects of Steam Injection on the Performance of Gas Turbine Power Cycles," ASME JOURNAL OF ENGINEERING FOR POWER, Vol. 101, Apr. 1979, pp. 217-227.

8 Tomlinson, L. O., and George, R. L., "Scelta di una turbina a gas e di un ciclo a vapore per il massimo rendimento di un ciclo combinato," *Nuovo Pignone, Energia Totale dalle Turbine a Gas*, Firenze, Nov. 6-7, 1981, pp. 1-9.

9 Caputo, C., "Una cifra di merito dei cicli termodinamici diretti," *Il Calore*, No. 7, 1967, pp. 291-300.

10 Keenan, J. A., Keyes, F. G., Hill, P. G., and Moore, J. G., *Thermodynamic Properties of Steam*, Wiley, New York, 1969.

11 Keenan, J. H., and Keyes, F. G., *Gas Tables*, Wiley, New York, 1948.

APPENDIX A

Evaluation of Thermal Source Concentration Indices, Cycle Reversibility Factors, and Merit Number

According to Caputo [9] the above parameters can be defined with reference to any cycle and to the heat exchanged with the external environment (dQ), positive if it enters the cycle, negative if leaves it. The mean temperature of positive/negative total heat exchange is

$$\hat{T}_{p/n}=\frac{Q_{p/n}}{\displaystyle\int_{p/n}\frac{dQ}{T}} \tag{13}$$

and therefore

$$\xi_p=\frac{\hat{T}_p}{T_{\max}} \tag{14}$$

$$\xi_n=\frac{\hat{T}_n}{T_{\min}} \tag{15}$$

$$\xi=\tau\frac{\hat{T}_p}{\hat{T}_n} \tag{16}$$

where

$$\tau=\frac{T_{\min}}{T_{\max}} \tag{17}$$

The heat exchanged with the external environment Q_p and Q_n causes the variations of entropy

$$\sigma_p=\int_p\frac{dQ}{T}=\frac{Q_p}{\hat{T}_p} \tag{18}$$

and

$$\sigma_n=\int_n\frac{dQ}{T}=\frac{Q_n}{\hat{T}_n} \tag{19}$$

and therefore

$$\sigma=\sigma_p/\sigma_n \tag{20}$$

ξ takes into account the temperature distribution of the thermal sources; σ takes into account the irreversibility of the transformation in the cycle. The values of the above quantities are: $\sigma\leq 1$ where the equals sign is for reversible cycles; $\xi_p\leq 1$, $\xi_n\geq 1$, $\xi\leq 1$ where the equal is valid when isothermal heat exchanges with the external environment occur (Carnot, Ericsson). The merit number $\mu=\xi\sigma$, for generating power cycles where $\tau\leq\mu\leq 1$. Thermal efficiency of the cycle is expressed as

$$\eta=1-\frac{\tau}{\mu} \tag{21}$$

The above quantities are easily estimated in the thermodynamic (T, S) chart. They permit a qualitative comparison among cycles and an intuitive evaluation of the influence of thermodynamic parameters when they vary.

APPENDIX B

Thermodynamic Calculation of the Cycle

We refer to plants with and without afterburning (Fig. 1), the cycle of which is shown in Fig. 2. Calculations are referred to a unit of mass of compressed air taking part in the combustion.

Compression. The final temperature of the compression is

$$T_{2a} = T_{1a}\beta^{\nu_{a12}/\eta_{pc}} \tag{22}$$

taking into account the fraction of compressed air for blade cooling and accessories:

$$\gamma = 0.05 \quad \text{if} \quad T_{3a} < 1273\ \text{K} \tag{23a}$$

$$\gamma = 0.05(T_{3a} - 273)/1000 \text{ if } T_{3a} > 1273\ \text{K} \tag{23b}$$

the work absorbed by the compressor is

$$W_c = \frac{C_{pa12}}{\eta_{mc}}(T_{2a} - T_{1a})(1+\gamma) \tag{24}$$

Gas Turbine Combustion. The energy balance of the combustion chamber is

$$\frac{\Gamma_i \eta_{bgt}}{\alpha_{gt}} = \left(1 + \frac{1}{\alpha_{gt}}\right) C_{pa23}(T_{3u} - T_{2a}) \tag{25a}$$

and the air fuel mass ratio results

$$\alpha_{gt} = \frac{\Gamma_i \eta_{bgt}}{C_{pa23}(T_{3a} - T_{2a})} - 1 \tag{25b}$$

Gas Turbine Expansion. Since $\beta_{gt} = k_p \beta_c$ [6] the end gas expansion temperature is:

$$T_{4a} = \frac{T_{3a}}{\beta_{gt}^{\nu_{a34}\eta_{pgt}}} \tag{26}$$

and the shaft work of the turbine is

$$W_{gt} = \left(1 + \frac{1}{\alpha_{gt}}\right) C_{pa34}(T_{3a} - T_{4a})\eta_{mgt} \tag{27}$$

Waste Exhaust Heat Recovery. If afterburning occurs, defining α_{ab} as the ratio between the compressed air and the fuel used in the afterburner, the final air fuel mass ratio is

$$\alpha = \frac{\alpha_{gt}\alpha_{ab}}{\alpha_{gt} + \alpha_{ab}} \tag{28}$$

which, expressed with the stoichiometric ratio and with excess of air, is

$$\alpha = \alpha_{st}(1+e) \tag{29}$$

Thus the ratio between the afterburning fuel and the fuel in the gas turbine combustion chamber is

$$q = \frac{\alpha_{gt}}{\alpha_{ab}} \tag{30}$$

or

$$q = \frac{\alpha_{gt}}{\alpha_{st}(1+e)} - 1 \tag{31}$$

The heat balance in the afterburner may be expressed as

$$\left(1 + \frac{1}{\alpha}\right) C_{pa5} T_{5a} = \left(1 + \frac{1}{\alpha_{gt}}\right) C_{pa4} T_{4a} + \frac{\Gamma_i \eta_{ab}}{\alpha_{ab}} \tag{32}$$

The enthalpy of the steam at the exit of the boiler is

$$H_{3s} = H(T_{3s}, p_{2s}) \tag{33}$$

The enthalpy of the feedwater from the condenser is

$$h_c = h(p_c) \tag{34}$$

The energy balance of the boiler may be expressed as

$$\left(1 + \frac{1}{\alpha}\right) C_{pa56}(T_{5a} - T_{6a})\epsilon_b = s(H_{3s} - h_c) \tag{35}$$

Since

$$T_{2s} = T(p_{2s}) \tag{36}$$

is the saturation steam temperature and

$$h_{2s} = h(p_{2s}) \tag{37}$$

is the corresponding enthalpy of the water, the pinch point can be found by means of the economizer heat balance

$$\left(1 + \frac{1}{\alpha}\right) C_{pae}(T_{aei} - T_{6a})\epsilon_b = s(h_{2s} - h_c) \tag{38}$$

and

$$\Delta T_{pp} = T_{aei} - T_{2s} \tag{39}$$

Steam Expansion Work. The adiabatic efficiency of the steam turbine expansion may be expressed by means of p_{2s}, p_c, and polytropic efficiency. Since $\beta_{st} = p_{2s}/p_c$ the adiabatic efficiency is

$$\eta_{ast} = \frac{\beta_{st}^{\nu_s \eta_{pst}} - 1}{\beta_{st}^{\nu_s} - 1} \beta_{st}^{\nu_s(1-\eta_{pst})} \tag{40}$$

and the entropy of the steam at the inlet of the turbine is known

$$S_{3s} = S(T_{3s}, p_{2s}) \tag{41}$$

we find the endpoint of the isentropic expansion

$$H_{cs} = H(S_{3s}, p_c) \tag{42}$$

and thus the steam turbine shaft work

$$W_{st} = s(H_{3s} - H_{cs})\eta_{ast}\eta_{mst} \tag{43}$$

Since the steam pressure drop and the feedwater pump power were found to be negligible they were not taken into account.

Specific Work and Efficiency. The specific work of the cycle is

$$W_0 = W_{gt} + W_{st} - W_c \tag{44}$$

and the overall efficiency is

$$\eta = \frac{W_0 \alpha}{\Gamma_i} \tag{45}$$

The following conditions must be satisfied in order that the preceding equations describe a thermodynamically possible cycle

$$T_{5a} - T_{3s} \geq \Delta T_{as} \tag{46}$$

$$\Delta T_{pp} \geq \Delta T_{pp}^l > 0 \tag{47}$$

$$T_{6a} \geq T_{6a}^l \tag{48}$$

$$\alpha \geq \alpha_{st}(1 + e^l) \tag{49}$$

Other limitations can be of technological or physical nature (such as the wetness fraction of the steam at the end of expansion, etc.).

The solution of equations (22)-(49) is possible for every set of the following variables: T_{3a}, β, s, T_{3s}, p_{2s}, q once the boundary values for the cycle (p_{1a}, T_{1a}, p_c, T_c, Γ_i, η_{pc}, η_{pgt}, η_{pst}, . . . etc.) have been assigned (these depend on environmental and economic factors and on the fuel).

The solution of the above equations can also be got under other conditions, for example on condition that the efficiency for a *subset* of the above six variables be maximum.

---

[6] The coefficient k_p is: $k_p = (1 - \Delta p_{2a}/p_{2a})/(1 + \Delta p_{4a}/p_{4a})$.

Steam-Injected Gas Turbines

E. D. Larson

R. H. Williams

Center for Energy and
Environmental Studies,
Princeton University,
Princeton, NJ 08544

Among cogeneration and central station power generating technologies, gas turbine systems are attractive largely because of their low capital cost and simplicity. However, poor part-load efficiencies have restricted simple-cycle gas turbines largely to base-load cogeneration applications, while relatively low efficiencies for the production of power only have restricted gas turbines largely to peaking central station applications. Steam-injected gas turbines overcome cogeneration part-load problems by providing for steam in excess of process requirements to be injected into the combustor to raise electrical output and generating efficiency. For central station applications, proposed steam-injected gas turbines would achieve higher efficiencies at smaller capacities than any existing commercial technology, including combined cycles. Their high efficiency and expected low capital cost would make them highly competitive for baseload power generation. This paper provides an overview of steam-injection technology, including performance calculations and an assessment of the economic significance of the technology for cogeneration and central station applications.

Introduction

Rising electricity prices, the near-term prospect of surplus natural gas supplies, and the provisions of the Public Utility Regulatory Policies Act (PURPA) and ensuing regulations that encourage cogeneration have stimulated a wave of innovation in gas turbine technology. Here the significance of one of these innovations, the steam-injected gas turbine, is assessed for both cogeneration and central station power generation.

Steam-Injected Gas Turbine Technology

The steam-injected gas turbine (STIG) cycle involves a variation on the simple gas turbine cycle, wherein steam recovered in a turbine exhaust heat recovery steam generator (HRSG) is injected into the combustor to augment power output and the efficiency of power generation (Fig. 1). Aircraft-derivative units are chosen for this modification because they are designed to accommodate turbine flows considerably in excess of their nominal ratings.

History. Injecting water or steam into a gas turbine is not a new idea. Water injection for short periods of thrust augmentation was at one time common in jet-aircraft engines, although fans commonly serve this purpose today [1]. It is now standard practice to inject water or steam into stationary gas turbines to control NO_x emissions [2, 3].

In 1951 a Swedish patent application was filed dealing with steam injection as a means of augmenting power output and efficiency in gas turbine applications [4], but it was rejected in 1953. The STIG cycle is discussed in textbooks [5, 6], and the number of articles on the subject has been increasing rapidly [7–14].

It is only recently that steam injection for power and efficiency augmentation has attracted commercial interest, following the awarding of several US patents in this area [15, 16]. Two US companies – International Power Technology (IPT), Palo Alto, CA [17] and Mechanical Technology, Inc. (MTI), Latham, NY [18] – now offer packaged STIG cogeneration systems based on the Detroit Diesel Allison 501-KH turbine. As of July 1985, IPT had installed a single unit at San Jose State University, San Jose, CA and dual units at a Sunkist Growers, Inc. processing plant in Ontario, CA [19]. Also, in 1985 a General Electric LM-5000, which had operated for about a year in a simple-cycle cogeneration mode at a Simpson Paper Company plant in Anderson, CA [20], was modified for steam-injected operation.

There are currently no utilities operating steam-injected gas turbines, although at least one large utility is interested in seeing the technology developed [21].

Performance Estimate. The performance of the STIG cycle can be estimated with a "back-of-the-envelope" calculation, details of which are given elsewhere [24], based on the

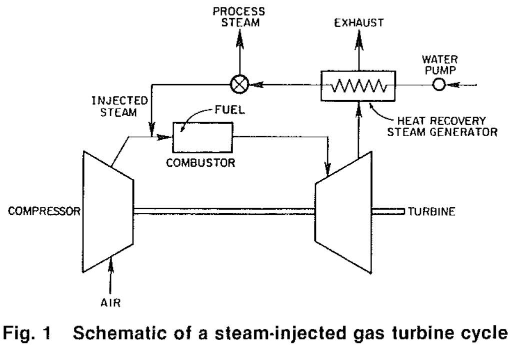

Fig. 1 Schematic of a steam-injected gas turbine cycle

Contributed by the Gas Turbine Division of The American Society of Mechanical Engineers and presented at the 31st International Gas Turbine Conference and Exhibit, Düsseldorf, Federal Republic of Germany, June 8–12, 1986. Manuscript received at ASME Headquarters January 9, 1986. Paper No. 86-GT-47.

Table 1 Estimated operating characteristics of simple-cycle Detroit-Diesel Allison 501-KB and General Electric LM-5000 turbine-generator sets

	Allison 501-KB (*a*)	General Electric LM-5000 (*b*)
Compressor:		
Pressure ratio	9.3	27.6
Air flow, kg/s (lb/s)	14.7 (32.3)	126 (277)
Adiabatic efficiency	0.83	0.88
Turbine:		
Inlet temp, °C (°F)	982 (1800)	1205 (2200)
Adiabatic efficiency	0.90	0.91
Generator efficiency:	0.93	0.98

(*a*) Data are compiled from [13, 14, 22, 23].
(*b*) Data are estimated from [21].

operating characteristics of the Allison 501-KB turbine (Table 1). As subsequent calculations will show, the peak efficiency for such a system occurs when a mass flow of steam somewhat greater than 15 percent of the compressor inlet flow is injected into the combustor. An assumed steam flow of this magnitude provides a point of departure for this calculation.

Step 1: Reference. A simplified calculation indicates that an Allison 501-KB turbine operated as a simple cycle with air as the working fluid will produce about 3.4 MW of electricity at an efficiency of 24 percent.[1]

Step 2: "Free" Extra Mass. One result of injecting steam is to increase the mass flow through the turbine. Suppose that 15 percent additional air, not steam, is supplied in an unspecified manner to the turbine inlet at the required temperature and pressure. The added mass causes back-pressuring of the compressor and hence an increase of about 22 percent in the compression ratio in the Allison turbine. The net effect of the increased compression ratio and turbine mass flow would be to increase the output and efficiency to 4.6 MW and 34 percent, respectively.

Step 3: Paying for the Extra Mass. The efficiency increase is large in step 2 because no account was taken of the heat needed to raise the extra mass to the turbine inlet conditions.[2] While enough energy can be recovered from the turbine exhaust to create steam for injection, additional heat must be supplied in the combustor to heat the steam from its injection temperature to the turbine inlet temperature. Providing the fuel for this extra heating reduces the efficiency to 31 percent.

Step 4: The Specific Heat Effect. Because the constant pressure specific heat of steam is about double that of air, the specific heat of the steam–air mixture flowing through the turbine is about 25 percent higher than that for air alone. The effect of the higher specific heat is to raise output to 5.4 MW and efficiency to 35 percent.

Summary. This back-of-the-envelope calculation illustrates that the most significant contribution to enhanced efficiency and output is the provision of extra working fluid without additional compressor work. The high specific heat of steam leads to still further gains.

More Formal Calculations. More accurate calculations of STIG-cycle performance require detailed information on the operating characteristics of particular engines and HRSGs. The results of a more formal calculation for the Allison 501-KH [24], based on reasonable estimates for these characteristics, will now be summarized.

A parameter which serves to illustrate well the operation of a STIG unit is the injected steam flow, expressed as a fraction of the compressor air flow. To calculate cycle efficiency and net power output as functions of this parameter, the compressor discharge temperature and work requirements are first determined, as in the case of a simple Brayton cycle. Then, with the turbine inlet temperature and the steam-to-air ratio specified, the turbine calculation can be performed to give the turbine outlet temperature and work output, also using the simple-cycle procedure, but with adjusted values for the specific heat parameters.

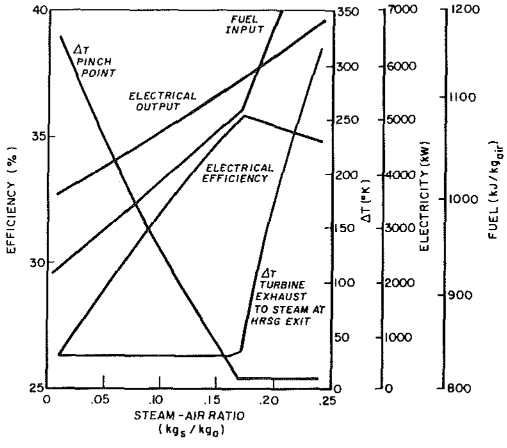

Fig. 2 Estimated operating characteristics of a steam-injected gas turbine system based on the Allison 501-KH turbine fired with natural gas

With the turbine exhaust temperature, the HRSG pressure, and the steam flow rate specified, the enthalpy of steam exiting the HRSG (typically through a superheater to recover as much heat as possible) is determined by the HRSG pinch-point temperature difference [25]. If the difference between the turbine outlet temperature and the temperature of the injected steam calculated for the specified enthalpy and pressure is less than a specified minimum (typically 15-30°C and determined by hardware considerations), then the steam temperature is instead set equal to the turbine outlet temperature minus the specified minimum, which implies an increase in the pinch point temperature difference. The total energy added in the combustor to heat the compressor discharge air and the injected steam up to the specified turbine inlet temperature can then be calculated.

Figure 2 shows the results of a sample calculation based on an Allison 501-KH turbine (Table 1) and a HRSG consisting of an economizer, boiler, and superheater. The calculated peak cycle efficiency occurs at a steam-to-air ratio of about 0.17. Up to this value, the superheat temperature of the steam is constrained by the specified minimum temperature difference between the turbine exhaust and the superheater exit, as there is enough energy and "temperature" in the turbine exhaust to heat all of the steam to the maximum allowable value. At low steam–air ratios, the pinch-point temperature difference is far above the assumed design value, indicating that much of the turbine exhaust heat is not being recovered. An increasing steam–air ratio implies a falling pinch point temperature difference, and hence greater heat recovery.

When the steam fraction passes beyond a critical value, the temperature difference between the turbine exhaust and the superheated steam rises dramatically, indicating that there is insufficient energy in the turbine exhaust to raise all of the steam to the specified maximum temperature. Beyond this critical value, the design pinch point temperature difference constrains the exit steam temperature. The additional energy input required to the combustor as a result of the lower injection-steam temperature is not offset by the additional work derived from the larger mass flow through the turbine, resulting in a drop in cycle efficiency.

Larger STIGs. Detailed performance calculations for larger steam-injected gas turbines, such as those based on GE's

---

[1] Higher heating values are used for fuels in this paper.

[2] Since the injected fluid is actually steam, the work required to raise the injected mass to the turbine inlet pressure can be neglected, as pumping the feedwater to boiler pressure requires negligible work compared to compressing air.

Table 2 Simplified assumptions of the operating characteristics of the LM-5000 ISTIG used for rough calculation of performance (*a*)

Low pressure compressor	
Pressure ratio	2.8
Air flow	157 kg/s (345 lb/s)
Efficiency	0.89
Intercooler	
Temperature at exit	25°C (76°F)
Pressure loss	8.3 kPa (1.2 psi)
High pressure compressor	
Efficiency	0.87

Air flow (*b*)		Compression ratio
123 kg/s	(271 lb/s)	12.8
18.7	(41.2)	8.55
8.6	(18.8)	5.72
4.2	(9.3)	2.96
0.4	(0.8)	1.53
1.6	(3.5)	1.06

Combustor	
Pressure loss	136 kPa (19.7 psi)
Injected steam flow (*c*)	18.1 kg/s (39.7 lb/s)
Injected steam temperature	424°C (795°F)
Turbine	
(HP, LP, and Power turbines treated as single unit)	
Inlet temperature	1355°C (2470°F)
Efficiency	0.91
Fuel flow	4.8 kg/s (10.6 lb/s) 42.7 MJ/kg (18,400 Btu/lb)

Air flow (*b*)		Exp. ratio	Entering temperature	
141 kg/s	(310 lb/s)	31.14	1628°C	(2470°F)
18.7	(41.2)	20.79	1018	(1864)
8.6	(18.8)	13.88	951	(1743)
4.2	(9.3)	7.17	821	(1509)
1.6	(3.5)	3.73	684	(1263)
0.4	(0.8)		unrecovered	

Generator	
Efficiency	0.98

(*a*) Estimates developed based on (21).
(*b*) Includes main and cooling air flows.
(*c*) For the calculation described in the text, it is assumed that all of the steam is injected into the combustor. The calculation of actual performance is more complicated, largely because multiple steam-injection points are used, including some leading to entrainment of steam into the cooling air.

LM-5000, are more complicated than for the Allison 501-KH, in part because they require better accounting for the multiple cooling flows from the compressor to the turbine. A particularly interesting modification of the LM-5000 is a proposed intercooled steam-injected gas turbine (ISTIG). In the ISTIG, steam enters at several points: into the compressor bleed air used to cool the turbine blades, at the compressor discharge into the combustor, and directly into one or more turbine stages [21]. Because of the lower temperature of the compressor bleed air than with the simple cycle (due to intercooling) and the higher heat-carrying capacity of the steam that mixes with the cooling air, turbine blade temperatures are expected to remain at an acceptable level, with a turbine inlet temperature of 1355°C (2470°F) [21], up from about 1205°C (2200°F) for the simple-cycle LM-5000.

An indication of cycle performance can be obtained using estimated operating characteristics of the LM-5000 and assuming that all of the steam is injected at the compressor discharge. Using the assumptions given in Table 2, the gross electrical output and generating efficiency of the ISTIG cycle are estimated to be 108 MW and 50 percent, respectively. Detailed evaluations by General Electric indicate that the actual efficiency of the LM-5000 ISTIG will be 47–48 percent, with an output of 110 MW [26].

Steam-Injected Gas Turbines for Cogeneration

Attraction of Gas Turbines. Historically, the predominant cogeneration technology was the steam turbine, which produces a relatively small amount of electricity per unit of process heat and usually does not lead to electricity production rates in excess of on-site needs. Gas turbines, with electricity-to-process heat ratios typically 4-5 times those of steam turbines, have a greater potential for generating electricity in excess of on-site needs [27].

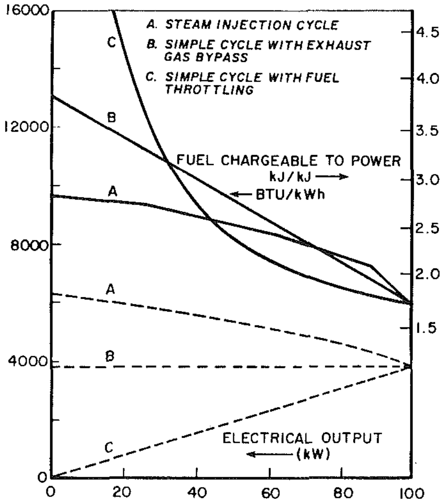

Fig. 3 Estimated part-load performance of gas turbine cogeneration systems based on Allison 501-K turbines

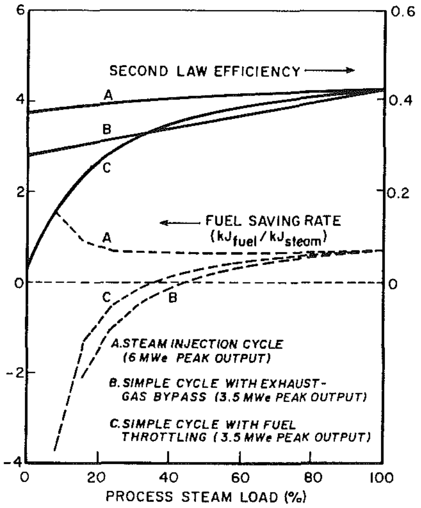

Fig. 4 Estimated part-load performance of gas turbine cogeneration systems based on Allison 501-K turbines

With low unit capital costs even at small scales [24] and good thermodynamic performance, the simple-cycle gas turbine is well suited for cogeneration in capital-intensive, energy-intensive industries characterized by relatively constant steam loads. PURPA, which facilitates the sale of excess electricity to the utility, has made gas turbine cogeneration technology more popular.

Part-Load Operation. The performance of gas turbines degrades substantially at part-load, however, which reduces the attractiveness of the technology for applications characterized by variable steam loads. For example, Figs. 3 and 4 (case C) show for the Allison 501-KB that as the process steam demand drops and the fuel input to the turbine is throttled, the second-law efficiency [24], the fuel savings rate (FSR) (defined as the amount of fuel saved in displacing central station electricity with cogenerated electricity), and the electrical output all fall off, while the fuel chargeable to power (FCP)

Table 3 Performance of gas turbines in cogeneration using unfired heat recovery steam generators (higher heating value basis)

	Electrical		Fuel charged to power, kJ/kJ (Btu/kWh) (*d*)	Electricity-heat ratio, kJ/kJ (kWh/MBtu)	Second-law efficiency (*e*)	Fuel saving rate (*f*)
	Output (kW)	Efficiency				
Allison 501-KH (*a*)						
Process Steam (*c*)						
Full						
Simple	3500	0.24	1.82 (6220)	0.51 (150)	0.37	0.57
STIG	3500	0.24	1.82 (6220)	0.51 (150)	0.37	0.57
Half						
Simple	3500	0.24	3.01 (10,260)	1.02 (300)	0.30	−0.08
STIG	4750	0.30	2.49 (8490)	1.36 (400)	0.34	0.60
None						
Simple	3500	0.24	4.20 (14,330)	–	0.22	–
STIG	6000	0.35	2.88 (9840)	–	0.33	–
GE LM-5000 (*b*)						
Process Steam (*c*)						
Full						
Simple	33,000	0.33	1.72 (5880)	0.96 (280)	0.42	1.14
STIG	33,000	0.33	1.72 (5880)	0.96 (280)	0.42	1.14
Half						
Simple	33,000	0.33	2.37 (8070)	1.91 (560)	0.37	1.08
STIG	40,000	0.36	2.29 (7810)	2.29 (670)	0.38	1.47
None						
Simple	33,000	0.33	2.99 (10,210)	–	0.31	–
STIG	47,000	0.38	2.64 (9020)	–	0.35	–

(*a*) Performance figures developed from [17].
(*b*) Performance figures developed from [26].
(*c*) Process steam is saturated at 1.4 MPa (200 psig). Full steam production is estimated to be 9850 kg/hr (21,670 lb/hr) in the Allison 501-KH and 50,000 kg/hr (110,000 lb/hr) in the GE LM-5000. Feedwater is assumed to be at 65°C (148°F). Injected steam is generally superheated, but accounting for the relatively small difference in enthalpy has little effect on the performance indicators in this table.
(*d*) Assuming a stand-alone boiler efficiency of 83 percent.
(*e*) Assuming 65°C (148°F) feedwater and an ambient temperature of 15°C (59°F).
(*f*) The fuel savings rate is a dimensionless ratio defined as the fuel saved by producing electricity (by cogeneration rather than central station generation) per unit of process steam produced.

rises sharply. For the mode of operation in which the hot exhaust gases bypass the HRSG to allow full electrical production to continue at the expense of an increasing FCP, the second-law efficiency falls off somewhat more slowly, but the FSR drop is equally sharp [Figs. 3 and 4 (case B)].

Steam-injected gas turbines extend the useful range of gas turbines to variable heat load applications by injecting steam not needed for process. With steam injection net electricity output increases significantly, the FCP increases only moderately, the second-law efficiency remains essentially constant, and the FSR actually rises as the process load drops [Figs. 3 and 4 (case A)].

Table 3 summarizes the actual performance of an Allison 501-KH turbine exhausting to an unfired HRSG for both the simple and STIG cycles. In the simple-cycle mode, when all steam is directed to process use, the performances of the two systems are indistinguishable. When the process steam load is reduced 50 percent, however, the steam-injected unit produces 4750 kW with a FCP of 1.82 kJ/kJ (6220 Btu/kWh), compared to 3500 kW at 3.01 kJ/kJ (10,260 Btu/kWh) for the simple cycle. In addition, there is only a modest reduction in the second-law efficiency (from 37 to 34 percent) with the STIG compared to the simple cycle (to 30 percent), reflecting the high thermodynamic value of the extra electricity produced. Furthermore, the simple cycle is saving no fuel compared to the separate generation of steam and electricity, while the STIG cycle saves somewhat more fuel per unit of process steam than when it is supplying the full process steam load. When the process steam load is eliminated, the STIG cycle performance is enhanced further relative to the simple cycle: Electrical output is up to 6 MW, and the FCP is still only 2.88 kJ/kJ (9840 Btu/kWh), lower than for large existing central station power plants.

Larger steam-injected gas turbines can perform even better. Rated to produce 33 MW at 33 percent efficiency in simple-cycle operation, the GE LM-5000 has a FCP of 1.72 kJ/kJ (5880 Btu/kWh), a second-law efficiency of 42 percent, and a fuel savings rate double that of the Allison 501-KH. With no process steam demand and full steam injection, it produces 14 additional megawatts with a total FCP of 2.64 kJ/kJ (9020 Btu/kWh), compared to 2.99 kJ/kJ (10,210 Btu/kWh) for the simple cycle.

Internal Rate of Return Analysis. The good part-load performance of STIG cogeneration systems contributes to attractive economic performance. Consider an application in California, where several STIG units are already installed. Suppose a STIG cogeneration unit replaces purchased electricity and a stand-alone natural-gas fired boiler (83 percent efficient) producing process steam. To simplify the analysis, a two-level plant load profile is assumed (Table 4).

The installed capital cost incurred to replace an existing stand-alone boiler is estimated to be $5 million for an Allison 501-KH STIG system, and operation and maintenance costs in excess of those for the stand-alone boiler are as estimated in Table 4. All subsidies and taxes (investment tax credit, property taxes, etc.) are neglected. Operating cost savings accrue from no longer having to purchase electricity and from being able to sell electricity to the grid at the utility's avoided cost. The rate structure of the Pacific Gas & Electric (PG&E) Company is assumed [28].

With prices constant at January 1985 values of $4.23/GJ ($4.46/MBtu) for gas, $0.106 per kWh (peak) for purchased electricity, and $0.086 per kWh (peak) for the avoided cost payment to cogenerators [28], the real internal rate of return on investment for the STIG system is about 21 percent per year. However, the rate of return for a simple-cycle system with exhaust-gas bypass during periods of low steam demand (Table 4) is about as high. Thus, for the assumed rate structure

Table 4 **Estimates and assumptions used in the economic analysis of simple-cycle and STIG cogeneration systems; costs are in 1985 dollars**

	Allison 501-KH (*a*)		GE LM-5000 (*b*)	
	Simple cycle	Steam injected	Simple cycle	Steam injected
Gross peak output (kW)	3500	6000	33,000	47,000
Installed capital cost (million $)	3.6	5.0	21	22
Incremental O&M costs (*c*)			2 mills/kWh	
Turbine overhaul once every 3 years	$220,000			
Other maintenance	60,000/yr			
Technical supervision	40,000/yr			
Insurance	37,500/yr			
Treated water	0.05 mills/liter (2 mills/gallon)		0.08 mills/liter (3 mills/gallon)	
Plant life (years)	20		30	
Assumed plant load profiles:				
Monday–Friday, 7am–6pm				
Electricity, kW	3500		33,000	
Saturated steam, 1.4 MPa (200 psig), kg/hr	9850		50,000	
(lb/hr)	(21,670)		(110,000)	
All other times				
Electricity, kW	1750		16,500	
Steam, kg/s	4925		25,000	
(lb/s)	(10,835)		(55,000)	

(*a*) Estimates are from [19], except for the capital cost of the simple-cycle unit, which is taken to be 60 percent of the steam-injected unit's cost [13].
(*b*) Estimates are from [26].
(*c*) Incremental O&M costs are costs in excess of those incurred to produce steam in an existing boiler.

and load profile, there appears to be no great incentive for a plant owner to invest in the STIG system.

However, the cogeneration systems were sized to operate with relatively high capacity factors for a situation involving predictable steam and electricity loads. Actual load profiles may be more variable due to unexpected shutdowns and other load changes that may occur in the future, e.g., due to plant equipment failures, strikes, process changes, steam load reductions from investments in energy efficiency, etc. By expressing such possible load variations in terms of an effective plant idle time, their influence on the internal rate of return can be discerned.

As the effective idle time increases, the rate of return in a simple-cycle unit drops substantially, but in the STIG system it is largely unaffected, since steam not needed for process can be redirected to produce additional electricity for sale to the utility (Fig. 5). Thus, investment in the STIG system instead of the simple-cycle unit under the provisions of PURPA can virtually eliminate the financial risks associated with unforeseen changes in a plant's steam and/or electricity load.

Even under a no idle-time scenario, the STIG system will annually produce about 25 percent more electricity and save nearly twice as much fuel per unit of process steam generated as the simple-cycle unit. As idle time rises, the electricity produced increases still further. At 20 weeks, the STIG system will produce 40 percent more electricity than the simple cycle.

Higher efficiency and lower unit capital cost lead to a rate of return of over 50 percent per year under a no-idle-time scenario for the LM-5000 STIG, based on the assumptions in Table 4. The rate of return for the simple cycle starts somewhat lower than for the STIG and falls off more rapidly with increasing idle time (Fig. 5). The LM-5000 STIG will produce annually about 20 percent more electricity than the simple cycle, assuming no idle time, while saving nearly 50 percent more fuel per unit of process steam.

These analyses show that, relative to simple-cycle systems, STIG cogeneration systems can benefit both the user, through reduced financial risk, and society, through greater power generation and fuel savings.

Short-Run Marginal Cost Analysis. The economics of STIG cogeneration can also be analyzed in terms of the short-run marginal cost (SRMC) of generation, i.e., the cost of fuel associated with generating excess electricity, to determine when it would be profitable to generate excess electricity for sale to the grid.

Case A – Without Supplemental Firing. When the process steam load falls in a STIG system, the extra fuel required to produce extra power, when the steam not needed for process is injected, is about 1.04 kJ/kJ (3550 Btu/kWh) for the Allison 501-KH turbine and about 1.88 kJ/kJ (6400 Btu/kWh) for the LM-5000 (based on Table 3).[3]

At the June 1985 US average industrial gas price of \$3.88/GJ (\$4.09/MBtu) [29], the avoided cost need be only 1.5 cents/kWh to make it economical to produce additional electricity for sale to the grid with the Allison system and about 2.6 cents/kWh with the LM-5000.

Case B – With Supplemental Firing. In the case where excess steam generated in the unfired HRSG is already being injected, the SRMC will determine whether to use supplemental firing to generate even more electricity for sale to the grid, while maintaining process steam production.

Supplemental firing in a duct burner can lead to a considerable expansion of the operating regime of a STIG system, defined in terms of electrical output and steam generation. The high air-fuel ratio and turbine exhaust temperature in a gas turbine cycle lead to high combustion efficiencies and corresponding steam-generating efficiencies as high as 86 percent [11]. Duct burners are standard equipment on the systems offered by IPT [17] and MTI [18]. One such system, based on the Allison 501-KH, can simultaneously produce between 3.5

---

[3] The lower incremental FCP is associated with the less efficient machine because of a lower turbine exhaust temperature (by about 60°C) in the higher pressure ratio LM-5000, which leads to lower injected-steam temperatures. Assuming similar HRSG characteristics, the LM-5000 combustor requires more additional fuel per kg of compressor flow than the Allison 501-KH when operating in the steam-injected mode.

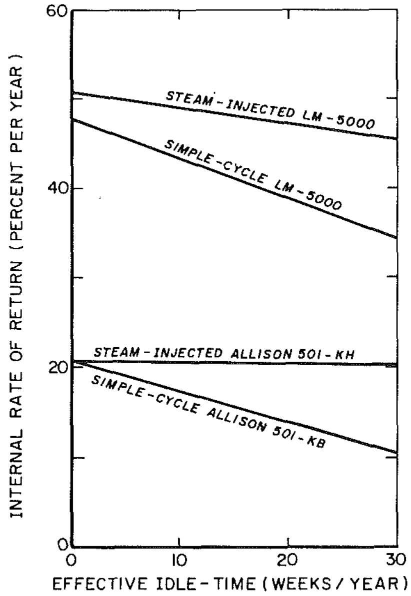

Fig. 5 Internal rates of return versus effective idle time for investments in gas turbine cogeneration systems operating with either steam-injection or exhaust-gas bypass at part process steam load

and 6 MW of electricity and 0-13 MW (45 MBtu/hr) of process steam [17].

With supplemental firing the incremental FCP is about 4.40 kJ/kJ (15,000 Btu/kWh) and 4.66 kJ/kJ (15,900 Btu/kWh) for the Allison 501-KH and LM-5000, respectively. Using supplemental firing to produce additional electricity for sale to the grid will only make sense, therefore, if avoided costs are considerably higher than in Case A. However, these values of the FCP are only 10–15 percent higher than the annual average heat rate for peaking turbines used by utilities [30]. Thus, steam-injected cogeneration systems with supplemental firing capability could be used as "zero capital cost" peaking capacity by the utility, provided an agreement could be reached with the cogenerator to make the capacity available on demand.

Significance. Steam-injected gas turbine cogeneration systems are already commercially available in small sizes [17, 18], and commercialization of larger units is not far off, as demonstrated by the recent trial operation of an LM-5000 modified for steam injection at the Simpson Paper plant in California [20] and current active negotiations between General Electric and interested customers for the sale of LM-5000 units delivered as STIGs [31].

This technology increases dramatically the potential for electricity generation via cogeneration, both because it can lead to higher electrical output in situations where simple cycles are economical and because it extends the economic viability of cogeneration to variable load applications. Assessments of the cogeneration potential that do not take this technology into account thus need to be redone.

Central Station Power Generation

Status. Further development of steam injection technology could lead to unprecedented power generating efficiencies in small central station power plants. The high efficiency and expected low capital costs of these systems would make them competitive with alternatives under a wide range of conditions.

Recent assessments of the ISTIG concept indicate that with 3-4 years of development work, General Electric's LM-5000 could be developed into an ISTIG producing 110 MW at 47-48 percent efficiency [26] for an installed capital cost of $400/kW [26] to $500/kW [21].

Potential for Replacing Natural Gas Generating Capacity. Despite the glut in electrical generating capacity in most parts of the US, a significant near-term market for ISTIG could be the displacement of the existing, inefficient, gas-fired steam-electric generating capacity.

The levelized busbar cost of electricity from the ISTIG plant (including fuel costs, O&M costs, and capital charges) would be less than the *operating* cost of existing gas-fired steam plants for gas prices in excess of about $3.03/GJ ($3.20/MBtu).[4] Since this is less than the average cost of gas to utilities in 1984, some $3.41/GJ ($3.60/MBtu) [36], it would typically be worthwhile to retire existing gas-fired steam-electric plants in favor of new ISTIG plants, even for steam-electric plants with many years of remaining useful life.

Shifting to ISTIG systems the 300 TWh of electricity produced in gas-fired steam plants in 1984 would require some 400 ISTIG units @ 110 MW each, thereby freeing up for other purposes gas supplies equivalent to more than ½ million barrels of oil per day. Alternatively, using in ISTIGs the same amount of gas now used for electricity generation would result in additional electricity equivalent to the output of 26 large (1000 MW) coal or nuclear power plants.

ISTIGs Compared to Coal and Nuclear Plants. Even with considerable escalation in the price of natural gas, ISTIGs could compete in many parts of the country with new coal and nuclear plants, the lower fuel costs of which would be more than offset by significantly higher capital costs and lower generating efficiencies (Table 5).

Estimates by the US Department of Energy (DOE) of the levelized busbar costs from power plants entering service in 1995 in different regions of the US range from 5.2 to 5.8 cents/kWh for nuclear electricity and from 3.8 to 6.0 cents/kWh for coal, as shown in Table 6. Also shown in Table 2 are busbar electricity costs for ISTIG units that would be brought on line in 1990 at a cost of $500/kW, for two different fuel price scenarios.

In Scenario A, the natural gas price is assumed to escalate, in real terms, at an annual average rate of 3 percent per year over the entire 30-year expected life of the facility, assuming for the base year the natural gas prices projected for that year by the American Gas Association [37]. Table 6 shows that under these conditions ISTIG would match or be less costly than nuclear power in 8 of 9 regions and coal in 6 of 9 regions.

The Scenario A gas price escalation assumption should be regarded as pessimistic and perhaps unrealistic. It implies that the US average gas price would increase from $3.73/GJ ($3.94/MBtu) in 1990 to $9.05/GJ ($9.56/MBtu) at the end of the plant's useful life. While indeed *natural gas prices* may rise this much, it is likely that ISTIG owners would switch to a cheaper synthetic fuel well before the natural gas price reaches this level – for example, to an intermediate heating value gas derived from coal. Indeed, an important attribute of ISTIG is its potential for being converted from operation on natural gas to operation on synthetic gas from coal [21].

An alternative Scenario B involves switching from natural gas to coal gas when the natural gas price reaches the cost of gas from coal, which is assumed to be $5.69/GJ ($6/MBtu), the average (in 1985$) of estimates made in a recent Electric Power Research Institute report of the cost of synthetic intermediate heating value gas from coal [a range of $5.12 to $6.35/GJ ($5.40–$6.70/MBtu)] [39]. Table 6 shows that the fuel switching scenario would result in 5–10 percent reductions in the ISTIG life-cycle busbar cost in regions where the natural gas price is initially high. Table 6 also shows that in most cases the switch to coal would take place in the second decade of operation, so that even with rapid natural gas price escalation, natural gas would play a major role as a transition fuel.

---

[4] Assuming for new ISTIG plants the economic conditions indicated in note (*b*) to Table 6 and for existing gas-fired steam-electric plants an average efficiency of 31.6 percent and an O&M cost of 2 mills per kWh.

Table 5 Comparison of central station power generating technologies

	Capacity, MW	Installed cap. cost, 1985$/kW (*a*)	Full-load efficiency (HHV) (*b*)	Time to install, yr (*c*)	availability (percent) (*d*)
Nuclear	1200	2000 (*e*)	0.32	11	61.8
Coal	1200	1200 (*e*)	0.33	8	69.5
Peaking gas turbine	150	300 (*f*)	0.29	3	80.6
Combined cycle	250	500 (*g*)	0.41	4	81.5
Advanced combined cycle	250	500 (*g*)	0.45	4	81.5
ISTIG	110	400-500 (*h*)	0.48	3	89.2 (*i*)

(*a*) Estimates have been expressed in 1985 dollars using the GNP deflator [32].
(*b*) Estimates of the Electric Power Research Institute [30], except for the intercooled steam-injected gas turbine (ISTIG), which is from [26].
(*c*) Estimate of the minimum time required for design, licensing, preconstruction, and construction [30]. Time to install the ISTIG is estimated from [21].
(*d*) Plant operating availability data are from the North American Electric Reliability Council (NERC) for the period 1974–1983 [33]. The NERC classifies combined cycles with miscellaneous cycles.
(*e*) Installed capital costs include direct, indirect, contingency, escalation, and interest during construction as estimated by the DOE for the average US plant entering service in 1995 [34].
(*f*) Estimate for a plant with two 75-MW units [30].
(*g*) The 240-MW GE Frame 7-E is estimated to cost $500/kW [35]. The Electric Power Research Institute estimates $505/kW [30] for a conventional combined cycle, $535/kW for an advanced unit [30].
(*h*) Estimated fully installed capital cost for the GE LM-5000 intercooled steam-injected gas turbine (ISTIG). The lower estimate is from [26]. The higher is from [21].
(*i*) The value for ISTIG is the NERC data point for aircraft-derivative units [33]. The Simpson Paper Company recently completed one year of operating a simple-cycle LM-5000 cogeneration plant with an availability in excess of 98 percent [20]. In their study of the ISTIG, the Pacific Gas and Electric Co. indicates that availabilities in excess of 90 percent should be attainable with ISTIG [21].

Table 6 Comparison of estimated regional busbar electricity costs from nuclear, coal, and ISTIG central station power plants

Region	1985 cents/kWh (*a*,*b*)				Year in which a switch is made to gas derived from coal, ISTIG B	Natural gas prices assumed for 1990, in 1985$/GJ ($/MBtu) (*c*)
	Nuclear	Coal	ISTIG A	ISTIG B		
New England	5.5	6.0	5.5	5.1	2001	4.09 (4.31)
Middle Atlantic	5.8	5.7	5.2	4.9	2003	3.82 (4.03)
E. North Central	5.6	5.5	5.5	5.1	2001	4.15 (4.38)
W. North Central	5.5	5.5	4.4	4.3	2012	2.99 (3.15)
South Atlantic	5.4	5.3	4.4	4.3	2012	2.99 (3.15)
E. South Central	5.2	5.7	4.5	4.5	2009	3.24 (3.42)
W. South Central	5.2	3.8	4.7	4.7	2007	3.44 (3.63)
Mountain	5.5	4.0	4.7	4.7	2006	3.49 (3.68)
Pacific	5.8	6.0	6.0	5.4	1997	4.65 (4.91) (*d*)
US average			5.1	4.9	2004	3.73 (3.94)

(*a*) Nuclear and coal busbar electricity costs are US Department of Energy estimates for plants entering service in 1995 [34], converted to 1985$ using the GNP deflator [32].
(*b*) The ISTIG scenarios are for a 110 MW ISTIG plant @ 48 percent efficiency entering service in 1990, assuming [21] an installed capital cost of $500/kW, a fixed O&M cost of $10.00/kW/yr, and a variable O&M cost of 4 mills/kWh. For Scenario A it is assumed that the plant always operates on natural gas, the price of which is assumed to escalate in real terms at an annual average rate of 3 percent per year over the life of the facility. For Scenario B it is assumed that the plant switches form natural gas to gas derived from coal when the natural gas price reaches $5.69/GJ ($6/MBtu), the assumed price of coal gas. In both cases a 10 percent discount rate, a 30-year plant life, and a 75 percent capacity factor are assumed.
(*c*) From [37].
(*d*) The higher projected gas price in the Pacific region is probably to some extent an artifact of regulatory practices and the structure of some of the large utilities in this region. For example, as of August 1985 at the Pacific Gas and Electric Company in California, the actual gas acquisition cost incurred by the gas division was about $3.13/GJ ($3.30/MBtu), while the price charged to the electric division was about $4.17/GJ ($4.40/MBtu) [38].

Complementing the economic advantages of ISTIG is the flexibility the technology offers utility planners with its short lead times and relatively small size (Table 5), which would enable the utility to better match supply expansion to evolving demand, an especially important consideration in the climate of uncertainty about the future that utility planners face today [40]. In addition, ISTIGs would be nearly as simple as simple-cycle gas turbine plants and would probably have operating availabilities at least as high (Table 5).

ISTIG Compared to Combined Cycles. The ISTIG would far outperform presently commercialized combined cycles, the best of which produce about 250 MW at about 40 percent efficiency and cost about $500/kW (Table 5). The technology which will come closest to matching the performance and cost of the ISTIG may be the next generation of combined cycles. Advanced combined cycles firing at 1200°C (2200°F) are expected to be about 45 percent efficient, with a capital cost of about $500/kW (Table 5). The capital cost of the 110 MW ISTIG is estimated to be close to this (Table 5), but its efficiency will be 2-3 percentage points higher. Since another generation of combined-cycle plants will be commercially available within the next 3–4 years, it is reasonable to question the merit of developing an entirely new ISTIG machine, at a cost of perhaps $100 million, for an efficiency gain of only 2-3 percentage points.

If it is assumed that the capital and O&M costs for ISTIGs and the next generation of combined cycles are the same, the efficiency advantage of a 48 percent efficient ISTIG unit would result in a levelized busbar cost about 5 percent lower than that of a 45 percent efficient combined cycle plant, assuming US average natural gas prices for plants brought on line in 1990 (Table 6).

Alternatively, if the busbar costs are equated, the discounted fuel savings over the life of the ISTIG plant would justify a "capital cost premium" of about \$160/kW for ISTIG units. Thus, the sale of only 5 or 6 ISTIGs incorporating this extra capital cost would be sufficient to recover \$100 million in R&D expenditures.

In addition to the lower busbar costs and the energy savings that would result with ISTIG, a number of other advantages suggest the desirability of developing the technology.

The modular construction of the aircraft-derivative turbines used in STIG systems permits repairs/replacements to be made more rapidly than comparable repairs on the heavy-duty industrial gas turbines typically used in combined cycles: Complete inspection (with any necessary replacements) of the hot section of an LM-2500 aircraft-derivative turbine requires a crew of five working 100 person-hours [41], compared to a similar procedure on a comparable-output industrial turbine, which requires a six-person crew working 480 p-hr [42]. Availabilities of aircraft-derivative gas turbine generating plants averaged 89.2 percent, compared to 80.6 percent for industrial turbines between 1974 and 1983 (Table 5). The availabilities of the turbines themselves over this period differed even more: 93.7 percent for aircraft-derivative units, versus 83.5 percent for industrial turbines [33].

Another practical benefit of steam injection is a relatively low level of NO_x emissions, which results from suppression of high flame temperatures in the combustor. It appears that no special stack-gas treatment, e.g., selective catalytic reduction, would be required with STIG units to meet NO_x limits imposed by current regulations [43]. In recent trial operation of a steam-injected LM-5000 cogeneration unit at the Simpson Paper Company in Anderson, California, NO_x emissions were lower than predicted and easily satisfied Northern California's regulations [20, 26]. Of course, provisions can be made to use steam for NO_x control in a combined cycle, but control is inherent in an ISTIG.

Research is continuing on more effective means of turbine blade cooling, which would permit the use of higher turbine inlet temperatures without increases in turbine metal temperatures, holding forth the possibility of still higher efficiencies for the ISTIG [21]. Such advances could, of course, benefit combined cycles as well, but because of demanding performance requirements, commercial aircraft gas turbine technology is already further advanced than industrial turbine technology. Indeed, industrial turbine designers have been borrowing some of the air-cooling technologies originally developed for aircraft engines [44].

Perhaps the most advanced combined cycle power plant in the near future will be one under development by the Japanese as part of a national project that was initiated in 1978. The project centers on the development of a 122-MW advanced reheat gas turbine, consisting of two axial flow compressors, an evaporative-spray intercooler, three turbines, a high-pressure [5.4 MPa (780 psi)] combustor, and a reheater, with a projected efficiency of 47-48 percent [45], in the same range as projected for the ISTIG. The Japanese plan to couple five such turbines to one large reheat steam turbine in a 1000-MW combined cycle to reach an efficiency of nearly 50 percent [46]. This would surpass the efficiency of the first generation of ISTIGs, but would probably do so only at a higher capital cost [21], increased complexity, and much larger size.

If a serious effort were undertaken to develop the ISTIG in this country, the performance of the large Japanese combined cycle might be approached or even exceeded in a simple, compact, 100-MW machine.

Institutional Obstacles. The Power Plant and Industrial Fuel Use Act (FUA) passed in 1978 prohibited the use of natural gas in newly constructed power plants and required that existing power plants be "off gas" by 1990. Subsequently, the Omnibus Budget Reconciliation Action of 1981 repealed the requirement that existing power plants be off gas by 1990. Present law thus prohibits the use of natural gas in efficient new utility plants (like ISTIG plants) but permits continued inefficient use of gas in steam-electric plants.

The prospects for repeal of the FUA to permit more efficient use of gas by utilities are uncertain. The law does stipulate that an exemption is obtainable for up to ten years (and possibly beyond) if a plan is in place to convert to an alternative fuel at a later time. The apparent ease with which an ISTIG plant can be converted to operation on synthetic gas derived from coal may lead some utilities to pursue the technology despite the constraints of the FUA, and indeed is one reason behind PG&E's interest in ISTIG [21]. Nevertheless, the FUA is an obstacle that will limit the potential markets for ISTIG technology in the US.

Potential Global Applications

There are vast potential markets for steam-injected gas turbines worldwide, for both cogeneration and central station applications.

Natural gas reserves exist in 50 developing countries, including 30 which import oil. Wellhead gas recovery costs in developing countries have been estimated to be in the range \$0.19-1.33/GJ (\$0.20-1.44/MBtu) [47], far lower than the US average wellhead price of \$2.37/GJ (\$2.50/MBtu) in 1984 [36]. With such low gas prices ISTIG power plants would often prove to be competitive even with hydroelectric power, currently the lowest cost electricity. In Brazil, for example, the busbar cost of firm baseload power from new hydroelectric facilities in the southeast is about 3 cents per kWh [48]. ISTIG would be competitive if the cost of gas were less than \$2.18/GJ (\$2.30/MBtu).

It may prove to be feasible to use steam-injected gas turbines with biomass feedstocks as well. The Aerospace Research Corporation (ARC) recently began trial operation of a direct-fired wood sawdust-burning Allison 501-KG at Red Boiling Springs, Tennessee [49], and plans call for increasing output and efficiency with steam injection [50]. If the ARC facility proves viable, the availability of biomass-fired STIG plants would be especially important for the many oil-importing developing countries that do not have alternative fossil fuel resources but have the potential for producing wood at relatively low cost on biomass farms or plantations. The use of biomass (a low-cost feedstock) in gas turbines (a low-capital-cost technology) operated with steam injection (providing high efficiency) would be a combination hard to beat, suggesting the importance of developmental efforts in this area [51].

Conclusion

The steam-injected gas turbine is an attractive electrical generating technology for mitigating the impacts of rising energy prices. The technology greatly extends the range of cost-effective gas turbine cogeneration to include many applications that involve variable and unpredictable process steam loads. The high efficiency of this technology makes it possible to produce electric power competitively and with low environmental impacts when fired with natural gas and relatively costly synthetic fuels. Emphasis on this technology would also stretch out limited oil and gas supplies, buying time to develop alternative electrical technologies for the long term. The steam-injected gas turbine thus stands out as an important technology for the transition to the Post-Petroleum Era.

References

1 Hill, P. G., and Peterson, C. R., *Mechanics and Thermodynamics of Propulsion*, Addison-Wesley, New York, 1965.

2 Allen, R. P., and Kovacik, J. M., "Gas Turbine Cogeneration – Prin-

ciples and Practice," ASME JOURNAL OF ENGINEERING FOR GAS TURBINES AND POWER, Vol. 106, Oct. 1984, pp. 725-730.

3 Touchton, G. L., "Influence of Gas Turbine Combustor Design and Operating Parameters on Effectiveness of NO_x Suppression by Injected Steam or Water," ASME JOURNAL OF ENGINEERING FOR GAS TURBINES AND POWER, Vol. 107, July 1985, pp. 706-713.

4 Nicolin, C., "A Gas Turbine With Steam Injection," Swedish patent application No. 8112/51, Stockholm, 1951.

5 Diamant, R. M. E., *Total Energy*, Pergamon Press, New York, 1970.

6 Haywood, R. W., *Analysis of Engineering Cycles*, 3rd ed., Pergamon Press, New York, 1980.

7 Maslennikov, V., and Shterenberg, V. Y., "Power Generating Steam Turbine-Gas Turbine Plant for Covering Peak Loads," *Thermal Engineering*, Vol. 21, No. 4, 1974, pp. 82-88.

8 Fraize, W. E., and Kinney, C., "Effects of Steam Injection on the Performance of Gas Turbine Power Cycles," ASME JOURNAL OF ENGINEERING FOR POWER, Vol. 101, Apr. 1979, pp. 217-227.

9 Davis, F., and Fraize, W., "Steam-Injected Coal-Fired Gas Turbine Power Cycles," MTR-79W00208, Mitre Corporation, McLean, VA, July 1979.

10 Brown, D. H., and Cohn, A., "An Evaluation of Steam Injected Combustion Turbine Systems," ASME JOURNAL OF ENGINEERING FOR POWER, Vol. 103, Jan. 1981, pp. 13-19.

11 Kosla, L., Hamill, J., and Strothers, J., "Inject Steam in a Gas Turbine – But Not Just for NO_x Control," *Power*, Feb. 1983.

12 Digumarthi, R., and Chang, C. N., "Cheng-Cycle Implementation on a Small Gas Turbine Engine," ASME JOURNAL OF ENGINEERING FOR GAS TURBINES AND POWER, Vol. 106, July 1984, pp. 699-702.

13 Jones, J. L., Flynn, B. R., and Strother, J. R., "Operating Flexibility and Economic Benefits of a Dual Fluid Cycle 501-KB Gas Turbine Engine in Cogeneration Applications," ASME Paper No. 82-GT-298.

14 Leibowitz, H., and Tabb, E., "The Integrated Approach to a Gas Turbine Topping Cycle Cogeneration System," ASME JOURNAL OF ENGINEERING FOR GAS TURBINES AND POWER, Vol. 106, Oct. 1984, pp. 731-736.

15 Cheng, D. Y., "Regenerative Parallel Compound Dual-Fluid Heat Engine," US Patent No. 4,128,994, Dec. 12, 1978.

16 Cheng, D. Y., "Control System for Cheng Dual-Fluid Cycle Engine System," US Patent No. 4,297,841, Nov. 3, 1981.

17 International Power Technology, "Cheng Cycle Series 7-Cogen," company publication, Palo Alto, CA, Mar. 1984.

18 Mechanical Technology, Inc., "Turbonetics Energy, Inc.: Gas Turbine Cogeneration System," company publication, Latham, NY, Mar. 1984.

19 Koloseus, C., Director of Market Development, International Power Technology, Inc., Palo Alto, CA, personal communication, Apr. 1985.

20 Clifford, L., LM-5000 Project Engineer, Simpson Paper Company, Anderson, CA, personal communication, Aug. 1985.

21 Engineering Department, "Scoping Study: LM5000 Steam-Injected Gas Turbine," Pacific Gas & Electric Company, based on work performed by the Marine and Industrial Engine Projects Department (Evendale, OH) of the General Electric Company, July 9, 1984.

22 Allison Gas Turbine Operations, "Allison Industrial Gas Turbines 501-K 570-K," General Motors Company publication, Indianapolis, IN, 1983.

23 Cain, G., Mechanical Technology, Inc., Latham, New York, personal communication, Apr. 1985.

24 Larson, E. D., and Williams, R. H., "Technical and Economic Analysis of Steam-Injected Gas-Turbine Cogeneration," in: *Energy Sources: Conservation and Renewables*, D. Hafemeister, H. Kelly, and B. Levi, eds., American Institute of Physics, New York, 1985.

25 Eriksen, V. L., Froemming, J. M., and Carroll, M. R., "Design of Gas Turbine Exhaust Heat Recovery Boiler Systems," ASME Paper No. 84-GT-126.

26 Oganowski, G., Manager of ISTIG Programs, Marine and Industrial Engines Division, General Electric Company, Cincinnati, OH, personal communication, Aug./Sept. 1985.

27 Williams, R. H., "Industrial Cogeneration," *The Annual Review of Energy*, Vol. 3, 1978, pp. 313-356.

28 Pacific Gas and Electric Company, company rate schedules, San Francisco, CA, Jan. 1985.

29 Department of Statistics, "Monthly Gas Utility Statistical Report," American Gas Association, Arlington, VA, June 1985.

30 Planning and Evaluation Division, *Technical Assessment Guide*, Electric Power Research Institute, P-2410-SR, Palo Alto, CA, May 1982.

31 Horner, M., Manager of Aircraft-Derivative Engineering and Manufacturing Programs, Turbine Marketing and Projects Division, General Electric Company, Schenectady, NY, personal communication, Sept. 1985.

32 Council of Economic Advisors, "Economic Indicators," prepared for the Joint Economic Committee, US Government Printing Office, Washington, May 1985.

33 North American Electric Reliability Council, "Equipment Availability Report, 1974-1983," NERC, Princeton, NJ, 1983.

34 Energy Information Administration, *Projected Costs of Electricity From Nuclear and Coal-Fired Power Plants*, Vol. 1, US Department of Energy, DOE/EIA-0356-1, Aug. 1982.

35 Policy Evaluation & Analysis Group, "Natural Gas-Fueled Combined Cycle Electric Power Generation – An Attractive Option," American Gas Association, Arlington, VA, May 10, 1985.

36 Energy Information Administration, *Monthly Energy Review, June 1985*, US Department of Energy, July 1985.

37 American Gas Association, TERA Base Case 1985-I: Scenario DM8450Z, Feb. 12, 1985.

38 Weatherwax, R., Sierra Energy and Risk Assessment, Sacramento, CA, personal communication, Nov. 1985.

39 Simbeck, D., Dickenson, R., and Oliver, E., "Coal-Gasification Systems: A Guide to Status, Applications, and Economics," Electric Power Research Institute, EPRI-AP3109, Palo Alto, CA, June 1983.

40 Williams, R. H., and Larson, E. D., "Steam-Injected Gas Turbines and Electric Utility Planning," *IEEE Technology and Society Magazine*, Vol. 5, No. 1, Mar. 1986, pp. 29-38.

41 Jackson, J. A., "Aircraft-Derivative Gas Turbine Maintenance Practices," General Electric Gas Turbine Division, Gas Turbine Reference Library (GER-3424), Schenectady, NY, 1984.

42 Knorr, R. H., "Heavy-Duty Gas Turbine Maintenance Practices," General Electric Gas Turbine Division, Gas Turbine Reference Library (GER-3412A), Schenectady, NY, 1984.

43 "Steam-Injection Enables Gas Turbines to Meet Strict NO_x Limits," *Power*, Oct. 1985, pp. 17-18.

44 Burton, D. C., "Combustion Turbines at the Crossroads," *Mechanical Engineering*, Apr. 1982, pp. 79-85.

45 Hori, A., and Takeya, K., "Outline of Plan for Advanced Reheat Gas Turbine," ASME JOURNAL OF ENGINEERING FOR POWER, Vol. 103, Oct. 1981, pp. 772-775.

46 Rice, I. G., Consultant and ASME Fellow, Spring, TX, personal communication, Aug. 1985.

47 The World Bank, *The Energy Transition in Developing Countries*, Aug. 1983.

48 Goldemberg, J., and Williams, R. H., "The Economics of Energy Conservation in Developing Countries," in: *Energy Sources: Conservation and Renewables*, D. Hafemeister, H. Kelly, and B. Levi, eds., American Institute of Physics, New York, 1985.

49 Hamrick, J. T., "Development of Wood-Burning Gas Turbine Systems," *Modern Power Systems*, Vol. 4, No. 6, June 1984, pp. 41-43.

50 Hamrick, J. T., Aerospace Research Corporation, Roanoke, VA, personal communication, Aug. 1985.

51 Williams, R. H., "Potential Roles for Bioenergy in an Energy Efficient World," *Ambio*, Vol. XIV, No. 4-5, 1985, pp. 201-209.

Part-Load Behavior of a Solar-Heated and Fossil-Fueled Gas Turbine Power Plant

K. Bammert
Professor Dr.-Ing.

H. Lange
Research Assistant.

Institute for Turbomachinery,
University of Hannover,
Hannover, Federal Republic of Germany

Solar energy can be converted effectively into electrical or mechanical energy. The radiant heat of the sun is collected by a parabolic dish, concentrated intensely, and reflected into a cavity receiver. Air flowing through tube panels in front of the receiver inner walls absorbs the radiant energy. Downstream of the receiver is a fossil-fired combustion chamber (hybrid construction). The fuel energy is converted at a higher utilization than in a straight fossil-fueled power plant. The overall efficiency of the hybrid plant rises with increasing turbine inlet temperature. The power delivered by the turbine serves to drive the compressor and the generator. A description of the thermodynamic design of the cycle is followed by statements on the performance characteristics of the individual components and by a description of the steady-state part-load behavior of the plant considering specific conditions such as variations in solar and fossil fuel-generated heat and fluctuating load on the power transmission grid.

Introduction

Solar energy can be converted effectively into mechanical or electrical energy by means of an intensely concentrating parabolic dish, a cavity receiver, and a gas turbine [1]. Utilization of the radiant energy of the sun rises with increasing working fluid temperature at the turbine inlet. In the cavity receiver, which is equipped with metallic tubes, the working fluid can be heated to temperatures up to 800°C [2]. Fossil heat input in a combustion chamber downstream of the receiver permits turbine inlet temperatures of up to 950°C and constant power operation at high efficiencies [3].

The external layout of the small-output solar power plant is shown in Fig. 1. The parabolic dish collector (*a*) supports on struts (*b*) the receiver (*c*) with combustion chamber and turbo set. The sun's rays hit the reflective surface of the parabolic dish, which focuses them intensely on a focal plane which can be located in front of, inside, or behind the opening (aperture) of the cavity receiver. The turbo set and combustion chamber are positioned above the receiver, the heat exchanger below the collector.

The strong variation in heat supply contingent upon the diurnal course of the sun, the supplementary use of fossil energy (substitution), and the variable power demand of the consumers call for precise knowledge of the part-load behavior of such a plant and of its individual components. The subject of this paper is a study of the steady-state behavior of a hybrid-heat-source solar plant of this kind.

Gas Turbine Cycle

The process configuration of an open-cycle gas turbine is shown in Fig. 2. Atmospheric air is drawn in through the filter (*a*) and the intake silencer (*b*) by the compressor (*c*) which compresses the working fluid to the highest process pressure. In the recuperative heat exchanger (*d*) the working fluid absorbs a large portion of the heat contained in the turbine exhaust gas, and then radiant energy of the sun in the receiver (*e*). Since the tube materials place limits on the receiver outlet temperature, the maximum process temperature is not reached in the receiver but in the connected fossil-fired combustion chamber (*f*). In this condition the flue gas enters the turbine (*g*) in which it expands to do work and then passes to the low-

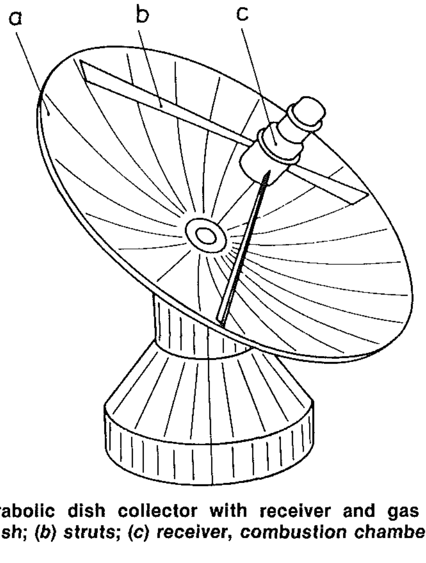

Fig. 1 Parabolic dish collector with receiver and gas turbine: (*a*) parabolic dish; (*b*) struts; (*c*) receiver, combustion chamber, and turbo set

---

Contributed by the Gas Turbine Division of THE AMERICAN SOCIETY OF MECHANICAL ENGINEERS and presented at the 31st International Gas Turbine Conference and Exhibit, Düsseldorf, Federal Republic of Germany, June 8-12, 1986. Manuscript received at ASME Headquarters March 7, 1986. Paper No. 86-GT-251.

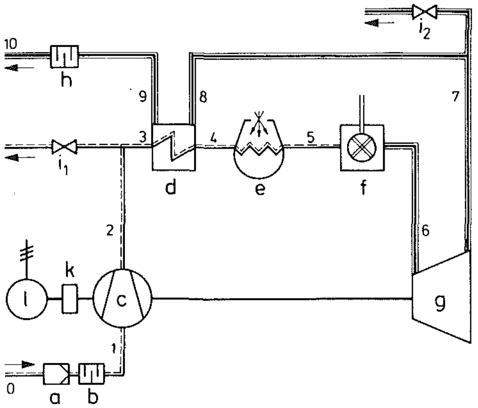

Fig. 2 Schematic diagram of the gas turbine cycle: (*a*) intake filter; (*b*) intake silencer; (*c*) compressor; (*d*) recuperator; (*e*) receiver; (*f*) combustion chamber; (*g*) turbine; (*h*) exhaust silencer; (i_1 i_2) blow-off valve; (*k*) gearbox; (*l*) generator; (1, . . . , 10) points of state

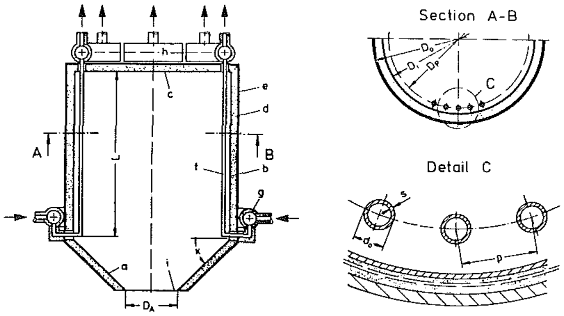

Fig. 3 Schematic diagram of receiver configuration: (*a*) cone; (*b*) inner wall; (*c*) ceiling; (*d*) insulation; (*e*) outer jacket; (*f*) tubes; (*g*) inlet header; (*h*) outlet header; (*i*) aperture

Table 1 Design parameters of the gas turbine cycle

CYCLE		
Electrical output at terminals	500	kW
Ambient temperature	25	°C
Ambient pressure	1.013	bar
Pressure ratio of compressor	5	-
Heat transferred in heat exchanger	1371	kW
Temp. difference of heat exchanger	50	K
Solar heat input	1034.4	kW
Receiver outlet temperature	800	°C
Turbine inlet temperature	950	°C
Cooling coefficient	2	%
Turbine mass flow rate	4.02	kg/s
PRESSURE LOSS		
Inlet filter and silencer	0.6	%
Heat exchanger HP	1.2	%
Heat exchanger LP	1.9	%
Receiver	5.0	%
Combustion chamber	3.5	%
Exhaust silencer	0.6	%
EFFICIENCY		
Isentropic efficiency of compressor	80	%
Isentropic efficiency of turbine	86	%
Parabolic dish efficiency	90	%
Receiver efficiency	85.7	%
Efficiency of combustion chamber	97.5	%
Gearbox efficiency	96	%
Generator efficiency	94	%
Efficiency at terminals	23.8	%

pressure side of the heat exchanger (*d*). After heat transfer to the high-pressure air, the flue gas is discharged to atmosphere via the exhaust silencer (*h*). The power generated in the turbine is used to drive both the compressor (*c*) via the machine shaft and the generator (*l*) via the gearbox (*k*). Furthermore the cycle is provided with two valves (i_1, i_2) with the aid of which the working fluid can be bled to the environment. The blow-off valve (i_1) serves to prevent surging by enlarged volumetric flow during startup of the compressor. The heat exchanger blow-off valve (i_2) enables the mass flow to be reduced on the LP side of the heat exchanger. This action may be taken for example when the thermal energy input into the cycle by the sun is larger than that which can be accepted by the generator.

The numbers of 0 to 10 entered in Fig. 2 divide the cycle up into various sections. The combustion chamber follows the receiver in section 5. The energy of the fossil fuel is added to the working fluid at a high temperature level, thus providing good fuel utilization [3]. The thermodynamic design data of the gas turbine plant are given in Table 1. The compressor draws in atmospheric air at 25°C and 1.013 bar. Its pressure ratio is 5. In the heat exchanger the high-pressure air receives a thermal input of 1371 kW so that, with the 1034.4 kW of heat transferred in the receiver, an outlet temperature of 800°C is reached. At the present state of the art, this value is considered to be the uppermost limit for metallic receiver tubing. In the interests of using "alternative" energy ("fuel saver") the working fluid temperature is raised by means of fossil fuel in the combustion chamber from 800 to 950°C. Cooling of the first turbine stages, which are subject to heavy thermal loadings, is ensured by a 2 percent part flow – relative to the turbine throughput – of cooling air. The heat exchanger is designed for a temperature difference of 50 K. The efficiencies of the compressor and the turbine are 80 and 86 percent, respectively, that of the parabolic dish 90 percent and that of the receiver 85.7 percent. 97.5 percent of the chemically bonded energy of the fuel is transferred to the working fluid in the combustion chamber. The gearbox works with an efficiency of 96 percent, the generator at 94 percent. The total pressure loss of the cycle is 12.8 percent. The overall efficiency taken as the ratio of the electric output at the generator terminals of 500 kW to the solar and fossil thermal input is 23.8 percent.

Characteristics of Components

Analysis of the part-load behavior of a gas turbine calls for knowledge of the characteristics of the individual components. The main components are the receiver, the turbomachines (compressor, turbine), and the heat exchanger. Their behavior at duty points which differ from the design point has a crucial effect on the overall behavior of the solar plant.

Receiver. Figure 3 shows a schematic diagram of the receiver design on which the present paper is based. The receiver housing which is of circular cross section comprises the cone (*a*), the inner wall (*b*), and the ceiling (*c*). It is enclosed by insulation (*d*) and the supporting outer jacket (*e*). The tubes (*f*) through which the working fluid flows are arranged in front of the inner wall. The entire receiver cavity is lined with a ceramic material (e.g., SiC panels). The working fluid arriving from the heat exchanger of the gas turbine enters the insulated inlet headers (*g*) and is heated as it flows through the tubes. Subsequently it passes into the similarly insulated outlet headers (*h*) from which it is routed to the combustion chamber. The insolation focused by the parabolic dish enters the cavity via the aperture (*i*).

Table 2 contains the design data of the receiver. The working fluid mass flow of 3.92 kg/s arriving from the heat exchanger of the gas turbine enters the insulated inlet header (*g*) (Fig. 3) at a temperature of 567°C and a pressure of 5.03 bar. The working air is heated in the tubes (*f*) to 800°C. This is equivalent to a useful thermal energy input into the working

Table 2 Receiver design data

CYCLE		
Air mass flow	3.92	kg/s
Inlet temperature	567	°C
Inlet pressure	5.03	bar
Outlet temperature	800	°C
Useful thermal power	1034.4	kW
Pressure loss	5	%
TUBE CAGE		
Tube outer diameter d_o	21.3	mm
Tube wall thickness s	2.0	mm
Tube length L	2.1	m
Number of tubes	125	-
Pitch ratio p/d_o	3.26	-
Tube cage diameter D_p	2.77	m
Heat flux	58.9	kW/m²
DIMENSION		
Receiver inner dia D_i	2.82	m
Receiver outer dia D_o	3.07	m
Cone angle κ	75	degrees
Aperture dia D_A	0.6	m
Ratio of focal length to dish diameter	1	-
Insolation flux	0.85	kW/m²
Dish diameter	47.9	m
EFFICIENCY		
Dish efficiency	90.0	%
Receiver losses		
radiation	6.3	%
convection	7.0	%
conduction	1.0	%
Receiver efficiency	85.7	%

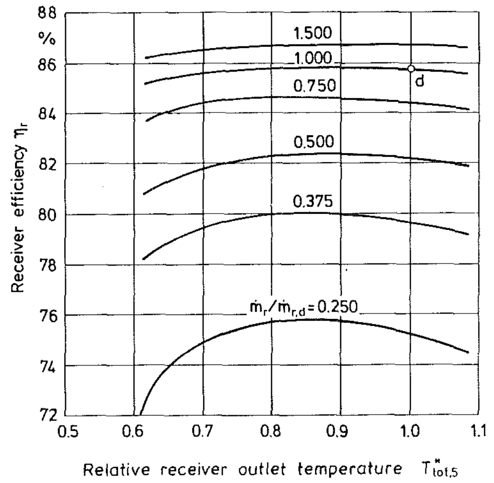

Fig. 4 Receiver characteristic map; design point *d*

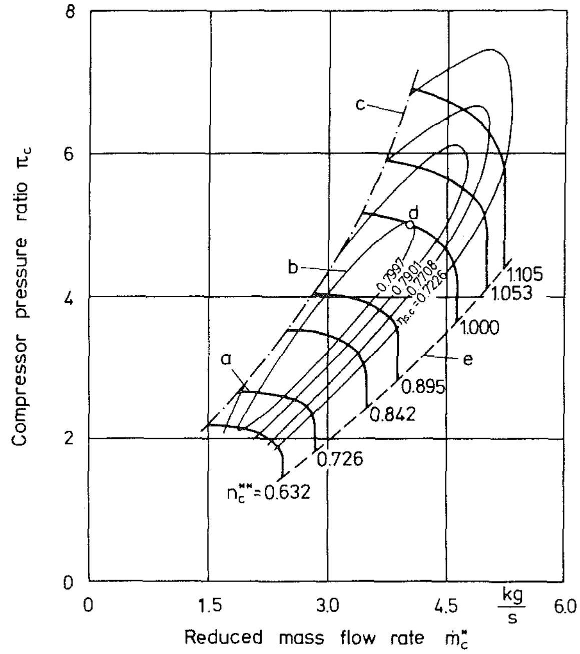

Fig. 5 Compressor characteristic map: (*a*) n_c^{**} = const; (*b*) $\eta_{s,c}$ = const; (*c*) surge line; (*d*) design point; (*e*) choke line

fluid of 1034.4 kW. The pressure loss is 5 percent. Optimization of the receiver design yielded a tube outside diameter of $d_o=21.3$ mm, a tube wall thickness of $s=2$ mm, and an irradiated tube length $L=2.1$ m. In front of the receiver inner walls are 125 tubes at a pitch of $p=69.5$ mm (pitch ratio $p/d_o=3.26$). Thus the tube cage diameter D_p is 2.77 m. The mean heat flux is 58.9 kW/m^2.

The geometric dimensions of the receiver housing are an outside diameter of $D_o=3.07$ m, an inside diameter of $D_i=2.82$ m, a cone angle of $\kappa=75$ deg, and an aperture diameter of $D_A=0.6$ m. Assuming an insolation of 0.85 kW/m^2 at the plant site, the diameter of the parabolic dish is obtained as 47.9 m, a figure which allows for shading by the receiver housing and the reflection coefficient of 90 percent of the mirror surface. The ratio of focal length to dish diameter is 1.

The receiver efficiency η_r is shown in Fig. 4 as a function of the receiver outlet temperature ($T_{\text{tot},5,d}=1073.15$ K) relative to the design point *d* and of the receiver mass flow rate $\dot{m}_{r,d}$ also relative to *d*. The receiver mass flow rate $\dot{m}_r$ is less than that through the compressor by the amount of the cooling gas flow which is branched off at the compressor outlet and fed directly to the turbine. At the design point 6.3 and 7 percent of the insolation beamed into the receiver are dissipated to the environment through the aperture as radiation and convection losses, respectively. Thermal conduction losses can be limited to 1 percent by suitable insulation of the receiver housing; thus a design efficiency of $\eta_{r,d}=85.7$ percent can be achieved (see Table 2). With the receiver mass flow rate kept constant, the working fluid outlet temperature and hence the cycle efficiency fall as insolation decreases. Simultaneously the temperature on the tubed receiver inner wall and hence the concomitant radiation, convection, and conduction losses also decrease significantly with the result that the receiver efficiency remains constant over a relatively broad duty range. If, however, the receiver outlet temperature is maintained constant by adjusting the compressor mass flow rate and hence that through the receiver, the temperature of the tubed receiver inner wall changes only slightly as insolation decreases; the relative receiver losses increase accordingly.

Turbine Generator Set. The behavior of a compressor designed for the cycle data given in Table 1 at duty points other than the design point is shown in the family of characterisics in Fig. 5 which plots the pressure ratio π_c versus the reduced mass flow rate $\dot{m}_c^*$. The latter is obtained from the actual compressor mass flow rate $\dot{m}_c$ and the totals of temperature $T_{\text{tot},1}$ and pressure $p_{\text{tot},1}$ at the compressor inlet as

$$\dot{m}_c^*=\dot{m}_c\cdot\frac{\sqrt{T_{\text{tot},1}/T_{\text{iso}}}}{p_{\text{tot},1}/p_{\text{iso}}} \tag{1}$$

where $T_{\text{iso}}=288.15$ K and $p_{\text{iso}}=1.0133$ bar are the ambient temperature and ambient pressure under standard conditions. The curves (*a*) reflect the rise in pressure which occurs when

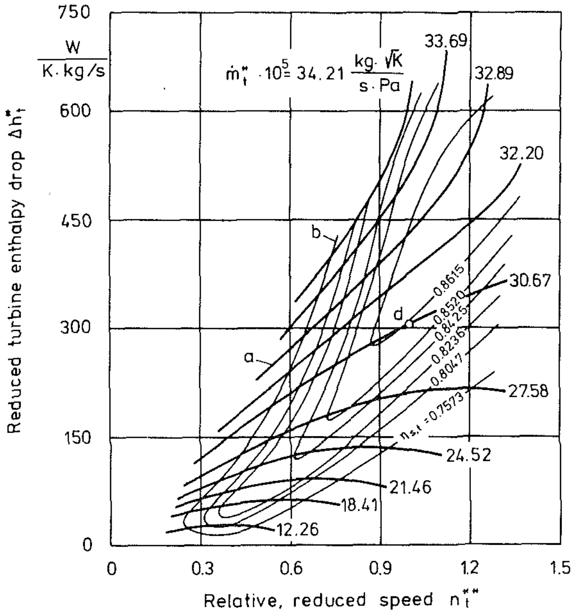

Fig. 6 Turbine characteristic map: (*a*) $\dot{m}_t^*$ = const; (*b*) $\eta_{s,t}$ = const; (*d*) design point

the relative, reduced compressor speed n_c^{**} is held constant. This is defined as

$$n_c^{**}=\frac{n_c}{n_{c,d}}\cdot\sqrt{\frac{T_{\mathrm{tot},1,d}}{T_{\mathrm{tot},1}}} \tag{2}$$

where n_c is the compressor speed and the subscript d represents the design values. It follows from equation (2) that n_c^{**}, in contrast to $\dot{m}_c^*$, is a dimensionless quantity. Lines representing a constant, isentropic compressor efficiency $\eta_{s,c}$ (curves *b*), the surge line (curve *c*), the design point (*d*), and the choke line (curve *e*) are also entered on the graph. When the compressor is operating in the vicinity of the choke line, that is, when the gas turbine is run at low inlet temperatures, sonic velocity is reached at the narrowest flow cross section for all speed characteristics. At this point it is no longer possible to increase the mass flow rate. As throttling, and hence the turbine inlet temperature, increases, the characteristic curves flatten out, while their increasing gradient as speed rises is attributed to the increase in the compressibility effect. All in all the compressor covers a relatively large duty range.

The family of characteristics for a turbine designed for the cycle parameters given in Table 1 is shown in Fig. 6. The reduced turbine enthalpy drop Δh_t^* is plotted against the relative, reduced turbine speed n_t^{**} for a number of reduced turbine mass flow rates $\dot{m}_t^*$ (curves *a*). If Δh_t and $\dot{m}_t$ denote the turbine enthalpy drop and mass flow rate, respectively, and $p_{\mathrm{tot},6}$ and $T_{\mathrm{tot},6}$ the total pressure and absolute total temperature of the working fluid at the turbine inlet, the defining equations for the dimensional quantities $\dot{m}_t^*$ and Δh_t^* are as follows

$$\dot{m}_t^*=\dot{m}_t\cdot\frac{\sqrt{T_{\mathrm{tot},6}}}{p_{\mathrm{tot},6}} \tag{3}$$

and

$$\Delta h_t^*=\frac{\Delta h_t}{T_{\mathrm{tot},6}} \tag{4}$$

The relative, reduced turbine speed n_t^{**} is, as in the compressor characteristic map, a dimensionless quantity and is obtained as

$$n_t^{**}=\frac{n_t}{n_{t,d}}\cdot\sqrt{\frac{T_{\mathrm{tot},6,d}}{T_{\mathrm{tot},6}}} \tag{5}$$

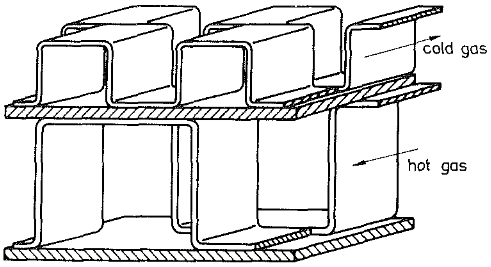

Fig. 7 Interior view of a plate-type recuperator

where n_t is the turbine speed, which in the single shaft set under consideration is always equal to that of the compressor. Again the subscript d denotes the design point. The diagram also contains the curves representing the constant, isentropic turbine efficiency $\eta_{s,t}$ (curves *b*), and the design point (*d*).

Heat Exchanger. The recuperative heat exchanger is voluminous and heavy. It is installed below the parabolic dish collector. This avoids shading of large areas of the collector by the recuperator and by the larger struts that would be required (see *b* in Fig. 1). The design basis is a plate-type heat exchanger, such as is shown in Fig. 7 [4]. Its actual size depends on the thermal power to be transferred, the allowable pressure losses on the low- and high-pressure side, and the difference between the temperatures of the incoming low-pressure gas and the outcoming high-pressure gas. The recuperator was designed and its part-load behavior determined on the basis of the parameters of Table 1 and [4, 5]. The calculations are based on measured and characteristic values.

Combustion Chamber. Design of the combustion chambers is based on test results which were obtained on installed gas turbine combustion chambers and which have been presented in empirical and universally valid form [4]. Thus it was possible to determine the combustion chamber efficiency, which is defined as the ratio of the heat transferred to the working fluid to the energy bonded in the fuel. Variations thereof at duty points other than the design point depend in essence on the combustion chamber load and on factors such as combustion plenum layout, inlet and outlet conditions of the working fluid, etc.

Consequently it was possible to analyze the part-load behavior of the recuperator and the combustion chamber with the aid of equations which are predominantly based on empirically determined quantities. Computer-assisted procedures were employed.

Part-Load Behavior of the Hybrid-Heated Plant

A solar plant can feed the electricity it generates into an interconnected power transmission grid or – in remote areas – can run in islanding operation. In the first instance a power output is fed onto the grid that corresponds to the available primary heat supply. In the second the primary energy input is governed by the demand placed by the load, and this demand can be met by a solar plant of hybrid construction. In this case the consumer load constitutes an imposed quantity, whereas the insolation cannot be regulated and varies only according to its diurnal and seasonal pattern. In islanding operation the plant has to provide frequency stabilization; the turbine generator set runs at constant speed. If variable speed is preferred, the temperature at the turbine inlet can be kept constant over a broad range, and the plant efficiencies are higher at part loads than if the speed is maintained constant. However, a frequency converter is indispensable if a constant grid frequency is required and, of course, permits then variable-speed operation on an interconnected

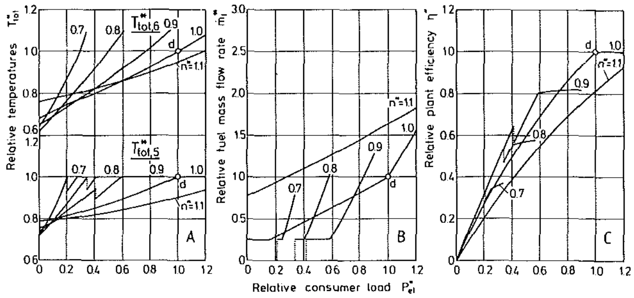

Fig. 8 Characteristics of the hybrid heated plant at the relative receiver power of 1.0; design point *d*

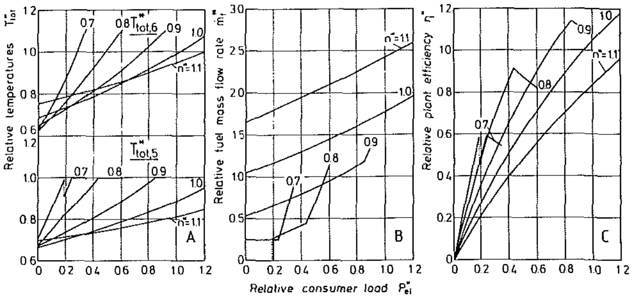

Fig. 9 Characteristics of the hybrid heated plant at the relative receiver power of 0.5

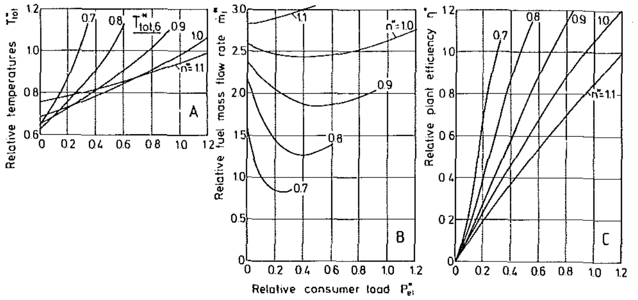

Fig. 10 Characteristics of the hybrid heated plant at the relative receiver power of 0

grid as well. In addition to the consumer load and insolation, the speed in this operating mode is the third independent parameter, and thus startup and shutdown processes can also be included in quasi-steady-state studies.

The manner in which the temperatures at the receiver outlet $T_{\text{tot},5}$ and turbine inlet $T_{\text{tot},6}$, the fuel flow to be fed into the combustion chamber $\dot{m}_f$ and the plant efficiency η vary as a function of the consumer load P_{el} and the speed of the turbo set is shown in Figs. 8 to 10. All quantities are represented as relative values obtained by dividing them with their corresponding values at the design point d and are plotted versus the likewise relative consumer load $P^*_{el} = P_{el}/P_{el,d}$. The relative speed $n^* = n/n_d$ is the parameter which, because the turbo set is of the single-shaft type, is identical to $n_c/n_{c,d}$ and $n_t/n_{t,d}$ (see equations (1) and (5)). The upper graph in Fig. 8(*A*) shows the trend of the relative temperatures $T^*_{\text{tot},6} = T_{\text{tot},6}/T_{\text{tot},6,d}$ and the lower $T^*_{\text{tot},5} = T_{\text{tot},5}/T_{\text{tot},5,d}$. The relative fuel mass flow rate $\dot{m}^*_f = \dot{m}_f/\dot{m}_{f,d}$ and the relative plant efficiency $\eta^* = \eta/\eta_d$ are plotted versus the relative consumer load P^*_{el} in Figs. 8(*B*) and 8(*C*), respectively. $T^*_{\text{tot},6} = 1.1$ is an upper limit for the loadability of the turbine blading and $T^*_{\text{tot},5} = 1$ that of the receiver tubing.

Figure 8 illustrates a plant operating mode in which the relative design insolation power $\dot{Q}^*_{ap} = \dot{Q}_{ap}/\dot{Q}_{ap,d} = 1.0$ is beamed into the receiver aperture at all consumer loads. Given that the working fluid absorbs 1034.4 kW in the receiver (Table 1) and that the receiver efficiency is 85.7 percent (Table 2), the insolation power at the design point is $\dot{Q}_{ap,\,d} = 1207$ kW.

The curves for $T^*_{\text{tot},\,6}$ are more or less linear and drop as the load decreases. Idling at $n^* = 1$ still calls for 0.68 times the turbine design temperature (832 K or 559°C). At $n^* < 1$ the necessary turbine inlet temperatures are greater in the upper power output range and less in the lower power output range than at design speed. The curves for $T^*_{\text{tot},\,5}$ feature a number of discontinuities which affect operation of the plant. If a relative turbine inlet temperature $T^*_{\text{tot},\,6} > 1$ is permitted at $n^* = 1$, $T^*_{\text{tot},\,5}$ also exceeds a value of 1, if control actions are not taken to counteract the trend. This means that the working fluid at the receiver outlet exceeds 800°C, and this reduces the service life expectancy of the receiver tubing [2]. To avoid this, the blow-off valve i_2 (Fig. 2) is opened and as large a mass of working fluid is extracted from the cycle as is necessary to reduce the heat transferred in the heat exchanger plus the insolation heat to the extent that the maximum allowable receiver outlet temperature of 800°C is restored. The heat deficiency thus caused in the cycle has to be made up by increased fossil fuel input in the combustion chamber, and this has a negative effect on the plate efficiency.

At nominal speed ($n^* = 1$) there is another discontinuity at $P^*_{el} = 0.16$. In this region the extracted electric power output is so low that only a little fossil-fuel-generated heat has to be input in addition to the heat absorbed by the working fluid in the receiver. Since a stable burner flame cannot be maintained at low fuel mass flow rates $\dot{m}^*_f$, a minimum cut-out limit of $\dot{m}^*_f = 0.25$ was introduced into the calculation. In order, however, to ensure equilibrium between the load and the plant, it is necessary to reduce the heat input at some other point of the cycle. For this purpose as well the blow-off valve i_2 is opened. Since the insolation is unaltered, the receiver outlet temperature can no longer reach the level attainable if this action were not taken, and the curve for $T^*_{\text{tot},\,5}$ drops more sharply. At $n^* < 1$ and low power P^*_{el} the combustion chamber can be shut down since the solar heat is adequate to generate the necessary temperatures. For example, the combustion chamber can be taken out of service at $n^* = 0.9$ when the power falls to $P^*_{el} = 0.41$. From idling up to this limit insolation the blow-off valve i_2 must, of course, be in operation since the insulation remains constant and is too large for low-power outputs. When P^*_{el} is raised further, the combustion chamber is placed in operation at a quarter of its design thermal output, thus ensuring stable burning of the flame. However, this requires again the opening of valve i_2 thus causing $T^*_{\text{tot},\,5}$ to fall as shown by the vertical dotted line. $T^*_{\text{tot},\,5} = 1$ is reached at $P^*_{el} = 0.59$. Operation thereafter is analogous to the temperature curve for $n^* = 1$. Operation at $n^* = 0.7$ and 0.8 features similar trends. In purely solar operation ($\dot{m}^*_f = 0$) the working fluid reaches its maximum allowable temperature of $T^*_{\text{tot},\,5} = 1$ because the mass flow rate through the receiver has further decreased.

In Fig. 8(*B*) the relative fuel mass flow rate $\dot{m}^*_f$ is plotted versus the relative consumer load P^*_{el}. The curves are based on the operating modes and control actions described for Fig. 8(*A*). The fuel consumption for $n^* > 1$ is higher over the entire power output range than for $n^* \leq 1$. The fuel demand rises sharply in the event of overload at $n^* = 1$. At low loads, the transition to less than nominal speeds provides fuel savings. If we follow for example the graph for $n^* = 0.9$, operation in the range $0 \leq P^*_{el} \leq 0.41$ is purely solar. The dotted line shows the start of supplementary fossil firing operation, which commences spontaneously with $\dot{m}^*_f = 0.25$. This minimum flow is adequate up to $P^*_{el} = 0.59$, and up to $P^*_{el} = 0.76$ the rising fuel demand $\dot{m}^*_f$ is below that for $n^* = 1$.

Figure 8(*C*) plots the relative plant efficiency η^* again versus the relative consumer load P^*_{el}. The curves correspond with

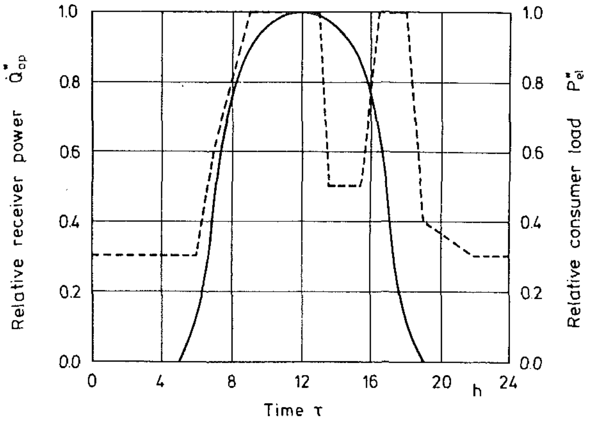

Fig. 11 Receiver power and consumer load versus time of day; ——— relative receiver power; - - - relative consumer load

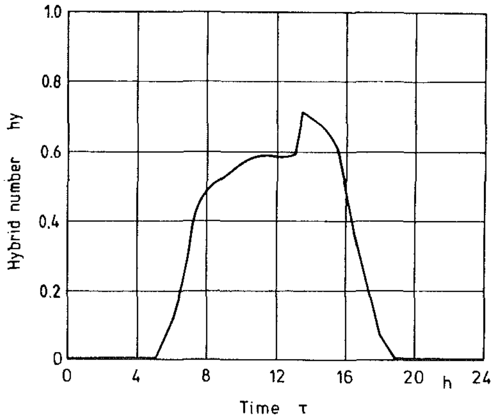

Fig. 12 Hybrid number versus time of day

those of Figs. 8(*A*) and 8(*B*). Higher efficiencies are achieved at low power outputs for $n^* < 1$ than for $n^* = 1$. Over the entire power output range the plant efficiencies are lower for $n^* > 1$ than for $n^* = 1$. If we leave aside the discontinuities described in the above, the efficiency for all speeds rises continuously with P^*_{el}. The pattern is precisely linear in the two regions in which the heat input into the cycle is constant ($\dot{m}^*_f = 0$ and $\dot{m}_f{}^* = 0.25$). The flattened parts of the curves result from the temperature limit in the receiver ($T^*_{\text{tot},5} = 1$); this is monitored by the blow-off control loop.

Figure 9 differs from Fig. 8 in that the insolation power $\dot{Q}^*_{ap}$ is reduced from 1 to 0.5, that is, this parameter of $\dot{Q}^*_{ap} = 0.5 \cdot \dot{Q}_{ap,\,d}$ applies to both full and part loads. As the upper graph in Fig. 9(*A*) shows, this circumstance has little effect on the turbine inlet temperature $T^*_{\text{tot},6}$. By contrast, the lower graph in Fig. 9(*A*) shows sharply reduced outlet temperatures $T^*_{\text{tot},5}$ of the working fluid leaving the receiver. Only at $n^* = 0.7$ does the condition occur in the range from $P^*_{el} = 0.19$ to 0.24 in which it is necessary to run at $\dot{m}^*_f = 0.25 = \text{const}$. Figure 9(*B*) clearly shows the rise in fuel demand due to the reduced insolation. At $P^*_{el} = 1$ the consumption rises from $\dot{m}^*_f = 1$ to 1.75. Generally the values of $\dot{m}^*_f$ are shifted upward for all speeds. The improved efficiency of the receiver at half load (Fig. 4), the lower pressure loss, the reduced blow-off mass flow rate of the working fluid, the increased recuperative heat transfer performance, etc., give rise, as Fig. 9(*C*) shows, to a steeper gradient of the efficiency curves, namely for $n^* < 1$, and to slightly better efficiencies.

Figure 10 deals with the condition in which there is no insulation into the receiver, that is, when $\dot{Q}^*_{ap} = 0$. The lower graph for $T^*_{\text{tot},5}$ is therefore omitted in Fig. 10(*A*). The inlet temperature into the combustion chamber is equal to the working fluid temperature at the outlet of the high-pressure side of the recuperator. Here as well, the turbine inlet temperatures $T^*_{\text{tot},6}$ differ only slightly from those for $\dot{Q}^*_{ap} = 0.5$ and 1. Of particular interest is the pattern of the speed curves in Fig. 10(*B*) with respect to $\dot{m}^*_f$. Starting from P^*_{el} at about 1.0 the fuel mass flow rate $\dot{m}^*_f$ initially falls with decreasing consumer load in the accustomed fashion. However, as the deviation from the design point increases, $\dot{m}^*_f$ rises considerably, and this is to be attributed to the low efficiency of the combustion chamber, the increased mass flow rate and the changed conditions of state of the working fluid, etc. As a result of loss of insolation, the fuel consumption at $n^* = 1$ and $P^*_{el} = 1$ is more than 2.5 times as high as for $\dot{Q}^*_{ap} = 1$. The graph for $n^* = 1.1$ exhibits the familiar slightly rising pattern with increasing P^*_{el} and requires a relative fuel mass flow rate of $\dot{m}^*_f = 3.5$ at $P^*_{el} = 1.2$. The efficiency curves of Fig. 10(*C*) are insignificantly different from those for $\dot{Q}^*_{ap} = 0.5$ and 1.

Figures 8 to 10 showed how a solar plant of hybrid construction coupled to a gas turbine has to be operated at full and part load and at normal and variable speeds when the consumer load and the insolation vary. The methods developed for this analysis are applied below to conditions which approximate those encountered in practice.

Figure 11 shows the dependence on the time of day (midnight to midnight) of a representative insolation pattern into the aperture of a receiver expressed as a relative quantity $\dot{Q}^*_{ap} = \dot{Q}_{ap}/\dot{Q}_{ap,\,d}$ (unbroken line). According to this curve, the sun rises at 5:00 a.m. and sets at 7:00 p.m. The maximum insolation is reached at 12 noon. At this point the receiver admits the insolation power of $\dot{Q}_{ap,\,d} = 1034.4/0.857 = 1207$ kW. By definition this is equivalent to a relative insolation of $\dot{Q}^*_{ap} = 1$; all other values are lower.

The dashed line illustrates a representative electric load demanded by the consumers, and this is plotted in the relative form of $P^*_{el} = P_{el}/P_{el,\,d}$. For most of the night the consumers draw a base load of $P^*_{el} = 0.3$. At 6:00 a.m. a sharp increase to $P^*_{el} = 0.6$ begins, followed by a slightly less steep gradient which culminates in $P^*_{el,\,d} = 1$ at about 9:00 a.m. at which point the design electric power output of 500 kW is reached. After midday the consumer demand falls to about half nominal load but rises again after two hours to full load, $P^*_{el} = 1$, which is reached at about 4:30 p.m. At 6:00 p.m. the consumer load drops considerably, reaching $P^*_{el} = 0.4$ at about 7:00 p.m. and returning to the nighttime base load level of $P^*_{el} = 0.3$ at 10:00 p.m.

A part-load calculation was conducted on the basis of the correlation between insolation and power demand shown in Fig. 11. This calculation yields the fossil-fuel-generated heat required for a given speed. Thus the heat inputs transferred to the working fluid in the receiver $\dot{Q}_s$ (solar) and in the combustion chamber $\dot{Q}_f$ (fossil) are known. It is therefore possible to formulate the proportion of the solar heat input relative to the total heat input into the working fluid ($\dot{Q}_s + \dot{Q}_f$) as a ratio which, because of the hybrid mode of operation of the plant, is referred to below as the "hybrid number." This is obtained as

$$hy = \frac{\dot{Q}_s}{\dot{Q}_s + \dot{Q}_f} \tag{6}$$

This number is plotted against the time of day in Fig. 12. $hy = 0$ indicates that no solar heat is available (nighttime). Throughout the morning fossil-fuel-generated heat is increasingly replaced by solar heat. This is apparent from the rise of the curve from 5:00 a.m. onward. The maximum value of *hy* is not reached at the time of maximum insolation but at the point at which the ratio of insolation to consumer load peaks. In the example selected here this is the case at 1:30 p.m. After that the solar proportion decreases again and reaches zero at 7:00 p.m. Integrating hy over the entire day (24 hr) gives an average solar portion of $hy = 0.248$; if it is integrated over the 14-hour period of sunshine the solar portion of the total thermal input is $hy = 0.425$. These average values of hy can be improved by feeding the heat of the turbine exhaust gas, otherwise dumped during blow-off operation, into a heat storage facility which would return this heat to the cycle during periods of little or no sunshine.

Conclusions

A concept has been developed for analysis of the part-load behavior of a solar plant coupled to a gas turbine. The method is based on the characteristic maps of the individual components. A configuration incorporating a fossil-fired combustion chamber downstream of the solar-heated receiver was selected in order to ensure all-day operation. It was demonstrated how a hybrid mode of operation can be adapted to the variations in insolation and consumer load throughout the day, how overheating of the receiver tubing and turbine blading can be prevented by control actions, and how the use of fossil fuel can be optimized by speed variation. A typical example illustrates the mode of operation for a given diurnal insolation and consumer load.

References

1 Bammert, K., and Seifert, P., "Design and Part-Load Behavior of a Receiver for a Solar-Heated Gas Turbine With a Parabolic Dish Collector," ASME Paper No. 84-GT-254.

2 Bammert, K., "The Thermal Load of Tubes in Radiation Heaters," *Forschung im Ingenieurwesen*, Vol. 48, 1982, pp. 160–165.

3 Bammert, K., and Finckh, H. H., "Upgrading of a Solar Thermal Power Plant by Fossil Fuel Addition," *International Journal of Turbo & Jet-Engines*, Tel Aviv, Israel, Vol. 1, 1984, pp. 273–282.

4 Münzberg, H. G., and Kurzke, J., "Operating Behavior and Optimization of Open Cycle Gas Turbines" [in German], Springer-Verlag, Berlin–Heidelberg–New York, 1977.

5 Kays, W. M., and London, A. L., *Compact Heat Exchangers*, 3rd ed., McGraw-Hill, New York, 1984.

K. Bammert
Professor Dr.-Ing.

J. Johanning
Research Assistant.

Institute for Turbomachinery,
University of Hannover,
Hannover, Federal Republic of Germany

Dynamic Behavior of a Solar-Heated Receiver of a Gas Turbine Plant

The mainly nonstationary operation of a solar-heated receiver can be simulated with sufficient accuracy only if data about the dynamic behavior are available. For this reason, the dynamic behavior of a solar cavity receiver with parabolic dish collector is investigated. The development of a mathematical simulation considering heat transfer and storage processes is presented and the procedure for a numerical solution is illustrated. The performance of the calculation method is finally demonstrated by simulating the passage of a cloud.

Introduction

One possibility of utilizing solar energy is the use of the radiation energy concentrated through a mirror system for heating the working fluid of a gas turbine plant [1, 2]. The interaction between the radiation receiver that conducts this heat transfer and different focusing mirror systems has been investigated in several papers. Ways for optimizing these systems have been shown [3–6].

In order to reach high efficiency with a gas turbine plant, very high turbine inlet temperatures are required which in turn can only be reached through a high concentration factor of solar radiation. Due to the low absorption capacity heat has to be transferred to the working medium of the gas turbine through conduction and convection and, therefore, major elements of the receiver work at a high temperature level. Without proper design measures, the receiver emits a large amount of the input energy to the environment by radiation and convection. It can be shown that a cavity receiver with an inner tube cage represents a viable solution for this level of temperature since smaller losses through radiation and convection can be achieved in comparison with outer tube cage receivers. Other concepts for guiding the working fluid, e.g., through channels inside the walls, are technically difficult to realize because of the high temperature level and the low heat transfer coefficient between wall and working fluid.

Heat input into the receiver is in principal nonstationary due to the daily motion of the sun. Added to this are short-term fluctuations of solar radiation caused by passing clouds and defects in the gas turbine cycle influencing the cooling of the tubes inside the receiver. During its entire operational period the receiver is working at the layout point only during short time spans.

The interaction of receiver and open-cycle gas turbine in varying load phases has been investigated and possibilities for expanding the working area of such plants through addition of a fossil-fired combustion chamber to the cycle have been shown [7]. The heat storage capacity of the receiver causes a certain time delay for changes in the solar radiation to influence the gas outlet temperature. The receiver has a time behavior of a delay element and, therefore, it is generally not permissible to introduce it in the calculations with its stationary behavior when simulating the behavior of the total plant (or for the concept of plant control).

The aim of this paper, therefore, is to develop a method describing the dynamic behavior of the receiver. The results can be transferred directly to computer programs simulating the dynamic behavior of total plants or taken as starting points to determine system parameters in a linearized concept of the receiver.

Setup Description

The formulation of a mathematical model is linked to the specific plant concept. For this reason, the investigation is based on a reference plant.

A paraboloid collector was chosen for the concentrating mirror system. Due to its rotational symmetry, the calculations are considerably simplified. Large radio antennas known from radio astronomy cannot be built in unlimited sizes. The coupled gas turbine plant is, therefore, limited in power. For this paper, a reference size of 265 kW electric output has been chosen. Figure 1 shows the schematic representation of the paraboloid collector with receiver and gas turbine. The paraboloid (*a*) rests on a mount (*b*) and is free to move in two axes in order to be pointing to the sun continuously. Struts (*c*) hold the receiver in the focal area of the paraboloid. To achieve a favorable layout for the gas turbine plant, which means short gas flow ducts, the gas turbine (*e*) is mounted together with the gearbox (*f*) and the generator (*g*) on top of the receiver.

Contributed by the Gas Turbine Division of The American Society of Mechanical Engineers and presented at the 31st International Gas Turbine Conference and Exhibit, Düsseldorf, Federal Republic of Germany, June 8–12, 1986. Manuscript received at ASME Headquarters March 7, 1986. Paper No. 86-GT-250.

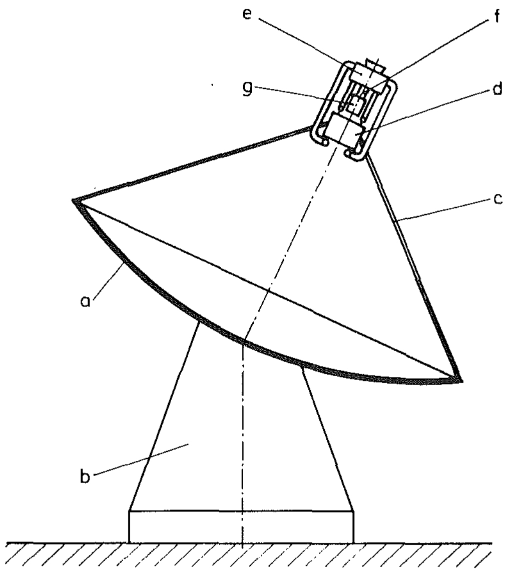

Fig. 1 Paraboloid collector with radiation receiver and gas turbine: (*a*) paraboloid; (*b*) mount; (*c*) struts; (*d*) cavity receiver; (*e*) gas turbine; (*f*) gearbox; (*g*) generator

Figure 2 shows the cycle diagram of the reference plant. For this level of power, a single shaft turbine with internal heat exchange and without intercooling has been chosen. After passing the inlet silencer (*a*) the working air is raised to its highest process pressure inside the compressor (*b*). Passing the recuperating heat exchanger (*c*) the air absorbs a part of the reject heat from the gas turbine and enters the solar receiver (*d*). A combustion chamber (*e*) is added through which the electric power can be influenced regardless of the specific solar radiation. Having passed the turbine (*f*) the working fluid releases part of its energy inside the heat exchanger to the air coming in from the compressor and then is exhausted through the exhaust silencer (*g*). The turbine drives the generator (*i*) via gearbox (*h*). The control valve (*k*) and the blow-off valve (*l*) serve for controlling the plant. Table 1 lists the most important layout data of the gas turbine plant.

The receiver of the reference plant has been designed using optimizing methods presented in [5, 6]. Figure 3 shows a cross section of this component. The receiver consists of an outer support structure (*a*), insulation (*b*), tube cage (*c*), and the collectors (*d*). Solar radiation enters the cavity through the aperture (*e*). For a better understanding of the data in Table 2 the geometric descriptions used were added to the figure. The receiver has an outer diameter D_a and an inner diameter D_i. The tubes are arranged on a circle D_t with the pitch t_r and

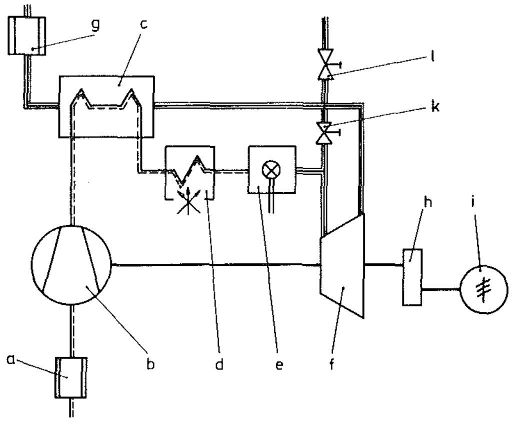

Fig. 2 Cycle diagram of an open cycle gas turbine plant: (*a*) inlet silencer; (*b*) compressor; (*c*) heat exchanger; (*d*) receiver; (*e*) combustion chamber; (*f*) turbine; (*g*) exhaust silencer; (*h*) gearbox; (*i*) generator; (*k*) control valve; (*l*) blow-off valve

Table 1 Layout parameters of the gas turbine cycle

Turbine pressure ratio	7.0	
Compressor mass flow rate	1.93	kg/s
Relative pressure loss	9	%
Isentropic compressor efficiency	83	%
Isentropic turbine efficiency	88	%
Rel. cooling gas mass flow rate	1	%
Receiver inlet temperature	454	°C
Receiver outlet temperature	800	°C
Turbine inlet temperature	900	°C
Heat exchanger temperature difference	50	°C
Mechanical efficiency	99	%
Gear efficiency	96	%
Generator efficiency	93	%
Efficiency at terminals	21,6	%
Electrical output at terminals	265	kW

Table 2 Receiver design data

Receiver outer diameter	2.12	m
Receiver inner diameter	2.02	m
Tube cage diameter	1.968	m
Pitch	32.2	mm
Tube outer diameter	14.0	mm
Tube inner diameter	11.4	mm
Number of tubes	192	
Tube length	1.28	m
Aperture diameter	0.6	m
Mean heating surface load	69.6	kW/m²
Receiver efficiency	86	%

Nomenclature

c = specific heat capacity
C_s = Stefan–Boltzmann constant
D = diameter
d = tube diameter
dA = surface element
E = energy content
F = radiation exchange factor
f_p = area reduction factor
$\dot{H}$ = enthalpy
I = radiation intensity
$\dot{m}$ = mass flow rate
$\dot{q}$ = specific heat flux
$\dot{Q}$ = heat flux
r = radial coordinate
s = distance
T = temperature
t = time
z = axial coordinate
α = absorptivity
β = angle of incidence
γ = aperture angle of radiation cone
ϵ = emission ratio
λ = heat conductivity
ρ = reflectivity

Subscripts

a = exterior, outer
b = cavity
c = inner surface
fl = fluid
i = interior, inner
j = in radial direction
N_j = number of grid points in radial direction
n = direction of time
p = paraboloid
r = cavity receiver, tube
s = sun
u = environment
w = wall
1, 2 = surface elements

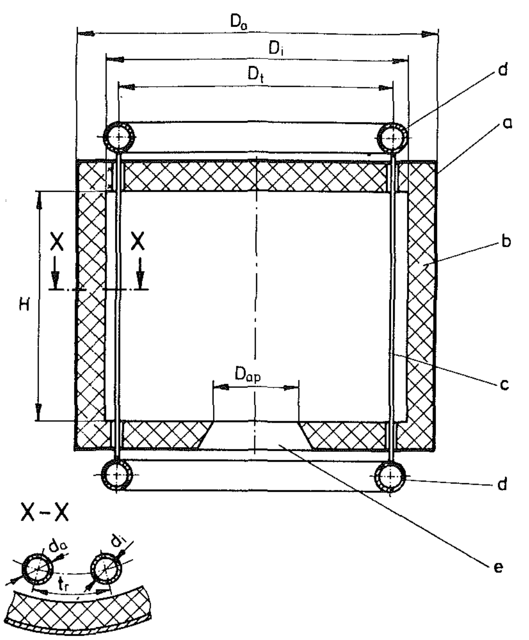

Fig. 3 Setup of a solar cavity receiver: (*a*) outer support structure; (*b*) insulation; (*c*) tubes; (*d*) collectors; (*e*) aperture

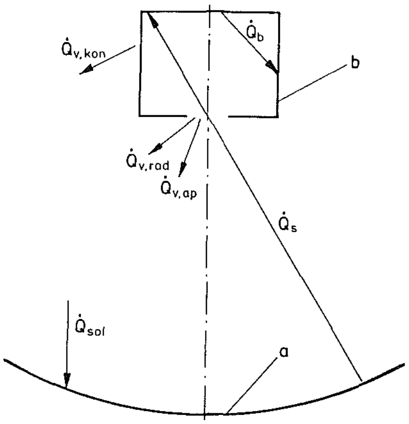

Fig. 4 Heat fluxes in the system receiver/paraboloid: (*a*) paraboloid; (*b*) receiver; $\dot{Q}$ = heat flux

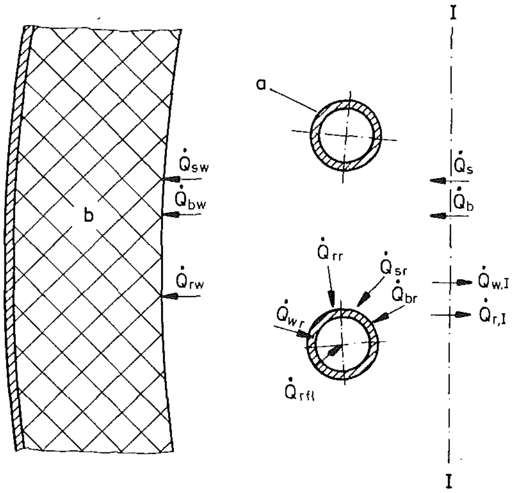

Fig. 5 Distribution of global heat fluxes within the tube cage: (*a*) tubes; (*b*) wall; *I* = balance line

have an outer diameter d_a and an inner diameter d_i. H is the irradiated tube length and at the same time the height of the receiver. The inlet aperture has a diameter D_{ap}. The wall of the receiver consists of ceramic insulation material of low density, e.g., glass wool. For the tubes, Incoloy 800H represents still the best solution in metallic materials, as ceramic tubes cannot be manufactured in sufficient lengths and joiner technology for connection to the collectors still presents problems.

Receiver Model

A model accessible to a mathematical calculation is developed from Figs. 1 and 3 which correctly represents the main heat transfer phenomena and above all the inner heat storage.

Figure 4 shows a cross section through the investigated system paraboloid and receiver. The primary heat fluxes are shown. The energy flux $\dot{Q}_{\text{sol}}$ from the sun hits the surface of the paraboloid. The major portion $\dot{Q}_s$ of this energy flux enters the aperture of the receiver and is distributed on the interior surface. The surface elements of the receiver exchange heat fluxes $\dot{Q}_b$ through radiation in the infrared spectral region. Part of the reradiation from the surface elements is irradiated through the aperture to the environment. This heat flux $\dot{Q}_{v,\text{rad}}$ is a loss and together with the convective loss $\dot{Q}_{v,\text{kon}}$ over the surface of the receiver and the convective loss $\dot{Q}_{v,\text{ap}}$ through the aperture responsible for the efficiency of the receiver.

A difficulty arises due to the necessary distribution of radiation components in the tubed wall section between tubes and receiver wall. Figure 5 shows this problem by the example of a cross section through the tube cage. The balance line I in front of the tubing is passed by heat fluxes $\dot{Q}_s$ emitted by the paraboloid and the whole surface of the cavity $\dot{Q}_b$. These heat fluxes are distributed corresponding to the geometry of the tube cage in $\dot{Q}_{sr}$ and $\dot{Q}_{br}$ on the tubes (*a*) and the walls (*b*) $\dot{Q}_{sw}$ and $\dot{Q}_{bw}$, respectively. Wall and tube surfaces exchange heat fluxes $\dot{Q}_{rw}$ and $\dot{Q}_{wr}$; moreover, certain heat fluxes $\dot{Q}_{w,I}$ and $\dot{Q}_{r,I}$ are reradiated from the wall and the tubes over the balance line back to the cavity, forming together the cavity radiation $\dot{Q}_b$. Inside the tubes the heat $\dot{Q}_{rfl}$ is transmitted to the working fluid.

To calculate the heat fluxes, the following approach is taken: The tube cage is replaced by a virtual cylindrical wall with the diameter of the tube cage. Thus, the cavity has a geometrically simple shape and the heat fluxes $\dot{Q}_s$ and $\dot{Q}_b$ can be calculated. The radiation exchange factors determine the distribution of the heat fluxes behind the virtual wall to tubes and inner wall surface and the heat transfer between these elements, respectively. These radiation exchange factors are calculated with the simplified assumption of plane radiation properties. In order to simplify the mathematical model, the tangential temperature dependence in the wall and in the tube wall are neglected. Inside the tube walls the radial dependence is also neglected.

Radiation Exchange

Each surface element at the wall of the receiver receives direct solar radiation from the paraboloid and diffuse infrared radiation from the cavity surfaces. Both of these components are decisive for the temperature distribution and thus have to be described in exact detail in their spatial distribution and intensity.

Distribution of Solar Radiation. Figure 6 shows the calculations of the incident solar radiation. The paraboloid (*a*) has an outer diameter D_{pa} and a focal length F. The receiver (*b*) is located in its axis of symmetry. The distance has been chosen for the aperture to be exactly in the focal area of the paraboloid. The receiver has the height H and a tube cage

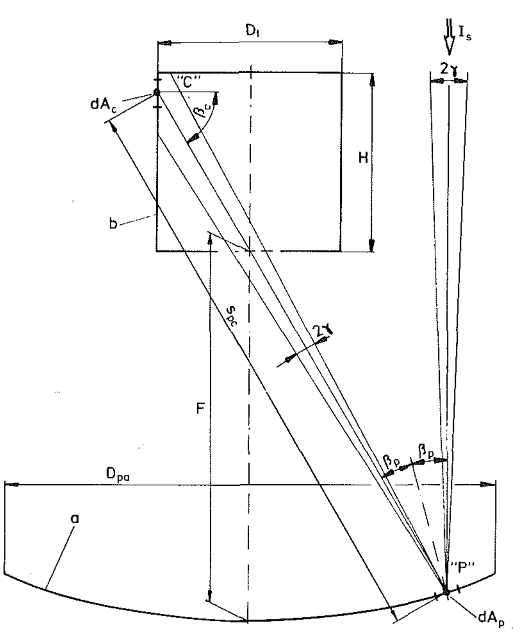

Fig. 6 Distribution of solar radiation inside receiver: (*a*) paraboloid; (*b*) receiver; I_s = solar radiation intensity

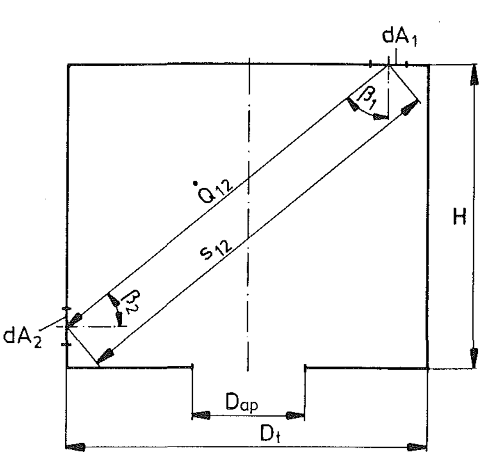

Fig. 7 Radiation exchange in the cavity

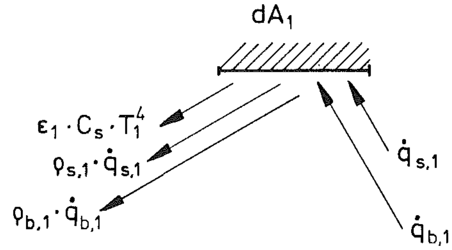

Fig. 8 Radiation intensity of a surface element in the cavity

diameter D_t, replaced by a virtual cylindrical wall (*b*) with a tube cage diameter D_t.

Seen from a point P on the paraboloid surface the sun is laying in a radiation cone with an aperture angle of $2\gamma = 32$ min. The sun has a time-variant radiation intensity I_s transmitting in P the heat flux $d\dot{Q}_{sp}$ over an area element dA_p. The central ray of the radiation cone forms an angle β_p with the perpendicular in P. The radiation cone is reflected in the direction of the focal plane of the paraboloid and the surface dA_p transmits to the receiver the energy

$$d\dot{Q}_{pr} = f_p \cdot \rho_p \cdot I_s(t) \cdot dA_p \qquad (1)$$

A differential area dA_c (Point C) on the inner surface of the receiver receives from this energy flux the part

$$d^2\dot{Q}_{pc} = \frac{\cos\beta_c \cdot \cos\beta_p}{\pi \cdot s_{pc}^2 \cdot \tan^2\gamma} \cdot f_p \cdot \rho_p \cdot I_s(t) \cdot dA_c \cdot dA_p \qquad (2)$$

In Fig. 6 s_{pc} is the distance between the points P and C and β_c the angle between the perpendicular in C and the connecting line between P and C. For further calculations the local solar flux $\dot{q}_s$ is primarily of importance. To determine this flux $d^2\dot{Q}_{pc}$ is related to the surface dA_c and formula (2) integrated over the surface of the paraboloid.

Because of the small aperture angle of the reflected solar radiation cone, a point C on the inside of the receiver can be reached only by a very limited area of the paraboloid surface. With acceptable approximation the values $\cos\beta_p$ = const, $\cos\beta_c$ = const, and s_{pc} = const can be assumed. Shape and size of the respective partial area under consideration on the paraboloid can only be determined analytically with a considerable amount of work. Therefore a numerical method of integration is proposed in [6].

The local solar insolation intensity $\dot{q}_s$ onto the virtual cylindrical wall with the tube cage diameter is thus known. The distribution over the tubes and the inner wall surface of the receiver depends on the ratio tube outer diameter over tube pitch.

Distribution of Infrared Cavity Radiation. During operation the inside of the receiver shows a nonhomogeneous temperature distribution. The partial areas under varying temperatures exchange considerable resulting heat fluxes through radiation. In particular, this mechanism transmits those heat fluxes incident onto the areas without tubing to the tubes. An area element dA_1 in the cavity radiates the heat flux

$$d^2\dot{Q}_{12} = \frac{\cos\beta_1 \cdot \cos\beta_2}{\pi s_{12}^2} \cdot I_1 \cdot dA_1 \cdot dA_2 \qquad (3)$$

onto another area element dA_2. Figure 7 shows the geometric properties. Areas dA_1 and dA_2 can be regarded as ring segments. dA_1 lies in the ceiling and dA_2 is situated on the virtual wall of the receiver with the diameter of the tube cage. The connecting line s_{12} forms the angle β_1 with the perpendicular in dA_1, angle β_2 in dA_2, respectively. The radiation intensity of element 1 is combined from

$$I_1 = \epsilon_1 \cdot C_s \cdot T_1^4 + \rho_{s,1} \cdot \dot{q}_{s,1} + \rho_{b,1} \cdot \dot{q}_{b,1} \qquad (4)$$

Figure 8 shows this connection. The area element with temperature T_1 radiates, therefore, the intensity $\epsilon_1 \cdot C_s \cdot T_1^4$ with ϵ_1 being the emissivity of the surface and C_s being the radiation number of a black body $C_s = 5.67 \times 10^{-8}$ W/m^{2}K^4. The sun produces the radiation intensity $\dot{q}_{s,1}$ over the area of which a portion $\rho_{s,1} \cdot \dot{q}_{s,1}$ is reflected. The cavity causes the radiation intensity $\dot{q}_{b,1}$ on dA_1 of which the portion $\rho_{b,1} \cdot \dot{q}_{b,1}$ is reflected. A direct integration of equation (3) over the entire cavity is not possible since the individual terms of equation (4) cannot be listed in the form of analytical functions. Therefore, a numerical approach is taken to determine the local radiation intensity $\dot{q}_b$ [5, 6].

Figure 5 shows the distribution of the heat fluxes penetrating the virtual wall in front of the tubes onto the tubes and the inner wall surface. To calculate these heat fluxes equation (3) has to be applied, integrated over the surfaces in question. The spatial character of the radiation phenomena leads to complicated equations. Integration of these equations is difficult. Therefore an approach for plane radiation has been chosen [8].

Solving equation (3) for the individual heat fluxes relating

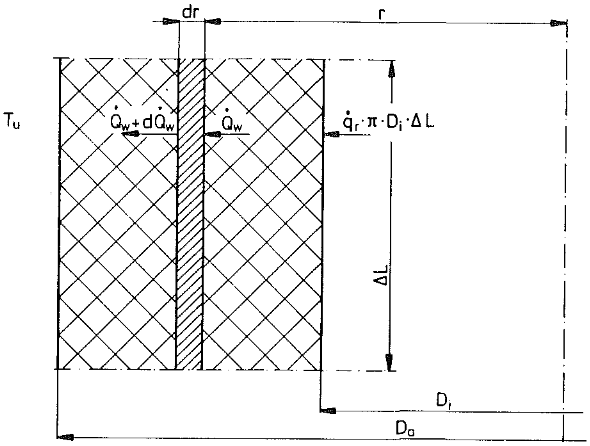

Fig. 9 Energy balance of a volume element inside the wall

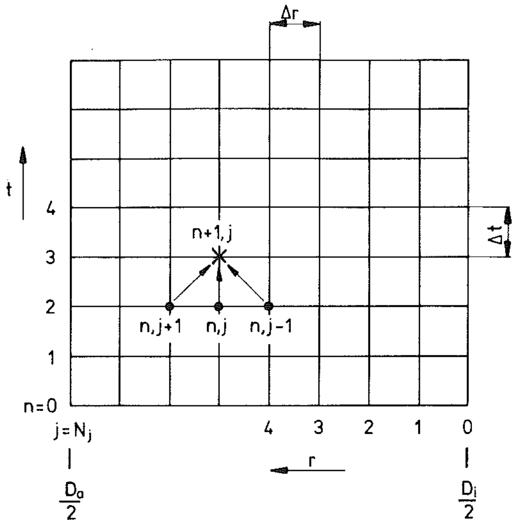

Fig. 10 Discretization scheme for the wall temperatures

them to the respective receiving area results in mean heat fluxes that can be expressed in the form

$$\dot{q}_2 = F_{12} \cdot I_1 \tag{5}$$

The subscript 1 stands for the emitting and 2 for the receiving surface. F_{12} is the respective radiation exchange factor. These exchanges are calculated according to [8]. The exchange factors contain all geometric units. Assuming a constant value for the radiation intensity the emitting surface permits the separation into radiation exchange factor and intensity. These simplifications permit calculating the resulting heat fluxes on the surfaces of the tubes and inner wall surface. Relating the heat fluxes presented in Fig. 5 to the respective areas, one receives the resulting heat fluxes for the surfaces of the tubes

$$\dot{q}_r = F_{sr} \cdot \dot{q}_s + F_{br} \cdot \dot{q}_b + F_{rr} \cdot \dot{q}_{rr} + F_{wr} \cdot \dot{q}_{wr} - C_s \cdot T_r^4 \tag{6}$$

and the surface of the wall

$$\dot{q}_w = F_{sw} \cdot \dot{q}_s \cdot \alpha_{ws} + F_{bw} \cdot \dot{q}_b \cdot \alpha_{wb} + F_{rw} \cdot \dot{q}_{rr} \cdot \alpha_{wb} - \epsilon_{wb} \cdot C_s \cdot T_{w,i}^4 \tag{7}$$

These resulting heat fluxes have to be transferred to or removed from the internal parts of the components through heat conduction. The subscripts used provide information about the direction of these heat fluxes. s stands for the sun, b for cavity radiation, r for tube or, generally, reradiation, respectively, and w for the wall. T_r is the temperature of the exterior tube surface and $T_{w,i}$ the temperature of the inner wall surface. The reflection of the tube surface has been neglected. This would not be permissible for ceramic wall surfaces; it is furthermore necessary to distinguish between absorption for solar α_{ws} and infrared radiation α_{wb}. By the same method the intensity of radiation $\dot{q}_{ab}$ of the tube cage can be found through the reradiation of the tubes and wall surface. In total they lead to the radiation flux $\dot{q}_b$.

Temperature Field in the Receiver Wall

Due to the symmetric radiation around the axis of rotation of the paraboloid into the receiver, a symmetric temperature distribution around the axis of rotation along the inside of the receiver takes place. The varying shading and insolation of the wall surface caused by the tubes leads to a periodic temperature field in tangential direction. The amplitude depends on the chosen tube pitch and the distance between the wall and the tubes. In general this dependence can be neglected. The temperature gradients along the longitudinal axis are approximately two magnitudes smaller than the radial gradients. For the calculations of the heat conduction and the temperature field inside the wall, the receiver is therefore divided axially into several segments of length ΔL. The heat conduction inside the wall is investigated in each of these segments one dimensionally and in the radial direction. Figure 9 shows a cross section through such a segment of the wall. The energy balance of a designated volume element

$$\frac{\partial}{\partial t} dE_w = \dot{Q}_w - (\dot{Q}_w + d\dot{Q}_w) \tag{8}$$

leads to the well-known partial differential equation of one-dimensional nonstationary heat conduction after inserting heat fluxes and geometric values

$$\frac{\partial T_w}{\partial t} = \frac{\lambda_w}{\rho_w \cdot c_w} \cdot \left[\frac{1}{r} \cdot \frac{\partial T_w}{\partial r} + \frac{\partial^2 T_w}{\partial r^2} \right] \tag{9}$$

Next to the initial condition this differential equation requires two spatial boundary conditions which must not contain more than first-order derivatives. The boundary conditions can easily be achieved via the heat transfer relations on the surfaces. It admits for the outer surface

$$\lambda_w \left. \frac{\partial T_w}{\partial r} \right|_{r=\frac{D_a}{2}} = -\alpha_a \cdot \left(T_w \Big|_{r=\frac{D_a}{2}} - T_u \right) \tag{10}$$

and for the inner, irradiated wall surface

$$\lambda_w \left. \frac{\partial T_w}{\partial r} \right|_{r=\frac{D_i}{2}} = -[F_{sw} \cdot \dot{q}_s \cdot \alpha_{ws} + F_{bw} \cdot \dot{q}_b \cdot \alpha_{wb} + F_{rw} \cdot \dot{q}_{rr} \cdot \alpha_{wb}] + \epsilon_{wb} \cdot C_s \cdot T_w^4 \Big|_{r=\frac{D_i}{2}} \tag{11}$$

The boundary condition for the inner wall surface (equation (11)) cannot be given analytically. Therefore no definite equations for the constants in the solution of equation (9) can be provided. Instead, a numerical solution using an explicit single-step difference formula is conducted. The partial derivatives are replaced by forward difference formulae in the direction of time and central difference formulae in the radial direction.

Figure 10 shows the spatial and time discretization scheme. On the abscissa the regular discretization of the receiver wall in equal spatial steps Δr is recorded. The ordinate is identical with the direction of time and also divided into equal steps Δt. Starting from the given temperature distribution at time step n over all points j in the radial direction one obtains the temperatures at time step $n+1$ from the difference equation

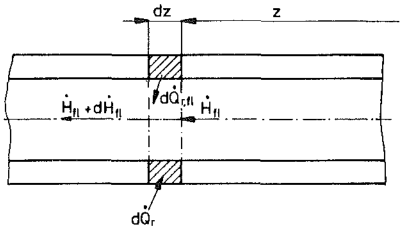

Fig. 11 Heat transfer to the working fluid

$$T_w^{n+1,j} = T_w^{n,j} + \Delta t \bullet \frac{\lambda_w}{\rho_w \bullet c_w} \bullet \left[\frac{T_w^{n,j+1} - 2 \bullet T_w^{n,j} + T_w^{n,j-1}}{\Delta r^2}\right] \tag{12}$$

Since $\Delta r / r \ll 1$ the first-order derivative in space was neglected while deriving the difference equation from equation (9). As shown in Fig. 10 equation (12) only yields the temperatures inside the wall. The surface temperatures are obtained using the boundary conditions

$$T_w^{n+1,N_j} = \frac{\lambda_w \bullet T_w^{n+1,N_j-1} + \alpha_a \bullet \Delta r \bullet T_u}{(\lambda_w + \alpha_a \bullet \Delta r)} \tag{13}$$

for the outer wall surface ($r = D_a/2$) and

$$(T_w^{n+1,0})^4 + \frac{\lambda_w}{\Delta r \bullet \epsilon_{wb} \bullet C_s} \bullet T_w^{n+1,0} = \frac{1}{\epsilon_{wb} \bullet C_s} \Big[F_{sw} \bullet \dot{q}_s \bullet \alpha_{ws}$$
$$+ F_{bw} \bullet \dot{q}_b \bullet \alpha_{wb} + F_{rw} \bullet \dot{q}_{rr} \bullet \alpha_{wb} + \frac{\lambda_w}{\Delta r} \bullet T_w^{n+1,1}\Big] \tag{14}$$

for the inner-irradiated-wall surface. Equation (14) requires an iteration because of the term T_w^4.

Heat Transfer to the Working Fluid

This model is aimed to simulate time-dependent processes where the dynamic properties of the receiver have a considerable influence on the behavior of the whole gas turbine plant. In this context the heat capacity of the fluid can be neglected. The flow speed of the medium is so high that a change in wall temperature during the passage of a fluid particle through the tubes can be neglected. Furthermore, the axial heat transfer inside the tube and in the working fluid can be neglected. The energy balances of tube and working fluid for the volume elements shown in Fig. 11 give

$$\frac{\partial}{\partial t} dE_r = d\dot{Q}_r - d\dot{Q}_{rfl} \tag{15}$$

and

$$\frac{\partial}{\partial t} dE_{fl} = 0 = \dot{H}_{fl} + d\dot{Q}_{rfl} - (\dot{H}_{fl} + d\dot{H}_{fl}) \tag{16}$$

Using equation (6) and expressing the energy fluxes with the help of geometric and physical data one obtains the system of differential equations

$$\frac{\partial T_r}{\partial t} = \frac{4}{\rho_r \bullet c_r \bullet (d_a^2 - d_i^2)} \bullet [(F_{sr} \bullet \dot{q}_s + F_{br} \bullet \dot{q}_b$$
$$+ F_{rr} \bullet \dot{q}_{rr} + F_{wr} \bullet \dot{q}_{wr} - C_s \bullet T_r^4) \bullet d_a$$
$$- \alpha_i \bullet (T_r - T_{fl}) \bullet d_i] \tag{17}$$

and

$$\frac{\partial T_{fl}}{\partial z} = \frac{\pi \bullet d_i \bullet \alpha_i}{\dot{m}_{fl} \bullet c_{p,fl}} \bullet (T_r - T_{fl}) \tag{18}$$

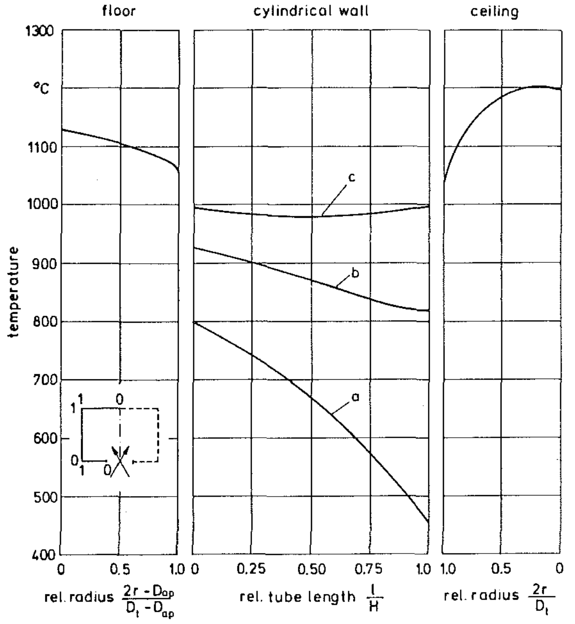

Fig. 12 Stationary temperature distribution inside the cavity: (*a*) temperature of the working fluid; (*b*) tube temperature; (*c*) inner wall temperature

An analytical solution of this system of differential equations is again not possible because the time dependence of the insolated energy cannot be given analytically. Therefore a numerical solution has to be used. Replacing the derivatives with the forward formula in spatial and time direction leads to the explicit formulae

$$T_r^{n+1,j} = T_r^{n,j} + \Delta t \bullet \frac{4}{\rho_r \bullet c_r \bullet (d_a^2 - d_i^2)} \bullet [(F_{sr} \bullet \dot{q}_s$$
$$+ F_{br} \bullet \dot{q}_b + F_{rr} \bullet \dot{q}_{rr} + F_{wr} \bullet \dot{q}_{wr}$$
$$- C_s \bullet (T_r^{n,j})^4) \bullet d_a - \alpha_i \bullet (T_r^{n,j} - T_{fl}^{n,fl}) \bullet d_i] \tag{19}$$

and

$$T_{fl}^{n,j+1} = T_{fl}^{n,j} + \Delta z \bullet \frac{\pi \bullet d_i \bullet \alpha_i}{\dot{m}_{fl} \bullet c_{p,fl}} \bullet (T_r^{n,j} - T_{fl}^{n,j}) \tag{20}$$

The course of the calculation is now as follows: The temperature distribution inside the tube wall at time step n is known; in the beginning at $t = 0 \mathrel{\hat{=}} n = 0$ because of the initial temperature distribution. This allows us to calculate the temperature of the working fluid over the tube length. The tube wall temperature distribution for time step $n+1$ can then be obtained from equation (19).

Results

A prerequisite for the simulation of a nonstationary operation is the temperature distribution as initial condition for the numerical calculation. The present case offers the stationary load of the receiver at the design point.

Figure 12 shows the characteristic temperature distribution inside the receiver of the reference plant under full-load condition. The figure contains three parts corresponding to the area floor, cylindrical wall, and ceiling. Abscissae have coordinates related to the radial dimension of the floor, the ceiling, and the height of the cylindrical wall, respectively. The floor has the coordinate 0 at the edge of the aperture and coordinate 1 at the tube cage diameter. The cylindrical wall area has its coordinate 0 at the edge of the floor connection and coordinate 1 at the link point to the ceiling. The fluid flows against this coordinate direction from 1 to 0. On the ceiling, coordinate 1 lies on the tube cage diameter and 0 in the receiver axis. The figure shows the temperatures of the working fluid (*a*), the tube wall (*b*), and the inner wall surface (*c*). As the

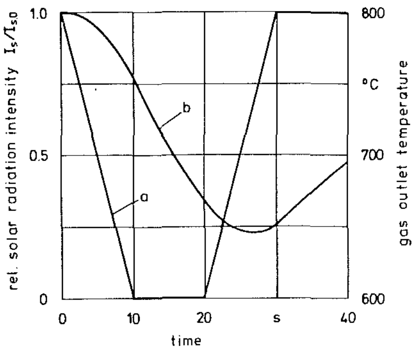

Fig. 13 Solar radiation intensity and gas outlet temperature: (*a*) solar radiation intensity; (*b*) gas outlet temperature

receiver has tubes only in the area of the cylindrical wall, tube and working fluid temperatures only appear in the center part of the figure. In accordance with the cycle layout the working fluid heats up from 454°C to 800°C when passing through the tubes. The mean tube temperature is 819°C at the inlet of the fluid and 925°C at the outlet. The inner wall area has a temperature of 1127°C at the edge of the aperture, decreasing toward the outside to the tube cage to 1054°C. The wall temperatures here are significantly lower due to the partial shading of the cylindrical wall by the tubes. With 990°C at the outlet of the fluid and 994°C at the inlet point the wall temperatures are only as much higher than the respective tube temperatures as is necessary to transfer the irradiated energy to the tubes. On the ceiling the wall surface heats up to approximately 1200°C.

The insulation of the receiver consists in this case of a highly reflective material. The wall temperatures are comparatively low, since a significant part of the irradiated solar energy is transmitted to the tubes by reflection only. This receiver, therefore, reacts very fast to changes of the solar radiation.

For demonstrating the workability of the proposed method a cloud passage was chosen from the possible nonstationary operating conditions. This cloud passage can be calculated disregarding the gas turbine because the power deficit of the receiver is covered by the combustion chamber within the cycle. The gas turbine remains in stationary condition.

Figure 13 shows the solar radiation intensity on the paraboloid related to the initial value of 900 W/m^2 over a time interval of 40 s (curve *a*). The intensity decreases from the initial value 1.0 in 10 s to 0, remains there for 10 s and returns within 10 s to the original value. In order to convey a first impression of the dynamic behavior of the receiver the gas exit temperature (curve *b*) has been added to Fig. 13. This temperature is the decisive parameter for the gas turbine. The fluid temperature reaches its lowest value of 646°C after approximately 26 s and then increases again, corresponding to the general heating up of the receiver. The initial value of 800°C is not achieved again during the interval considered. This result shows very clearly the importance of the dynamic behavior of a receiver when considering the time-dependent behavior of such a plant. In a merely solar-fired gas turbine the power output would be subjected to significant changes due to the course of gas temperature. An adaptation of the load requirements would be necessary in the case mentioned before. The power deficit of the receiver is taken up by the combustion chamber as mentioned previously; the plant continues running with constant turbine inlet temperature and thus constant power output.

The time behavior of the gas outlet temperature is caused by the interaction of the heat storing components of the receiver. Figure 14 gives an impression of these phenomena. The same representation as in Fig. 12 is chosen. Due to the many curves

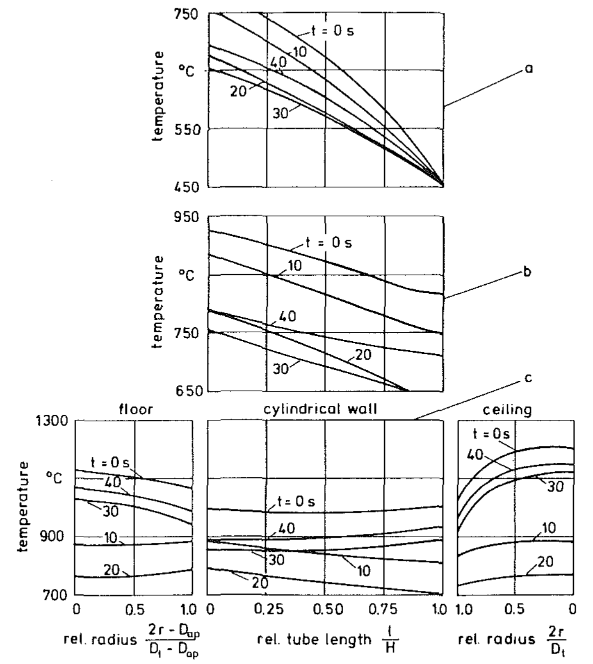

Fig. 14 Temperature distribution inside the cavity receiver: (*a*) gas temperature; (*b*) tube temperature; (*c*) inner wall temperature

the representation of the gas temperature (*a*), the tube temperature (*b*), and the inner wall temperature (*c*) are separated. In addition to time $t = 0$ (identical with the stationary temperature distribution in Fig. 12) time steps 10, 20, 30, and 40 seconds are listed. Noticeable is the strong decrease in wall surface temperatures in the areas without tubing (floor, ceiling) and on the whole the tendency to a uniform distribution of the overall temperatures (floor, cylindrical wall, ceiling). The low heat conductivity of the insulation material chosen for the walls is responsible for these phenomena. The heat stored in the interior parts of the walls cannot come out within a short period of time.

Conclusion

Based on a concept for the utilization of solar energy to produce electric energy, a method to calculate the nonstationary behavior of the solar receiver was presented and results given. The receiver is part of a reference plant. Cycle diagram and layout parameters have been shown. In the investigation it was assumed that the power deficit due to the dynamic behavior of the receiver is covered by the combustion chamber without time delay. Dynamic repercussions of the gas turbine to the receiver can be neglected. In the explanation of the receiver model used special emphasis has been given to the representation of the radiation exchange phenomena. The system of equations derived cannot be solved analytically so that a numerical approach had to be chosen.

The usefulness of the method was proven by a simulation. Starting from full-load operating condition a cloud passage was calculated and the development of the temperatures inside the receiver shown. The results demonstrate that the receiver is of importance to the plant behavior and cannot be neglected. The choice of the wall material has a considerable influence to the dynamic behavior of the receiver. The method presented is capable of simulating the nonstationary behavior of a solar cavity receiver. The computer program was established in such a way that it can be combined with other computer code to form a simulation program for an entire plant.

References

1 Lucas, J. W., and Marriott, A. T., "Solar Parabolic Thermal Power Systems, Technology and Applications," 14th IECEC Meeting, Boston, Aug. 1979.

2 Bammert, K., Simon, M., and Sutsch, A., "Large Parabolic Dish Collectors With Gas Turbines," *Atomkernenergie/Kerntechnik*, Vol. 38, 1981, pp. 257-267.

3 Sutsch, A., "Comparison Between Heliostat-Tower Concept and Large Parabolic Dish Collectors for Solar Thermal Power Plant," Institute for Computer-Assisted Research in Astronomy, Observatory, Alterswil, Switzerland, May 1980.

4 Bammert, K., Hegazy, A., and Seifert, P., "The Solar Flux Distribution in Cavity Receivers With Parabolic Dish Collector" [in German], *Atomkernenergie/Kerntechnik*, Vol. 40, 1982, pp. 145-154.

5 Bammert, K., and Seifert, P., "The Design of Receivers of Solar Heated Gas Turbines" [in German], VDI-Forschungsheft 620, 1983, pp. 1-48.

6 Bammert, K., and Hegazy, A., "Optimization of Solar Heated Cavity Receivers With Parabolic Dish Collectors" [in German], VDI Progress Report, Series 6, No. 160, 1984, pp. 1-158.

7 Bammert, K., Lange, H., and Seifert, P., "Part-Load Behavior of Fossil-Fueled and Solar-Heated Gas Turbine Plants," *International Journal of Turbo & Jet Engines*, Tel Aviv, Israel, Vol. 1, 1984, pp. 301-312.

8 Pich, R., "The Theoretical Determination of Temperatures in the Walls of Combustion Chambers" [in German], *Energie*, Vol. 15, 1963, pp. 402-411.

T. J. Retka
Account Manager,
Gas Turbine Systems,
Donaldson Company, Inc.,
Minneapolis, MN 55440

G. S. Wylie
Operations Supervisor,
West Sak Pilot Project,
Arco Alaska, Inc.,
Anchorage, AK 99510

Field Experience With Pulse-Jet Self-Cleaning Air Filtration on Gas Turbines in an Arctic Environment

This paper discusses the results of continuous duty operation of automatic self-cleaning air filtration systems on a gas turbine application during a winter season in a North Slope Alaska arctic environment where equipment is subjected to extremely low ambient temperatures, ice fog, and blowing snow. The effects of wind direction, temperature change, and filter installation configurations relative to filter performance are discussed. Recommendations for setup and operation of self-cleaning air filters in cold weather and arctic environments are presented.

Introduction

The technical literature [1, 2] and turbine industry publications have in the past presented information relative to the performance of pulse-jet self-cleaning air filtration systems on gas turbine applications in high dust concentration desert environments. In this type of environment, it has been thoroughly demonstrated that pulse-jet automatic self-cleaning systems have provided high efficiency maintenance-free air filtration at a relatively low system pressure drop.

However, since 1975 it has been recognized by certain individuals closely associated with the design, selection, operation, and maintenance of gas turbine air filtration equipment that the pulse-jet self-cleaning air filtration system is a highly effective and desirable filtration device for cold weather gas turbine applications. It has provided the gas turbine with inlet air protection from a variety of air quality hazards present in cold weather areas such as blowing snow, hoarfrost, and ice fog [3]. It is interesting that the first pulse-jet self-cleaning air filtration system applied to a commercial gas turbine anywhere in the world was applied to a cold weather application (Solar Turbines, Inc. Saturn gas compressor set, Union Oil application, Kenai, Alaska, 1976).

Since 1976, pulse-jet self-cleaning air filtration systems have been applied to an extremely high percentage of gas turbine applications where hazards of blowing snow, hoarfrost, and ice fog are expected to be encountered. Industry sources estimate that at present over 800 gas turbines [4] are equipped with self-cleaning filters in cold weather environments (those areas in which blowing snow, hoarfrost, and ice fog are expected to be encountered at least once annually).

With a large population of gas turbines equipped with pulse-jet self-cleaning air filters, the technical literature has lacked a published study on performance and operational details of these filters in cold weather locations. Donaldson Company, Inc., in cooperation and in association with Arco Alaska, Inc., closely monitored the performance of two self-cleaning filters during the period 11/21/84 to 7/2/85. The data collected provide interesting and informative details relative to the performance of pulse-jet self-cleaning air filtration systems for gas turbines in an arctic environment, and have a high degree of relevance for nonarctic but nonetheless cold weather areas.

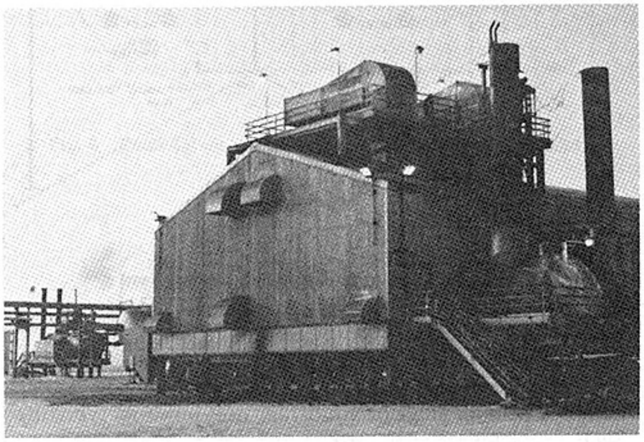
Fig. 1 Donaldson TTD00-4019 pulse-jet self-cleaning air filters (2) at Arco West Sak facility

Arctic Application

Arco Alaska, Inc. operates a number of industrial-type gas turbines on the North Slope of Alaska just inland from Prudhoe Bay. These gas turbines are used as power sources for oil production activities including electric power generation, gas compression, water and crude oil pumping. Normal airborne contaminants (dust, salts, carbon, etc.) are of concern for gas turbine users on the North Slope. In addition, the arctic weather produces airborne moisture-related contaminants which must be dealt with. Prior to the introduction of pulse-jet air filters, the arctic installed gas turbines as used by Arco and other oil companies had historically suffered from several problems associated with poor air quality when faced with severe blowing snow, hoarfrost, and ice fog. These problems

---

Contributed by the Gas Turbine Division of The American Society of Mechanical Engineers and presented at the 31st International Gas Turbine Conference and Exhibit, Düsseldorf, Federal Republic of Germany, June 8–12, 1986. Manuscript received at ASME Headquarters January 24, 1986. Paper No. 86-GT-126.

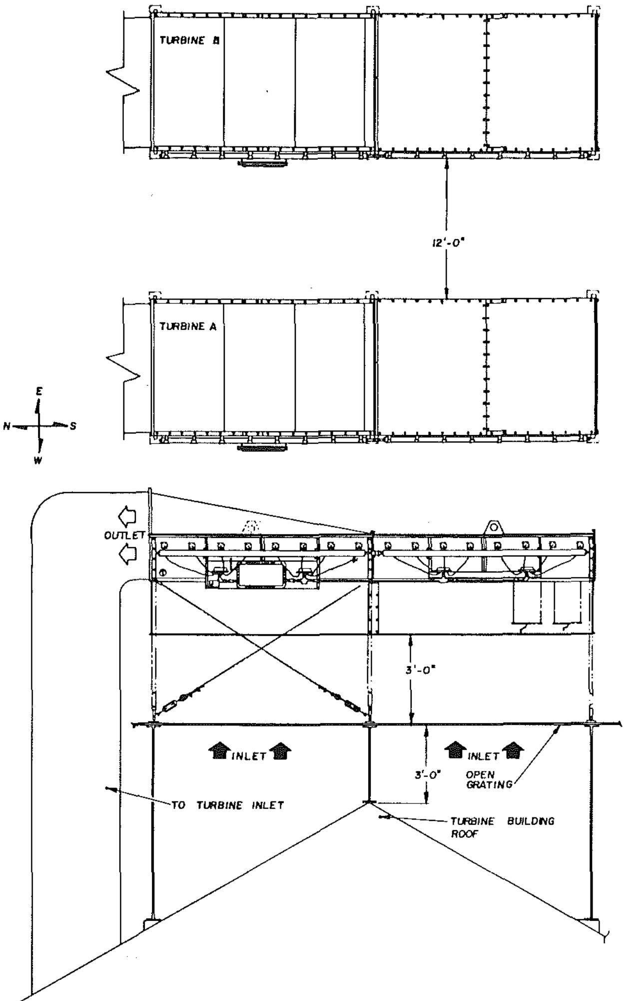

Fig. 2 Filter/turbine building arrangement

have included turbine foreign object damage due to ice ingestion, and excessively high inlet restrictions due to snow/ice buildup on single stage or multistage non-pulse-jet type filters. Such problems can jeopardize and limit oil production activities as well as increase maintenance costs. Gas turbine air inlet heating systems can prevent high inlet restriction buildup caused by severe blowing snow, hoarfrost and ice fog problems, but must be used with a high-efficiency filter downstream to arrive at an overall acceptable inlet filter system. In addition, in certain applications the horsepower losses that can accompany inlet heating are not attractive. The single-stage pulse-jet air filter provides the desired cold weather performance in a simpler, more economical fashion.

The arctic gas turbine pulse-jet filter application which was studied 11/21/84 to 7/2/85 was at Arco Alaska, Inc.'s West Sak Pilot Project facility. West Sak is located approximately 40 miles west of Prudhoe Bay, Alaska and approximately 6 miles from the Kuparuk Base Camp. The two gas turbines involved were Solar Turbines, Inc. Centaur electrical generator sets developing 2800 kW each. The gas turbines each require 30,000 cfm of combustion air. The pulse-jet self-cleaning air filters involved were Donaldson model TTD00-4019. The filters were located side by side on a roof top mezzanine over the turbine building as illustrated in Fig. 1. Overall height above grade was 30–35 ft. The gas turbines and air filters were first operational in July 1984.

TTD00-4019 Filter Design Parameters

Airflow: 30,000 cfm

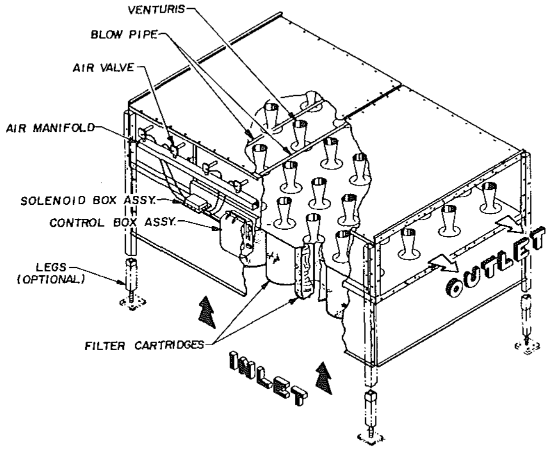

Fig. 3 Basic pulse-cleaning filter module

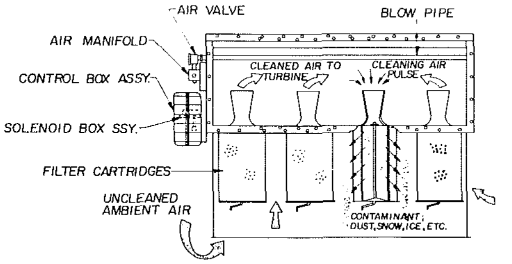

Fig. 4 Operational components of a pulse-cleaning filter module

Total number of cylindrical filter cartridges: 64
Overall size of system:
  Length: 20′4-1/8″
  Width: 6′10-15/16″
  Height: 10′9-15/16″
Initial clean ΔP: 0.7 in. wg (across filter)
Velocity through the filter media: 2.4 ft/min

Figure 2 presents an illustration of the air filter/turbine building arrangement.

Principle of Operation

Details on the principle of pulse-jet self-cleaning air filter operation have been previously presented and are generally well known, but are presented here as they relate to the arctic cold weather application.

The concept of the pulse-jet self-cleaning air filter is simple. High-efficiency filter elements or cartridges are automatically cleaned when they become loaded with contaminants (snow, ice, etc.).

The system operation is described here with reference to a basic "module" or collection of high-efficiency filters. Figure 3 illustrates a typical module consisting of 32 cartridges.

The high-efficiency cylindrical filter cartridges are attached to the bottom of a horizontal plate and hang vertically downward. Above each filter cartridge, in the clean air plenum, is a venturi flow nozzle. During normal operation, ambient air flows upward through the venturi and finally to the turbine. This flow path is depicted in Fig. 4.

Up to this point, the device is operating basically as just a high-efficiency filter. Each cartridge is rated for 450–550 cfm at an initial system pressure drop of 0.7–1.0 in. of water, hence the total number of cartridges required for any installation is controlled by this operating range. The system pressure drop is primarily due to the exit restriction in the venturi above the filter element. The pressure drop across the filter element itself is on the order of 0.2–0.4 in. water. Skirts are suspended around the exposed sides of the cartridges to protect them from damage and to force the incoming air to travel upward.

As the contaminants build up on the surface of the cylindrical cartridges, the pressure drop across the cartridges will continually increase. When the pressure drop reaches a preset limit (typically 0.5–1.0 in. of water above the "new and clean" initial pressure drop) the automatic pulse-cleaning sequence is activated.

A pressure switch senses that this upper limit has been reached and activates the timer/sequencer. The timer/sequencer signals the solenoid valve to open, releasing the pressure holding the pneumatic air valve closed. The opening of the air valve (typically for only 50–100 ms) allows a "blast" of compressed air (80–100 psig) to leave the air manifold and proceed out through the blow pipe. Above each venturi is an outlet hole in the blow pipe. This "blast" of compressed air exits through the hole, enters the venturi and effectively "closes off" the flow through the cartridge for a fraction of a second. The compressed air pressure wave continues down into the cartridge and then radially outward, blowing the accumulated contaminant (snow, ice) off the cartridge. At air flows of 450–550 cfm per filter cartridge, the velocity through the filter media is on the order of 2.4 to 2.9 feet per minute. Due to this low "velocity" of the entering air flow, the filter media "face loads." This enables the compressed air pressure wave from the cleaning pulse to effectively remove the accumulated particulate. Some of the finer particulate does reentrain on adjacent filter cartridges. The tendency is for the contaminant to agglomerate and to blow off in particulates large enough to fall down, through the low velocity updraft, to the ground below. In the 32-element module illustrated in Fig. 3, a row of four cartridges is pulsed at one time. Then 10–20 s later the timer/sequencer chooses another row of cartridges and the pulse-cleaning procedure is repeated. The timer/sequencer continues to sequence the cleaning operation throughout the elements until the overall pressure drop reaches a preset lower limit, at which time the cleaning process ceases until called upon again by a high-pressure drop reading. The number of elements cleaned at any instant and the timer interval between are chosen so that no significant distortion of the airflow is presented to the turbine.

Data Collected

After initial inspection of the air filter equipment and gas turbine installation at West Sak and with assurances that all equipment was operationally correct, the TTD00-4019 air filter control systems were adjusted as follows.

Air Filter Control Settings (Both Turbine A and Turbine B)

Program control on-time	50 m-s
Program control off-time	10 s
Start clean set point	1.5 in. wg
Stop clean set point	1.3 in. wg

With this setup the air filters would initiate pulse-jet self-cleaning when inlet restriction reached 1.5 in. wg and would continue until inlet restriction was lowered to 1.3 in. wg.

Starting November 21, 1984 and running up to July 2, 1985, Arco personnel collected the following data:

1 PAS (in. wg) – Air filter inlet restriction as read in control room (Turbine A)

2 PBS (in. wg) – Air filter inlet restriction as read in control room (Turbine B)

3 PAA (in. wg) – Actual air filter inlet restriction as read on air filter outdoors (Turbine A)

4 PBA (in. wg) – Actual air filter inlet restriction as read on air filter outdoors (Turbine B). Note: PAS and PBS inlet restriction levels measured (0.1–0.4 in. wg) higher than PAA and PBA actual inlet restrictions at any point in time due to positive pressurization of instrument room which was ventilated.

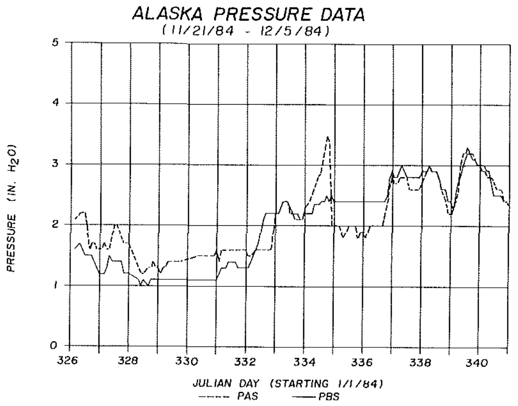

Fig. 5 Pulse-jet air filter inlet restrictions 11/21/84 to 12/5/84

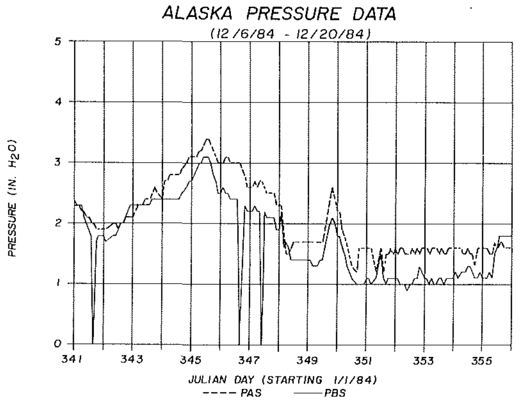

Fig. 6 Pulse-jet air filter inlet restrictions 12/6/84-12/20/84

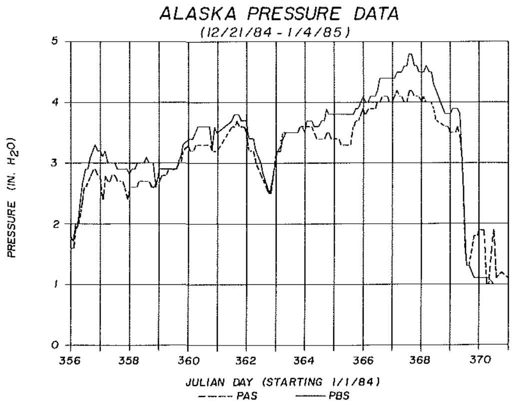

Fig. 7 Pulse-jet air filter inlet restrictions 12/21/84-1/4/85

5 Meteorological data including:
- (*A*) Ambient air temperature
- (*B*) Wind chill
- (*C*) Wind speed
- (*D*) Wind direction
- (*E*) Ceiling height and condition
- (*F*) Ground visibility distance and condition

The PAS, PBS, PAA, and PBA data were collected on a multidaily basis (maximum of 12 times daily/minimum of 4 times daily). Meteorological data were collected by Arco once daily at 6:00 A.M. Additional meteorological data on a more frequent basis (6–12 times daily) were collected from sources at nearby Kuparuk Airport (6 miles distance).

Arco personnel observed the performance of the air filters with walk-by inspections on a regular basis as part of the standard operational activities.

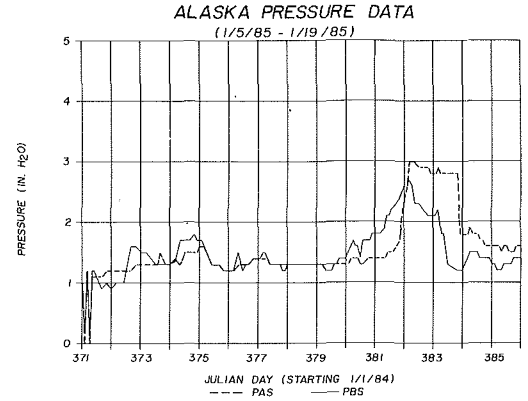

Fig. 8 Pulse-jet air filter inlet restrictions 1/5/85-1/19/85

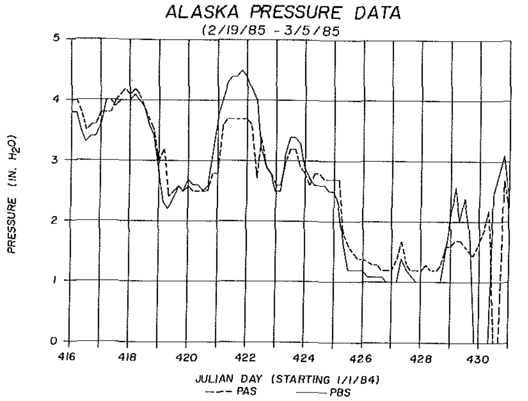

Fig. 11 Pulse-jet air filter inlet restrictions 2/19/85-3/5/85

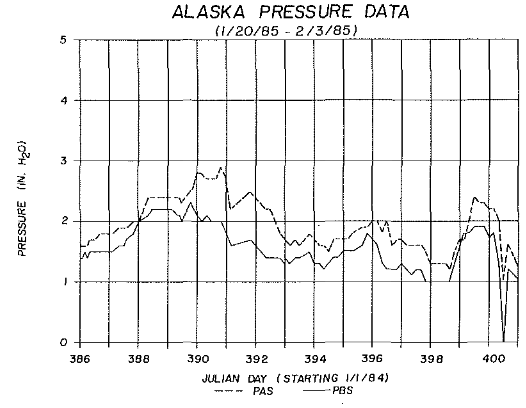

Fig. 9 Pulse-jet air filter inlet restrictions 1/20/85-2/3/85

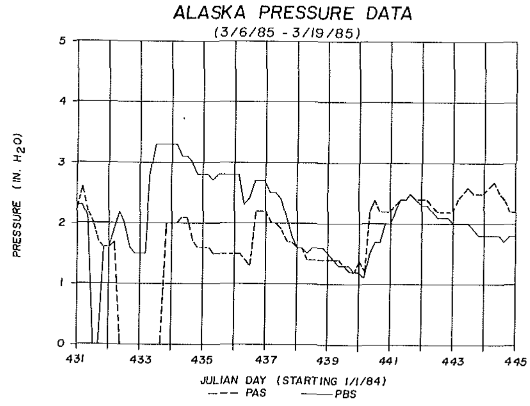

Fig. 12 Pulse-jet air filter inlet restrictions 3/6/85-3/19/85

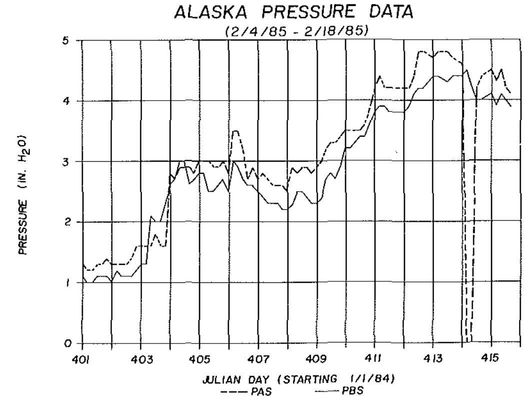

Fig. 10 Pulse-jet air filter inlet restrictions 2/4/85-2/18/85

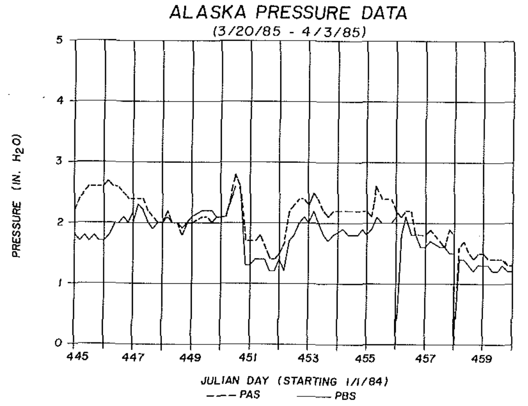

Fig. 13 Pulse-jet air filter inlet restrictions 3/20/85-4/3/85

The sum total of 223 days' worth of pressure data and meteorological data was loaded into a computer and the data compilation was subjected to tests for correlation and regression analysis at Donaldson Company's facility.

Results

Figures 5-19 present graphic records of air filter inlet restriction levels for both gas turbines at West Sak (PAS, PBS) for 15-day increments within the 223-day period 11/21/84 through 7/2/85. Note: Filter pressures which fall to zero (0) indicate intervals in which turbines were shut down.

Observations/Analysis

1 The weather was below freezing (<32°F) for the period 11/21/84 through 5/19/85. Lowest temperature encountered was −54°F. Lowest wind chill was −90°F. Data indicate that during the 11/21/84 through 5/19/85 period, filter restrictions were controlled:

(*a*) Below 2.0 in. wg more than 52 percent of the operational time

(*b*) Below 3.0 in. wg more than 81.6 percent of the operational time

(*c*) Below 4.0 in. wg more than 94 percent of the operational time

2 Analysis of the collected data indicates that:

(*a*) Air filter "A" spent 182,880 min in a pulse-cleaning mode

(*b*) Air filter "B" spent 138,240 min in a pulse-cleaning mode

(*c*) Each filter cartridge in filter "A" underwent 109,509 pulse-cleaning events

(*d*) Each filter cartridge in filter "B" underwent 82,778 pulse-cleaning events

3 Analysis and comparison of restriction levels versus meteorological data indicate that the highest inlet restriction

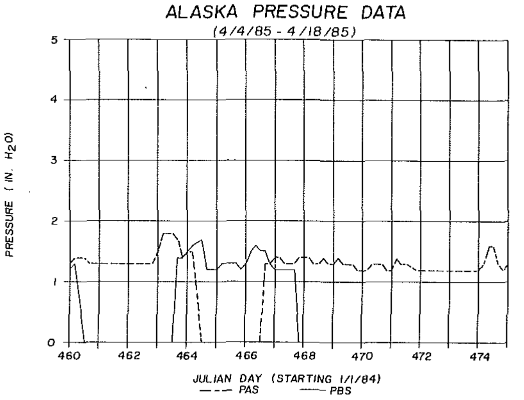

Fig. 14 Pulse-jet air filter inlet restrictions 4/4/85-4/18/85

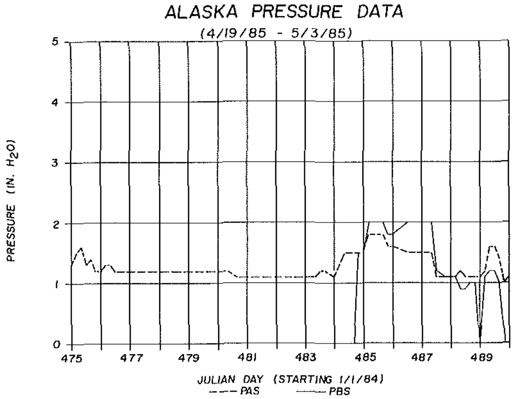

Fig. 15 Pulse-jet air filter inlet restrictions 4/19/85-5/3/85

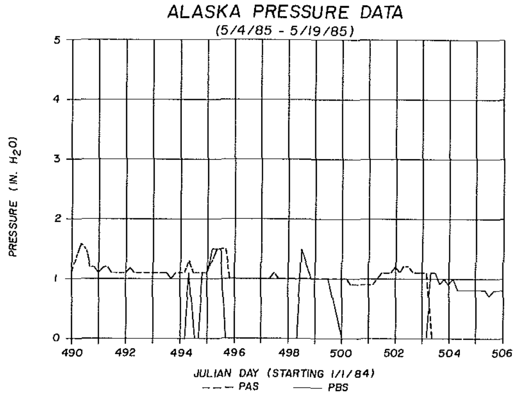

Fig. 16 Pulse-jet air filter inlet restrictions 5/4/85-5/19/85

levels occurred during periods of ice fog (fog at temperatures −15 to −40°F). The continued presence of ice fog resulted in escalating inlet restriction to maximum levels of 4.4 in. wg (actual). Increasing temperatures during ice fog conditions corresponded to decreasing air filter inlet restriction conditions.

4 The maximum filter inlet restriction recorded during the winter test period was 4.8 in. wg for PBS and PAS (actually 4.40 in. wg). This occurred for portions of just 3 days during the 223-day test period.

5 Relative to effects on pulse-jet air filters, ice fog was a more severe natural phenomenon to deal with than blowing snow. Ice fog produced faster increases in filter inlet restriction than did blowing snow.

6 Decreasing temperatures below the −15°F level generally produced increasing air filter inlet restrictions. This temperature condition was also consistent with the formation of ice fog or air ice crystals. Likewise, air temperature reductions of more than approximately 10°F in a short time period (less than 12 hr) at temperature levels down to −15°F corresponds to slightly increasing filter restrictions.

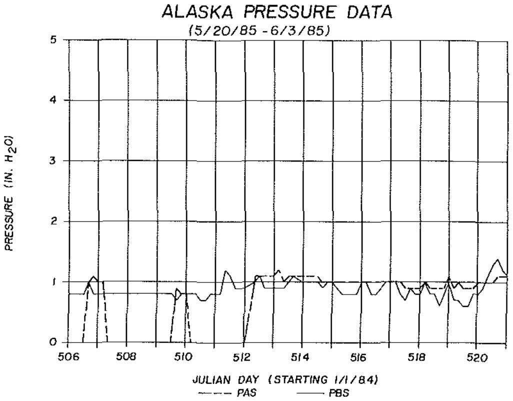

Fig. 17 Pulse-jet air filter inlet restrictions 5/20/85-6/3/85

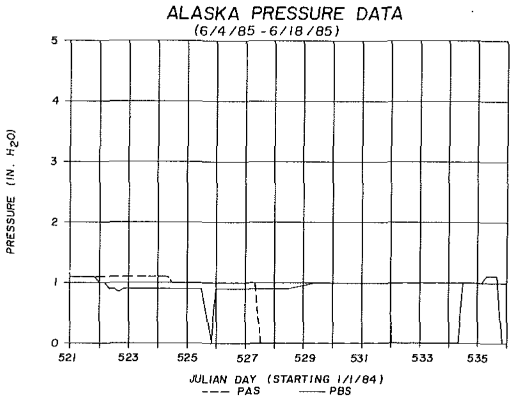

Fig. 18 Pulse-jet air filter inlet restrictions 6/4/85-6/18/85

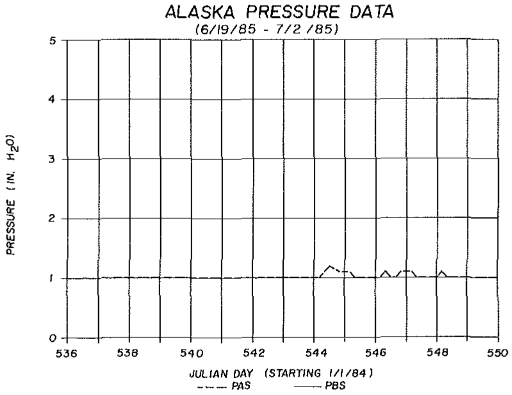

Fig. 19 Pulse-jet air filter inlet restrictions 6/19/85-7/2/85

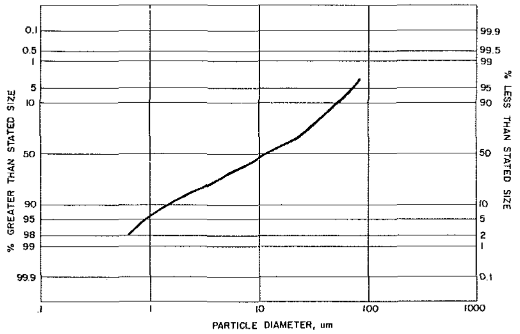

Fig. 20 Dust particle size from North Slope filter cartridge

7 Faced with severe blowing snow, the pulse-jet filters at West Sak experienced slowly escalating inlet restriction. However, the inlet restriction declined when less severe particulate contamination levels existed, even when temperatures remained extremely cold.

Table 1 Summary of filter cartridge media test

Cartridge	Tensile strength Dry	Tensile strength Wet	Permeability
Typical new	100 percent	100 percent	100 percent
Used cartridge No. 1	78 percent	73 percent	100 percent
Used cartridge No. 2	94 percent	84 percent	97 percent

8 There are strong indications from the data that descending air filter inlet restriction corresponded to improvement in ground visibility, which is consistent with reduced particulates (snow, ice) suspended in the air.

9 Increases in air filter inlet restriction are highly correlated with reduction in ground visibility (i.e., if ground visibility was 3 miles or less, pressure drop would generally increase). However, if conditions of limited ground visibility (<3 miles) were accompanied by a warming trend, air filter inlet restriction would generally decline.

10 From the data, it was apparent that in high wind blown snow conditions (wind velocity greater than 15 kt), that the downwind air filter operates at a higher inlet restriction than the upwind air filter (i.e., when wind is from NE, air filter "A" has higher inlet restriction than air filter "B"). Prevailing wind at West Sak is a 060 deg wind (approximately NE). It is believed that the mounting arrangement at West Sak produces a particulate settling area in the vicinity of the downwind air filter, which increases the particulate concentration in this area.

11 Ground winds of 15 kt and greater generally produce an increase in air filter restriction, which is consistent with an increased amount of wind-carried snow particulate and reduced ground visibility.

12 Increasing temperatures and clearing periods (i.e., from $-25°F$ to $0°F$) or simply clearing periods, corresponded to reductions in air filter inlet restriction levels. This owed to the pulse-jet filters' action in removing snow and ice during periods of light snow/ice particulate concentration levels.

13 Sublimation of snow and ice is probably responsible for declining inlet restriction below the lower set point of the pulse clean filter (i.e., 1.3 in. wg in the situation at West Sak).

Cartridge Condition

Two used filter cartridges were removed from filter unit B at West Sak by Arco personnel and returned to Donaldson Company laboratories for analysis of filter media.

Table 1 lists the resulting media characteristics on the used cartridges when compared against new cartridges. The results are presented as a percentage of expected values on new cartridges.

No media pin holes or pleat tip splits were evident during an inspection of the used cartridges. Cartridge liners had undergone some discoloration due to corrosion (nearby ocean waters).

Figure 20 shows the particle size distribution by mass of the dry dust contaminant collected on the analyzed filter cartridges. This particle size distribution, as expected, is smaller than that found in desert applications of the pulse-jet air filters. The dust loading on the inspected cartridges was also, as expected, very light averaging 11.12 g of dust per cartridge.

The chemical ingredients of dust collected on the filter cartridges consisted of silica, quartz, carbon, iron, and iron oxide.

Pulse-Jet Self-Cleaning Filter Modifications for Cold Weather

Several design features as employed by Arco Alaska should be considered for inclusion in cold weather applications of pulse-jet filters. These include:

1 Solenoid box heaters

2 Control box heaters or remote mounted control box to a heated area

3 Trace heating of manifolds, air valves, solenoid boxes

4 Trace heating of air lines to the pulse-jet filter

5 Stainless steel air lines between solenoid boxes and air valves

Further Recommendations

1 Because the pulse-jet air filter in cold weather will pulse clean for lengthy periods, it is essential that adequate compressed air be available. A dedicated air compressor for the pulse-jet filter is recommended.

2 Wind deflecting structures in the proximity of the pulse-jet air filter can negatively influence the ability of the pulse jet to remove blowing snow, ice, and hoarfrost. Higher inlet restrictions will result during adverse weather conditions. Structures which direct wind against the pulse-jet cartridge apparently impede self-cleaning by prompting more re-entrainment of snow and ice particles.

3 Filter elements will not be totally cleaned of snow and ice during operation in severe winter weather. However, because of the pulse-cleaning action, some portion of the media in the filter cartridge will remain open to accept air flow. Manual brushing of filter cartridges because of appearance of snow or ice should not be attempted. Media damage could result.

4 Wet or damp filter cartridges should never be installed in pulse-jet air filters at temperatures below 32°F. Formation of ice throughout the media surface due to this moisture will result in adverse performance of the pulse jet filter.

Conclusions

1 Arctic weather effects (ice fog, blowing snow) do increase the amount of airborne particulate which gas turbines would normally ingest without air filter protection. The pulse-jet self-cleaning filter operation is influenced both positively and negatively by arctic weather effects.

2 The pulse-jet self-cleaning filters controlled the gas turbine inlet restrictions at the West Sak facility within acceptable levels, for the duration of testing during the arctic winter. This included extended periods of extreme cold, blowing snow and ice fogs. The air filters provided high levels of filtration protection for the two gas turbines.

3 After 12 months of operation, the pulse-jet filter cartridges showed a somewhat diminished media strength from the new cartridge condition, but are projected to be adequately strong to operate for at least an additional 12 months in the arctic environment.

Acknowledgments

The authors gratefully acknowledge the assistance of Mr. Dennis Meyer, Information Systems Department and Mr. Gary Rocklitz of Computer Engineering, both of Donaldson Company. We appreciate the help of Arco West Sak operating and engineering personnel in the collection of the presented data. We thank the Arctic Environmental Information and Data Center at the University of Alaska for their assistance with weather data.

References

1 Neaman, R. G., and Anderson, A. W., "Development and Operating Experience of Automatic Pulse-Jet Self-Cleaning Air Filters for Combustion Gas Turbines," ASME Paper No. 80-GT-83.

2 Neaman, R. G., and Anderson, A. W., "Field Experience With Pulse-Jet Self-Cleaning Air Filtration on Gas Turbines in a Desert Environment," ASME Paper No. 82-GT-283.

3 U.S. Department of Commerce, "Glossary of Meteorology," R. E. Huschke, ed., 1959.

4 Donaldson Company, Inc., "Self-Cleaning Filter User List – March 15, 1985."

Wetness and Efficiency Measurements in L.P. Turbines With an Optical Probe As an Aid to Improving Performance

P. T. Walters
Central Electricity Research Laboratories,
Leatherhead, Surrey, United Kingdom

An absolute value for the wetness fraction in a partially condensed steam flow may be calculated from measurements of light transmission using the results of fundamental electromagnetic scattering theory. A probe is described that uses this principle for measuring radial wetness profiles in the final stages of L.P. turbines. Results are presented to show that the probe will provide reliable values for overall L.P. turbine efficiency and valuable diagnostic data on the performance of individual stages operating with wet or condensing flows.

Introduction

Developments in the CEGB have shown that substantial gains in efficiency can be achieved by retrofitting improved blading designs in older steam turbines. Such developments, however, have been hindered by the difficulties of establishing the efficiencies of the wet steam stages. For this purpose the information required is the enthalpy flux entering and leaving the section of the turbine under investigation which in turn necessitates the measurement of the wetness fraction of the steam.

It has been recognized for some time however that it should be possible to obtain this missing property for wet flows optically, since the optical characteristics of the submicroscopic droplets that make up the wetness are known exactly from Mie Scattering Theory [1].

On this basis an optical system was developed at CERL by the author [2] to obtain wetness and droplet size from measurements of spectral transmission. This was first used successfully to study the nucleation of wetness in steam expanded in Laval nozzles [3] and a miniature version installed in a traversing probe was subsequently tested in a full-size low-pressure (L.P.) turbine by Walters and Skingley [4].

This prototype instrument, however, was only partly successful since, although it demonstrated the potential of the technique for measuring real turbine flows, the results obtained were not considered to be sufficiently reliable in view of the relatively narrow spectral range of the optical system. A considerable amount of further development followed to overcome this problem, which principally involved redesigning the system that generates and supplies light to the probe head. This new version of the probe is now considered to be a viable instrument for measuring wetness in L.P. turbines. Results are presented to show that it will provide both reliable values for overall L.P. turbine efficiency and valuable diagnostic data on the performance of the individual stages operating with wet or condensing flows.

Optical Measurement of Wetness in Steam Flows

Obtaining the concentration of droplets in a wet flow from measurements of light transmission starts with the basic Bouguer transmission law

$$I = I_0 e^{-gt} \tag{1}$$

where I is the intensity of the beam at a point in the suspension which has decayed from an incident level I_0 after traveling a distance t, and g is the turbidity

$$g\left(\nu = \frac{1}{\lambda}\right) = C_n \frac{\pi t}{4} \int_0^\infty E(\nu, D) N_r(D) D^2 dD \tag{2}$$

In this expression $N_r(D)$ is the probability density distribution of the droplet diameter D and C_n is a concentration factor such that $C_n N_r(D)$ is the probable number of droplets occurring per unit volume in the size interval D to $D + dD$. The function E is the Mie extinction coefficient defined for transparent particles as

$$E = \frac{\text{Total light flux scattered by particle}}{\text{Light flux geometrically incident on particle}}$$

E is obtained from scattering theory as a unique function of the particle size parameter ($\alpha = \pi D/\lambda$) and has been evaluated for the refractive indices of most common species of liquid droplet by Penndorf [5].

Combining equations (1) and (2) provides the governing integral equation

$$g(\nu) = \frac{1}{t} \ln\left(\frac{I_0}{I}\right) = C_n \frac{\pi}{4} \int_0^\infty E(\nu, D) N_r(D) D^2 dD \tag{3}$$

Contributed by the Gas Turbine Division and presented at the Joint ASME/IEEE Power Generation Conference, Milwaukee, Wisconsin, October 20–24, 1985. Manuscript received at ASME Headquarters July 23, 1985. Paper No. 85-JPGC-GT-9.

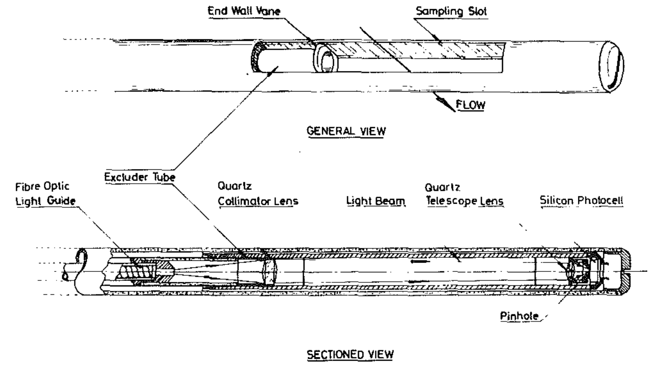

Fig. 1 Optical wetness probe

An inverse of equation (3) for j measurements $g_j(\nu)$ is obtained numerically by first defining the function

$$f(D) = \frac{\pi}{4} C_n N_r(D) D^2 \tag{4}$$

to reduce equation (3) to the linear system

$$g_j = \int_0^{D_\infty} E_j(D) f(D) dD \qquad (j = 1, \ldots, n) \tag{5}$$

where D_∞ is an arbitrary estimate for the upper limit of the droplet size range. Then, introducing the matrix notation

$$A_{ij} \equiv w_i E_{ij} \tag{6}$$

gives

$$\mathbf{g} = A\mathbf{f} \tag{7}$$

for which a stable inverse $\mathbf{f}^s$ is obtained using the Phillips–Twomey [6] inversion formula

$$\mathbf{f}^s = (A^T A + \gamma H)^{-1} A^T \mathbf{g} \tag{8}$$

Here, H is a smoothing matrix composed essentially of the fourth difference coefficients 1, -4, 6, -4, 1 (centered on the diagonal $H_{jj} = 6$) and γ is an undetermined parameter that controls the amount of smoothing induced to suppress the unwanted oscillations in f resulting from the ill-conditioning of equation (7). A more detailed account of inverting spectral turbidities of steam flow using equation (8) is given by Walters [7] but the procedure is essentially straightforward, since the matrix A can be set up directly from Penndorf's [5] tabulations of $E(\alpha)$ using weightings w_i (equation (6)) for trapezoidal quadrature. Moreover it has been found from analyzing many cases that for wet flow in turbines

$$D_\infty \simeq 2.4\, D_{32} \tag{9}$$

where D_{32} is the Sauter mean droplet diameter defined as

$$D_{32} = \int_0^{D_\infty} N_r(D) D^3 dD \Big/ \int_0^{D_\infty} N_r(D) D^2 dD \tag{10}$$

Now although this is neither an essential nor a critical assumption it simplifies considerably the determination of D_∞ and γ. An arbitrarily chosen D_∞ can be modified iteratively using equations (8) and (10) until the condition (9) is satisfied. It then only remains to find, by a few trials, the smallest value of γ that will provide a stable inverse.

The wetness fraction may then be calculated from the n elements of the numerical solution f by evaluating the suspended mass per unit volume

$$C_m = \frac{\pi}{6 v_f} C_n \int_0^{D_\infty} N_r(D) D^3 dD = \frac{2}{3} \sum_{i=1}^{n} f_i D_i \Delta D \tag{11}$$

where ΔD is the droplet size interval of the quadrature equation (7), giving the wetness Y finally as

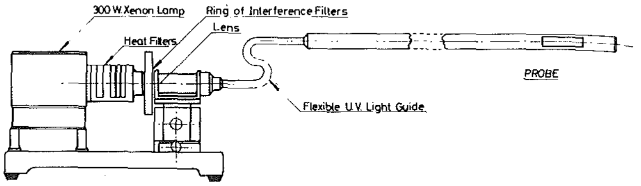

Fig. 2 Optical wetness probe light input unit

$$Y = C_m v_g / (1 + C_m v_g) \tag{12}$$

where v_f and v_g are the specific volumes of the liquid and gas phases at the local saturation pressure.

Finally, it should be noted from equations (3), (7), (8), and (11) that the amount of liquid water present in the flow C_m is calculated directly from its optical transmission. This is therefore an absolute measurement and its validity depends only on that of the Mie extinction kernel $E(\alpha)$, a fundamental result of electromagnetic theory. That this is indeed a valid basis for absolute measurements of real liquid droplets however is emphatically demonstrated by the experiments of Marshall et al. [8] and Dobbins and Eklund [9].

Description of the Optical Probe

The optical system for measuring the spectral transmission of wet steam flows is shown installed in the turbine probe in Fig. 1. Steam sampled in situ within the turbine flows transversely through a slot in the sensing head of the probe and the intensity of monochromatic light transmitted by this flow is detected by a photocell at the end of the probe axis. Transmission is measured using a tubular shutter which surrounds the optical system and may be extended along the sampling slot to exclude the flow from the light beam. The intensity then detected is the reference level I_0 which is attenuated by the wet flow, immediately after the excluder is withdrawn, to give the transmission I/I_0 at that particular wavelength. In this way errors resulting from drift in the signal strength or from contamination of the optical system are effectively eliminated and the accuracy of transmission values is limited (to approximately ± 1 percent) only by the signal-to-noise ratio of the detector. The end of the excluder carries a dummy end wall to ensure the smooth passage of the flow when the excluder is withdrawn to intermediate positions (also shown in Fig. 1) to provide a variable slot length. This extends the working range of the instrument considerably since the absolute level of ultraviolet (U.V.) transmission by very wet flows over the full 12.5 cm slot ($Y \geq 0.01$, $I/I_0 \leq 0.05$) is sometimes difficult to measure accurately. To align the sampling slot with the flow the probe is rotated about its axis with the excluder withdrawn to find the arc of minimum light transmission which extends by about 20 deg either side of the mean setting angle. Purge air is supplied to both ends of the slot to prevent steam from entering the optical system and to cool the photocell.

The optical system is optimized for operation with U.V. light since it is most difficult to generate and detect intensity at this end of the spectrum. All transmitting components are quartz, the photocell (Hamamatsu S1336-8BQ) is sensitive down to $\lambda = 200$ nm, and the aperture of the collimator lens is matched with that of the input fiber in blue light. At the receiving end of the system a high-aperture telescope lens is used to reduce the dead space at the end of the probe and a pinhole is located at its focal plane to intercept stray reflections from the interior of the excluder.

"Monochromatic" light is generated at a range of wavelengths in a separate unit shown in Fig. 2 by inserting a sequence of 12 narrow-band width interference filters into the

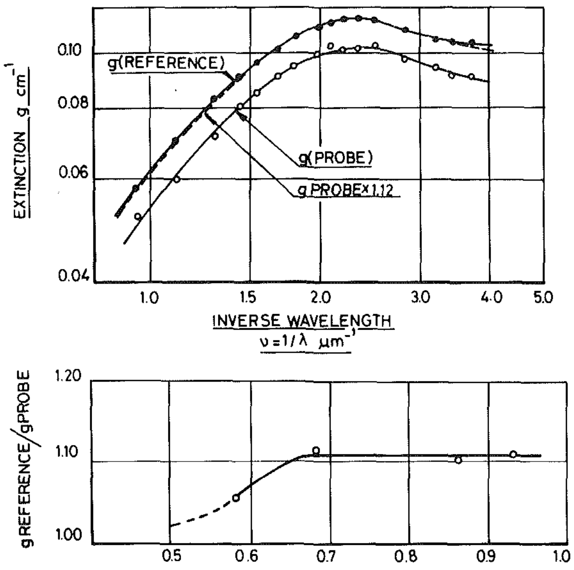

Fig. 3 Slotted probe light extinction calibration

collimated output beam from a xenon arc lamp (ILC Cermax 300 U.V.). This beam is then condensed by a simple f.3. planoconvex quartz lens and the light is conducted to the probe by a further section of flexible U.V. light guide (Schott Glass—3 mm core). Heat-absorbing filters are used to protect the interference filters over the visible spectrum and where these have to be removed for U.V. and infrared (I.R.) transmission exposure is limited by a mechanical shutter. The spectral range of the current system is $300 < \lambda < 1050$ nm and although this is considered to be adequate it is intended to extend the U.V. limit to below 250 nm by improved optical filtering.

The probe is inserted into the steam space via guide tubes that run through the inner and outer casings of the L.P. turbine and terminate on the outside by gate valves, that enable probes to be installed and removed while the machine is on load. The probe is contained in a 25.4 mm tube and is built in versions of up to 4 m in length in order to reach the hub of large L.P. turbines along radial traverse lines.

Practical Aspects of Measuring Wetness With the Optical Probe

Probe Calibration. Although the optical measurement of wetness is absolute in fundamental terms it does, in the case of L.P. turbines, involve physically introducing a sensing probe into the flow. It is necessary therefore to establish the relation between the wetness sensed by the probe and that of the undisturbed flow which is being sought.

It was already known, from wind tunnel measurements on a model probe [4], that the flow velocity increased by about 20 percent in passing through the slot which locally dilutes the suspension. The concentration sensed by the probe as light extinction g (see equation (2)) must therefore be corrected for the change in vapor density during sampling to obtain the free-stream value. To establish this correction definitively the probe head was calibrated in the CERL steam tunnel [3] against a nonintrusive reference system. The probe installed traversely through a rectangular test duct (15 cm × 30 cm) only occupied 4.3 percent of the flow area, and since the reference system (see [2]) transmits light between clean side walls ahead of the probe, a true comparison between free-stream and sampled conditions could be made for Mach numbers up to and exceeding 0.9.

A typical result is shown in Fig. 3, where the extinction measured by the probe is related to the reference condition over the entire spectral range by a constant factor. Several tests of this type provided the calibration curve included in Fig. 3 as an extinction/turbidity correction in terms of free-stream Mach number.

Correction for Coarse Water. Although the wetness formed in L.P. turbines by spontaneous condensation consists almost entirely of submicron droplets, a certain amount of this suspended water is deposited on the blading and re-entrained by the flow as coarse droplets. This has a direct effect on the measured light transmission since the cross-sectional area of a given mass of liquid suspended as droplets is inversely proportional to the droplet size. Hence when a proportion of the fog droplets, which typically have a mean diameter of 1/3 μm, are converted by deposition into coarse droplets ($D \simeq 50$ μm [10]) the cross section this fraction of the wetness presents to the light beam is reduced by over 99 percent. Further, since coarse water accounts for only about 10 percent of the wetness its contribution to the extinction is negligible regardless of any realistic difference between the scattering efficiencies E of the two species of droplet. In terms of obtaining wetness from optical transmission therefore coarse water is effectively lost from the measurement. A correction for this deficit, however, is provided by Williams and Lord [11] who made extensive measurements of coarse water in L.P. turbines. By traversing a catchpot probe at exit from the wet stages of several machines they established that coarse water generally accounted for 5.1 to 7.6 percent of the wetness inferred from local steam conditions. Since then however the reference wetness levels that these values are based on have been measured directly with the optical probe indicating the upper limit of this range to be the best overall mean estimate. A correction of 8 percent is therefore applied to give

$$Y = Y_{\text{optical}} + Y_{\text{coarse water}} = 1.08\ Y_{\text{optical}} \qquad (14)$$

Ideally, more coarse water measurements should now be made to refine this correction by establishing its dependence on fog droplet size since this controls the amount of deposition. In terms of determining enthalpy levels, however, which is the essential purpose of the wetness measurement, this improvement would only be marginal. The entire range of coarse water content measured by Williams and Lord [11] of ± 1.25 percent from a mean level only represents an enthalpy variation of ± 2.5 kJ/kg for a typical exhaust wetness of around 8 percent. This is an acceptable uncertainty in a measurement of the 600–800 kJ/kg enthalpy drop incurred by an L.P. turbine.

Spectral Transmission Data Obtained From L.P. Turbines. An extinction curve for a wet steam flow measured at exhaust from the L.P. cylinder of a 320 MW turbine is shown in Fig. 4. The measurement was made at about midblade height, where the static pressure was 70 mbar and provided a wetness fraction of $Y = 0.10$ with a mean droplet diameter $D_{32} = 0.38$ μm. It therefore represents typical conditions at outlet from fairly efficient L.P. turbines.

The data values given in Fig. 4 are the measured g_j normalized by the total cross section of droplets per unit volume, which converts them into j values of the mean extinction coefficient of the flow $\bar{E}$ defined

$$\bar{E} = \int_0^{D_\infty} E(\nu, D) N_r(D) D^2 dD \Big/ \int_0^{D_\infty} N_r(D) D^2 dD \qquad (15)$$

or numerically from equations (4)–(11)

$$\bar{E}_j(\alpha_{32}) = g_j \Big/ \sum_{i=1}^{n} f_i \Delta D \qquad (16)$$

where $\alpha_{32} = \pi D_{32}/\lambda$ is the particle size parameter based on D_{32}.

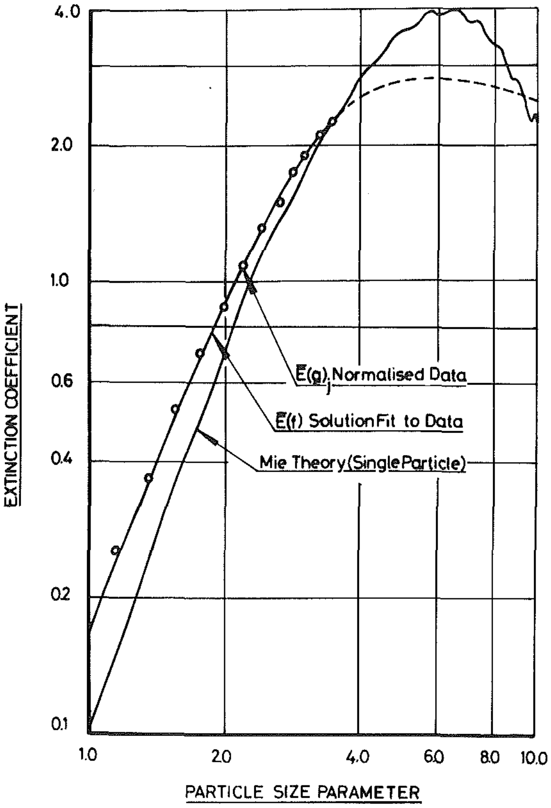

Fig. 4 Extinction coefficient of a wet steam flow measured in an L.P. turbine

The measured extinction expressed in this form may be compared directly with the Mie particle extinction curve, to which it is related by the integral transform, equation (3), to illustrate some important properties of the wet flows in L.P. turbines and their optical measurement. It is immediately clear, for example, that the droplets are very small since the measured extinction is evidently the transform of the rising part of the Mie curve ($\alpha \leq 6$) that relates to submicron droplets. Moreover since the form of this result is entirely typical of several hundred similar measurements made in a variety of machines, it appears that the wetness in L.P. turbines consists in general mainly of submicron droplets. Were this not the case in fact, the results would resemble the steam tunnel result given in Fig. 3 where the measured extinction is derived from the main peak in $E(\alpha)$ indicating that a significant proportion of the suspended liquid mass consists of droplets with $D \geq 1.0\ \mu$m.

The curve $\bar{E}(f)$ given in Fig. 4 for the measured extinction is not simply an arbitrary graphic interpretation of the given data but is calculated separately by replacing the measurements g_j in equation (16) with the corresponding elements of the vector $\mathbf{g}^s = A\,\mathbf{f}^s$. This process of substituting the smoothed solution $\mathbf{f}^s$ generated from the data by the Phillips-Twomey [6] inversion (equation (8)) back into the basic equation $A\mathbf{f} = g$ provides an indication of how close the smoothed solution $\mathbf{f}^s$ (from which the wetness is calculated) is to the true solution $\mathbf{f}$. Distortion of $\mathbf{f}^s$ by excessive smoothing, for example, will generate $\mathbf{g}^s$ values that depart significantly from the given $\mathbf{g}$, resulting in a relatively large value of the residual

$$\mathrm{ave}|\epsilon_j| = \sum_{j=1}^{m} |Af_j - g_j| \qquad (17)$$

In this case, however, as may be expected from the graphic agreement between $\bar{E}(f)$ and $\bar{E}(g)$ ($\mathbf{g}^s$ and g scaled by the same normalizing constant) ave$|\epsilon_j|$ is fairly small. The actual value obtained of ave$|\epsilon_j| = 0.0295$ is in fact only about 1 percent of the mean value of g and since this is within the measurement error for this case a more accurately defined inverse cannot be expected.

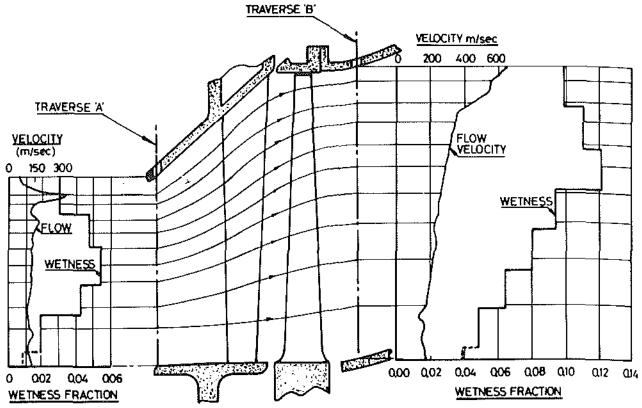

Fig. 5 Flow and wetness distributions measured upstream and downstream from the final stage of a 660 MW turbine

At the relatively high wetness for this case ($\bar{Y} = 0.10$) the flow is optically dense. Transmissions in fact fell to below 1 percent at the U.V. end of the spectral range which is an optical depth τ ($\tau = gt$ in $I/I_0 = e^{-\tau}$) of up to about 5. It should be noted however that the only problem this poses is that of detecting the low intensity transmitted by the flow since Zuev et al. [12] have shown by experiment that the Bouguer Law (equation (3)) is valid for optical depths of up to at least 12. The optical depth gt and hence the droplet concentration are therefore proportional to $\ln(I_0/I)$ for transmissions down to below $I/I_0 = 10^{-5}$ and any data within a practically measurable range will therefore in principle provide a reliable value of wetness.

Obtaining L.P. Turbine Stage and Cylinder Efficiencies From Flow and Wetness Traverses

Flow and Wetness Traverses. In order to obtain the efficiency of an L.P. turbine or that of an individual wet steam stage from wetness probe traverses it is necessary also to establish the corresponding distributions of pressure and mass flow. Radial distributions of total enthalpy flux can then be computed to provide a measure of the internal work done by the turbine or by a section of the expansion between particular traverse planes. Pressure probe traverses are therefore required in addition to the optical measurements to provide the necessary flow data. Details of the probes used for this measurement are given by Moore [13] but essentially they provide the distribution of static pressure, total pressure, and flow velocity vector for the same radial traverses as the optical measurement and at the same flow conditions.

A typical result is given in Fig. 5, where the velocity and wetness profiles measured on traverses upstream and downstream from the final stage of an L.P. turbine are shown related to the casing and blading geometry. The velocity profile is derived from about 30 point measurements and can therefore be specified as a continuous curve. In contrast the optical probe samples the flow over a considerable radial interval and the probe is therefore traversed in steps equal to the length of the sampling slot. This is continued until all the flow up to the casing has been examined and as a consequence the wetness distributions consist of a series of mean levels over the sampled intervals in the form of a histogram as shown in Fig. 5. The last 5 cm of the annulus toward the hub are inaccessible to the optical probe because the receiver optics section extends beyond the sampling slot (see Fig. 1). The wetness pro-

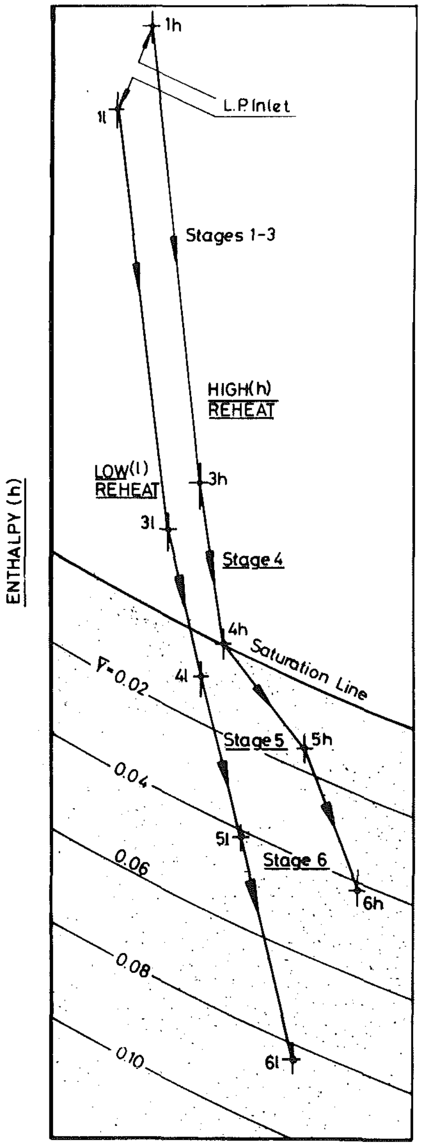

Fig. 6 Condition lines for an L.P. turbine at high and low reheat temperatures

file is therefore completed by linear extrapolation through this region on the basis that it involves only a very small fraction of the mass flow.

Calculation of Efficiency From Traverse Data. A traverse test on an L.P. turbine provides radial flow and wetness distributions for the turbine exhaust and usually for two or three other axial stations within the cylinder. The first step in calculating efficiencies from these data is to compute the corresponding distributions of the state parameters ρ, h, and s for each traverse plane from the measured static pressure and wetness using the equilibrium relationships

$$\left.\begin{aligned} h &= (1-Y)h_g + Y h_f \\ s &= (1-Y)s_g + Y s_f \\ v &= \frac{1}{\rho} = (1-Y)v_g + Yv_f \end{aligned}\right\} \qquad (18)$$

where Y is the wetness and the subscripts g and f refer conventionally to the local saturation states of the gas and liquid phases. Then, by introducing the measured velocity profile $C(r)$ the total enthalpy profile is obtained from

$$h_0 = h + C^2/2 \qquad (19)$$

and assuming the flow to be axisymmetric the cumulative mass flow distribution is calculated as

$$G(r) = \int_{r_i}^{r} \rho\, C_{ax} 2\pi r dr = 2\pi \int_{r_i}^{r} g r dr \qquad (20)$$

where C_{ax} is the axial component of the absolute velocity C, ρ is the mixture density, and $G(r)$ is the mass flow through the plane between the hub ($r = r_i$) and radius r. Finally a mean thermodynamic state ($\bar h$, $\bar s$) and a mean total enthalpy $\bar h_0$ are calculated for each traverse plane from integrals of the form

$$\bar h = \frac{1}{G(r_0)} \int_{r_i}^{r_0} g(r) h(r) 2\pi r dr \qquad (21)$$

where r_0 is the outer radius of the annulus and $G(r_0)$ the total mass flow, providing the efficiency of the expansion between any two traverse planes (such as 1 and 2 in Fig. 6) from

$$\eta(\text{total to total}) = (\bar h_{0_1} - \bar h_{0_2})/(\bar h_{0_1} - \bar h_{0_{2s}}) \qquad (22)$$

The end point $\bar h_{0_2}$ of the isentropic process is determined by the mean outlet total pressure $\bar p_{0_2}$ and is obtained from the measured quantities as

$$h_{0_{2s}} = h(\bar p_{0_2}, s_1) \text{ where } \bar p_{0_2} = p(\bar h_{0_2}, s_2) \qquad (23)$$

Alternatively however, an overall total to static L.P. turbine efficiency may be obtained by terminating the isentropic enthalpy drop at the condenser inlet pressure $\{\bar h_{0_{2s}} = h(p_{\text{condenser}}, \bar s_1)\}$ and by specifying the initial state $(\bar h_{0_1}, \bar s_1)$ from the measured L.P. inlet temperature and pressure.

No allowance is made in these calculations for flow extracted from the L.P. turbine for feed heating since this is found in practice to have a small effect. In a few trial cases the correction involved, which is obtained by subtracting a proportion of the total enthalpy flux at the same intermediate pressures from both the real and isentropic processes, amounted to less than 1 efficiency percentage point. Since in reality this is probably within the overall uncertainty in efficiencies derived from probe measurements, values based on end points are usually retained.

In order to examine the performance of an individual stage in more detail, the mass flow distribution $G(r)$ (equation (20)) is interpolated to provide the radii r_j ($j = 1, \ldots, n+1$) defining n notional stream tubes, which have been constructed in Fig. 5 using measured flow angles. In principle these establish the streamwise relation between local conditions upstream and downstream from the stage and enable the radial variation in efficiency to be calculated by applying equation (22) to the flow along individual streamlines.

Condition Lines and Condensation. Condition lines connecting the mean states ($\bar h$, $\bar s$) measured with traversing probes at exit from the last four stages of a six-stage L.P. turbine are plotted on a Mollier diagram in Fig. 6. The results given are for tests conducted on a particular turbine at different inlet temperatures to establish whether the position of the condensation front within the L.P. expansion was responsible in any way for the apparent local reduction in efficiency of the penultimate stage. As shown in Fig. 6 for the higher temperature case, this appears as a pronounced inflection in the condition line which, although emphasized in this illustration, was also detected to some extent in each of the four other L.P. turbines for which similar detailed condition lines had been measured.

In the case shown in Fig. 6, the measurements clearly indicated dry conditions at entry to stage 5 for the high L.P. inlet temperature test. The flow was optically transparent ($f/f_0 = 1.0$ for all λ) and the mean state $4h$, although close to

Table 1 Comparison of L.P. turbine performance derived from optical wetness measurements and heat rate tests

Turbine nameplate rating	Number of L.P. flows	Test load	Mean exhaust wetness	Range of droplet diameter	Mean exhaust total enthalpy (probe traverse)	Mean exhaust total enthalpy (heat rate tests)	Difference in L.P. turbine efficiency
MW		MW	percent	μm	kJ/kg	kJ/kg	percent
160	2	80	6.0	0.2–0.4	2435	2426	−1.5
160	2	120	8.7	0.3–0.4	2384	2384	0.0
320	4	320	8.4	0.4–0.6	2396	2384	−1.3
500	6	492	5.9	0.3–0.4	2447	2448	−0.2
660	6	599	9.2	0.4–0.5	2388	2389	−0.1

saturation, was derived from a stagnation temperature profile that was entirely superheated. The onset of condensation therefore occurred in this stage, and to establish what effect this had on stage performance, the measurements were repeated with the reheater outlet temperature reduced by about 40°C. As shown in Fig. 6 this moved the condensation front upstream into stage 4 whereupon the efficiency of stage 5 improved considerably. Moreover, since this local improvement was reflected by a commensurate improvement in the efficiency of the whole L.P. turbine the observed change was clearly a real effect, which must be related to the position of the condensation front since this was the only flow condition that had changed appreciably.

It is not known at present however how enhanced losses are caused by condensation. The inherent thermodynamic loss associated with the departure from equilibrium at the onset of the process is not in isolation a sufficiently large effect. Yeoh [14] for example, who incorporated a spontaneous condensation calculation into a L.P. turbine throughflow analysis, predicted a local reduction in efficiency of only a few percentage points for the condensing stage. An additional possibility however is the aerodynamic shock wave that can arise during spontaneous condensation at low supersonic Mach numbers when the local pressure is raised by the release of latent heat to a supercritical level. This effect, and the way in which the unstable stock waves produced interact with boundary layers, is reviewed by Davids et al. [15]. Subsequent field tests in pursuance of this study however [16] provide some evidence to suggest that this shock boundary layer interaction may be related to the phenomenon illustrated in Fig. 6. Whirlow et al. [16] detected nonsynchronous rotor blade vibrations in the penultimate stages of both L.P. cylinders of a particular machine only when the stage exhaust wetness was confined to within narrow limits (3–4 percent in one case, 2 percent in the other). This occurred over a wide range of operating conditions and if the responsible mechanism, which was clearly related to the position of the condensation front in the machine, produced detectable flow induced blade vibrations it could also result in a loss of aerodynamic performance.

Concluding Discussion

The potential value of the optical wetness probe as a diagnostic tool for examining the performance of L.P. turbines is clear from the results presented in this paper. In addition to providing direct measurements of turbine efficiency it also enables specific problem areas within the wet zone of an L.P. cylinder to be identified. In an example given, the efficiency of the penultimate stage of a particular turbine was found to depend on the location of the initial condensation front within the expansion to a much greater extent than was previously expected. Another example could have been given equally well to show how the improved performance of a modified L.P. stage had been indicated by a greater streamwise increase in wetness over the flow annulus. The probe therefore is a useful indicator of change within the turbine and in conclusion it is worth assessing to what extent performance parameters derived from optical measurements of wetness are reliable in an absolute sense.

Efficiency values derived from probe traverses are most likely to be in error either directly from error in the measured wetness or because the conditions measured on a single traverse line do not provide an accurate mean for the entire flow in up to six parallel expansions. The specific error arising from either of these sources however cannot be estimated reliably. For wetness there is no method available for providing a calibration reference and since the value obtained is related to the measured optical transmission by an integral transform the probable error is not a simple function of the uncertainty in the raw data. Radial probe guides are usually installed in L.P. turbines in a plane at about 45 deg from vertical in the direction of rotation which is considered most likely to provide mean conditions at turbine exhaust. Validating this for a large L.P. turbine would require a prohibitive number of simultaneous traverses in all six flows.

The only independent confirmation for the efficiencies provided by probe traverses currently available therefore are the corresponding values obtained from heat rate tests. Here again however, the results obtained are subject to uncertainty since the drop in total enthalpy incurred by the flow through the L.P. turbine is obtained essentially by subtracting the measured enthalpy drops for the superheated H.P. and I.P. flows from the generator output. The value obtained is therefore subject to corrections such as mechanical losses and generator efficiency which are not directly quantifiable and is sensitive to measurement errors particularly for example in the feed flow to the boiler.

However, despite the uncertainties inherent in both methods, good agreement is usually obtained as shown in Table 1.

Here the outlet mean total enthalpies derived from optical wetness traverses are compared with those obtained from heat rate tests. The examples given are for those turbines where heat rate tests and probe traverses were made either simultaneously or close enough in time for the state of the machine and the operating conditions to be virtually identical. Even so the agreement obtained is not unrepresentative. Altogether 17 such measurements have been made on L.P. turbines with the optical probe, including examples from Europe and the USA, for which efficiencies derived from heat rate tests are available. In 15 of these cases the two efficiency values agree to within less than 2 percent and in 7 to within 1 percent. This level of agreement is better than was originally expected since not all the heat rate tests were conducted to the strictest code of practice. The available evidence therefore suggests that the optical wetness probe will indeed provide reliable measurements of L.P. performance. Perhaps its greatest value however is that it enables the performance of the wet zone of an L.P. turbine to be measured on a stage-by-stage basis thus providing detailed information that is otherwise completely inaccessible.

Acknowledgments

The author would like to acknowledge the assistance of Mr. P. C. Skingley who built the optical probe and contributed materially to its design.

The work is published by permission of the Central Electricity Generating Board.

References

1 Kerker, M., *The Scattering of Light and Other Electromagnetic Radiation*, Academic Press, New York, 1969.

2 Walters, P. T., "Optical Measurement of Water Droplets in Wet Steam Flows," *Conference Proceedings*, Institution of Mechanical Engineers, London, 1973, Vol. 3.

3 Moore, M. J., Walters, P. T., Crane, R. I., and Davidson, B. J., "Predicting the Fog-Drop Size in Wet Steam Turbines," *Conference Proceedings*, Institution of Mechanical Engineers, London, 1973, Vol. 3.

4 Walters, P. T., and Skingley, P. C., "An Optical Instrument for Measuring the Wetness Fraction and Droplet Size of Wet Steam Flows in L.P. Turbines," *Proceedings of Design Conference on Steam Turbines for the 1980's*, Institution of Mechanical Engineers, London, 1979.

5 Penndorf, R. B., "New Tables of Mie Scattering Functions for Spherical Particles," Geographysical Research Paper No. 45, Part 6, 1956.

6 Twomey, S., "On the Numerical Solution of Fredholm Integral Equations of the First Kind by the Inversion of the Linear System Produced by Quadrature," *J. Assoc. Comput. Mach.*, Vol. 10, 1963, p. 97.

7 Walters, P. T., "Practical Applications of Inverting Spectral Turbidity Data to Provide Aerosol Size Distributions," *Applied Optics*, Vol. 19, 1980, p. 2383.

8 Marshall, T. R., Parmenter, C. S., and Seaver, M., "Precision Measurement of Particulates by Light Scattering at Optical Resonance," *Journal of Colloid and Interface Science*, Vol. 55, 1976, p. 624.

9 Dobbins, R. A., and Eklund, T. I., "Ripple Structure of the Extinction Coefficient," *Applied Optics*, Vol. 16, 1977, p. 281.

10 Statsny, M., "An Experimental Research Into Flow of Wet Steam Through the Last Stage of Full-Scale Turbine," Sixth Thermodynamics and Fluid Mechanics Convention, I. Mech. E., University of Durham, 1976.

11 Williams, G. J., and Lord, M. J., "Measurement of Coarse Water Distribution in L.P. Cylinders of Operating Steam Turbines," *Proceedings of the Institute of Mechanical Engineers*, Vol. 190, 1976.

12 Zuev, V. E., Kabanov, M. V., and Savel'ev, B. A., "The Limits of Applicability of the Bouguer Law in Scattering Media for Collimated Light Beams," *Izv., Atmospheric and Oceanic Physics*, Vol. 3, No. 7, 1967, pp. 724–736.

13 Moore, M. J., "Instrumentation for Wet Steam," in: *Two Phase Steam Flow in Turbines and Separators*, M. J. Moore and C. H. Sieverding, eds., Hemisphere Publishing Corporation, London, 1976.

14 Yeoh, C. C., "Non Equilibrium Throughflow Calculations in Steam Turbines," Ph.D. Thesis, University of Cambridge, 1981.

15 Davids, J., Farn, C. L. S., Kadambi, J. R., and Whirlow, D. K., "Steam Turbine Condensation-Shock Wave Interaction," Final Report, Project 1407-1, EPRI CS 3251, Nov. 1983.

16 Whirlow, D. K., McCloskey, T. S., Davids, J., Chen, S., Kadambi, J. R., and Farn, C. L. S., "Flow Instability in Low Pressure Turbine Blade Passages," ASME Paper No. 84-JPGC-GT-15, 1984.

Advances in Defining a Closed Brayton Conversion System for Future ARIANE 5 Space Nuclear Power Applications

Z. P. Tilliette
Commissariat à l'Energie Atomique,
IRDI/DEDR/DEMT,
Centre d'Etudes Nucléaires de Saclay,
91191 Gif sur Yvette, France

The present European ARIANE space program will expand into the large ARIANE 5 launch vehicle from 1995. It is assumed that important associated missions would require the generation of 200 kWe or more in space during several years at the very beginning of the next century. For this reason, in 1983, the French C.N.E.S. (Centre National d'Etudes Spatiales) and C.E.A. (Commissariat à l'Energie Atomique) have initiated preliminary studies of a space nuclear power system. The currently selected conversion system is a closed Brayton cycle. Reasons for this choice are given: high efficiency of a dynamic system; monophasic, inert working fluid; extensive turbomachinery experience, etc. A key aspect of the project is the adaptation to heat rejection conditions, namely to the radiator geometry which depends upon the dimensions of the ARIANE 5 spacecraft. In addition to usual concepts already studied for space applications, another cycle arrangement is being investigated which could offer satisfactory compromises among many considerations, increase the efficiency of the system, and make it more attractive as far as the specific mass (kg/kWe), the specific radiator area (m^2/kWe), and various technological aspects are concerned. Comparative details are presented.

Introduction

The European space program is gaining significance primarily through the launch of several satellites, mainly geosynchronous, per year for various countries by using the ARIANE rocket. ARIANE is a wide family of launch vehicles, as illustrated in Fig. 1. ARIANE 1 was qualified in 1981. ARIANE 3 has been in operation since the end of 1984. Several models of ARIANE 4 will be used in the next few years. An important stage was reached in 1984 with the decision of the European governments to study and develop the large ARIANE 5 launch vehicle for operation starting in 1995. Figure 2 shows some versions of ARIANE 5 which is designed to launch a payload of 17,000 kg in 400 km low earth orbits and of about 5000 kg in geosynchronous orbits. Several large launchers are compared in Fig. 3.

With ARIANE 5, important space missions are made possible around the end of this century, such as Orbital Transfer Vehicles (O.T.V.), communication satellites, earth observation, and space stations. It is now admitted that, within about 15 years, a power generation of 50 kWe to 400 kWe during several years would be required in space. Because of these relatively high power levels and extended operation time requirements, the heat source would necessarily be a nuclear reactor. This is the reason that, in France, the study of a space nuclear power system has been initiated. It is cosponsored by the "Centre National d'Etudes Spatiales" (C.N.E.S.) and the "Commissariat à l'Energie Atomique" (C.E.A.). Following preliminary investigations (1983–1984), a two-year (mid-1984–mid-1986) phase of assessment studies is in progress [1–3]. The purpose of the present phase is to estimate the technical feasibility and the cost of the program with a view to decisions around the end of 1986. The precise reference application is an electrical O.T.V. which is the most demanding from the specific mass point of view.

It is clear that the development of a space nuclear power system represents a very ambitious program within reach of a very few industrially advanced countries. Europe could certainly manage such a program because its present space program is already significant and expanding (COLUMBUS, HERMES Projects). Moreover, as far as nuclear energy is concerned, France is one of the leading countries in the world.

Selected Space Conversion System

In the preliminary phase, several space-related energy conversion concepts were investigated and compared. For the present two-year phase, a system selection has been made as shown in Fig. 4. It concerns a closed Brayton cycle of which the basic principles are given by Fig. 5. This present choice is based on several attributes of the system which are as follows:

Contributed by the Gas Turbine Division of THE AMERICAN SOCIETY OF MECHANICAL ENGINEERS and presented at the 31st International Gas Turbine Conference and Exhibit, Düsseldorf, Federal Republic of Germany, June 8–12, 1986. Manuscript received at ASME Headquarters December 26, 1985. Paper No. 86-GT-15.

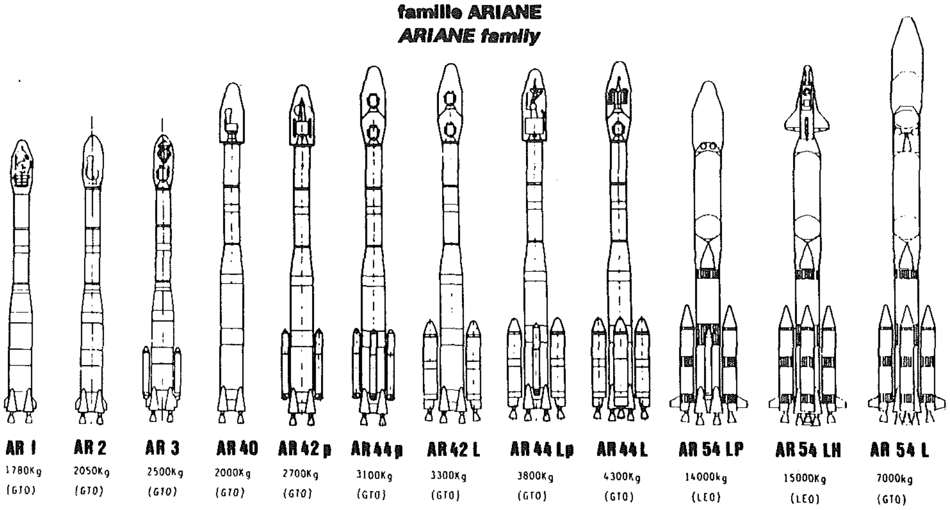

Fig. 1 ARIANE family of European launch vehicles

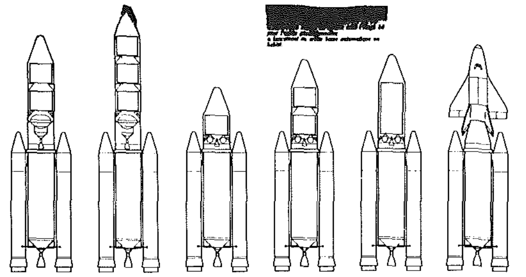

Fig. 2 Outline of possible models of the future ARIANE 5 European launch vehicle

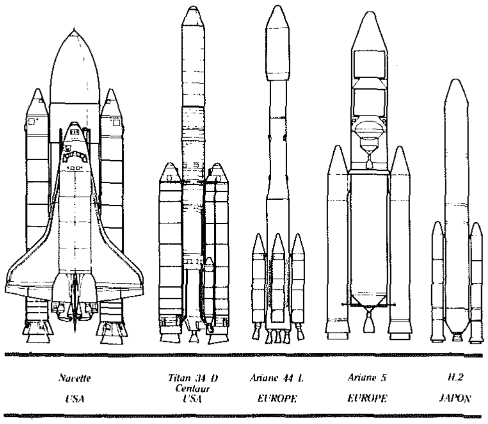

Fig. 3 Comparison of several large launch vehicles

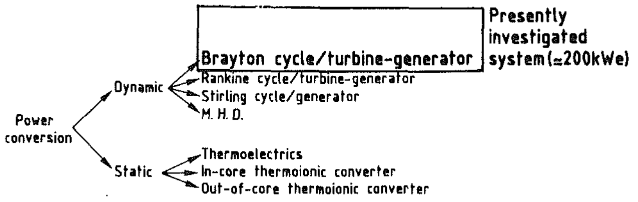

Fig. 4 Present French selection of a space nuclear power conversion system

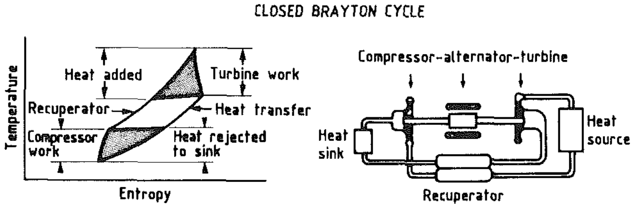

Fig. 5 Principle and arrangement of a recuperated closed Brayton cycle

- relatively high efficiency
- moderate reactor thermal power level
- extensive industrial turbomachinery experience
- already well-developed components
- clean, noncorrosive working fluid (He-Xe mixture)
- relatively low temperature level at one end of the cycle
- easy power conditioning

Brayton cycles have been studied and developed for many space power systems over the last 20 years. The reliability of the compressor-generator-turbine assembly has been demonstrated in space conditions by a unit at NASA Lewis Research Center (LeRC) that successfully operated essentially unattended for almost 40,000 hr [4, 5]. Some past projects are worth mentioning: the 50 kWe 1971 space station [5], the 400 kWe nuclear electric propulsion (NEP) project (O.T.V.) [6], the SP-100 Westinghouse direct cycle [7], and Rockwell indirect cycle [8] projects. More recently, a closed gas cycle "solar dynamic" system is being considered for the future U.S. space station program [9]. Concerning the preliminary French studies, some investigations have been carried out [3, 10].

It appears from these works that the Brayton cycle is definitely a possible space power generation system. It compares well with the other main candidates; however, it has to be carefully studied to improve its potential.

Power System Conditions

In space, the power system design is determined by both the required power level and the heat rejection capacity, namely, the possible area of the radiator.

Considering that the future power needs in space at the beginning of the next century could range from about 50 kWe to 400 kWe, a reference power level of 200 kWe (net) has been adopted for the present assessment study. According to Fig. 6, it offers an acceptable transfer time from a LEO to a GEO orbit in the case of an electrical O.T.V. adapted to ARIANE 5.

The available radiator area is a basic conversion system parameter. The power level, the efficiency, and the upper temperature level depend upon it directly.

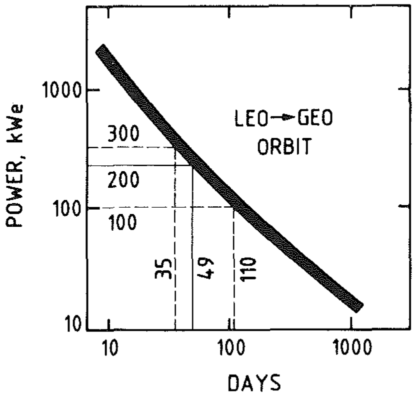

Fig. 6 Needed electric power versus LEO-GEO orbits transfer time for ARIANE 5 applications

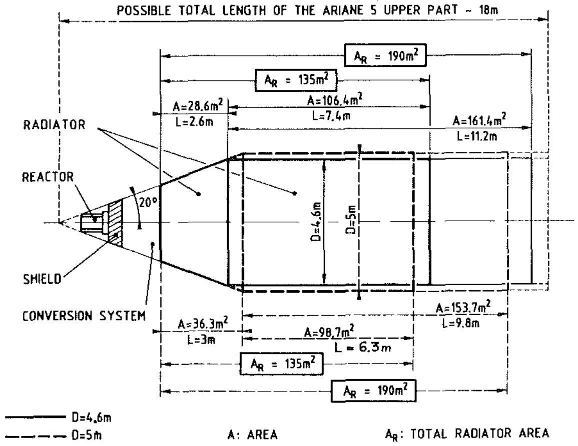

Fig. 7 Reference and extended radiator areas of a future ARIANE 5 spacecraft

In order to illustrate in more detail the possible radiator areas offered by the ARIANE 5 spacecraft shown by Fig. 2, Fig. 7 is presented. Up to now, only the fixed peripheral part of the space vehicle was used for the radiator, which extends on both the cone and the cylinder. Two radiator diameters of 4.6 m and 5 m are considered. According to the appropriation of either a large or a small area at the bottom of the cylinder for the waste heat rejection from power processing and payload, either a reduced or an extended coverage of the cylinder is possible for the main radiator. It follows that two radiator areas can be taken into account in the present investigation: 135 m^2 and 190 m^2. These two values permit a satisfactory preliminary estimate of the ARIANE 5 power system capacity in different cases.

It is sure that deployable radiator concepts, conceivable in the future, would significantly increase the power generation capacity.

Investigated Closed Brayton Cycles

The basic space closed Brayton cycle is the simple, recuperated one shown in Fig. 5. It is the cycle adopted for the first preliminary studies and the reference French project.

Given the need to enlarge the scope of the investigation and following a better understanding of the space power generation problems, other closed gas cycles have also been examined, as illustrated in Fig. 8. This additional cycle investigation has been carried out by taking account of the leading parameters of a space power system, namely:

- the technology
- the specific mass (kg/kWe)
- the specific radiator area (m^2/kWe)

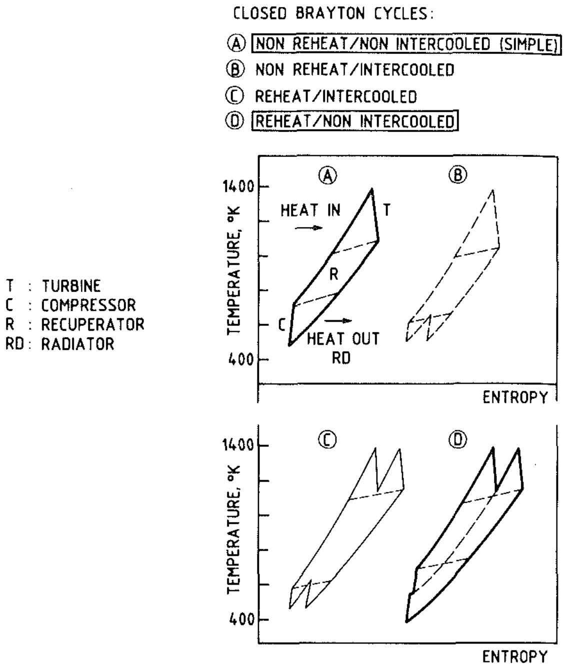

Fig. 8 Brayton cycles investigated for space energy conversion applications

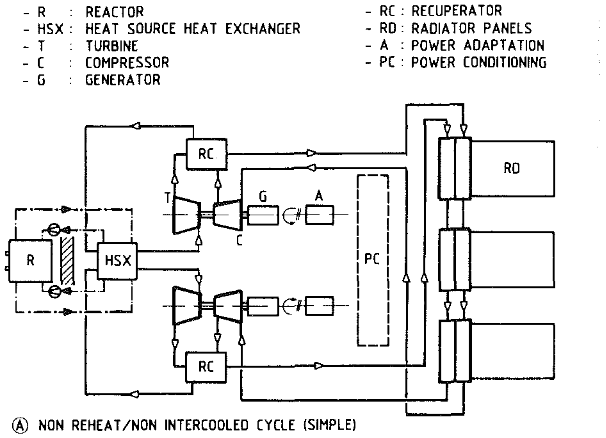

Ⓐ NON REHEAT/NON INTERCOOLED CYCLE (SIMPLE)

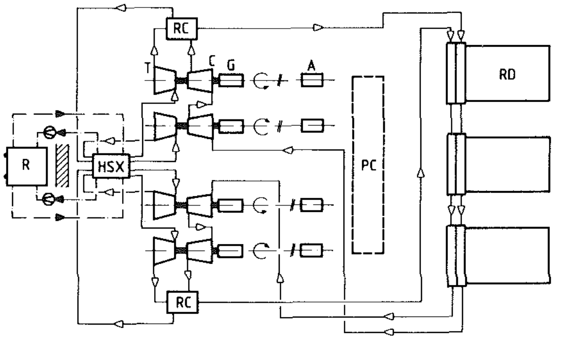

Ⓓ REHEAT/NON INTERCOOLED CYCLE

Fig. 9 Comparative diagrams of nonreheat and reheat Brayton cycle systems for space applications

For the temperature levels presently considered, only recuperated cycles are studied. So, the possible cycle modifications include intercooling or reheat.

The nonreheat, intercooled cycle (B) of Fig. 8 could not be a satisfactory solution for space applications. The increase in efficiency and the relative decrease in working fluid mass flow

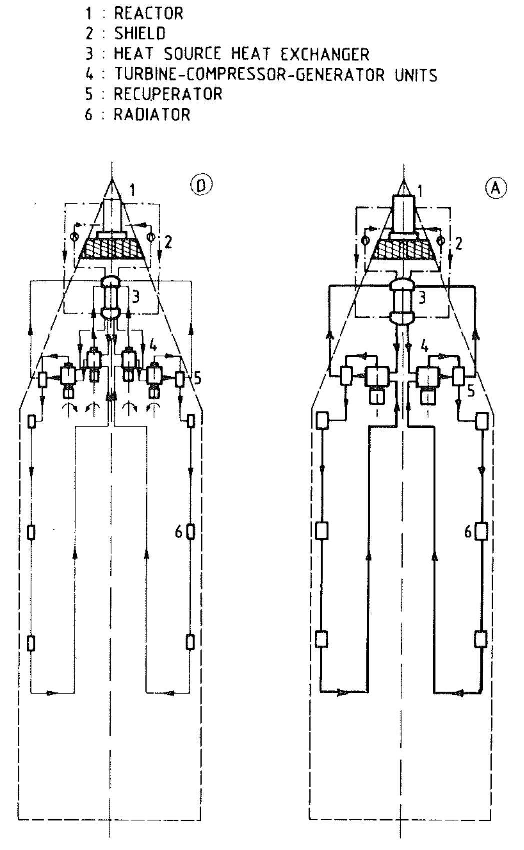

REHEAT, NON-INTERCOOLED CYCLE

NON-REHEAT, NON-INTERCOOLED CYCLE

Fig. 10 Comparative schematic arrangements of nonreheat and reheat Brayton cycle systems for space applications

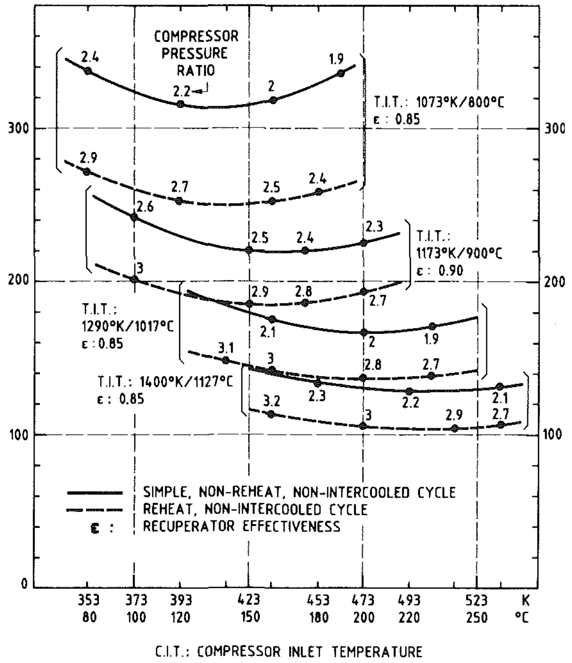

Fig. 11 Variation of the radiator area as a function of the turbine and compressor inlet temperatures

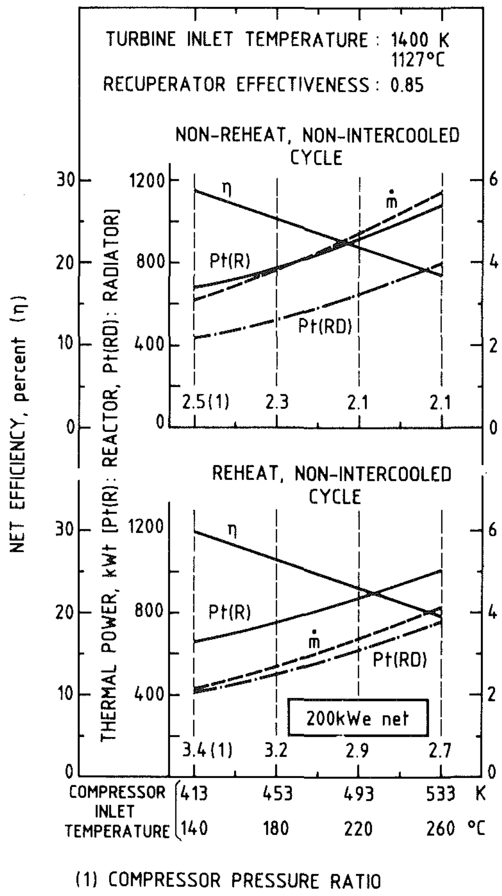

Fig. 12 Typical variation of the main power system characteristics as a function of the compressor inlet temperature

are probably offset by an increase in the radiator area because of a lower mean heat rejection temperature. The reheat, intercooled cycle (C) is the most efficient and leads to the minimum working fluid mass flow. Comparisons also show a decrease of almost 10 percent in the radiator area. This cycle could nevertheless offer no advantage in space because the abovementioned gains are probably offset by the circuit complications concerning not only the high-temperature end but also the more extended low-temperature part. As a matter of fact, it is superseded by the reheat, nonintercooled cycle configuration (D) which combines an increase in efficiency, a decrease in working fluid mass flow with a more significant decrease in radiator area ranging from 15 to 20 percent. This result is a logical consequence of the smaller waste heat amount resulting from the reheat and the higher pressure ratio combined with a moderate increase of the radiator temperature range only toward the higher values of this radiator temperature.

Consequently, results have been obtained and compared for the simple, reference, nonreheat, nonintercooled (A) cycle and the reheat, nonintercooled (D) cycle of Fig. 8.

Example of Compared Conversion Circuits

Before presenting the results of the cycle investigation, it is necessary to detail somewhat the arrangement of the compared circuits as they are shown in Fig. 9.

In both cases, the heat source is a fast-spectrum, lithium-cooled (for higher temperatures) reactor. The primary circuit consists of two loops. Heat is transferred to the conversion circuit through a liquid metal–gas heat exchanger. The secondary circuit also consists of two loops, each essentially comprising a combined rotating assembly, a recuperator, and a radiator made of three panels of heat pipes in series. Provision is made to supply full power in the case of the unavailability of one turbogenerator by doubling the gas inventory in the operating loop and using the entire radiator area.

The (A) diagram of Fig. 9 represents the reference, nonreheat, nonintercooled cycle version. In this case and before a more detailed study, a configuration has been adopted which probably is pessimistic from the mass balance point of view but is more satisfactory as far as the combined rotating units are concerned. Two separate turbocompressor-generator assemblies have been adopted for each loop in order to avoid an overly large departure from the present concepts of space rotating units. In this way, reheat between the two turbines in series is achieved relatively easily. In addition, the optimum higher pressure ratio is also more easily obtained by two separate compressor stages with a better efficiency than by one stage only. One turbomachine with two turbine stages and one or two compressor wheels could be lighter but would certainly be judged complicated for space applications. Moreover, given their lower power level and their lower pressure ratio per stage, the rotational speed of each unit could be increased, which would reduce their mass.

The two associated turbogenerator units rotate in opposite directions in order to minimize the stability problems of the spacecraft. It is assumed that two such units in series on the gas circuit could operate in parallel electrically. For this purpose, a power adaptation exists between each generator and the power conditioning.

Technical aspects of this concept are being investigated in more detail.

A careful look at Fig. 9 makes it possible to roughly appreciate the differences between the circuits (A) and (D). The latter has four smaller turbogenerators instead of two larger ones, but all the other components are smaller; in addition, ducts have smaller diameters, particularly the long ones to the cold end of the radiator. The heat exchangers between the working fluid and the radiator panels are also reduced.

Figure 10 also gives an idea of the differences between the two concepts. It superimposes the circuit diagram on the ARIANE 5 spacecraft geometry, which presents a more accurate representation of the duct network.

Comparative Results

Results are presented in a comparative form between the reference nonreheat, nonintercooled simple cycle (A) and the reheat, nonintercooled cycle (D).

In each case, four turbine inlet temperatures (T.I.T.) are considered:

- 1400 K / 1127°C
- 1290 K / 1017°C
- 1173 K / 900°C
- 1073 K / 800°C

The first two temperature levels imply the use of refractory alloys for both the primary lithium circuit and the secondary gas circuit. The third temperature level implies the use of refractory alloys for only the primary lithium circuit but makes it possible to use superalloys for the gas circuit. The 1073 K T.I.T. level could also allow the utilization of superalloys for both the secondary and the primary circuit, the adoption of liquid sodium instead of liquid lithium becoming possible for the latter.

Variation of the Radiator Area. Firstly, a sensitivity study of the variation of the radiator area as a function of the compressor inlet temperature (C.I.T.) is illustrated in Fig. 11. It appears that the radiator area varies relatively slightly within the considered C.I.T. range. This can be explained by the regular increase in pressure ratio and the relatively significant decrease in cycle and radiator thermal power, in working fluid mass flow, in parallel with an increase in efficiency in proportion as the C.I.T. decreases, as shown by Fig. 12. The variation of the heat transfer conditions between the working fluid and the radiator has been taken into account.

Table 1 Key data of nonreheat and reheat Brayton systems for 1400 K and 1290 K turbine inlet temperatures and for 135 m^2 and 190 m^2 radiator areas

Technology { - Primary Circuit - Conversion System		Refractory Alloys / Liquid Lithium Refractory Alloys / He - Xe							
Turbine Inlet Temperature	K/°C	1400 / 1127				1290 / 1017			
Radiator Area (2) (3)	m^2	135		190		135		190	
Cycle : Reheat or not		NO	YES	NO	YES	NO	YES	NO	YES
Net Power	kWe	200	200	280	355	160	200	200	260
Compressor Inlet Temperature	K	513	368	473	453	473	473	413	413
	°C	240	95	200	180	200	200	140	140
Pressure Ratio		2.1	3.8	2.2	3.2	2	3	2.2	3.2
Recuperator Effectiveness		0.80	0.85	0.80	0.85	0.85	0.85	0.85	0.85
Reactor Thermal Power	kWt	1036	588	1211	1339	758	940	754	963
Efficiency - Cycle	per cent	23	40.4	27.7	31.6	25.2	25.4	31.6	32.2
Efficiency - Net	per cent	19.3	34	23.1	26.5	21.1	21.3	26.5	27
Working Fluid Mass Flow (He-Xe)	kg/s	5.3	1.8	5.8	4.65	4.6	3.8	4.1	3.6
Outlet Temperature - Turbine (1)	K	1103	1120	1083	1155	1033	1076	998	1064
Outlet Temperature - Compressor	K	724	680	679	769	651	780	593	700
Recuperator -Thermal Power	kWt	831	355	971	800	780	505	726	644
Recuperator -Temperature Difference	K	76	68	80	59	57	45	61	55
Main Radiator - Thermal Power	kWt	787	346	863	903	565	697	509	644
Main Radiator - Temperature Range (Metal)	K	495-712	362-671	460-685	442-730	460-648	460-729	405-607	405-682
Main Radiator - Specific Area	m^2/kWe	0.67	0.67	0.68	0.53	0.84	0.67	0.95	0.73
Power System - Total Mass (6)	kg	5100	4500	6250	6550	5000	5350	5400	5900
Power System - Net Specific Mass	kg/kWe	25.5	22.5	22.3	18.4	31.3	26.7	27	22.7
		(2)	(5)	(3)	(3)	(2)	(2)	(4)	

(1) Mean Temperature
(2) Minimum Radiator Area] Emissivity : 0.85
(3) Almost Minimum Radiator Area] Emissivity : 0.85
(4) Non Efficiency - optimum pressure ratio
(5) High Efficiency Conversion System
(6) Reactor + Shield + Conversion System + Radiator + Power Conditionning + Structures (shielding for low radiation dose)

Table 2 Key data of nonreheat and reheat Brayton systems for 1173 K and 1073 K turbine inlet temperatures and for various radiator areas

Technology { - Primary Circuit - Conversion System		Refractory Alloys/Liq.Lithium Super Alloys / He - Xe				Liquid Sodium Super Alloys	
Turbine Inlet Temperature	K/°C	1173/900				1073/800	
Radiator Area (2) (3)	m^2	135		190		315	254
Cycle : Reheat or not		NO	YES	NO	YES	NO	YES
Net Power	kWe	122	142	172	200	200	200
Compressor Inlet Temperature	K	423	398	423	398	393	383
	°C	150	125	150	125	120	110
Pressure Ratio		2.2	3	2.2	3	2.2	2.75
Recuperator Effectiveness		0.90	0.90	0.90	0.90	0.85	0.85
Reactor Thermal Power	kWt	533	553	748	775	952	847
Efficiency - Cycle	per cent	27.3	30.7	27.4	30.8	25	28.1
Efficiency - Net	per cent	22.9	25.7	23	25.8	21	23.6
Working Fluid Mass Flow (He-Xe)	kg/s	3.45	2.5	4.85	3.5	6.4	4.3
Outlet Temperature - Turbine (1)	K	908	979	908	979	817	907
Outlet Temperature - Compressor	K	608	656	608	656	577	608
Recuperator -Thermal Power	kWt	481	380	680	535	750	575
Recuperator -*Temperature* Difference	K	30	33	30	33	40	45.5
Main Radiator - Thermal Power	kWt	384	379	540	530	706	605
Main Radiator - Temperature Range (Metal)	K	414-594	391-634	414-594	391-634	386-569	377-607
Main Radiator - Specific Area	m^2/kWe	1.11	0.95	1.10	0.95	1.58	1.27
Power System - Total Mass (4)	kg	4450	4600	5600	5560	6400	5800
Power System - Net Specific Mass	kg/kWe	36.5	32.4	32.6	27.8	32	29
		(2)	(3)	(2)	(3)	(3)	(3)

(1) Mean Temperature
(2) Minimum Radiator Area] Emissivity : 0.85
(3) Almost Minimum Radiator Area] Emissivity : 0.85
(4) Reactor + Shield + Conversion System + Radiator + Power Conditioning + Structures (shielding for low radiation dose)

Figure 11 makes it possible to estimate quickly the gain in radiator area expected with the reheat, nonintercooled Brayton cycle. This area reduction is of the order of 16 to 20 percent, a very noticeable value.

Table 3 Performance comparison between nonreheat and reheat Brayton cycles and a Stirling cycle for space applications

Conversion Cycle		BRAYTON		STIRLING (1)
		No Reheat	Reheat	
Temperature				
- Reactor Outlet	K	1110	1110	1100
	°C	837	837	827
- Conversion In	K	1073	1073	1050
	°C	800	800	777
- Radiator	K	386 - 569	378 - 608	∼ 500
	°C	113 - 296	105-335	∼ 227
Reactor Thermal Power	kWt	476	424	450
Net Efficiency	per cent	$\boxed{21}$	$\boxed{23.6}$	$\boxed{22.2}$
Radiator Area	m^2	158	127	128
Radiator Specific Area	m^2/kWe	$\boxed{1.58}$	$\boxed{1.27}$	$\boxed{1.28}$
Net Power	kWe	100		

(1) REFERENCE (11)

In Fig. 11, the strong effect of the T.I.T. on the value of the radiator area appears also. In comparison with a 1400 K (1127°C) T.I.T. conversion system, and for the specified pressure ratios, 1290 K (1017°C), 1173 K (900°C), and 1073 K (800°C) T.I.T. cycles need about 1.28, 1.7, and 2.4 times more radiator area, respectively.

Comparative Brayton Cycle Results. Comparative values for the two considered Brayton cycles are presented in Tables 1 and 2. The main parameters are:

- the "conversion in" temperature (T.I.T.)
- the main radiator area
- the net power level
- the main radiator specific area
- the power system net specific mass

The two main radiator areas of 135 m^2 and 190 m^2 are considered, except for the T.I.T. value of 1073 K. All the mass estimates, including the whole power system, are made for the same conditions. In this way, they are comparable, although further estimates would have to be carried out as the project develops. It must be taken into account that the neutron and gamma shield is designed for a low radiation dose on the equipment.

For a T.I.T. of 1400 K, and a radiator area of 135 m^2, a simple cycle conversion system meets the requirement of supplying a net power of 200 kWe. However, for the same power level, the use of a reheat, nonintercooled cycle results in a decrease in the net specific mass by about 12 percent (22.5 kg/kWe) instead of 25.5 kg/kWe). In this case, the reheat cycle is a very efficient one but its conditions are far from corresponding to the minimum radiator area requirements, because a low C.I.T. can be adopted.

For the same T.I.T. of 1400 K and C.I.T. values almost squaring with the minimum radiator area conditions, an available radiator area of 190 m^2 would make it possible to obtain net power levels of 280 kWe and 355 kWe with a simple cycle and a reheat cycle, respectively. Correlatively with this increase in power level of more than 26 percent, a reduction of about 17 percent in the net specific mass (18.4 kg/kWe instead of 22.3 kg/kWe) would be possible by utilizing a reheat cycle.

The 1290 K T.I.T. is 110 K lower than the previous one. For such a noticeable decrease in temperature level, the simple cycle system generates only 160 kWe net, whereas it remains possible to meet the 200 kWe requirements with the reheat cycle, which, furthermore, offers an advantage in specific mass of about 15 percent.

The T.I.T. value of 1173 K would make it possible to use superalloys instead of more sensitive, exacting refractory alloys for the conversion system. It appears that the 200 kWe power level can be reached with a radiator area of 190 m^2 but only with a reheat cycle. The capacity of the simple cycle is limited to 172 kWe and its specific mass would again be about 15 percent higher.

The comparison also concerns the T.I.T. of 1073 K, which corresponds to the possible use of superalloys instead of refractory alloys for both the primary and the secondary circuits. For the reference power level of 200 kWe net, the needed radiator area is 315 m^2 for the simple cycle, but only 255 m^2 for the reheat cycle, which is a reduction of almost 20 percent (sodium could also be used instead of lithium).

All the other data given by Table 1 and Table 2, particularly the various thermal powers and the working fluid mass flow, make it possible to appraise the differences in system parameters between the considered circuits.

Brayton Cycle-Stirling Cycle Comparison. The Stirling cycle conversion system is considered as another potential solution for future space applications. Some papers have been published. One of them [11] gives some characteristics available for a comparison. In Table 3, this 1050 K space

Stirling cycle is compared with the abovementioned two versions of a 1073 K Brayton cycle. The two "conversion in" temperatures can be considered as similar, given the differences existing between the engine concepts.

The comparison is made for the power level of 100 kWe of U.S. SP-100 projects. For the moment, only the system efficiency and the radiator specific area are mentioned. A mass comparison would need further studies; for instance, the dimensioning of the neutron and gamma shield of the SP-100 project is made for a significantly higher radiation dose on equipment than in the French project.

It appears, as it is generally thought, that the simple Brayton cycle has performances somewhat lower than the Stirling cycle, but the Brayton reheat cycle compares favorably with the latter at least from a thermodynamic point of view for space power systems.

Summary

Preliminary studies of a closed Brayton cycle conversion system for ARIANE 5 nuclear power applications have been initiated in France. An adequate adaptation to possible radiator areas is searched. Power level and mass requirements can be met by using a simple cycle but it appears that another interesting solution could be a reheat, nonintercooled cycle which presents some favorable aspects for space.

It is certain that several questions in this field have to be discussed with conversant specialists.

Unless deployable radiators could be used, power levels higher than about 150 kWe would require high-temperature systems involving the utilization of refractory alloys.

Acknowledgments

The two first phases (1983–1984; 1984–1986) of the French space nuclear power studies are cosponsored by the Government Agencies "Centre National d'Etudes Spatiales" and "Commissariat à l'Energie Atomique."

The sponsoring Agencies and the author wish to gratefully acknowledge the Garrett Corporation, Phoenix, AZ, and particularly Mr. A. Pietsch, for information about various advanced Brayton Cycle power systems.

References

1 Poher, C., Cacheux, J., Bliaux, J., and Tilliette, Z. P., "Space Electronuclear Generators: Comparison Between Different Kinds of Energy Conversion Methods," I.A.F. Conference, Lausanne, 1984, Paper No. 285.

2 Poher, C., et al., "French Activity on Space Nuclear Power Systems," Second Symposium on Space Nuclear Power Systems, Albuquerque, NM, Jan. 14–16, 1985, Paper No. MS-2.

3 Carré, F., Proust, E., and Schwartz, J. P., "Liquid Metal Versus Gas-Cooled Reactor Concepts for a Turbo-Electric Powered Space Vehicle," Second Symposium on Space Nuclear Power Systems, Albuquerque, NM, Jan. 14–16, 1985, Paper No. RS-1.

4 English, R. E., "Power Generation From Nuclear Reactors in Aerospace Applications," NASA Technical Memorandum 83342, Symposium on Advanced Compact Reactors, Washington, D.C., Nov. 15–17, 1982.

5 Garrett Corporation, "Closed Brayton Cycle Applications," Garrett Company Reports, Phoenix, AZ, 1979–1983.

6 Layton, J. P., "Reactor/Brayton Power Systems for Nuclear Electric Spacecraft (NEP 400 kWe Project, Garrett Power System)," *15th Intersociety Energy Conversion Engineering Conference*, Seattle, WA, Aug. 18–22, 1980, pp. 732–737.

7 Parker, G. H., Pierce, B. L., and Thompson, R. E., "Design Considerations for Nuclear Reactor Gas Turbine Space Power Systems," ASME Paper No. 83-GT-20.

8 Anderson, R. V., "A Lithium-Cooled Reactor-Brayton Turboelectric Power Converter Design for 100 kWe Class Space Reactor Electric Systems," *19th Intersociety Energy Conversion Engineering Conference*, San Francisco, CA, Aug. 18–24, 1984, pp. 481–486.

9 Pietsch, A., and Trimble, S., "Space Station Brayton Cycle Power System," *20th Intersociety Energy Conversion Engineering Conference*, Miami Beach, FL, Aug. 18–23, 1985, pp. 1.119–1.124.

10 Tilliette, Z. P., "Utilization of a Brayton Cycle Energy Conversion System in Space Nuclear Power Applications," Second Symposium on Space Nuclear Power Systems, Albuquerque, NM, Jan. 14–16, 1985, Paper No. EC-8.

11 Moriarty, M. P., and French, E. P., "Optimization of a Heat-Pipe-Cooled Space Radiator for Use With a Reactor-Powered Stirling Engine," Second Symposium on Space Nuclear Power Systems," Albuquerque, NM, Jan. 14–16, 1985, Paper No. TM-3.

R. Castillo
Product Reliability Department,
Turbine and Generator Division,
Westinghouse Canada Inc.,
Hamilton, Ontario, Canada L8N 3K2

A. K. Koul
Structures and Materials Laboratory,
National Research Council,
Ottawa, Ontario, Canada K1A 0R6

E. H. Toscano
Centro Ceramico—Bologna,
40138 Bologna, Italy

Lifetime Prediction Under Constant Load Creep Conditions for a Cast Ni-Base Superalloy

Creep and stress-rupture properties of cast IN-738LC turbine blades have been analyzed to review the suitability of the Monkman–Grant relationship as a reliable life prediction method where $t_r \dot{\epsilon}_s^m = C$ *and* m *and* C *are material constants. The constants* m *and* C *in the Monkman–Grant relationship are temperature dependent and the relationship predicts lives within a factor of ±4 relative to the observed values. A modified form of this relationship is derived where* $(-b\, t_r^{n_1} + t_r)\, \dot{\epsilon}_s^{m_1} = K$ *and* b, n, m_1, *and* K *are material constants. The modified relationship is more accurate and predicts lives within a factor of 2 relative to the observed values. The constants* b, n, m, *and* k *are independent of stress and temperature.*

1 Introduction

Nickel-base superalloys are widely used in the manufacture of hot gas path rotating turbine components. IN-738LC is one such conventional gamma prime strengthened superalloy containing a high percentage of chromium which is extensively used in industrial gas turbines. The alloy was selected for turbine blade application because of its excellent hot corrosion resistance and good creep properties in the hot isostatically pressed (HIP) and heat treated (HT) condition. The HIP-HT thermal cycle used in these blades was developed by WECAN to meet these specific requirements.

In applications where components are subjected to elevated temperatures under low to medium stresses for prolonged periods of time, creep is known to be the major form of deformation under service conditions. However, questions always arise regarding the remaining useful life of turbine blades under assumed future operating conditions. The remaining life prediction becomes particularly difficult in components whose design lives are originally established by extrapolating uniaxial short term creep data, and consequently, the future service life cannot be accurately determined.

Analysis of creep deformation and prediction of creep life are complex tasks, and there are no established guidelines for testing and analysis. Creep-rupture life prediction is particularly difficult because of the length of time needed to confirm theoretical predictions experimentally. A further complication arises from the microstructural degradation that takes place in Ni-base superalloys during long-term exposure at high temperatures. Since creep behavior is structure sensitive, the creep response will depend on the microstructural stability and large reductions in creep strength and ductility may result from service-induced microstructural degradation [1, 2]. Due to the complexities associated with obtaining a fundamental understanding of the creep properties of Ni-base superalloys, empirical approaches have normally been used to extrapolate creep-rupture data [3]. These empirical extrapolation procedures have also been applied to predict the remaining life of components in service. Of the many empirical relationships proposed to analyze data from accelerated uniaxial constant-load creep tests, one which is most prominent is that originally proposed by Monkman and Grant [4]. Although the applicability of the Monkman–Grant (MG) relationship to complex engineering alloys has been demonstrated [4, 5] attempts have seldom been made to examine its usefulness in predicting the remaining useful lives of service exposed cast nickel-base superalloy components. The purpose of the present paper is to examine the usefulness of the MG relationship as a life prediction tool and to explore the possibility of improving its accuracy through various modifications.

2 Experimental Materials and Methods

The nominal chemical composition of the experimental material IN-738LC in weight percent is given below:

C	Cr	W	Co	Al	Ti	Nb	Ta	Zr	B	Ni
0.09	16.0	2.5	8.3	3.4	3.39	0.7	1.7	0.03	0.01	Bal

The creep data were generated on four different material conditions. These were:

1 Material in the cast, hot isostatically pressed, and heat treated condition.

2 Material in three conditions of service exposure, 13,300, 13,600, and 14,159 hr of service.

The material in the unexposed condition was Hipped at 1473 K for 2 hr and controlled furnace cooled to 1393 K and then fast cooled. The material was then solution heat-treated at 1393 K for 2 hr followed by an air cool and aged at 1118 K

Contributed by the Gas Turbine Division of The American Society of Mechanical Engineers and presented at the 31st International Gas Turbine Conference and Exhibit, Düsseldorf, Federal Republic of Germany, June 8–12, 1986. Manuscript received at ASME Headquarters February 28, 1986. Paper No. 86-GT-241.

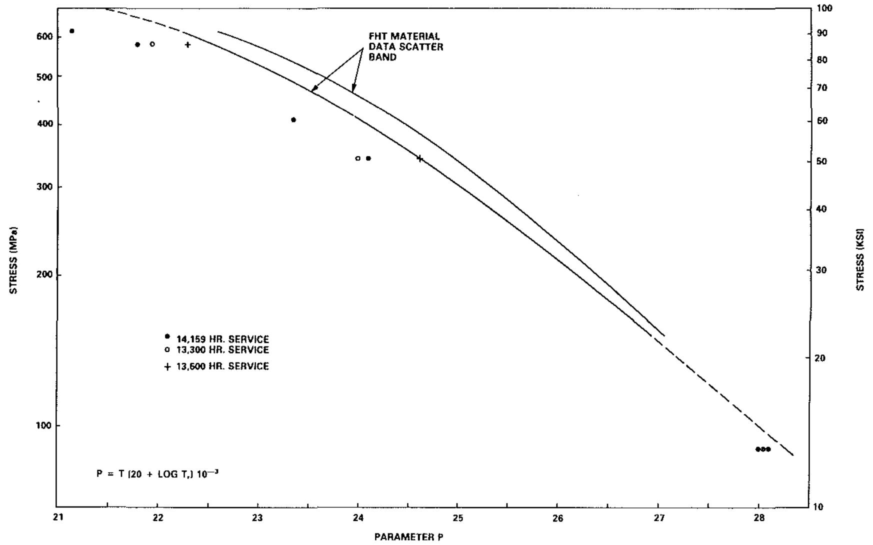

Fig. 1 Larson-Miller plot ($P = T(20 + \log t_r) \times 10^{-3}$, where T is in K and t_r in hr) of cast and hipped IN-738LC turbine blades showing unexposed and service exposed creep-rupture properties

for 24 hr followed by an air cool. Similar treatments had been applied to the service exposed blades, prior to their operation in various machines.

In the fully heat treated condition, the alloy contained a bimodal gamma prime (γ') distribution within the gamma matrix (γ) consisting of primary cuboidal γ' and secondary spheroidal γ', with two main carbide phases, MC carbides and discrete grain boundary M_{23} C_6 carbides. A more comprehensive description of the microstructure has been reported by Bieber and Mihalisin [6].

The creep specimens were machined out of blade airfoils in a spanwise direction, in order to ensure that the test stress was in the same direction as the major service stress caused by centrifugal loading. Creep rupture specimens having 4.0 mm gage diameter and 19.0 mm gage length were tested. All specimens were provided with shoulder grooves for extensometer attachment. The creep tests at constant load were conducted at temperatures ranging between 1033 and 1269 K and stresses ranging between 90 and 620 MPa. The test stresses and temperatures were chosen in a manner such that a direct comparison between the service exposed and unexposed material could be made under similar testing conditions. In addition, a selected number of tests were also conducted at the average operating stress.

3 Results and Discussion

3.1 Life Prediction Based on Time-Temperature Parameters. The search for an accurate method for predicting creep life during long-time, high-temperature service has led to the development of a number of time-temperature parameters which can be used to predict long-term creep behavior by extrapolating short-term creep data [7–11].

Based on operational parameters, a blade creep life well in excess of 10^5 hr was calculated for IN-738LC blades. The blade life was extrapolated from accelerated high-stress–high-temperature data using a widely accepted parametric technique proposed by Larson and Miller [7] since testing under blade operating conditions was obviously impractical. The Larson-Miller parameter has been shown to give reliable predictions so long as no microstructural changes occur in the blade alloy during prolonged exposure in a high-temperature environment. Should microstructural changes occur then the actual test results will be lower than the extrapolated values. No such changes were anticipated in IN-738LC blades because low operating temperatures were predicted during design stages of the machines.

However, accelerated stress rupture tests on specimens machined from the turbine blades that had been in operation for various time periods showed an increasing reduction in creep rupture life with operating time relative to the creep rupture life of new material (Fig. 1). Microstructural examination of the material showed significant changes in the morphology of the gamma prime and carbide distribution [12]. The gamma prime was growing and grain boundary M_{23} C_6 carbides were increasing in volume fraction. It is generally recognized that nickel-base superalloys are microstructurally metastable during prolonged exposures at high temperatures. For example, the primary MC carbides are metastable and undergo a complex series of transformations to form thermodynamically stable carbides. In addition, temperature and stress assisted growth of the gamma prime precipitates takes place through a diffusion controlled Ostwald ripening type mechanism during service. Such microstructural changes lead to a progressive loss of creep strength at service temperatures and stresses. Inevitably, rupture life extrapolations based on short-term creep rupture tests, where the type and magnitude of microstructural degeneration can be very different from that incurred during service, lead to errors in actual long-term life prediction.

All parametric methods however assume that the deformation and fracture modes of the material remain unchanged irrespective of the test or service conditions used. Consideration of the parametric methods in terms of the above damage processes indicates reasons for their unreliability and unsuitability as extrapolation techniques [13, 14].

3.2 Relation Between Time to Rupture and Minimum Creep Rate. The use of creep-rupture tests to assess the remaining creep life of materials after prolonged service exposure at high operating temperatures has long held appeal over other methods because it directly attempts to measure the required property.

Under high-temperature creep conditions, fracture usually occurs in an intergranular manner by the formation, growth, and link-up of grain boundary cavities which leads to the crack formation or by the development of oxidized surface cracks or a combination of both processes. Irrespective of the detailed mode of fracture, the creep characteristics of simple crystalline solids with a certain grain size are normally assessed

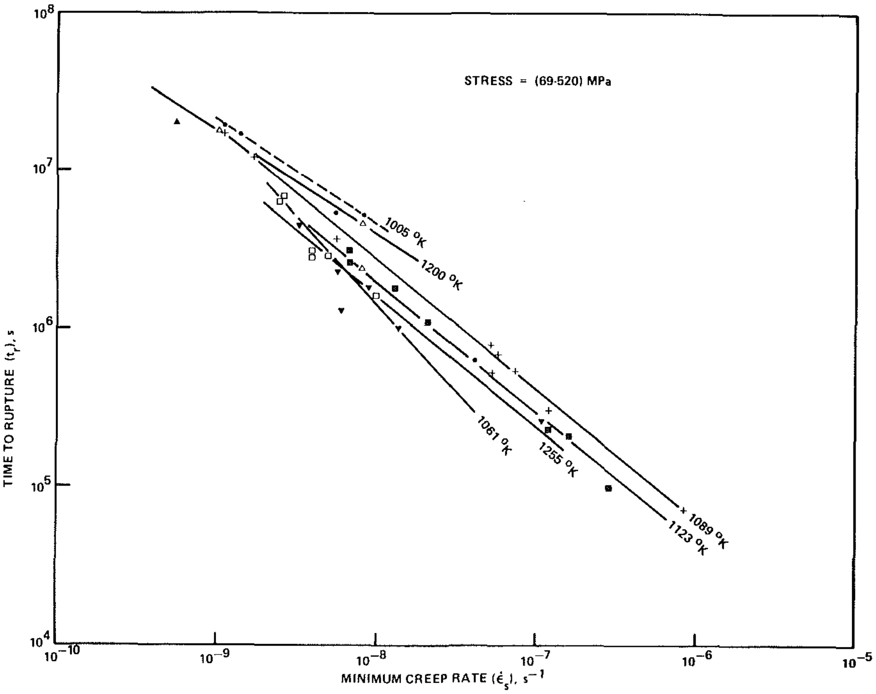

Fig. 2 Dependence of the time to rupture on the minimum creep rate, for IN-738LC (Monkman-Grant relationship)

by reference to the variation of the secondary or minimum creep rate $\dot{\epsilon}_s$ and the rupture life t_r, with stress σ and temperature T, using a power law relationship of the form

$$\frac{1}{t_r} \propto \dot{\epsilon}_s = A\sigma^m \exp - Q_c/RT \tag{1}$$

The processes governing creep and creep fracture in different stress-temperature regimes are then usually considered in relation to the magnitudes of the stress exponent n and the activation energy for creep Q_c. However, this standard approach leads to numerous theoretical and practical problems, especially for precipitation hardened alloys. The central problem in the development of a quantitative relationship between the variables is the lack of suitable parameters to quantify changes in the creep curve shape as a function of microstructure and testing conditions. The estimation of rupture life under creep conditions then becomes a considerable problem.

Many empirical relationships between the steady state or minimum creep rate $\dot{\epsilon}_s$ and the time to rupture t_r have been proposed to analyze data from accelerated uniaxial constant-load creep-rupture tests. The object has been to predict the time to rupture from relatively short time laboratory tests on the basis of the minimum creep rate, since the time to reach the steady-state creep rate usually comprises only a small portion of the time to rupture. The relationship between these quantities for wrought alloys is most commonly described by the relation suggested by Monkman and Grant [4] where the time to rupture and steady-state creep rate are correlated by a function of the form

$$t_r \, \dot{\epsilon}_s^m = C \tag{2}$$

where m and C are material constants. The importance of this relation is considerable. If constants m and C for a given material are known, it is possible to predict the time to rupture simply by measuring the minimum creep rate without any knowledge of either the fracture mechanism or the failure strain.

3.2.1 Assessment of Monkman-Grant Relationship. A selected number of our creep test results are presented in Table 1. In contrast to the results reported by Finnie and Bayce [15] on 9 Cr–1 Mo steel and Cullen et al. [16] on a 1.25 Cr–0.5 Mo steel, who found that the creep lives at high stresses of the service exposed material were reduced while those at low stresses were essentially unchanged. However, postexposure creep tests on long-term service exposed IN-738LC indicated that the effect on the creep properties can be considerable, Table 1. The creep life was reduced by an order of magnitude at high stresses and to a lesser extent at low stresses (90 MPa). This degradation in properties was primarily attributed to microstructural changes in the material during service because creep cavities were not detected in the service exposed material. This theory was substantiated by creep-rupture testing of the service exposed material after a full heat treatment (FHT), where the original microstructure and properties were restored [12]. Evidently, the microstructural state of the material will influence the contributions of various deformation mechanisms toward overall deformation and ultimately the rupture time.

Table 1 Creep test results in the fully heat treated and service exposed IN-738LC

Exposure Time hr.	Test Conditions Temp. K	Stress MPa	Minimum Creep Rate s-1		Rupture Time s	
FHT	1061	620.5	2.1	10^{-6}	2.8	10^4
14,159	1061	620.5	6.3	10^{-5}	1.3	10^3
FHT	1033	586.1	1.3	10^{-7}	3.1	10^5
13,300	1033	586.1	1.8	10^{-6}	3.1	10^4
FHT	1089	413.7	5.5	10^{-8}	6.9	10^5
14,159	1089	413.7	8.5	10^{-7}	7.2	10^4
FTH	1102	344.7	3.9	10^{-8}	1.1	10^6
14,159	1102	344.7	3.6	10^{-7}	2.0	10^5
FHT	1250	89.6	5.8	10^{-9}	2.3	10^6
14,159	1250	89.6	9.0	10^{-9}	1.8	10^6
FHT	1261	89.6	7.7	10^{-9}	1.3	10^6
14,159	1261	89.6	1.9	10^{-8}	9.8	10^5

Graphic representations of the time to rupture versus the steady-state creep rate based on the Monkman-Grant relationship for IN-738 data collected from a number of different sources [17–22] and from data generated in the present study are illustrated in Fig. 2. The scatter band is almost an order of magnitude in width. The scatter of the data is certainly due to

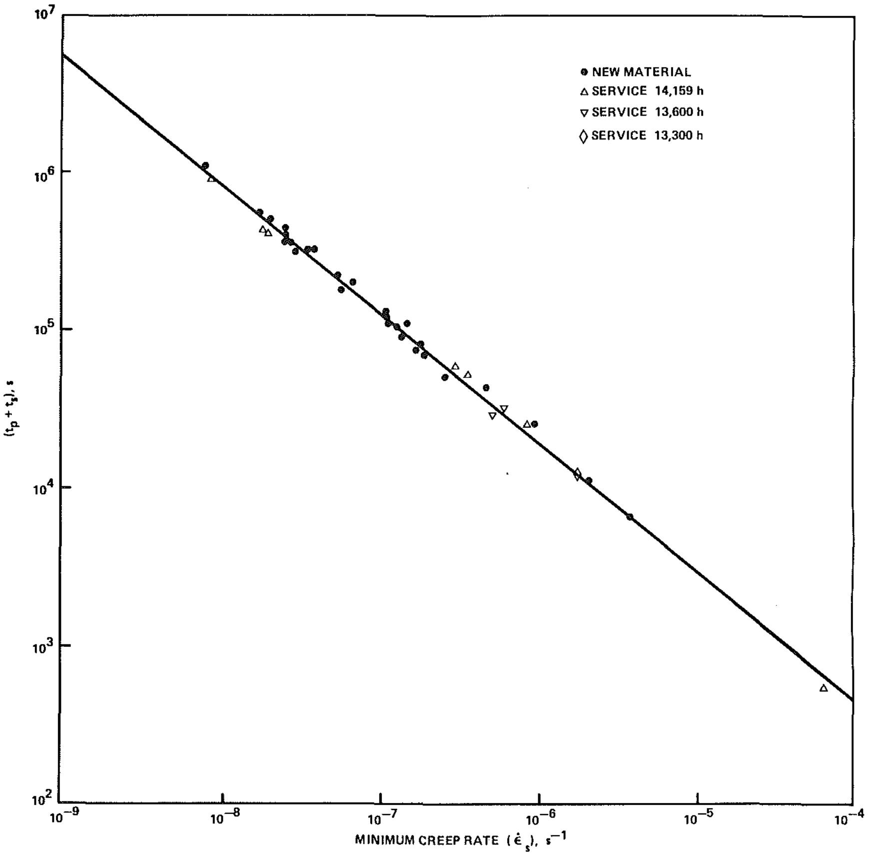

Fig. 3 Dependence of primary plus secondary, creep life on the minimum creep rate for cast IN-738LC

the temperature dependence of the material constants, rather than due to any significant variations in alloy composition from one heat to another [23-25]. A scatter of this magnitude in the plots of time to rupture versus the steady-state creep rate renders equation (2) unreliable as a life prediction tool.

3.2.2 Modifications of Monkman-Grant Relationship. Several modifications to the Monkman-Grant relationship that incorporate creep strain parameters have been proposed which substantially reduce the scatter in experimental data [13, 23]. However, these relationships cannot readily be used for life prediction because various creep strain values need to be known at service temperatures and stresses. In addition, some comment should also be made with respect to life criteria based on creep strain to ensure acceptable limits. Long-term creep tests performed at the design stress and temperatures above those expected in service indicated that rupture occurs at low creep strains (2 to 3 percent), well below the values established from short-term testing. When it became apparent from experimental evidence that ductility dropped with exposure time, the use of an arbitrary creep strain as a failure criterion was not totally practical and therefore, greater attention was directed toward rupture time rather than creep strain as the correlating parameter.

For IN-738LC alloy, as with most nickel-base superalloy materials, the creep curve shape presents a distinctive pattern. While it exhibits the usual three stages of creep, the time spent in the secondary creep stage is short and considerable time is spent in the tertiary stage. Analysis of the creep curves suggests that factors other than those considered in the Monkman-Grant relationship play a dominant rôle in cast IN-738LC. The assumption that tertiary creep is a variable of the secondary creep rate in equation (2) seems inappropriate. The product of the minimum creep rate and the primary plus secondary creep life ($t_p + t_s$) is an approximate measure of the elongation taking place at the end of the secondary stage, whereas the tertiary component represents a regime of creep strain that is accumulated well beyond the secondary creep stage and therefore, may not be directly related to $\dot{\epsilon}_s$. The tertiary component of creep life was thus isolated from the overall stress-rupture life. In both service exposed and unexposed material the sum of primary creep life plus the secondary creep life, ($t_p + t_s$), varying as a function of the steady-state creep rate $\dot{\epsilon}_s$, was then plotted on a log-log scale, Fig. 3. All symbols given in Fig. 3 represent experimental data generated in the present study. The open triangles and rhombus represent the data from blades that were retired from service at different times. The solid line in Fig. 3 represents the best-fit curve to the experimental data and this can be represented by a modified Monkman-Grant equation of the form

$$(t_p + t_s) = K\,\dot{\epsilon}_s^{m_1} \tag{3}$$

where K and m_1 are material constants.

A rigorous analysis of the experimental results also indicated that the tertiary creep life exhibits a linear relationship with the rupture life on a log-log plot. Taking this into account, the experimental data could be represented by the following relation

$$t_t = b t_r^{n_1} \tag{4}$$

where b and n_1 are constants and t_t and t_r are the tertiary and stress-rupture lives, respectively. Figure 4 shows a representation of the data plotted according to equation (4) over a wide range of stresses and temperatures. The values of the constants leading to the best fit of the data presented in Figs. 3 and 4 were evaluated by means of a linear regression computer program. The coefficients were determined by least-squares fit method and the analysis of variances is summarized in Table

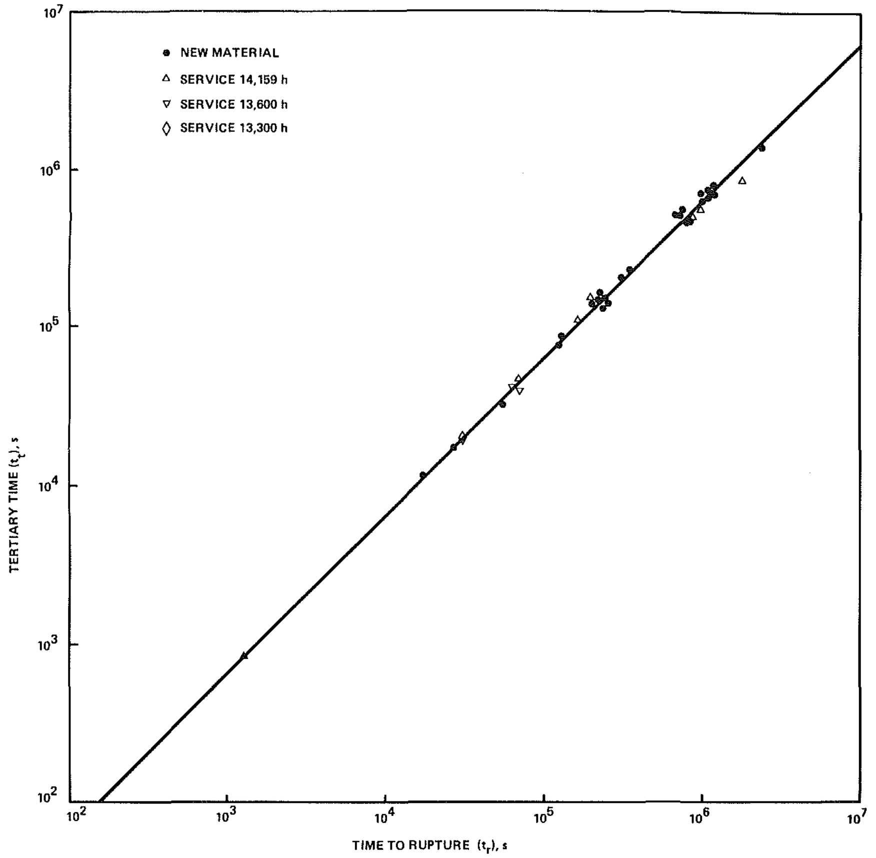

Fig. 4 Time to rupture dependence of the tertiary life for cast IN-738LC

Table 2 Experimental values of material constants in equations (3) and (4)

Equation	Constants	Coef. of Det. (R^2)
[3]	k = 0.2199 m = 0.8246	0.995
[4]	b = 0.6515 n = 0.996	0.995
[7]	Same as in Equations [3] and [4]	0.98

Table 3 Experimental values of constants in equations (2) and (8)

Equation	Temperature K	Constants c	m	Coef. of Det (R^2)
[2]	1005	14.38	0.68	0.98
	1061	0.86	0.79	0.97
	1089	2.14	0.77	0.96
	1123	5.98	0.95	0.97
	1200	6.38	0.71	0.92
	1255	1.86	0.73	0.92
[8]	1033 to 1269	0.631	0.8346	

2. The best fit lines through the data suggest that the material constants in equations (3) and (4) are independent of stress and temperature.

Equations (3) and (4) can further be combined to give a generalized relationship for t_r alone, where

$$t_r = t_p + t_s + t_t \tag{5}$$

Rearranging and substituting equations (3) and (4) into equation (5) and solving for t_r gives the following expression

$$t_r - bt_r^{n_1} = K\,\dot{\epsilon}_s^{-m_1} \tag{6}$$

or

$$(-bt_r^{n_1} + t_r)\dot{\epsilon}_s^{m_1} = K \tag{7}$$

From equation (6), a linear relationship on a log-log plot is to be expected between the time to rupture and the minimum creep rate upon substituting for constants b and n_1 from equation (4). Figure 5 shows a log-log plot of $(-bt_r^{n_1} + t_r)$ against the minimum creep rate $\dot{\epsilon}_s$ for the data generated on cast IN-738LC blades in the unexposed and service exposed conditions.

When the n_1 value in equation (4) equals unity, equation (7) reduces to

$$t_r\,\dot{\epsilon}_s^{m_1} = K/(1-b) = C \tag{8}$$

where equation (8) has the same form as equation (2). In the case of IN-738LC an n_1 value of 0.996 was observed experimentally, Table 2. An n_1 value of 0.996 is very close to unity, yet the rupture life predictions based on equations (2) or (8) lie within a factor of ±4, Figs. 2 and 6. In contrast, the *lifetime predictions computed through equation* (7) lie within a factor of ±2 of the observed lives in Fig. (7).

The correlation based on the modified treatment of the creep data clearly shows that the creep lives were consistently predicted with greater accuracy by equation (7) rather than by equations (2) or (8), Figs. 6 and 7. These results are particularly satisfying because the majority of the data used for life prediction involved tests, heat treatments, and heats of material which were not used to establish the baseline constants for IN-738LC in equation (7) [18, 19, 21]. Only the constant load creep data generated in the present study were used to determine the necessary material constants. It is also evident that equations (2) and (8) will only predict lives with greater accuracy providing the value of n_1 in equation (4) ex-

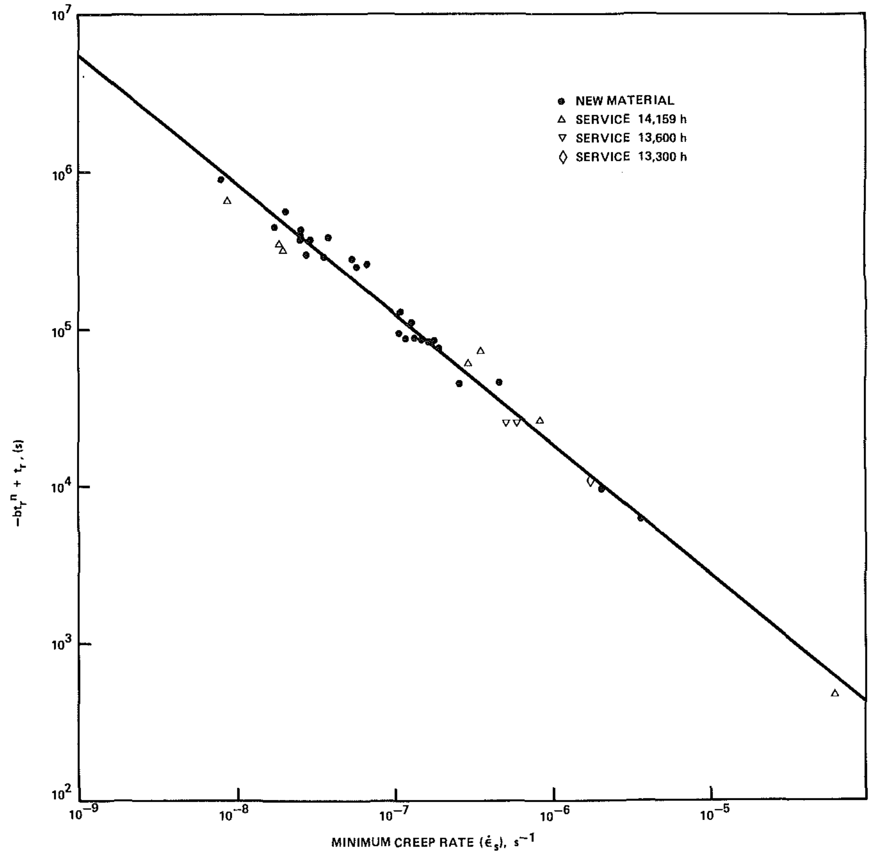

Fig. 5 Logarithmic plot of $-bt_r^n + t_r$ versus the minimum creep rate, equation (6)

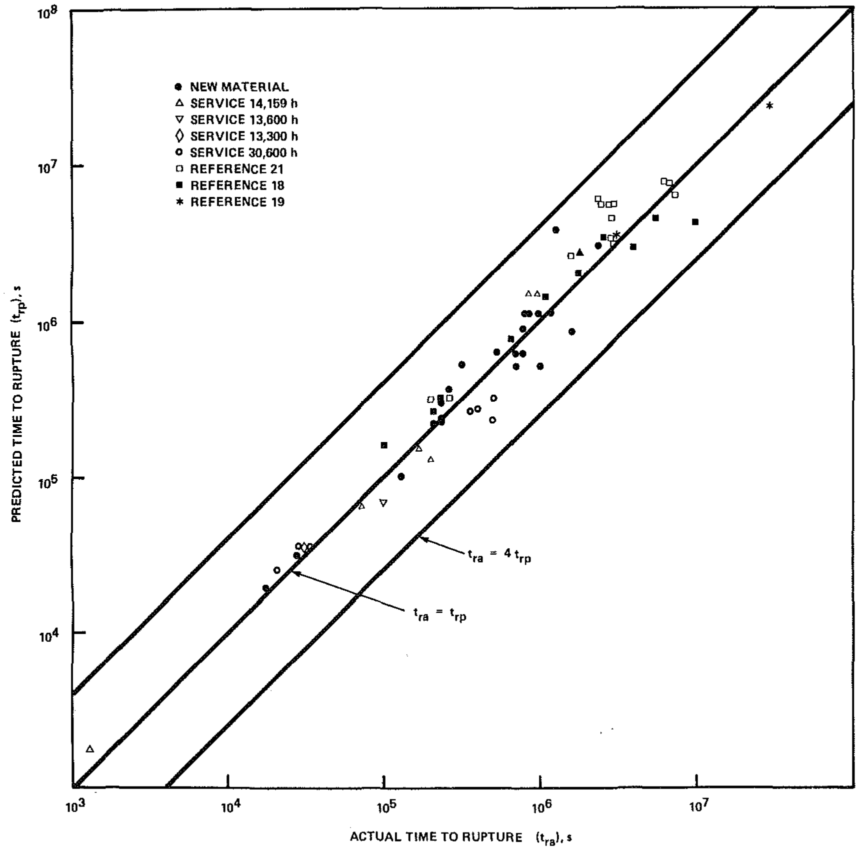

Fig. 6 A comparison between the measured creep life and those calculated using equation (8) for IN-738LC

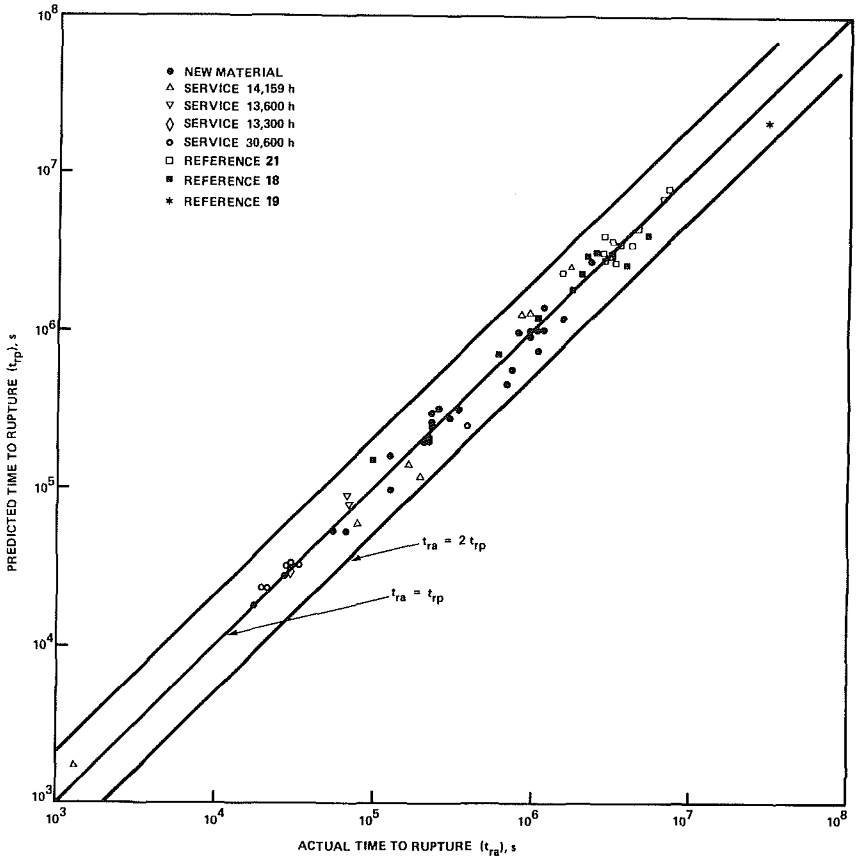

Fig. 7 A comparison between the measured creep life and those calculated using equation (7) for IN-738LC

actly equates unity, i.e., 0.999. Even an n_1 value of 0.996 cannot be treated as unity in equation (4), since life predictions based on equation (8) lie only within a factor of ±4. The scatter problems of equation (8) are appropriately compensated by the $-bt_r^{n_1}$ term in equation (7). So far, all discussion has been related to cast IN-738LC. It is expected that a similar analysis would be applicable to a material which shows a temperature dependence in the Monkman-Grant constants, providing that the primary, the secondary, and the tertiary lives are determined accurately from the creep curves.

4 Conclusions

A life prediction method, originally proposed by Monkman-Grant, has been investigated for its ability to predict the long-term rupture life from relatively short-term laboratory creep tests in IN-738LC turbine blades. Creep tests at constant load were conducted on bars machined from investment cast blades in the cast, hipped, and fully heat treated and service exposed conditions. The tests were conducted at temperatures ranging between 1033 and 1269 K and stresses ranging between 90 and 620 MPa. The results clearly show that the material constants in the Monkman-Grant relationship are temperature dependent which leads to a large scatter in the log t_r versus $\dot{\epsilon}_s$ plots. The MG relationship also produces a poor correlation between time to rupture and minimum creep rate in service exposed material and predicts lives within a factor of ±4. In an attempt to overcome these restrictions, an alternative procedure for the treatment of creep data is proposed where the primary, the secondary, and the tertiary creep life components are extracted from the overall creep curve. A strong correlation between the tertiary creep life versus the rupture life and the primary plus the secondary creep life versus the observed minimum creep rate is indicated over a wide range of creep loads and temperatures. Using these correlations, a relationship between t_r and $\dot{\epsilon}_s$ is derived and the new relationship in its functional form is given by

$$(-bt_r^{n_1}+t_r)\dot{\epsilon}_s^{m_1}=K$$

where b, K, n_1, and m_1 are material constants that are independent of the stress and test temperature. Rupture life predictions based on this relationship have been compared with the observed rupture lives taken from several sources within the literature and data generated in this study at appropriate creep rates. These predictions are in good agreement with the observed rupture life values and only vary by a factor of two across the mean.

This approach has advantages over the existing relationship because it provides a single framework through which short-term test data can be extrapolated to provide an estimate of long-term service lives.

Acknowledgments

This paper is published by permission of Turbine and Generator Division of Westinghouse Canada Inc., Hamilton, Ontario, Canada. The revision of the manuscript by Dr. J-P. A. Immarigeon of the National Research Council is very much appreciated.

References

1 Sullivan, C. P., and Donachie, M. J., *Metals Eng. Quarterly*, Vol. 7, No. 1, 1967, p. 36.
2 Collins, H. E., *Met. Trans.*, Vol. 5, No. 1, 1974, p. 189.
3 Conway, J. B., *Numerical Methods for Creep and Fracture Analysis*, Gordon and Breach, eds., New York, 1967, p. 19.
4 Monkman, F. C., and Grant, N. J., *Proc. ASTM*, Vol. 56, 1956, p. 593.
5 Dennison, J. P., Holmes, P. D., and Wilshire, B., *Materials Science and Eng.*, Vol. 33, 1978, p. 35.

6 Bieber, C. G., and Mihalisin, J. R., Technical Paper 695-T-OP, The Int. Nickel Co., Inc., Paul D. Merica Research Laboratories, Sterling Forest, Suffern, NY, Nov. 11, 1970.

7 Larson, F. R., and Miller, J., *Trans. ASME*, Vol. 74, 1952, p. 765.

8 Orr, R. L., Sherby, O. D., and Dorn, J. E., *Trans. ASM*, Vol. 46, 1954, p. 113.

9 Manson, S. S., and Haferd, A. M., NASA TN-2890, Mar. 1953.

10 Manson, S. S., and Succop, G., ASTM Spec. Tech. Publication, STP No. 174, 1956, p. 40.

11 Manson, S. S., and Ensign, C. R., "A Specialized Model for Analysis of Creep Rupture Data by the Minimum Commitment Station Function Approach," NASA Tech. Memo, NASA TM-X-52999, 1986.

12 Koul, A. K., and Castillo, R., "Assessment of Service Induced Microstructural Damage and Its Rejuvenation in Turbine Blades," submitted to *Met. Trans.*, 1985.

13 Koul, A. K., Castillo, R., and Willett, K. P., *Mat. Science and Eng.*, Vol. 66, 1984, p. 213.

14 Sidey, D., et al., *Canadian Metallurgical Quarterly*, Vol. 18, 1979, p. 49.

15 Finnie, I., and Bayce, A. E., *Proc. of Joint Int. Conf. on Creep*, The Institute of Mech. Eng., London, Vol. 1, 1963, p. 5-1.

16 Cullen, T. M., Rohrig, I. A., and Freeman, J. W., *Trans. ASME*, 1965, Paper No. 65-WA/Met-3.

17 Mazzei, P. J., Westinghouse Canada Inc., Tech Reports PAL78-76 and PAL78-77, 1978.

18 Stevens, R. A., and Flewitt, P. E. J., *Acta Met.*, Vol. 29, 1981, p. 867.

19 Tipler, H. R., "Maintenance in Service of High Temperature Parts," AGARD CP-317, 1981, Paper No. 12-1.

20 "International Nickel INCO Alloy IN-738—Technical Data," International Nickel Company, Inc., New York, 1981.

21 Tipler, H. R., Lindblom, Y., and Davidson, J. H., *Conf. Proceed. on High Temp. Alloys for Gas Turbines*, Leige, Belgium, Sept. 25–27, 1978; Applied Science Publishers Ltd., London, 1978, p. 359.

22 Beck, C. G., and Burke, M. A., Westinghouse, Research and Development Centre, Research Memo 81-124-STABL-M2, Sept. 25, 1981.

23 Dobes, F., and Milica, K., *Met. Sci.*, Vol. 10, 1976, p. 382.

24 Toscano, E. H., and Bocek, M., *Journal of Nuc. Materials*, Vol. 96, 1981, p. 29.

25 Ellis, F. V., and Bymun, J. E., *ASME Int. Conf. on Advances in Life Prediction Methods*, D. A. Woodford and J. R. Whitehead, eds., Albany, New York, Apr. 18–20, 1983, p. 337.

26 Povolo, F., *Journal of Mat. Science*, Vol. 20, 1985, p. 2005.

Multiaxial Life Prediction System for Turbine Components

S. T. Arvanitis
Senior Analytical Engineer.

Y. B. Symko
Senior Analytical Engineer.

R. N. Tadros
Chief, Structures and Dynamics.

Pratt and Whitney Canada Inc.,
Montreal, Canada

The objective of this paper is to present a complete three-dimensional life prediction system which was developed for turbine engine components. It will deal primarily with turbine blades and vanes which are subjected to hostile thermal and combustion environments under load which creates cyclic and/or steady multiaxial stress and strain fields. All of the above factors combined are detrimental to the service life of these components and need very careful consideration at the design stage. The developed multiaxial system for a mission includes evaluation of transient metal temperatures, corresponding elastic and inelastic strains, creep strains, and subsequently creep/fatigue lives. The calculations are performed using the ductility exhaustion method. The maximum principal normal strain ranges used in the life analysis are found by a developed procedure for a multiaxial system. The concept is based on analyzing all of the time steps computed in the mission, in order to develop the maximum principal normal strain range whose direction and magnitude is strictly a function of the component geometry and mission loading. The mission creep is then developed by maximizing a cumulative creep function. Directional consistency is maintained in accumulating creep/fatigue damage with respect to the incurred multiaxial stress and strain fields. Also the most damaging mission modes (creep or fatigue) will be separated. Further development in the model includes the capability of analytically obtaining the fatigue curve for any ratio R *of minimum to maximum strain using baseline fatigue material properties* (R = −*1.0*)*. Application of the model to an actual uncooled vane correlates well with test rig development experience.*

Introduction

Modern gas turbine engines are required to produce a large amount of thrust or shaft horsepower and also withstand very severe thermal conditions and high loads which arise during cyclic mission operation. The engine hot section experiences the full effect of the above factors because it is this section of the engine which develops power. Subsequently most of the life problems are encountered in this area. Typical failure modes are listed for each of the components that suffer degradation during engine operation, i.e., combustor liners (thermal fatigue, creep buckling, and corrosion), seals (wear), disks (low cycle fatigue), vanes (thermal low cycle fatigue and corrosion), and blades (thermal and high and low cycle fatigue, creep and corrosion).

In order to determine the life of these components during the design stage, one begins with a determination of the operating environment and a calculation of the thermal and mechanical loading to which they are subjected. With the exception of centrifugal loads on the blades and disks, the primary source of fatigue loading is due to the severe thermal cycling associated with each startup and shutdown of the engine, although high-frequency excitation problems are sometimes encountered as well.

Low cycle fatigue and thermal fatigue occur in component parts at highly localized regions. The strain in such small localized regions is larger than the surrounding region as a result of notches that concentrate it, or of constrained thermal expansion as in the case of thermal fatigue. The key feature is that the local strain is prevented from exceeding certain bounds due to the surrounding material which remains elastic. Hence, the local material is caused to cycle between approximately constant strain limits. When the local strains are large, inelastic strain occurs and the cyclic stress-strain behavior becomes nonlinear.

Creep damage is primarily encountered by turbine blades and combustion chambers which are subjected to constant centrifugal loading and internal gas pressure, respectively, in conjunction with high thermal gradients. Under creep, blades deform up to the point where interference occurs with the shroud or rupture thus limiting their useful life.

During the course of a mission these components are subjected to a combination of creep and fatigue which gives rise to cyclic damage accumulation and subsequently failure. To accurately determine these cyclic lives it becomes necessary to compute the transient and steady-state temperatures and the elastoplastic and creep strains of the component, using the engine mission. Past practice in airfoil inelastic stress analysis has been to use programs based on the beam theory assumption that plane sections remain plane. However this practice

---

Contributed by the Gas Turbine Division of The American Society of Mechanical Engineers and presented at the 31st International Gas Turbine Conference and Exhibit, Düsseldorf, Federal Republic of Germany, June 8–12, 1986. Manuscript received at ASME Headquarters February 21, 1986. Paper No. 86-GT-242.

produces very pessimistic airfoil lives due to the conservative nature of beam theory. In recent years nonlinear finite element computer programs have been developed that perform three-dimensional thermal, elasto-plastic stress and creep analysis. These nonlinear computer programs have been primarily used at engine development stages due to the extensive work and computing times involved. Once the cyclic stress-strain and creep behavior of the engine materials has been determined a finite element structural analysis may be performed. The result of the analysis is the local three-dimensional stress-strain-temperature versus time response of the material at critical locations in the component part. Finally, from a knowledge of the fatigue, creep, and fracture resistance of the materials, a prediction of the lifetime of the component part can be made.

This paper will focus primarily on the progress of the development of a multiaxial life prediction system using the ductility exhaustion approach. Application to a typical uncooled vane will also be described.

Multiaxial Creep/Fatigue Model

The components employed in the engine hot section are subjected to extremely high temperatures and corrosive environments in conjunction with high external loads. These components must retain adequate strength at high temperatures. In order to achieve this, cast nickel-based superalloys are used. The characteristics of these superalloys are good high-temperature creep strength and low ductility along with good high-temperature corrosion resistance. As a consequence these materials exhibit brittleness.

Tensile test results indicate that both shearing and normal stresses under axial loading are important in distinguishing the type of fracture. A brittle material loaded in tension will fail on the transverse plane, whereas a ductile material loaded in tension will fail in shear on the 45 deg plane. Therefore the concept of maximum principal normal stress or strain becomes very important in any life evaluation concerning brittle materials.

Mission Maximum Principal Normal Strain Range and Corresponding Mean Strain. In a turbine component mission, there will generally exist various strain cycles or subcycles along with constant condition time periods. A typical component will experience a triaxial stress or strain field. Due to the uniaxial nature of strain controlled fatigue tests all data refer to a principal normal strain range value.

It now becomes important to develop a set of relations enabling one to evaluate the maximum principal normal strain for a triaxial strain field varying in time. Figure 1 depicts a general triaxial state of strain also showing the normal strain tensor acting in an arbitrary direction defined by three angles (θ_x, θ_y, θ_z).

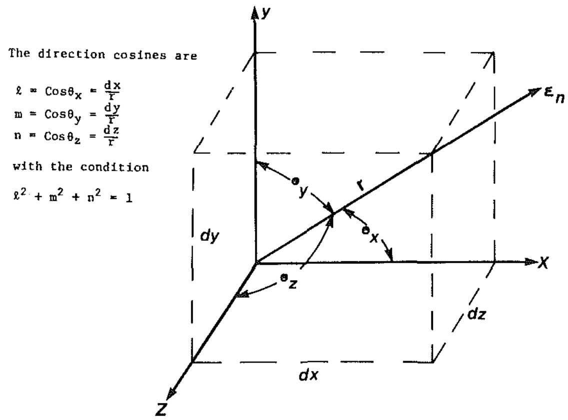

Fig. 1 Triaxial state of strain showing normal strain tensor

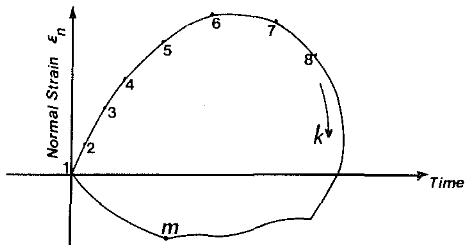

Fig. 2 Typical mission cycle with $k=1$, m strain points

The normal strain [1] may be written as a function of θ_x, θ_y, θ_x and all of the strain components ϵ_x, ϵ_y, ϵ_z, ϵ_{xy}, ϵ_{xz}, ϵ_{yz} as follows

$$\epsilon_n = \epsilon_x l^2 + \epsilon_y m^2 + \epsilon_z n^2 + 2\epsilon_{xy} lm + 2\epsilon_{xz} ln + 2\epsilon_{yz} mn \qquad (1)$$

In a typical mission cycle or subcycle there will be $k=1$, m strain points as shown in Fig. 2. In order to obtain the maximum principal normal strain range over the mission cycle or subcycle it will become necessary to evaluate

$$\sum_{k=1}^{m} (k-1) \qquad (2)$$

Nomenclature

A, B, C, D = creep function constant
A, B_{mis} = mission creep constants
a, b = fatigue ductility exponent and coefficient
F_p, F_s, F_t = primary, secondary, and tertiary creep curves
k = operational index
K = subscript refers to creep mission condition
m = number of mission calculation points
No, N = number of fatigue cycles to failure
N' = number of cycles after an elapsed 1/4 cycle
N_P = number of cycles repeated at a strain range
NCC = number of creep conditions in mission
R = strain ratio on maximum absolute strain
t = time
t_K = hold time at mission condition
t_{E_1}, t_{E_2} = incremental creep times elapsed in mission
t_{EQ_1}, t_{EQ_2} = equivalent creep time to fatigue cycles
x, y, z = Cartesian coordinate system
ϵ_{ij} = strain tensor
$\Delta\epsilon_{ij}$ = strain difference between time instances
ϵ_f = fracture strain in monotonic tension
$\epsilon_{\max}$ = maximum strain
ϵ_m = mean strain
$\epsilon_{\min}$ = minimum strain
ϵ_n = normal strain
ϵ_0 = initial strain upon loading
ϵ_{cum} = cumulative creep function for mission
λ = Lagrange multiplier or eigenvalue
$\theta_x, \theta_y, \theta_z$ = orientation angles for normal strain tensor
$\theta_{xp}, \theta_{yp}, \theta_{zp}$ = principal angles for normal strain range
σ_{ij} = stress tensor

Superscript

c = relating to creep

principal normal strain ranges. The normal strain range at any point in a component between any two mission times k and $k-1$ is defined as follows

$$\Delta\epsilon_n(\theta_x,\theta_y,\theta_z) = |\epsilon_n(\theta_x,\theta_y,\theta_z)_{k-1} - \epsilon_n(\theta_x,\theta_y,\theta_z)_k| \tag{3}$$

In order to be consistent with the definition of strain range and also with uniaxial strain controlled fatigue data, the directions of the normal strains at the two time instances k and $k-1$ must be the same. Thus the expression for the strain range derived from equation (3) now takes on the following form

$$\Delta\epsilon_n = |\Delta\epsilon_x l^2 + \Delta\epsilon_y m^2 + \Delta\epsilon_z n^2 + 2\Delta\epsilon_{xy} lm + 2\Delta\epsilon_{xz} ln + 2\Delta\epsilon_{yz} mn| \tag{4}$$

where the strain difference components are

$$\begin{aligned} \Delta\epsilon_x &= \epsilon_{x_k} - \epsilon_{x_{k-1}} & \Delta\epsilon_{xy} &= \epsilon_{xy_k} - \epsilon_{xy_{k-1}} \\ \Delta\epsilon_y &= \epsilon_{y_k} - \epsilon_{y_{k-1}} & \Delta\epsilon_{xz} &= \epsilon_{xz_k} - \epsilon_{xz_{k-1}} \\ \Delta\epsilon_z &= \epsilon_{z_k} - \epsilon_{z_{k-1}} & \Delta\epsilon_{yz} &= \epsilon_{yz_k} - \epsilon_{yz_{k-1}} \end{aligned} \tag{5}$$

The principal normal strain range will occur parallel to a plane oriented at three principal angles θ_x, θ_y, θ_z. In order to determine the three principal angles and thus the principal normal strain range, equation (4) must be maximized with respect to θ_x, θ_y, θ_z which are constrained by the following

$$l^2 + m^2 + n^2 = 1 \tag{6}$$

When a condition such as (6) is imposed on a function such as (4), the problem of determining the maximum and minimum of that function is called a problem of constrained maxima and minima with a side condition. By employing Lagrange multipliers the above problem may be transformed to a free maxima and minima problem. The expression for the strain range becomes as follows

$$\Delta\epsilon_n(\theta_x,\theta_y,\theta_z,\lambda) = \Delta\epsilon_n(\theta_x,\theta_y,\theta_z) + \lambda(l^2+m^2+n^2-1) \tag{7}$$

The condition for stationary value is applied

$$\begin{aligned} \frac{\partial}{\partial\theta_x}\Delta\epsilon_n(\theta_x,\theta_y,\theta_z,\lambda) &= 0 \\ \frac{\partial}{\partial\theta_y}\Delta\epsilon_n(\theta_x,\theta_y,\theta_z,\lambda) &= 0 \\ \frac{\partial}{\partial\theta_z}\Delta\epsilon_n(\theta_x,\theta_y,\theta_z,\lambda) &= 0 \end{aligned} \tag{8}$$

to yield a set of equations in matrix form

$$\begin{bmatrix} \Delta\epsilon_x + \lambda & \Delta\epsilon_{xy} & \Delta\epsilon_{xz} \\ \Delta\epsilon_{yx} & \Delta\epsilon_y + \lambda & \Delta\epsilon_{yz} \\ \Delta\epsilon_{zx} & \Delta\epsilon_{xy} & \Delta\epsilon_z + \lambda \end{bmatrix} \begin{Bmatrix} \cos\theta_x \\ \cos\theta_y \\ \cos\theta_z \end{Bmatrix} = \begin{Bmatrix} 0 \\ 0 \\ 0 \end{Bmatrix} \tag{9}$$

This is now a standard eigenproblem, where λ refers to the eigenvalue and $\cos\theta_x$, $\cos\theta_y$, $\cos\theta_z$ to the eigenvector. The solution of (9) will yield three eigenvalues (or principal strain ranges) and each eigenvalue will subsequently give rise to an eigenvector (or principal directions). The largest eigenvalue gives the principal value of maximum normal strain range and its three principal directions are obtained from the corresponding eigenvector, i.e.

$$\Delta\epsilon_n, \theta_{xp}, \theta_{yp}, \theta_{zp} \tag{10}$$

The above procedure is followed for all combinations in the mission cycle or subcycle (equation (2)) until the maximum principal normal mission (cycle or subcycle) strain range is determined. The corresponding principal angles θ_{xp}, θ_{yp}, θ_{zp} may now be employed to determine the mean strain and ratio (R) of minimum to maximum or maximum to minimum strain as follows. By definition the mean strain acting in the direction of the maximum principal normal strain range is

$$\epsilon_m(\theta_{xp},\theta_{yp},\theta_{zp}) = \frac{1}{2}|\epsilon_n(\theta_{xp},\theta_{yp},\theta_{zp})_k + \epsilon_n(\theta_{xp},\theta_{yp},\theta_{zp})_{k-1}| \tag{11}$$

The ratio R is defined as follows

$$\begin{aligned} &\text{for } |\epsilon_n(\theta_{xp},\theta_{yp},\theta_{zp})_{k-1}| > |\epsilon_n(\theta_{xp},\theta_{yp},\theta_{zp})_k|, \\ &\qquad R = \frac{\epsilon_n(\theta_{xp},\theta_{yp},\theta_{zp})_k}{\epsilon_n(\theta_{xp},\theta_{yp},\theta_{zp})_{k-1}} \\ &\text{for } |\epsilon_n(\theta_{xp},\theta_{yp},\theta_{zp})_k| < |\epsilon_n(\theta_{xp},\theta_{yp},\theta_{zp})_{k-1}|, \\ &\qquad R = \frac{\epsilon_n(\theta_{xp},\theta_{yp},\theta_{zp})_{k-1}}{\epsilon_n(\theta_{xp},\theta_{yp},\theta_{zp})_k} \end{aligned} \tag{12}$$

Evaluation of Principal Normal Mission Creep. During the course of an operating mission, hot turbine components are subjected to long constant loading time periods, which causes them to slowly permanently deform. At high temperatures this slow plastic deformation or creep deformation may proceed indefinitely and eventually the material fractures. The creep curve exhibits various stages. Directly on loading, the component undergoes an instantaneous strain. This is followed by the primary stage. The creep rate declines gradually in this region and eventually reaches a constant (steady-state) value in the secondary stage. In the tertiary stage the creep rate starts to accelerate and this leads to final fracture. Usually material creep data are obtained from uniaxial tests at various conditions. It is generally a function of the following variables, i.e.

$$\epsilon_{ij}^c = F(\sigma_{ij}, t, T) \tag{13}$$

where the σ_{ij} are the creep stresses, ϵ_{ij}^c are the creep strain components, and t and T are, respectively, time and temperature. The three stages of creep (primary, secondary, tertiary) may be described by a suitable piecewise continuous function, i.e.,

$$\epsilon_{ij}^c = F_p(\sigma_{ij}, t, T) + F_s(\sigma_{ij}, t, T) + F_t(\sigma_{ij}, t, T) \tag{14}$$

Depending on the shape of the creep curve for the particular material in question the function described by equation (14) may be of polynomial or exponential form.

The treatment of the creep problem may be described best upon consideration of a typical engine mission shown in Fig. 3. As may be seen, this figure depicts an aircraft engine mission with four constant-condition intervals: ground idle, takeoff, cruise, and ground idle.

As a simplified illustration of how the creep problem will be approached only the two most damaging creep conditions of takeoff and cruise will be considered for analysis.

Fig. 3 Typical aircraft engine mission

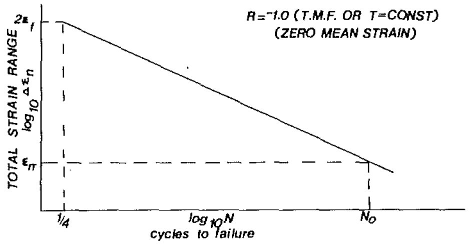

Fig. 4 Typical fatigue diagram

The component in question is analyzed for creep under takeoff and cruise conditions, separately (each condition is taken to rupture). The analytical tool to be employed is a three-dimensional F.E. creep analysis. Upon completion of the creep analysis for mission conditions 1 and 2 (Fig. 3) the nodal distribution for creep strain in all directions will be obtained for both mission creep hold times as follows

$$\epsilon_{ij}^c(t_1) \text{ and } \epsilon_{ij}^c(t_2) \tag{15}$$

Now having obtained all of the creep strain components as a function of time, for conditions 1 and 2 (Fig. 3) the expressions for the normal creep strain as a function of θ_x, θ_y, θ_z for each condition may now be developed as follows:

$$\epsilon_n^c(t_1) = \epsilon_x(t_1)l^2 + \epsilon_y(t_1)m^2 + \epsilon_z(t_1)n^2 + 2\epsilon_{xy}(t_1)lm + 2\epsilon_{xz}(t_1)ln + 2\epsilon_{yz}(t_1)mn \tag{16}$$

and

$$\epsilon_n^c(t_2) = \epsilon_x(t_2)l^2 + \epsilon_y(t_2)m^2 + \epsilon_z(t_2)n^2 + 2\epsilon_{xy}(t_2)lm + 2\epsilon_{xz}(t_2)ln + 2\epsilon_{yz}(t_2)mn \tag{17}$$

where t_1 and t_2 are the mission cycle hold times at conditions 1 and 2, respectively.

The next step is to determine the direction of maximum accumulated creep damage. This may be found upon maximization of a cumulative creep function which is defined as follows

$$\epsilon_{\text{cum}}^c(\theta_x, \theta_y, \theta_z) = \sum_{K=1}^{\text{NCC}} \epsilon_n^c(t_K, \theta_x, \theta_y, \theta_z) \tag{18}$$

where NCC represents the number of creep conditions under consideration in the mission. In order to determine the three principal normal creep directions equation (18) must be maximized with respect to θ_x, θ_y, and θ_z. This is carried out with the constraint condition (equation (6)) satisfied

$$\epsilon_{\text{cum}}^c(\theta_x, \theta_y, \theta_z, \lambda) = \sum_{K=1}^{\text{NCC}} \epsilon_n^c(t_K, \theta_x, \theta_y, \theta_z) + \lambda(l^2 + m^2 + n^2 - 1) \tag{19}$$

Equation (19) may be solved by the Lagrange multiplier method by setting up the typical eigenvalue problem as was previously carried out for the principal normal strain range. In this case the eigenvalue with the maximum magnitude will be the principal normal cumulative creep strain and its corresponding eigenvector yields the principal directions, i.e.

$$\max \epsilon_{\text{cum}}^c, \theta_{xp}^c, \theta_{yp}^c, \theta_{zp}^c \tag{20}$$

Once the principal planes have been determined their values may be resubstituted into equations (16) and (17) to obtain functions of the form

$$\epsilon_n^c(t_1, \theta_{xp}^c, \theta_{yp}^c, \theta_{zp}^c) \quad \text{and} \quad \epsilon_n^c(t_2, \theta_{xp}^c, \theta_{yp}^c, \theta_{zp}^c) \tag{21}$$

Upon consideration of conditions 1 and 2 and by using equations (21) and the life fraction rule it becomes an easy task to fit a general creep expression for the principal normal creep for the entire mission which in this case is assumed to be comprised of conditions 1 and 2 as follows

$$\epsilon_{\text{mis}}(t) = A_{\text{mis}} t^{B_{\text{mis}}} \tag{22}$$

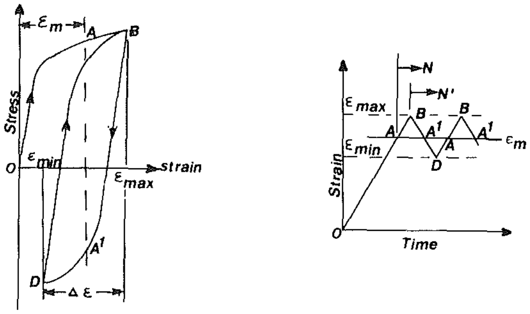

Fig. 5 Progressive strain cycling about mean strain

Life Evaluation by Ductility Exhaustion. Use will now be made of the equations, derived in previous sections, concerning maximum principal value of normal strain range and principal normal mission creep. Creep and fatigue may now be combined, based on the ductility exhaustion model [2], in order to evaluate component life.

Generally the fatigue behavior in the low cycle regime obeys the following relationship

$$N = b\Delta\epsilon_n^{-a} \tag{23}$$

where a is the fatigue ductility exponent defined by the slope of the $\Delta\epsilon$-N curve and b is the fatigue ductility coefficient given by the strain intercept. A typical total strain range versus fatigue curve is depicted in Fig. 4. From Fig. 4, ϵ_f is the fracture strain in static tension and $N_{1/4}$ refers to one quarter of a cycle, thus

$$No = b\Delta\epsilon_n^{-a} \text{ and } N_{1/4} = b\Delta\epsilon_n^{-a} = \frac{1}{4} \tag{24}$$

Since

$$\frac{No}{N_{1/4}} = 4No = \left\{\frac{\Delta\epsilon_n}{\Delta\epsilon n_{1/4}}\right\}^{-a}$$

thus

$$No = \frac{1}{4}\left\{\frac{2\epsilon_f}{\Delta\epsilon_n}\right\}^a$$

or, giving a relationship of the form

$$\Delta\epsilon_n^a No = \text{const} \tag{25}$$

The constant in the above equation [2] may be considered as $(2\epsilon_f)^a/4$ by interpreting a static tension test as 1/4 cycle with a strain range of twice the fracture strain ϵ_f. No is the number of cycles at which the material ductility has been exhausted for a strain range $\Delta\epsilon_n$.

Knowing the above baseline stabilized hysteresis loop properties where $R = -1.0$ one may analytically generate or determine the life for any R ratio by the approach adopted in [3]. Figure 5 shows a usual loading path for the first strain cycle with a mean strain of ϵ_m. This diagram may be interpreted as follows. Strain is initially increased to its maximum value B and then is repeated between this maximum value B and the minimum value D. The number of cycles counted from the initial maximum point B is denoted by N'. The relationship between No and N' is given as

$$N' = No - \frac{1}{4} \tag{26}$$

In what follows, analytical equations expressed in terms of No will be derived. The damage due to initial straining to ϵ_{max} is given by $(2\,\epsilon_{\text{max}})^a/4$. The number of cycles No to fracture is expressed as

$$\Delta\epsilon_n^a\left(No - \frac{1}{4}\right) = \frac{(2\epsilon_f)^a}{4} - \frac{(2\epsilon_{\text{max}})^a}{4} \tag{27}$$

This equation can be rewritten as

$$\left[\frac{\Delta\epsilon_n}{2\epsilon_f}\right]^a (4No-1)+\left[\frac{\epsilon_{\max}}{\epsilon_f}\right]^a=1 \tag{28}$$

A more convenient expression than the above is presented in terms of $\Delta\epsilon_n$ and ϵ_m as follows

$$\left[\frac{\Delta\epsilon_n}{2\epsilon_f}\right]^a (4No-1)+\left[\frac{\Delta\epsilon_n}{2\epsilon_f}+\frac{\epsilon_m}{\epsilon_f}\right]^a=1 \tag{29}$$

In the case of compressive mean strain, i.e., $|\epsilon_{\min}|>|\epsilon_{\max}|$, $\epsilon_{\max}$ and ϵ_m in these equations should be replaced by $|\epsilon_{\min}|$ and $|\epsilon_m|$, respectively. In other words, $\epsilon_{\max}$ is defined as the maximum absolute value of strain. A more convenient way of expressing the foregoing equations is to use a strain ratio R, as defined in equation (12), where

$$R=\frac{\epsilon_{\min}}{\epsilon_{\max}} \quad \text{for } |\epsilon_{\max}|>|\epsilon_{\min}|$$

$$R=\frac{\epsilon_{\max}}{\epsilon_{\min}} \quad \text{for } |\epsilon_{\max}|<|\epsilon_{\min}| \tag{30}$$

With R defined, the above equation for $\Delta\epsilon_n$ now becomes

$$\Delta\epsilon_n=\frac{2(1-R)\epsilon_f}{[(4No-1)(1-R)^a+2^a]^{1/a}} \tag{31}$$

or

$$No=\frac{1}{4}\left[1+\left[\frac{2\epsilon_f}{\Delta\epsilon_n}\right]^a-\left[\frac{2}{1-R}\right]^a\right] \tag{32}$$

If the material were to be cycled to N_P cycles at a strain range $\Delta\epsilon_n$ and if the original ductility were ϵ_f then the remaining ductility would be

$$\epsilon_{f_i}=\epsilon_f\left\{1-\frac{N_P}{No}\right\}^{1/a} \tag{33}$$

This would imply the material has undergone a loss of ductility of

$$d\epsilon=\epsilon_f\left\{1-\left[1-\frac{N_P}{No}\right]^{1/a}\right\} \tag{34}$$

or

$$d\epsilon=\epsilon_f\left[1-\left[1-\frac{4N_P}{1+\left[\frac{2\epsilon_f}{\Delta\epsilon_n}\right]^a-\left[\frac{2}{1-R}\right]^a}\right]^{1/a}\right] \tag{35}$$

where $\Delta\epsilon_n$ and R have been developed in equations (10) and (12).

The cumulative creep damage can be incorporated in this model by the method which will be described below. A typical creep curve for a given load and temperature is shown in Fig. 6, where

$$\epsilon^c(t)=\epsilon_0+At^B+Ct^D \qquad (B<1 \text{ and } D>1) \tag{36}$$

In general ϵ_0 is taken as a reference point and the Ct^D term may be dropped, which reduces the above equation to

$$\epsilon_n^c=At^B$$

or as previously derived (equation (22)) for the entire creep mission of the component.

Since both cycling and creep are assumed to contribute to the same failure mechanism, the damage that resulted during the first increment in cycles is equivalent to an increment of creep strain, whose equivalent time is evaluated by knowledge of the mission creep parameters and the proper strain range. Thus

$$t_{EQ_1}=\left[\frac{d\epsilon_1}{A_{\text{mis}}}\right]^{1/B_{\text{mis}}} \tag{37}$$

where

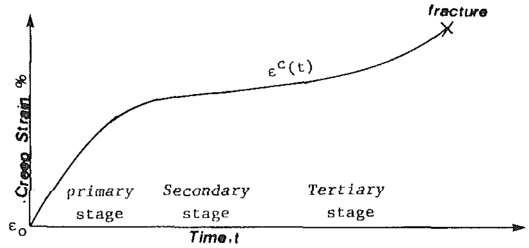

Fig. 6 Typical creep curve

$$d\epsilon_1=\epsilon_f\left[1-\left[1-\frac{4N_1}{1+\left[\frac{2\epsilon_f}{\Delta\epsilon_{n_1}}\right]^a-\left[\frac{2}{1-R_1}\right]^a}\right]^{1/a}\right] \tag{38}$$

is the ductility decrement which the material has undergone after N_1 cycles at a certain strain range $\Delta\epsilon_{n_1}$ and ratio R_1. During the N_1 mission cycles or subcycles and elapsed mission time t_{E_1} some creep took place whose magnitude may be evaluated from the mission creep parameters as follows

$$\epsilon_{\text{mis}}=A_{\text{mis}}t_{E_1}^{B_{\text{mis}}} \tag{39}$$

Now combining the creep and strain cycle the remaining system ductility will be

$$\epsilon_{f_i}=\epsilon_f-A_{\text{mis}}(t_{E_1}+t_{EQ_1})^{B_{\text{mis}}} \tag{40}$$

The solution proceeds with the addition of another increment of cycles or subcycles which may have the same strain amplitude or a different one. In either case, an additional decrement in ductility results, which is evaluated by replacing N_1, $\Delta\epsilon_{n_1}$, ϵ_f, and R_1 with N_2, $\Delta\epsilon_{n_2}$, ϵ_{f_i}, and R_2, respectively

$$d\epsilon_2=\epsilon_{f_i}\left[1-\left[1-\frac{4N_2}{1+\left[\frac{2\epsilon_{f_i}}{\Delta\epsilon_{n_2}}\right]^a-\left[\frac{1}{1-R_2}\right]^a}\right]^{1/a}\right] \tag{41}$$

The equivalent creep time for the new decrement in ductility now becomes

$$t_{EQ_2}=\left[\frac{d\epsilon_2}{A_{\text{mis}}}\right]^{1/B_{\text{mis}}} \tag{42}$$

Also during the second increment of subcycles there will exist an elapsed mission time t_{E_2} over which some more creep took place and when it is combined with t_{EQ_2} it will give a remaining system ductility of

$$\epsilon_{f_{i+1}}=\epsilon_{f_i}-A_{\text{mis}}(t_E+t_{EQ})^{B_{\text{mis}}} \tag{43}$$

The above procedure is repeated until the remaining ductility is exhausted, and failure occurs. An evaluation of the life must be made by creep/fatigue interaction (or ductility exhaustion) by observing the following steps for each node of the finite element model:

1 Determine the maximum principal normal strain range (and θ_{xp}, θ_{yp}, θ_{zp}) and also the normal mean strain on this plane, for each mission cycle or subcycle.

2 Determine the mission principal normal creep parameters (and θ^c_{xp}, θ^c_{yp}, θ^c_{zp}).

3 Evaluate creep/fatigue life by exhausting the ductility in the maximum principal normal strain range direction (θ_{xp}, θ_{yp}, θ_{zp}) of each mission cycle or subcycle.

4 Evaluate creep/fatigue life by exhausting the ductility in the mission principal normal creep direction (θ^c_{xp}, θ^c_{yp}, θ^c_{zp}).

5 Select the lowest life (from 3 or 4) to determine the structural integrity of the turbine component.

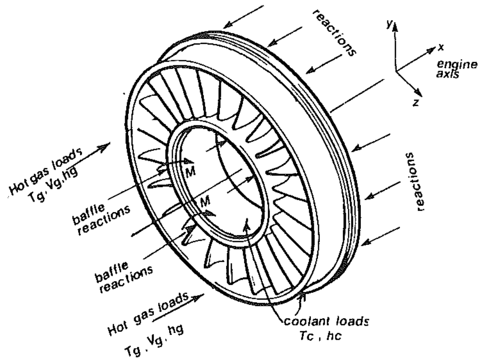

Fig. 7 Vane ring and loads acted upon

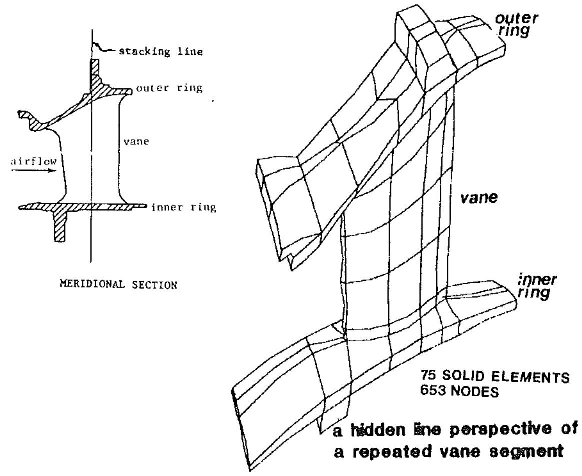

Fig. 8 F.E. model of turbine vane ring

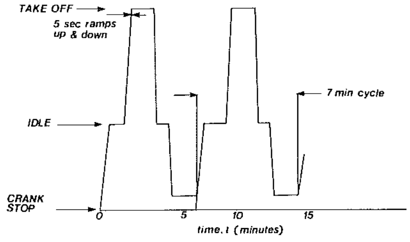

Fig. 9 Short cyclic endurance mission used in block test

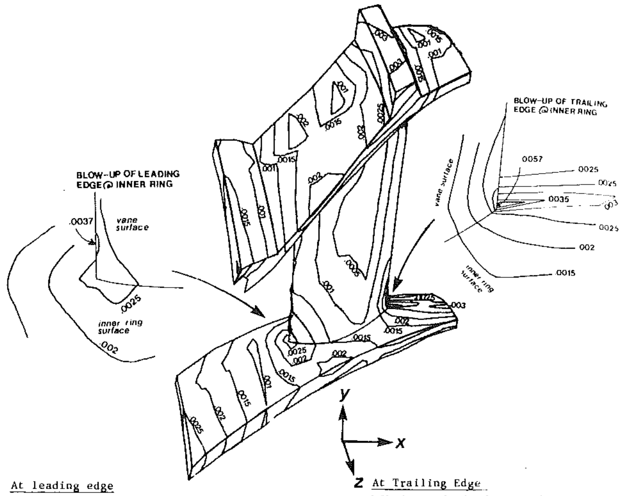

At leading edge
Mission principal normal strain range direction

θ_{xp}	θ_{yp}	θ_{zp}
74.	145.	120.

At Trailing Edge
Mission principal normal strain range direction

θ_{xp}	θ_{yp}	θ_{zp}
62.	34.	108.

Fig. 10 Isocontours of mission maximum principal normal strain range on vane

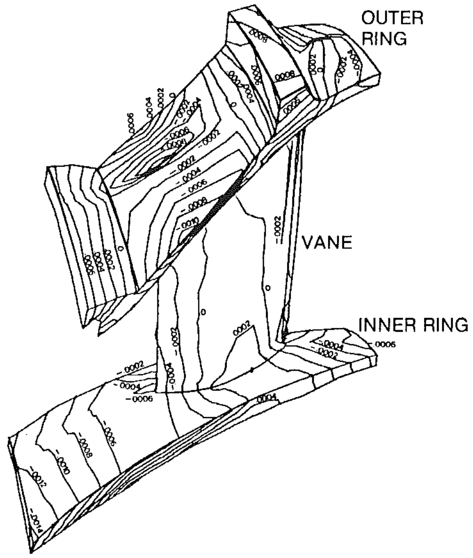

Fig. 11 Isocontours of normal mean strains on vane surfaces

Uncooled Airfoil Study

In order to evaluate the approach developed herein a typical integral uncooled low-pressure turbine vane was analyzed and the results of the analysis were then compared to a test rig study. The study was performed in four phases as follows: (*i*) finite element model generation (yielding 653 nodes and 75 twenty node isoparametric solid elements); (*ii*) finite element nonlinear thermal mission analysis; (*iii*) finite element elastoplastic mission stress/strain analysis; (*iv*) low cycle fatigue life analysis and comparison to test rig results.

Analytical Life Prediction. Due to the primarily constant strain nature of the mission experienced by the vane and also based on previous experience, it was assumed that the fatigue portion of the loading spectrum would be more detrimental to the life of this component rather than the creep portion.

The components' geometry and three-dimensional finite element model used for thermal, stress, and life analyses are depicted in Figs. 7 and 8, respectively. The type of mission which was used in this study was a short cyclic endurance type mission between cold, ground idle and takeoff conditions (shown in Fig. 9). The vane was primarily subjected to transient thermal loads arising from hot gas flow and external loads due to a pressure difference across its baffle attachment. All of these loads are shown schematically in Fig. 7.

Nonlinear finite element thermal and stress analyses were carried out on the component throughout its mission. The same 20-node isoparametric solid elements were used in both analyses. Instantaneous temperature distributions were evaluated for successive time intervals throughout the time history. Subsequently they were followed with the strain-stress calculation for each load increment. With progressive plastic deformation, each increment of stress and strain was computed by iterating for equilibrium and was accumulated over the mission. The incremental formulation readily gives a pure elastic response to unloading. The plastic behavior was characterized by the von Mises yield criterion and its associated flow and hardening rules.

The above facilitated the evaluation of the mission max-

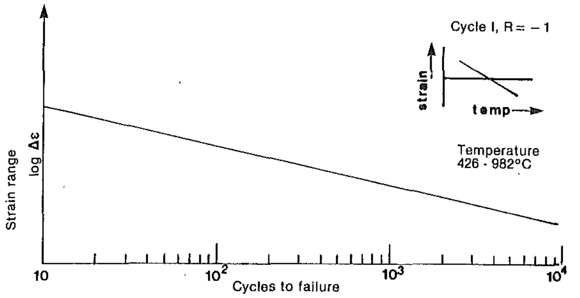

Fig. 12 Minimum (−3σ) baseline TMF properties of INCO-792

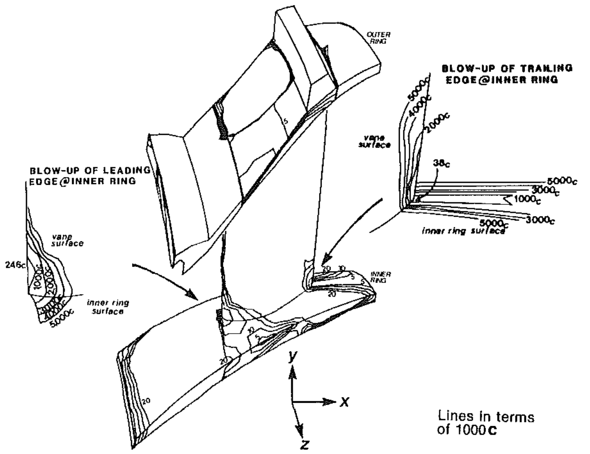

Fig. 13 Isolife lines on vane surfaces and blowup of critical regions

imum principal normal strain ranges and mean strains by the method earlier developed. Figures 10 and 11 show isocontour plots of the mission maximum principal normal strain ranges and corresponding mean strains on the vane surfaces. Also shown in these figures are the directions of the mission maximum principal normal strain range and mean strain. These are shown in a blown up view at the critical leading and trailing edge locations.

In order to determine analytically the low cycle fatigue life of the component, what is needed in conjunction with the mission maximum principal normal strain range and mean strain is the fatigue behavior of the material, usually characterized by specimen testing. This is represented in terms of the total strain range versus the number of cycles to failure. In the case at hand the material used for the solid vane under study was INCO-792, a nickel-based superalloy. During the mission, the vane was also subjected to thermal cycling in conjunction with primarily strain cycling. The baseline thermomechanical minimum (−3σ) fatigue life of this material is shown in Fig. 12 for temperature cycling limits between 426 and 982°C and strain and temperature out of phase. Linking all of the above information allowed for a life prediction of the component. Figure 13 shows isocontour plots of the life on the surface of the component.

As may be seen from this figure the most critical regions of this component seem to be concentrated at the airfoil junctions with the inner ring of the vane, on the leading and trailing edges. The predicted lives vary between 246 and 331 cycles at the leading edge root junction while they range between 38.5 and 316 cycles to failure at various locations at the trailing edge root junction.

Comparison to Test Rig Results. The results were compared to test rig results in order to evaluate the analytical life prediction. This involved a development turbine vane ring sustaining the type of cyclic loading depicted in Fig. 9. The test rig was stripped down after after 390 cycles of the type shown in Fig. 9. Subsequently microcracks were detected, at the vane leading and trailing edges, not visible to the naked eye (less than 0.80 mm long). These cracks propagated at an angle of 45 deg to the plane of the engine axis. The ratios of the predicted to actual lives range between 63 and 85 percent at the leading edge root junction and between 10 and 81 percent at the trailing edge root junction. The difference implies that an earlier rig strip would have shown cracks originating at the trailing edge. Figure 14 shows photographs of leading and trailing edge cracks on the vane after it had sustained 520 cycles of total running. Upon comparison of the orientation of these cracks (Fig. 14) with those predicted by analysis (Figs. 10 and 11) it may be seen that the two correspond directly.

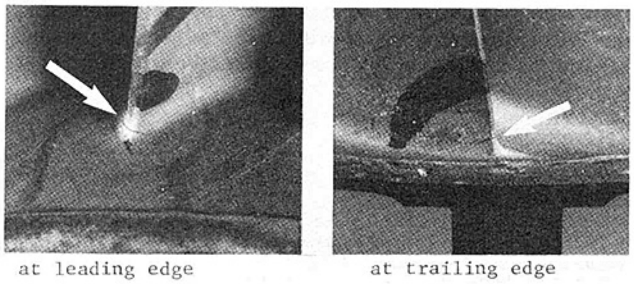
at leading edge at trailing edge

Fig. 14 Cracks at ring juncture on all guide vanes

Conclusions

Design of ever-improving turbine components subjected to high rotational speeds and temperatures with acceptable durability is critical to the gas turbine product. This paper has examined the problem and has identified the need for very complex three-dimensional thermal, stress and life analysis to allow for more reliable gas turbine engine designs.

A method of determining the mission (cycle or subcycle) maximum principal normal strain range has been conceived and developed. The prerequisite for the use of this method is knowledge of the three-dimensional state of strain of the component under mission loading. This state of strain may be determined from three-dimensional finite element thermal and elastoplastic stress analyses. The normal strain range function is then developed and its magnitude is maximized in time and three-dimensional space. The space maximization reduces to an eigenvalue solution by the use of Lagrange multipliers while the time maximization is achieved by numerical scanning of all time step combinations in the mission.

In order to determine the creep behavior of a component a mission creep function was developed and maximized. This function may be established by prior knowledge of the component creep behavior under each creep condition in the mission. This involves a three-dimensional finite element creep rupture analysis for each creep condition in the mission. Once the behavior is established, a cumulative creep function is maximized with respect to space, by the use of Lagrange multipliers.

The life due to creep/fatigue interaction is evaluated by the ductility exhaustion method. It is determined in two principal directions: the direction of the mission (cycle or subcycle) maximum principal normal strain range and in the direction of maximum principal normal mission creep. The lowest life yielded by the above is considered in the integrity of the design.

The method has been applied to a solid (uncooled) vane and has been correlated to test rig experience. The results pertaining to life and crack orientation between analysis and rig testing are in excellent agreement.

In conclusion the approach presented has been applied toward fatigue life prediction of available hardware. Testing of this hardware verified the approach. The method should be implemented in and tested with more advanced nonlinear damage accumulation concepts recently developed for creep/fatigue interaction.

References

1 Timoshenko, S., and Goodier, J., *Theory of Elasticity*, 2nd ed., McGraw-Hill, New York, 1951, p. 223.

2 Polhemus, J. F., Spaeth, C. E., and Vogel, W. H., "Ductility Exhaustion Model for Prediction of Thermal Fatigue and Creep Interaction," in: *Thermal Fatigue at Elevated Temperatures*, ASME STP 520, 1973, pp. 625-635.

3 Ohji, K., Miller, W. R., and Marin, J., "Cumulative Damage and Effect of Mean Strain in Low-Cycle Fatigue of a 2024-T351 Aluminum Alloy," ASME *Journal of Basic Engineering*, Vol. 88, 1966, pp. 801-810.

4 Kaufman, A., and Gaugler, R., "Nonlinear, Three-Dimensional Finite Element Analysis of Air-Cooled Gas Turbine Blades," NASA TP 1669, 1980.

5 Manson, S. S., *Thermal Stress and Low Cycle Fatigue*, McGraw-Hill, New York, 1966.

6 Manson, S. S., and Hirshberg, M. H., *Fatigue, an Interdisciplinary Approach*, Syracuse University Press, Syracuse, NY, 1964, pp. 133-172.

7 Zamrik, S. Y., "The Application of SRP Method to Multiaxial Creep-Fatigue Interaction," Meeting on the SRP Method in Aalborg, Denmark, Apr. 1978.

8 Halford, G. R., "High-Temperature Fatigue in Metals – A Brief Review of Life Prediction Methods Developed at the Lewis Research Center of NASA," *SAMPE Quarterly*, Apr. 1983.

9 Sachs, G., Gerberich, W. W., Weiss, V., and Latorre, J. V., "Low-Cycle Fatigue of Pressure Vessel Materials," *Proc. ASTM*, Vol. 60, 1960, pp. 512-529.

10 Morrow, J. D., and Tuler, F. R., "Low Cycle Fatigue at Evaluation of Inconel 713 C and Waspaloy," ASME *Journal of Basic Engineering*, Vol. 60, 1961.

11 Zamrik, S. Y., and Frishmuth, R. E., "The Effects of Out of Phase, Biaxial Strain Cycling on Low Cycle Fatigue," SESA Fall Meeting, 1969.

12 Mom, A. J., "Overview of the AGARD SMP Activities on Turbine Engine Materials Technology in the 1972-82 Period."

13 Lemaitre, J., and Chaboche, J. L., "Aspect phenomenologique de la rupture par endommagement," *Journal de Mécanique Appliqué*, Vol. 2, 1978, pp. 317-365.

14 Gomuc, R., and Bui-Quoc, T., "Analysis of the Fatigue/Creep Behavior of 304 Stainless Steel Using Continuous Damage Approach," ASME Paper No. 84-PVP-38, June 1984.

15 Henderson, J., "An Investigation of Multi-axial Creep Characteristics of Metals," *Transactions of the ASME*, Vol. 101, 1979, pp. 356-364.

R. Viswanathan
A. C. Dolbec
Electric Power Research Institute,
Palo Alto, CA 94303

Life Assessment Technology for Combustion Turbine Blades

Combustion turbine blades operating in the hot gas path are subject to degradation by embrittlement, creep, thermal fatigue, hot corrosion, and synergistic effects among the above. Development of techniques to assess the extent of degradation of the blades under these conditions can have a significant and favorable economic impact for the utility industry. The Electric Power Research Institute (EPRI) is currently engaged in a number of research activities aimed at the development of such techniques. This paper is an overview of the present and planned activities relating to life assessment technology for blades.

Need for Life Assessment Technology

Combustion turbines constitute approximately 7 percent of the total power generation capacity in the U.S. electric utility industry. There has been a growing need in the industry to assess the remaining life of aging components. The need for life assessment technology is driven by a number of economic factors. A number of turbines currently in operation have been in service in excess of 50,000 hr and are likely to perform reliably even after exceeding the original "design life." A properly managed life assessment and refurbishment program may help extend the life of these turbines by another 10–20 years, thus avoiding major capital expenditures for the utilities.

In most utilities, the turbine manufacturer's recommendations constitute the principal basis for replacement of components. Often, these recommendations are based on the manufacturer's past experience and are not machine specific. The methodologies and criteria by which they are arrived at are unclear to the utilities. Utilities would like the capability for independent assessment of the condition of their components. This concern has become increasingly serious as the cost of replacement parts has escalated. The cost of superalloy components alone may constitute as much as 15–20 percent of the total cost of a turbine. Operating practices also vary widely among utilities and can be at variance with the manufacturer's recommended practice. Both above-design (e.g., rapid cycling, excess temperature) and below-design (derating) operation are common. In such cases, utilities need the technology to assess the penalties associated with above-design operation, as well as the excess life to be derived from below-design operation on a unit specific basis.

Intelligent scheduling of inspections also requires proper techniques and tools for assessing life expenditure of components. Lengthening inspection intervals based on judicious life assessment can translate into significant cost savings. The correct choice of schedules can also help avoid unforeseen outages.

Table 1 Strategy for life assessment of blades

Step 1: Analytical Methods

Input Needed	Sources/Issues
o Stress and temperature distribution	o From Design o From Monitoring
o Service History	o From Records o From Monitoring
o Material Properties	o Standard virgin material data from past compilations o Need degraded property data base o Need to develop correction factors for environmental interaction for uncoated blades o Need to develop data base on coated blade properties o Need TMF data o Damage rules need validation

Step 2: Nondestructive Evaluation Methods

Method	Issues
o Conventional UT, PT	o Cannot pick up incipient damage preceding crack initiation
o Replication	o Need to establish correlation between microstructural observations and life expenditures o Need to demonstrate capability for in-situ field replication

Step 3: Destructive Evaluation Methods

Tests	Issues
o Accelerated rupture tests	o Feasibility of miniature samples o Verification and refinement of damage rules to permit extrapolation to service conditions
o Accelerated creep/ fatigue tests	o Correction factors for coatings/environment
o Accelerated TMF tests	o Identification of service temperature. Possible use of corrosion profiles
o Impact tests	o Need to define kinetics of degradation* o Need to define threshold for FOD*

One reality of turbine operation in the utility context, which is often ignored, is the possibility of foreign object damage to the hot section components. The foreign objects are frequently loose parts, nuts, bolts, and tools left inside the turbine after overhauls by negligent maintenance personnel. In order to withstand such damage as well as to possess tolerance to pre-existing or service-induced flaws, it is essential that blade materials have adequate impact strength. Since the impact strength is subject to in-service degradation, periodic assessment of this property is an inevitable part of life assessment strategies.

Contributed by the Gas Turbine Division of THE AMERICAN SOCIETY OF MECHANICAL ENGINEERS and presented at the 31st International Gas Turbine Conference and Exhibit, Düsseldorf, Federal Republic of Germany, June 8–12, 1986. Manuscript received at ASME Headquarters February 28, 1986. Paper No. 86-GT-257.

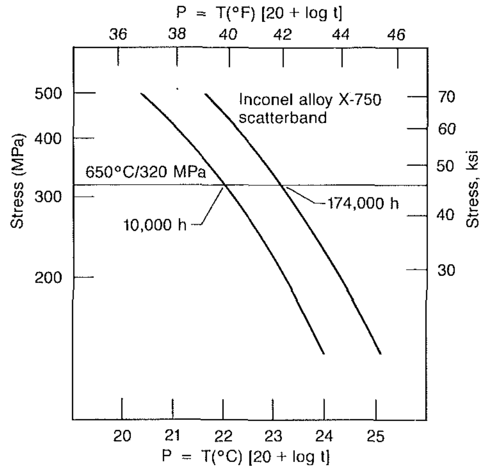

Fig. 1 Scatter in stress rupture data for Inconel X-750. At 650°C/320 MPa, the rupture life can vary from 10,000 hr to 174,000 hr due to heat-to-heat variation in properties.

Future trends in turbine usage also dictate the need for improved life assessment techniques. There is an increasing trend in the use of combustion turbines in cogeneration and in combined-cycle plants, operating in base load or intermediate load configurations. These types of duty cycles require high-reliability components with greater longevity than is expected of machines operating under peaking duty. There is also a trend toward increasing turbine inlet temperatures to increase turbine efficiency. Time-dependent damage mechanisms, such as creep, can become more important in this context.

A final, important consideration is the safety of plant and plant personnel. Failure of blades can lead to consequential damage of other components downstream, and to catastrophic failure of the turbine. Accurate life assessment techniques can help avoid such occurrences.

Current Techniques and Limitations

During the design stage, turbine manufacturers build in margins of safety to provide against premature mechanical failure of blades. In spite of this, premature failures of components do occur in practice, due to operational, environmental, and metallurgical factors outside the scope of the original design. Significant among these are unanticipated residual and system stresses, stress concentrations, excessive temperatures, cycling, corrosion, and long-term material degradation.

The principal damage mechanisms imparing the integrity of turbine blades[1] are microstructural coarsening, creep, thermal fatigue, hot corrosion, and synergistic effects among the above. Microstructural coarsening can lead to loss of impact strength and hence loss of tolerance to flaws. Hot corrosion can lead to increased stresses by loss of net-section. Localized penetration due to corrosion can also adversely affect the creep rupture and low-cycle fatigue strength. Since blades are highly stressed and blade materials inherently have a low-impact strength, failure is essentially governed by initiation of small cracks. Life assessment technology for blades, therefore, centers around events leading up to crack initiation.

A tentative overall strategy for life assessment of blades is outlined in Table 1 for the purpose of providing a framework in which the current state of the art and its limitations can be discussed. It involves a three-step process such that the user may elect to proceed from one step to the next, depending on the results from the previous step, the level of accuracy needed in the life prediction, and the resources available to achieve the desired level of accuracy.

Calculation-based methods analytically derive the total creep/fatigue life expended. This requires a knowledge of the steady-state and transient stress distribution, service history and material properties. In this procedure, major uncertainties arise due to a lack of precise knowledge of all of the above factors and due to inaccuracies in the assumed damage rules. Most utilities do not maintain adequate records of the service history of the turbines. Instrumentation and monitoring of the blades may often be required to surmise the past history. Material properties are inherently subject to considerable scatter and can lead to uncertainties in predicted life by one order of magnitude as may be seen from Fig. 1. Furthermore, available properties usually pertain to virgin materials tested in air. Accurate life assessment, on the other hand, requires properties of the blade material in the service-degraded condition exposed to environments typicial of turbine operation. In the case of coated blades, the coating cycle as well as the coating itself can have an adverse or favorable effect on the blade material. Thermomechanical fatigue data on materials are scarce and are invariably substituted for by isothermally generated low-cycle fatigue data. There is thus a total dearth of the "appropriate" material property data required for proper life assessment. In spite of the many deficiencies, calculation-based methods serve a useful function in determining if and when the more expensive and time-consuming direct examination procedures are warranted. As a rule of thumb, if the calculated life expenditure exceeds 50 percent, further evaluations may be deemed necessary.

The second step in the life assessment strategy involves direct examination of the blades using nondestructive techniques. Conventional nondestructive techniques are incapable of detecting incipient damage such as creep cavitation and carbide coarsening. Plastic replication techniques on the other hand have the capability to reveal damage on a microstructural level. Quantitative correlations between microstructurally observable features and expended life and the capability for in-situ replication of blades need to be demonstrated before this technique can be more fully exploited. For coated components, spot coating techniques need to be developed to enable field replication. Since the major component of cost in component assessment is the cost of opening and reassembly of the casing, remote techniques for replication would be desirable.

The third step in life assessment, which is the most accurate and expensive step, involves removal of sacrificial blades and subjecting them to metallographic and mechanical tests. Since the number of test samples that can be machined is limited, development of miniature specimens may be valuable. In order to use the accelerated mechanical tests to predict the long-term behavior, the damage rules currently in use need to be verified and improved, if necessary. The effects of environments and coatings need to be taken into account in a quantitative fashion. In order to relate the extent of observed degradation after service conditions, knowledge of the operating history would be desirable. In this regard, possible use of microstructural features or corrosion features as built-in monitors of service history need to be explored.

In recognition of the various deficiencies in the current strategy for life assessment as described above, EPRI has been evaluating and refining a number of techniques for life assessment of blades. A damage algorithm for predicting the fatigue life usage based on laboratory thermomechanical fatigue tests is being developed and will be validated on turbine components specifically instrumented for the purpose under research project RP2421. The existence of different types of hot corrosion mechanisms and potential interactions between these and the creep properties of blade materials have been recognized. The use of microstructural and replication tech-

---

[1] The terms blades and buckets, vanes and nozzles, are used interchangeably depending on the turbine manufacturer's preference. For consistency, the terms blades and vanes will be used in this paper.

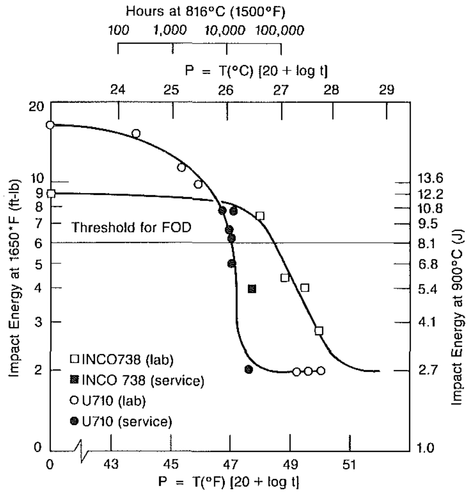

Fig. 2 Degradation of impact toughness at 900°C (1650°F) following laboratory and field exposure in the range 788-871°C (1450-1600°F), based on [1, 2]

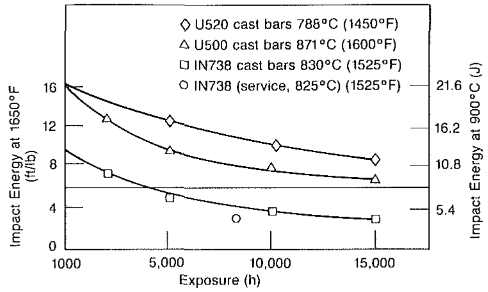

Fig. 3 Degradation of impact toughness at 900°C (1650°F) following exposure at 788-871°C (1450-1600°F), for U520, U500, and INCO 738

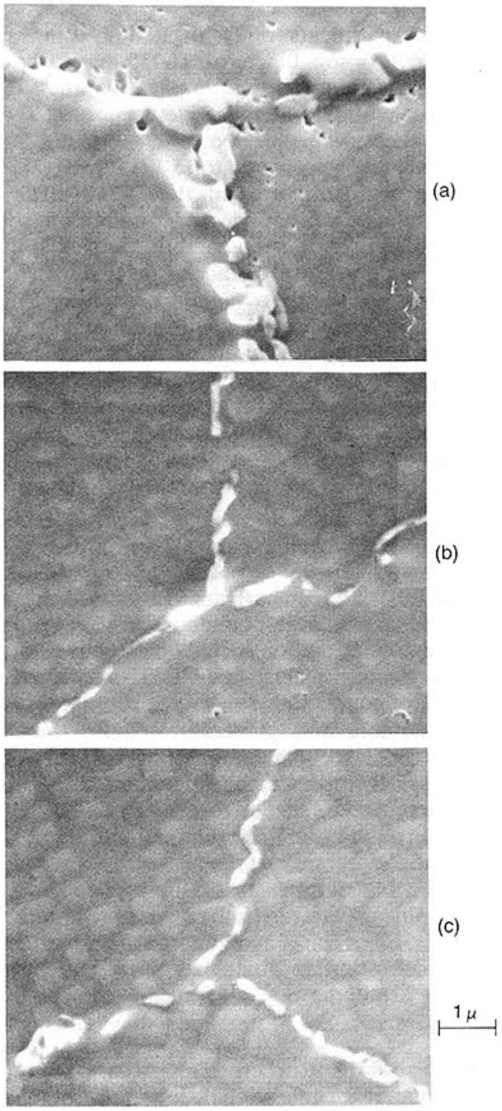

Fig. 4 SEM micrographs of a Udimet-710 blade retrieved from service after 10,000 hr at 830°C (1525°F): (*a*) airfoil, (*b*) cooler areas from shank, (*c*) material from airfoil after a rejuvenation heat treatment

niques for assessing the degradation of toughness and the onset of creep cavitation is being explored in RP2253. This paper will present a review of the various issues that are considered important by EPRI, within the overall framework of the life assessment strategy outlined in Table 1.

In-Service Degradation of Impact Toughness

It has been known for some time that the impact toughness of blades can degrade in service, thereby reducing their tolerance to defects and resistance to impact damage by foreign objects (FOD). The problem has been particularly acute with blades made of alloy U-710, whose service lives have been curtailed to as low as 10,000 hr. Currently, it is estimated that there are a large number of "affected" blade rows of U-710 worth well over $60 million in the United States. Assessment of the condition of these blades and development of rejuvenation procedures for these can have considerable payback.

Figure 2 illustrates the decrease in impact toughness at 900°C (1650°F) with increasing time of exposure in the range 780-900°C (1450-1650°F). The time and temperature of exposure have been combined in the form of a Larson-Miller parameter. The usual exposure temperature of first row blades of U-710 is about 816°C (1500°F). Figure 2 shows that a precipitous drop in the impact energy occurs at 816°C (1500°F) between 3000 and 20,000 hr of exposure. It has been reported that 8.13 Joules (6 ft-lbs) at 900°C might represent the threshold value below which significant FOD might be observed [1]. According to Fig. 2, the threshold value will be reached after 10,000 hr of service at 816°C (1500°F) in the case of U-710.

Figure 3 shows the degradation behavior with duration of exposure in the range 788-871°C (1450-1600°F) for three other superalloys, U-520, U-500, and IN 738. The results show that these alloys also might eventually become subject to FOD. When the data for IN 738 are plotted on the parametric plot in Fig. 2, the threshold value for FOD is reached in about 49,000 hr at an assumed service temperature of 816°C (1500°F). In fact, a first row blade of IN 738, returned from service after 8242 hr, had impact energy as low as 5.15 J (3.8 ft-lbs) [2].

As part of an EPRI-sponsored project at Rockwell International Co., samples from four superalloys—U-700, U-710, U-720, and Inco 738—are being subjected to thermal aging at 788°C (1450°F), 830°C (1525°F), and 871°C (1600°F) for 1000, 5000, and 10,000 hr, respectively. The impact properties as well as the stress rupture properties of the samples at 830°C (1525°F) will be characterized. Aged samples will also be subjected to reheat treatment following the original heat treatment cycle, and the extent of restoration in the mechanical properties will be documented. Correlations between microstructure and impact strength will also be developed, so that the condition of blades in service can be assessed based on metallographic observations alone.

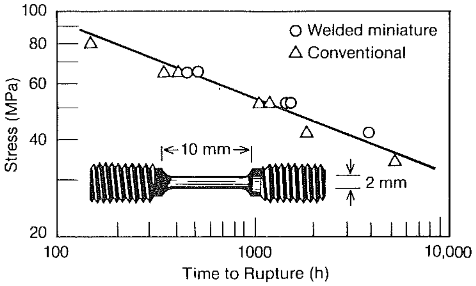

Fig. 5 Comparison of stress rupture tests results based on conventional and miniature size samples of 1 Cr-0.5 Mo steel at 630°C [5]

Preliminary experiments on rejuvenation using samples from a service exposed blade of U-710 have shown the feasibility of partial restoration of impact toughness. Following approximately 10,000 hr of service exposure, the blade yielded impact energy values of about 9.5 J (7 ft-lb). By reheat treatment this value was increased to 15 J (11 ft-lb) [2]. A comparison of the microstructures of the U-710 blade in the degraded condition (air foil), undegraded condition (root) and in the degraded and rejuvenated condition is shown in Fig 4. The principal microstructural change associated with degradation is a coarsening of the grain boundary carbides. The size of the carbides in the rejuvenated condition is identical to that found in the undegraded condition prevailing at the blade root [2]. A number of blades with known service history have been retrieved. They will be used for development of correlation between microstructure and impact strength. Such correlations will eventually enable assessment of impact strength of blades in the field based on replication techniques.

Creep Damage

It is well known that the creep strength of superalloy blades deteriorates in service due to both microstructural changes and formation of cavities at grain boundaries. Current procedures for assessing the deterioration include destructive tests [3] as well as nondestructive evaluations [4]. The destructive procedure consists of conducting accelerated rupture tests on the service exposed material at temperatures higher than the service temperature. The results are then extrapolated to the service temperature to estimate the remaining creep life. The nondestructive procedure may involve observing the extent of cavitation by direct microscopic examination of the blades [4] or extraction of plastic replicas; the observed degree of cavitation can then be related to fractional life expended. EPRI has made considerable progress in both of these areas with respect to ferritic steels. Since the general approaches are directly applicable to combustion turbine blades, they are described below. Efforts are underway to extend these approaches to superalloy blades.

Miniature Specimen Rupture Tests. To overcome difficulties in obtaining conventional-sized test samples from critical components, the potential for using miniaturized samples (10 mm long, 3 mm dia round) has been explored [5]. Stress rupture tests were conducted on conventional sized and miniature-sized samples of 1 Cr-0.5 Mo steel in argon at 630°C. Results of these tests (see Fig. 5) show that the rupture lives are independent of the specimen size and that miniature samples may be adequate to estimate the remaining life. Extension of this approach to superalloy blade material is under investigation.

Validation of Life Fraction Rule. The current techniques for remaining life assessment by accelerated tests at high temperatures assumes the validity of the Robinson life fraction rule (LFR) [6]

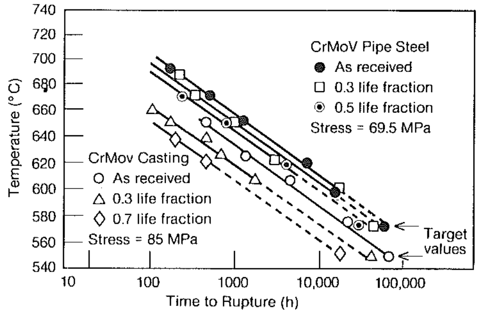

Fig. 6 Isostress accelerated tests on steel samples precrept to various life fractions. The precrept samples produce stress rupture plots which are parallel to the plot for the as-received material [5].

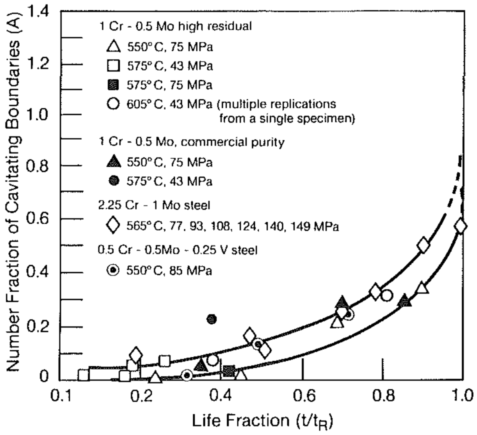

Fig. 7 Evolution of creep cavitation damage with creep life for ferritic steels [5]

$$\sum \frac{t_i}{t_R} = 1$$

where t_i is the time spent at a given stress and temperature and t_R is the rupture life for the same conditions. When the damage fractions incurred under different sets of stress-temperature conditions add up to unity, failure is presumed to occur. Hart [7], Woodford [8], and Bolton et al. [9] have demonstrated that the LFR is valid for temperature changes but not for stress changes. Industry practice has therefore been to conduct rupture tests in which acceleration is achieved by increasing the temperature, holding the stress at the same level as the service stress.

Under the EPRI project, RP2253, two heats of Cr-Mo-V steel have been evaluated: a 0.5 Cr-0.5 Mo-0.25 V steampipe steel and a 0.5 Cr-0.5 Mo-0.25 V turbine casting steel with high and low ductilities, respectively. The pipe steel specimens were subjected to initial creep damage fractions of 0.3, 0.5, 0.7, and 0.9 at 575°C at a stress of 69.5 MPa. The samples were then tested to rupture at the same stress but at higher temperatures. The casting steel specimens were subjected to the same sequence of tests following initial creep tests at 550°C at a stress of 85 MPa (12 ksi). Results from these tests are shown in Fig. 6. Within limits of scatter, the rupture data plots for the precrept samples are lower and parallel compared to the as-received samples, indicating that the LFR is valid for both the steels [5]. Long-time rupture tests of the precrept samples at the lowest temperatures (575 and 550°C, respectively) are in progress and will serve to verify the predictions based on the extrapolations.

Creep Cavitation. Based on stress rupture tests on ferritic steels, quantitative correlations have been established between the degree of cavitation and the expended life fraction [5]. Specimens were creep tested to various fractions of rupture

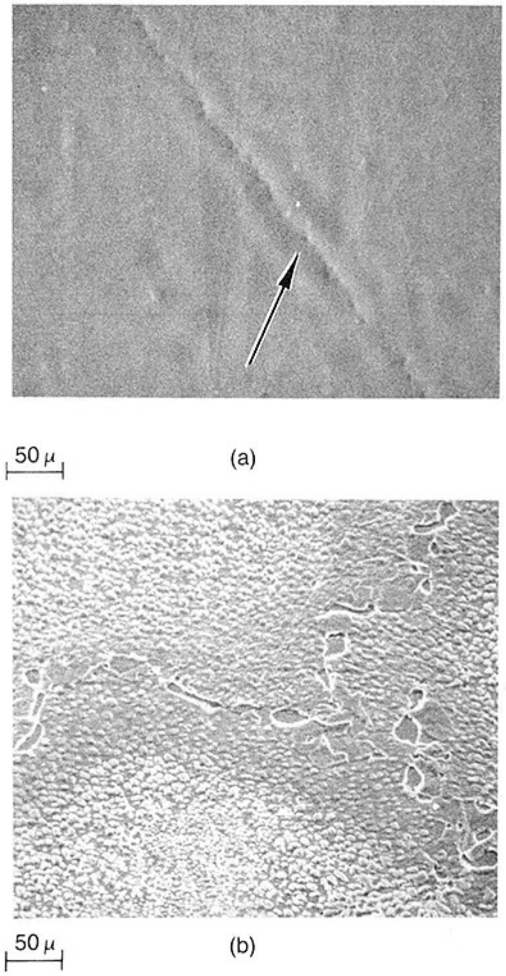

Fig. 8 Examples of in-situ field replication of blades: (*a*) INCOX750 after 67,000 hr of service at about 607°C (1125°F), (*b*) IN738 after 8000 hr of service at about 830°C (1525°F); both are SEM photomicrographs

life, and were then evaluated metallographically to determine the extent of cavitation. In addition, a series of surface replications was carried out on a single specimen at various rupture life fractions.

Among the different parameters evaluated, the best correlation was obtained between the number fraction of grain boundaries containing cavities (A) and the life fraction, as shown in Fig. 7. In the figure, data from different steels tested at various stresses and temperatures are plotted together. The entire body of data could be represented on this plot within a small band of scatter. In addition, data points derived from replication of interrupted single specimen tests fall within the scatter band obtained by destructive examination of multiple specimens. These results are extremely encouraging and hold out the promise that the life fraction consumed can be estimated from replication, using a master curve such as that shown in Fig. 7. An interesting aspect of Fig. 7 is that the life fraction expended increases significantly for small changes in the parameter A, but levels off with further increases in A. This trend is identical to that for a superalloy, Nimonic 100, as reported by Lindblom [4]. These results essentially indicate the rapid progression of creep cavitation, once it has started, and point out the need for early detection of such damage. Based solely on the similarity between Fig. 7 and the data reported by Lindblom, it appears that Fig. 7 can be used directly to assess creep damage in superalloys.

Field Replication. Due to scatter in material properties, the extent of creep and microstructural damage can vary from blade to blade even in a given row of blades in a turbine. Destructive mechanical and metallographic evaluations using one or two sacrificial blades may not therefore be adequate to ensure the integrity of the other blades. The plastic replication technique offers a nondestructive method for evaluating the conditions of many blades at many locations [2]. It permits detection and monitoring of creep damage from its very early stages. Since the replicas can be examined at high magnification using the scanning electron microscope (SEM), a very high degree of resolution can be achieved. The technique is capable of detecting damage in selected localized regions, such as airfoils, root, trailing edge, etc., which is impossible to do through destructive tests. When the replication technique eventually lends itself to a more quantitative interpretation, based on the damage correlations under development, it will be a powerful technique for remaining life assessment.

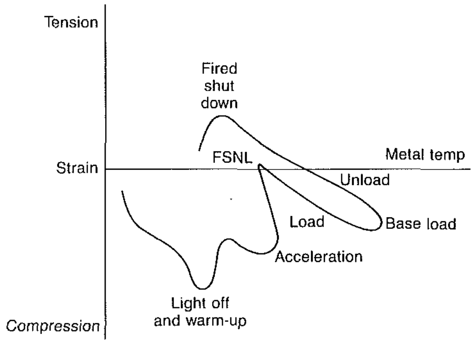

Fig 9 MS7001 stage 1 bucket leading edge strain-temperature variation for a normal startup and shutdown

To demonstrate the potential of the replication technique for field application, replication has been carried out at two utility sites. In one instance, replicas were made in situ on two Inconel X750 blades at Jersey Central Power & Light Co. These blades had experienced about 67,000 hr of service at an estimated temperature of 607°C (1125°F). Since the replicas were made to check for creep cavitation type damage, the blade surface was not etched. The replicas were shadowed with chromium and carbon and were examined in a light microscope at 1000×. No creep cavitation was found at any location (see Fig. 8*a*), thus assuring continued safe operation.

In a second instance, replicas were made in situ on two first-row blades (uncoated IN 738) of a turbine at the DeBary Generating Station of the Florida Power Corporation. The blades had been in service for about 8000 hr at an estimated service temperature of 830°C (1525°F). The surfaces were prepared on the pressure side near the platform at the leading edge. After polishing the surface through 0.05 μm alumina, they were etched with modified marble agent and replicated. An SEM micrograph of the replica (Fig. 8*b*) revealed the microstructure with good resolution. No evidence of creep damage or deterioration in toughness was detected. In view of the successful experience with field replication, further replication at utility sites is planned.

While the replication technique can be readily applied to uncoated blades to detect base metal damage, coated blades present a problem. The surface preparation associated with replication will cause the coating to be destroyed locally. In such cases, unless a field technique for spot coating is developed, replication may not prove to be viable.

Thermal Fatigue

The hot gas path components of a turbine experience a complex thermal and mechanical history during a typical cycle of operation, consisting of startup, steady-state operation, and shutdown. A typical thermal-mechanical cycle for a first-stage

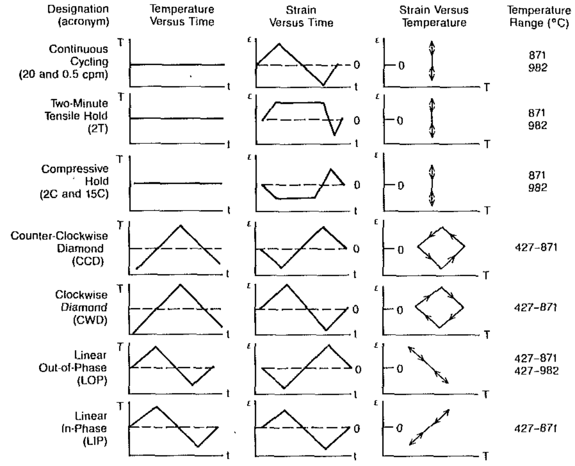

Fig. 10 Simple thermal-mechanical fatigue cycles

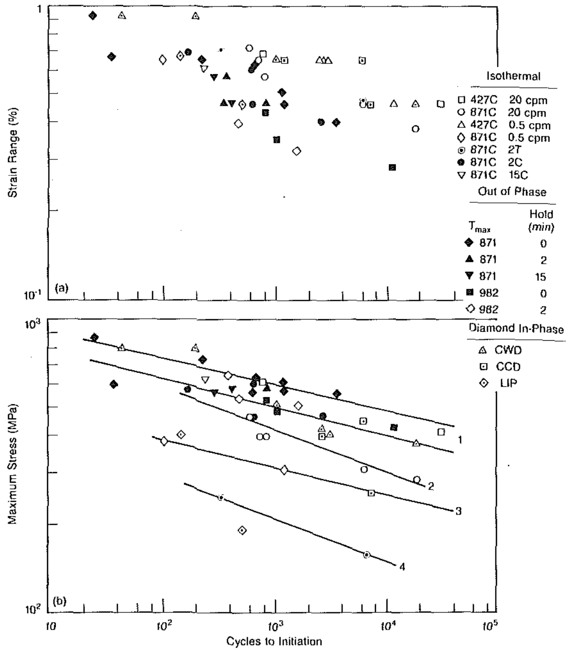

Fig. 11 Fatigue life data for Inco 738 samples tested under thermal-mechanical fatigue condition: (a) plot using strain range criterion; (b) plot using maximum tensile stress criterion

blade is shown in Fig. 9, where temperature and mechanical strain variations are plotted for a normal startup–shutdown cycle. Temperature gradients and mechanical constraints during such complex cycles give rise to cyclic thermal stresses which can give rise to fatigue damage and eventual failure. Life prediction models in the past have been based on the incorrect premise that the damage processes occurring during thermal-mechanical fatigue (TMF) can be simulated by isothermal low-cycle fatigue tests (LCF) conducted at the peak temperature. A more accurate life prediction and management system (LMS) that will take into account the material behavior under the complex TMF cycles normally encountered in turbine operation is being developed under EPRI-sponsored project RP2421.

The purpose of the Life Mangement System (LMS) program, currently being carried out at the General Electric Company, is to develop a hot gas path parts Life Management approach which will allow prediction of component life as a function of gas turbine operating parameters.[2] The program scope includes development of a field data acquisition system with requisite data processing techniques, acquisition of essential field data, development of a thermal mechanical fatigue data base, definition of necessary life-prediction algorithms, and calibration with field inspection and component materials tests. To support development of appropriate life predictive algorithms, two materials behavior tasks are included. These are component material test and thermal mechanical fatigue.

The objective of the component materials tests is to obtain data from used but unfailed parts to assess remaining life and calibrate life-prediction models. The primary failure modes considered are airfoil thermal mechanical fatigue (TMF) and creep rupture, with cracks initiating at and propagating from leading or trailing edges. To evaluate these types of damage, the leading and trailing edges are being removed from each bucket evaluated and tested in special TMF and creep test fixtures. Standard creep, rupture, and TMF specimens will be taken from the interior. Testing of trailing edge creep specimens is currently underway. Nondestructive techniques are also being used. For example, extensive replication of each blade surface is being carried out in order to define the level of damage that can be detected in situ. In addition to calibration of life prediction methods, the results of this task are expected to lead to incorporation of plans for evaluation of field returned parts into an overall life extension plan.

The primary objective of the Thermal Mechanical Fatigue (TMF) tests is to develop a fatigue life-predictive algorithm that can be directly applied in a LMS. The results will also lead to establishment of design and operational requirements that maximize fatigue life and thus improve reliability and minimize maintenance. This effort requires component analysis, TMF testing, and analytical evaluation of material behavior. Key elements of the methodology that are being established in the program include:

- the differences between simple isothermal cycles and more representative TMF cycles
- the effect of variations in the actual TMF cycle
- the effect of coatings on thermal fatigue life

The TMF fatigue test facility includes several closed-loop servohydraulic machines under computer control which subject a test specimen to a specified thermal-mechanical cycle [10]. Initial testing, using simple TMF cycles, such as those shown in Fig. 10, has been completed and is providing the basic data upon which to build the predictive methodology. Results shown in Fig. 11(*a*) indicated that, at lower total strain ranges, life can differ almost by a factor of 100, depending on the thermal-mechanical cycle. The lowest lives were exhibited by the 427–982°C OP cycles, with or without a 2-min hold. The longest lives were with diamond cycles, for which strain at maximum temperature was zero.

Among the results not immediately explainable with the total strain correlation is the fact that the isothermal 871°C results with a 2-min tension hold show longer lives than the 427–871°C IP cycle. Similarly, there is no obvious reason why the diamond cycles should be better than low temperature (427°C) isothermal cycles. As discussed in [10], correlations based on plastic strain or the net hysteresis energy model were no more successful in gaining an understanding of the data. On the other hand, correlations based on the maximum tensile stress for each cycle provide a more rational basis for ranking the different cycles in terms of their severity [10].

Figure 11(*b*) is a plot of tensile stress versus life for TMF and isothermal data on IN-738 [11]. The lines show that several types of cycle can be identified, and that they are, without exception, ranked according to the relative severity of high-temperature, high-stress exposure. The least severe cycles

---

[2] Although the program scope includes the transition piece and the first stage vane in addition to the first stage blades, only the work pertaining to blades is discussed here.

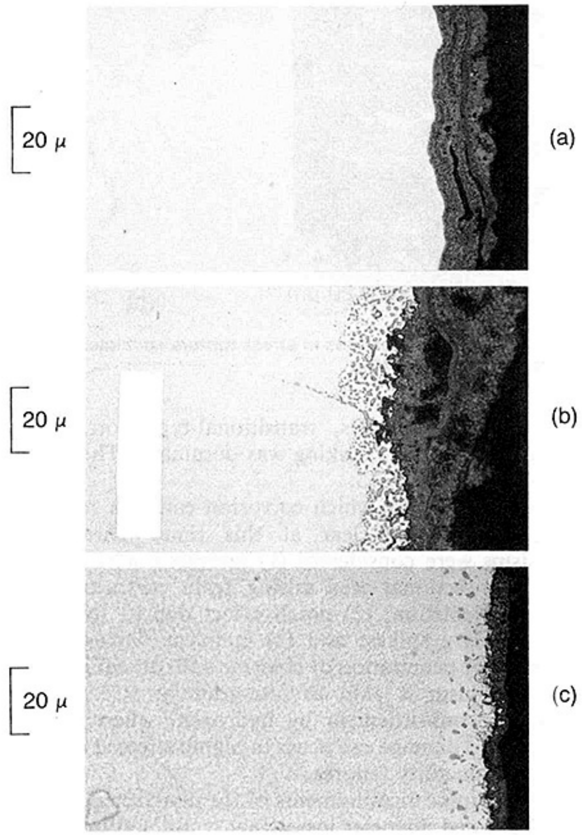

Fig. 12 Three different forms of hot corrosion observed in Udimet 710 blades: (*a*) layer type, (*b*) transition type, (*c*) nonlayer type

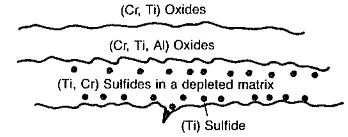

(a) Non-Layer Type Hot Corrosion

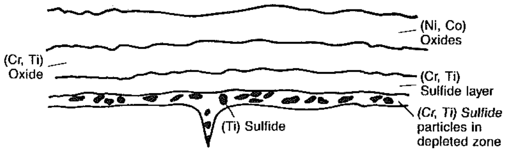

(b) Transition Hot Corrosion

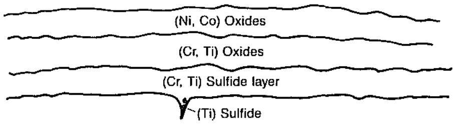

(c) Layer Type Hot Corrosion

Fig. 13 Schematic characterization of corrosion products found at areas typical of the three different hot corrosion regions [12]

are those which reach maximum tensile stress at a low temperature; these are the OP and 427°C isothermal cycles. Diamond cycles, for which the temperature at tensile stress is somewhat higher (649°C), fall slightly lower, especially at longer lives. The next lower curve is for the 871°C isothermal results, 20 cpm and 2*C*, which do not dwell long at tensile stress. Considerably lower are the cycles which have a slower cyclic rate, 0.5 cpm, at high temperature, tensile stress; these are the IP and 871°C, 0.5 cpm isothermal cycles. The lowest is the 871°C, 2*T* isothermal, which has a hold time at tensile stress.

In addition to the simple cycles evaluated so far, the more complex component cycles that have been defined by design analysis (similar to Fig. 9) will also be investigated. Additional specialized testing will assess the effects of periodic overloads (e.g., trips) and superimposed creep damage on fatigue life. All of the information ensuing from the laboratory tests and field evaluations will ultimately be incorporated into computer software that will enable utilities to estimate blade life expenditure based on operating history.

Hot Corrosion

Until about 1976, research relating to hot corrosion of superalloys was centered mainly around temperatures above 816°C (1500°F). Subsequent publications reporting on the severe corrosion problems at temperatures well below 816°C (1500°F) in marine turbines kindled interest in the potential for similar hot corrosion problems in land-based turbines. Against this background, several blades of Udimet 710 which had been in operation in #2 oil-fired machines at different utility sites were acquired and subjected to detailed metallographic, x-ray, and microprobe analysis [12].

Metallographic examination showed three different types of hot corrosion, depending on the location of the specimen. In the cooler regions of the blades, a "layer type" corrosion[3] characterized by an uneven oxide-base metal interface and the absence of subscale sulfides and precipitate-depleted zones, was found to be present. In the hotter regions of the same blade, a "nonlayer type" corrosion was present, characterized by a smooth oxide metal interface and a continuous, uniform precipitate-depleted zone containing discrete sulfide particles beneath the oxide scale. The transition from one type to the other type was characterized by an uneven oxide metal interface containing intermittent pockets of subscale alloy-depleted zones and sulfides. The layer-type, the transitional-type, and the nonlayer-type corrosion are illustrated in Fig. 12. Based on prior laboratory corrosion tests [13], it is estimated that the layer-type corrosion occurs below about 700°C (1300°F), while the nonlayer-type corrosion occurs above 775°C (1425°F). In the range 700–774°C, corrosion is of the transition type.

The corrosion products at several different locations were examined with the help of the electron beam microanalyzer. Results of these various analyses can be synthesized to define the elemental compositions typical of the different types of corrosion. A schematic representation of the corrosion products, based on such an overall evaluation, is provided in Fig. 13. The essential features of the corrosion products associated with the different types of corrosion are as follows. In the nonlayer-type, high-temperature form of hot corrosion, discrete sulfide particles of chromium and titanium are present in a region depleted in these elements, adjacent to the base metal. The surface scales consist of protective chromium oxide. With decreasing temperature (i.e., increasing layer type), the sulfides of chromium and titanium are increasingly agglomerated into large interconnecting sulfide networks, and the surface scales contain predominantly the oxides of nickel and cobalt. The complete layer type corrosion is characterized by the chromium and titanium sulfides forming a continuous layer. The surface scale in this case contains only the unprotective oxides of nickel and cobalt.

In addition to the general corrosion features described above, grain boundary spikes were also present in the zone of

---

[3] The layer type and transition type corrosion are also referred to in the literature as "low temperature" or "low power" hot corrosion.

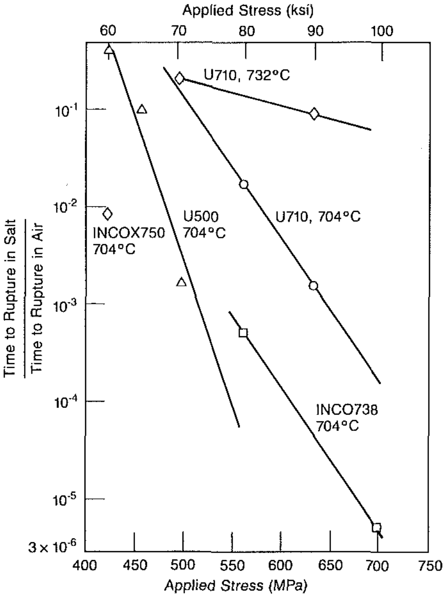

Fig .14 Rupture life degradation for superalloys due to hot corrosion at 704°C (1300°F) and 743°C (1350°F)

transition type corrosion. The spikes usually contained sulfides alone or sulfides followed by oxide penetration depending upon their location in the blade. They occurred over a narrow region, in the form of a window of spiking activity, in a manner suggestive of stress dependence.

Observations relating to hot corrosion features as described above suggest an interesting method for estimating temperature and stress patterns in uncoated service blades. Such information is valuable in the context of life assessment of the blades. Knowing the temperature distribution and using standard material properties, the creep life consumption can be estimated.

The occurrence of different forms of corrosion in the same blade at different locations has posed a major challenge for the developers of coatings to resist hot corrosion. Coating compositions need to be optimized to resist the different corrosion processes occurring at the different temperatures.

Effect of Hot Corrosion on Creep Rupture Strength

A search of published literature shows few papers dealing with the adverse effects of hot corrosion on the mechanical behavior of superalloys [14–17]. These studies have mainly addressed the issue of the nonlayer-type corrosion occurring at high temperatures.

To assess the effect of hot corrosion occurring at low temperatures (layer type), stress rupture tests were conducted on several superalloys [18] in the presence of a molten salt mixture of 47 percent $MgSO_4$, 52 percent Na_2SO_4 and 1 percent NaCl. Figure 14 depicts the variation of the ratio of time to rupture in the environment to the time to rupture in air with applied stress at 704°C. The figure shows the pronounced degradation of the stress rupture life, sometimes by a factor of as much as 10^5, due to the corrosive action of the salt mixture. There appears to be a trend for the plots to converge at low stresses, indicating that a threshold stress level may exist for each alloy, below which the rupture life may become insensitive to corrosion.

The effect of temperature on the environmental degradation of alloy Udimet 710 is also illustrated in Fig. 14. It is evident that the relative degradation in rupture life is more severe at 704°C (1300°F) than at 732°C (1350°F). Metallographic examination of the ruptured samples showed that at 704°C (1300°F), the layer-type corrosion was dominant, while in 732°C (1350°F) samples, transitional-type corrosion with severe grain boundary spiking was dominant. These features are illustrated in Fig. 15.

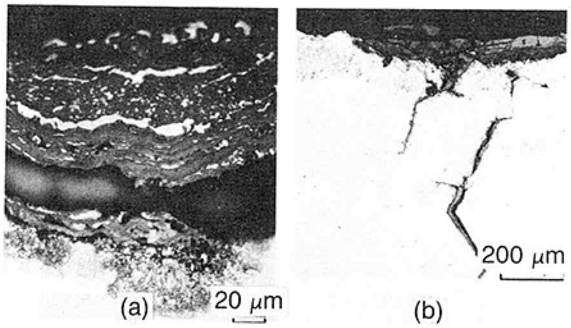

Fig. 15 Hot corrosion features in stress rupture specimens: (*a*) 704°C, 621 MPa, (*b*) 732°C, 483 MPa

The mechanism by which corrosion causes a reduction in rupture life is not clear at this time. Three possible mechanisms were considered: (1) increased stress due to reduced cross-sectional area arising from corrosion or from precipitate depletion; (2) notch effect due to formation of grain boundary spikes; and (3) incipient damage to grain boundaries by penetration of chlorine and/or sulfur. The last-cited mechanism is akin to intergranular stress corrosion cracking or embrittlement by hydrogen, wherein localized stress-assisted damage can occur in highly stressed regions and lead to low-ductility failures.

Metallographic measurements of the unaffected metal cross sections showed diameter losses that could account for stress increases only on the order of 10 to 20 percent. These increases cannot explain the very large (10^3–10^4 factor) reduction in rupture life observed. Presence of precipitate-depleted zones was often not observed. No clear correlation could be observed between the tendency to form grain boundary penetration and the rupture life. It is clear, therefore, that neither mechanism 1 nor 2 can solely be responsible for the effects reported here. A stress corrosion-type mechanism, on the other hand, could explain how localized low-ductility failures can occur without manifest evidence of damage in other parts of the specimen. It is well known that stress corrosion mechanism are very sensitive to stress and operate only when a characteristic threshold level of stress is exceeded. The tendency for the rupture curves in salt and in air to converge at low stresses, as observed in this study, is indicative of the threshold stress concept. Auger and microprobe analysis of grain boundary penetrations of samples from field blades often showed sulfur to be present well ahead of the microscopically visible portions of the penetrations. A cyclic sequence in which corrosion and creep assist each other appears to be logical. One possible sequence of events is as follows: (*a*) sulfur and/or chlorine penetrate at grain boundaries, assisted by stress, and cause embrittlement, (*b*) a small crack is initiated along the embrittled boundary, and (*c*) the embrittler now diffuses to the crack tip region of triaxial stresses and causes further embrittlement. The process can repeat itself, leading to rapid fracture of the sample. Other variants of the above sequence may also exist, resulting in a further refinement of the model. For instance, oxidation proceeding in the wake of sulfur penetration can be envisaged as an additional mechanism of driving the sulfur inward in an autocatalytic manner [19].

It must be pointed out that the laboratory test described here was intended to be an accelerated test in which the specimens were exposed to a reservoir of severe corrodents under high stresses. Environmental conditions and stresses in actual blades would be far less severe. Hence the results shown in Fig. 14 should be viewed only as an indicator of the fact that finite reductions in anticipated rupture life could occur due to environmental interactions. Hence creep life calculation procedures for blades should take into account environmental effects and not just design data obtained in air. It may be possible to develop correlation factors to do this, but considerably more laboratory studies and characterization of service blades would be needed before this can be accomplished.

Additional Research Needed

Based on the experience gained to date, which has been reviewed in this paper, a number of areas can be identified as deserving further investigation. These are itemized below:

- A data base on material properties should be established for service exposed blade materials. The relation between degradation of mechanical properties and service history should be established on a statistical basis.
- Quantitative correlations should be established between life expenditure and microstructurally observable damage features, such as creep cavities, carbide size, size of precipitates, etc. Service-exposed samples, as well as laboratory-tested samples, should be evaluated for this purpose. Development of such correlations would enable estimation of the expended life of in-service blades, based on nondestructive replication techniques.
- The potential of the replication technique should be more widely explored. For coated blades, spot coating techniques should be developed to enable field replication. Since the major component of cost in component assessment is the cost of opening and reassembly of the casing, remote techniques for replication would be desirable.
- Literature relating to other advanced nondestructive techniques for detecting incipient creep and fatigue damage should be carefully monitored. Exploration of the more promising techniques by the industry would also be useful.
- Thermomechanical fatigue studies should be continued and should address fatigue, creep, and stress relaxation damage mechanisms. Based on laboratory tests, current rules for damage summation should be carefully reviewed and improved as necessary. These laboratory studies should be validated on field machinery by comparing predictions from the laboratory models and actual incidence of damage. In this connection, the application of miniature specimens in conjunction with testing of sacrificial blades should be more fully investigated.
- The effect of corrosion resistant coatings and coating cycles on the virgin and service-degraded blade materials should be investigated more extensively.
- The interaction between hot corrosion and creep/fatigue properties under simulated turbine environments should be more fully documented, based on laboratory and field evaluations. It is anticipated that "correction factors" can be developed in life prediction to make allowance for environmental effects. The possibility of using hot corrosion mapping as a "built-in" monitor of service history should be investigated. For instance, measurement of steamside scale is widely used as a tool for estimating the remaining creep life of superheater tubes in fossil boilers.
- Refurbishment technology for blades, such as heat treatment, hot isostatic pressing, welding, and brazing should be assessed. Although considerable capabilities relating to these have been developed in recent years [4, 20–23], widespread application of these methods in the U.S. utility industry has been hampered primarily due to lack of awareness. Additionally, validation of the methods based on long-term laboratory tests and on field experience is lacking. Both these areas, i.e., technology dissemination and validation, need to be addressed. A review of refurbishment technology is beyond the scope of this paper and therefore has not been covered here in detail.

References

1 Crombie, E., McCall, W., Beck, C. G., and Moon, D. M., "Degradation of High-Temperature Impact Properties of Nickel-Base Gas Turbine Blade Alloy," *Proc. of the 12th CIMAC Conference*, Vol. C, Tokyo, 1977.

2 Pard, A. G., Kramer, D. A., and Viswanathan, R., unpublished work, EPRI Project RP1802-4, 1985.

3 Liburdi, J., and Stephens, J. O., "Experience in Extending the Life of Gas Turbine Blades," ASME Paper No. 80-GT-101.

4 Lindblom, Y., "Refurbishing Superalloy Components for Gas Turbine Components," *Materials Science and Technology*, Vol. 1, 1985, pp. 636–664.

5 Viswanathan, R., and Dooley, R. B., "Creep Life Assessment Techniques for Fossil Power Plant Boiler Pressure Parts," *Proc. of the International Conference on Creep*, Tokyo, Apr. 1986.

6 Robinson, E. L., *Trans. ASME*, Vol. 60, 1983, pp. 253–259.

7 Hart, R. V., *Metals Technology*, Vol. 3, 1976, p. 1–15.

8 Woodford, D. A., ASME *Journal of Engineering Materials and Technology*, Vol. 101, 1979, pp. 334–340.

9 Bolton, C. J., Dyson, B. F., and Williams, K. R., *Materials Science and Engineering*, Vol. 46, 1980, p. 231–245.

10 Embley, G. T., and Russel, E. S., "Thermal Mechanical Fatigue of Gas Turbine Bucket Alloys," *First Parsons International Turbine Conference*, Dublin, Ireland, June 1984, pp. 157–164.

11 Russel, E. S., "Practical Life Prediction Methods for Thermal-Mechanical Fatigue of Gas Turbine Bucket," presented at the EPRI-Syracuse University Workshop on Life Prediction, Minnowbrook, Aug. 27–30, 1985.

12 Viswanathan, R., and Beck, C. G., unpublished research, Westinghouse R&D Center, Pittsburgh, PA, 1979.

13 Viswanathan, R., and Spengler, C. J., unpublished research, Westinghouse R&D Center, Pittsburgh, PA, 1979.

14 Betz, W., "High-Temperature Alloys for Gas Turbines," in: *Applied Science*, D. Coutsouradis et al., eds., London, 1978, pp. 409–422.

15 Schmitt Thomas, Kh. G., Miesel, H., and Dorn, J. J., *Werkstoffe und Korrosion*, Vol. 29, 1978, pp. 1–9.

16 Galsworthy, J., "Environmental Degradation of High-Temperature Materials," Series 3, 13, 2, The Institution of Metallurgists, London, 1980, pp. 2/40–2/44.

17 Schmitz, F., and Keienburg, K., "Corrosion and Mechanical Stress at High Temperatures," *Applied Science*, V. Guttmann and M. Merz, eds., London, 1981, pp. 223–242.

18 Whitlow. G. A., Beck, C. G., Viswanathan, R., and Crombie, E. A., "The Effects of a Liquid Sulfate/Chloride Environment on Superalloy Stress Rupture Properties at 1300°F (704°C)," *Met. Trans.*, Vol. 15A, 1984, pp. 23–28.

19 Spengler, C. J., and Viswanathan, R., "Effect of Sequential Sulfidation and Oxidation on the Propagation of Sulfur in an 85 Ni-15 Cr Alloy," *Met. Trans.*, Vol. 3, 1972, pp. 161–166.

20 Matthew, J. H. G., "Role of Brazing in Repair of Superalloy Components—Advantages and Limitations," *Materials Science and Technology*, Vol. 1, 1985, pp. 608–612.

21 Schneider, K., Jahnke, B., Burgel, R., and Ellner, A., "Experience with Repair of Stationary Gas Turbine Blades—View of a Turbine Manufacturer," *Materials Science and Technology*, Vol. 1, 1985, pp. 613–619.

22 Keienburg, K. H., Eber, W., and Deblon, B., "Refurbishing Procedures for Blades of Large Stationary Gas Turbines," *Materials Science and Technology*, Vol. 1, 1985, pp. 620–628.

23 Bell, S. R., "Repair and Rejuvenation Procedures for Aero Gas-Turbine Hot Section Components," *Materials Science and Technology*, Vol. 1, 1985, pp. 629–634.

Journal of Engineering for Gas Turbines and Power

Technical Briefs

An Experimental Investigation of Recirculation and Interference on Modeled Forced-Draft Round Cooling Towers

G. J. Hitchman[1] and P. R. Slawson[1]

Introduction

When the heated effluent from one cooling tower is either ingested across that tower's heat exchange surface (recirculation) or that of an adjacent tower (interference), the cooling system's ability to reject waste heat may be adversely affected.

The majority of available data on recirculation and interference has been obtained at the laboratory scale for site-specific cooling towers. Reisman [4], Chan et al. [1], Onishi and Trent [3], Sullivan and Slawson [6], and Jain and Kennedy [2] have documented the following behavior: (*a*) Recirculation varies with the tower exit velocity to wind speed ratio; (*b*) the orientation of a rectangular tower to the wind strongly influences recirculation; (*c*) the three-dimensional end vortices on rectangular towers increase dilution resulting in reduced recirculation as the length-to-height ratio of a tower is decreased; (*d*) the proximity of adjacent rows of rectangular towers may increase recirculation for both the upstream and downstream towers over that of a single row of towers; and (*e*) the aerodynamic shape of a round tower with resulting smaller wake leads to significantly less recirculation than rectangular towers. The present study attempts to further quantify the effects of specific round cooling tower design features on recirculation and interference. Details on these experiments may be found in Slawson et al. [5].

Experimental Design and Technique

The objective of the physical modeling was to measure recirculation and interference and document near-field cooling tower plume behavior for combinations of three fan-packing ratios, three fan shroud heights, three splitter plate diameters, and tower separation distances of one-half (1/2*D*) and one (1*D*) tower diameter. A typical fan shroud–splitter plate configuration is shown in Fig. 2(*b*). Densimetric Froude number similarity was maintained between the tower models and proposed prototype units [5] at a constant value of 6.5. A particularly important scale parameter for near-field simulation of jets and plumes in a cross-flow is the ratio of the jet to ambient velocities *K*. This ratio was varied over a range of 0.3 to 1.6 in these experiments.

Recirculation and/or interference values for a given tower were obtained by measuring the temperatures in the ratio defined by

$$R = (T_w - T_a)/(T_j - T_a)$$

where T_w is the temperature of the water withdrawn through the tower, T_a is the ambient flume water temperature, and T_j is the tower jet discharge temperature.

Results and Discussion

Figure 1 illustrates typical results of the single tower recirculation measurements for three combinations of fan shrouds and splitter plates. Figure 2 illustrates the effects that fan shrouds and splitter plates have on the plume cross-sectional temperature distribution downstream of a single tower and on the plume ingestion at the tower intake surface as indicated by the hatched areas.

Substantial reductions in recirculation were achieved by either decreasing the fan-packing ratio, using fan shrouds or splitter plates, or combinations of the above. When an appropriate combination of the three design features was used, the average recirculation for the range of *K* values measured was reduced from about 10 percent to the point of almost total elimination (<0.1 percent). The use of splitter plates produced the single most dramatic reduction in recirculation but at low values of *K*. Splitter plates displaced laterally the tip vortices shed from the top edges of the tower. The resulting counterrotating vortex structure in the wake of the tower was thus greatly enhanced, and became more intense as the *K* value was reduced resulting in more efficient dilution of the plume within the tower wake. Figure 2(*b*) (solid arrows) illustrates the sense of the flow within the vortex structure. Fan shrouds became relatively more effective at reducing recirculation at

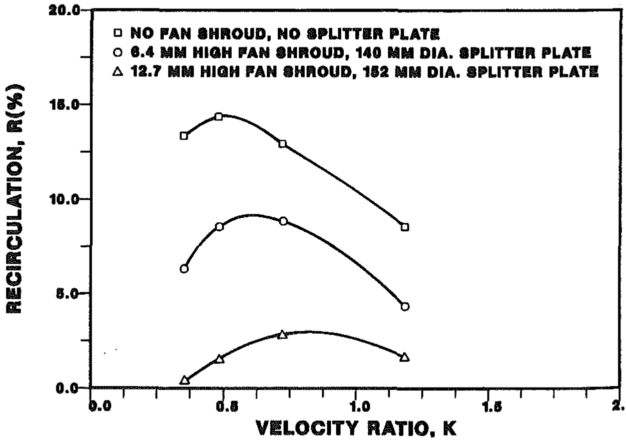

Fig. 1 Single tower recirculation as a function of velocity ratio for a fan-packing ratio of 0.9 to illustrate the effect of fan shrouds and splitter plates combined

---

[1] Department of Mechanical Engineering, University of Waterloo, Waterloo, Ontario, Canada N2L 3G1.

Contributed by the Power Division for publication in the JOURNAL OF ENGINEERING FOR GAS TURBINES AND POWER. Manuscript received by the Power Division July 31, 1985.

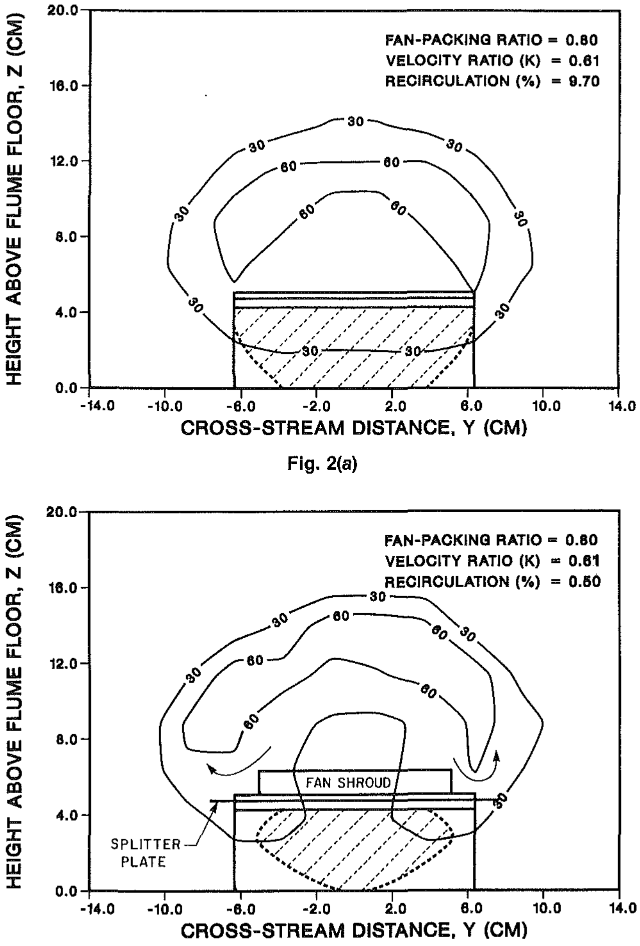

Fig. 2(a)

Fig. 2(b)

Fig. 2 Normalized cross-sectional temperature contours of 30 and 60 at 1/2 tower diameter downstream from a single tower with: (*a*) no fan shroud or splitter plate and (*b*) large fan shroud and large splitter plate

the higher *K* values while increasing fan shroud height at lower *K* values had little effect on plume-tower wake interaction and subsequently recirculation.

Recirculation and interference measurements were obtained for dual towers in-line at two tower separation distances and two *K* values (0.61 and 1.49). The use of large fan shrouds or large splitter plates alone similarly reduced the *R* ratio of the downstream tower. However, for the upstream tower, much lower *R* ratios were observed when large splitter plates were used in place of large fan shrouds. These results indicate that effective relief from recirculation and interference was achieved for both towers in a dual tower arrangement when both fan shrouds and splitter plates were used.

A comparison of *R* ratios measured at different tower spacings indicates that the upstream tower is free from the interference effects of the downstream tower at the 1*D* spacing, but not at the 1/2*D* spacing. However, the two-tower *R* ratio at the 1/2*D* spacing was typically 1/2 of that at the 1*D* spacing (without a fan shroud-splitter plate) when a fan shroud-splitter plate combination was used. With the fan shroud-splitter plate combination, increasing the tower separation distance from 1/2 to 1*D* produced a modest decrease in *R* ratio (20 percent). These results illustrate possible benefits associated with tower design modifications for reducing recirculation and interference over increasing tower separation as a design option.

Acknowledgments

This work was supported by the Electric Power Research Institute under contract RP422-2 to Union Carbide Corporation, Linde Division, New York and by the Natural Sciences and Engineering Research Council of Canada.

References

1 Chan, T. L., Hsu, S. T., Lin, J. T., Hsu, K. H., Huang, N. S., Jain, S. C., Tsai, C. E., Croley, T. E., II, Fordyce, H., and Kennedy, J. F., "Plume Recirculation and Interference in Mechanical Draft Cooling Tower," IIHR Report No. 160, Iowa Institute of Hydraulic Research, The University of Iowa, Iowa City, IA, 1974.

2 Jain, S. C., and Kennedy, J. F., "Development and Verification of Laboratory Model Techniques for Prediction of Near-Field Behaviour of Cooling-Tower Plumes," EPRI CS-1370 RP732-1, Iowa Institute of Hydraulic Research, The University of Iowa, Iowa City, IA, 1980.

3 Onishi, Y., and Trent, D. S., "Mathematical and Experimental Investigations on Dispersion and Recirculation of Plumes From Dry Cooling Towers at Wyodak Power Plant in Wyoming," BNWL-1982, Battelle Pacific Northwest Laboratories, 1976.

4 Reisman, J. I., "A Study of Cooling Tower Recirculation," ASME 93rd Winter Annual Meeting, 1972.

5 Slawson, P. R., Hitchman, G. J., and Sullivan, H. F., "Design Considerations on Round Dry Cooling Towers for Optimum Air Distribution," Final Report under EPRI RP 422-2, Envirodyne Limited, 1981.

6 Sullivan, H. F., and Slawson, P. R., "Dry Cooling Tower Design and Arrangement for Optimum Air Distribution," Final Report under EPRI RP422-2, Envirodyne Limited, 1978.